University of Strathclyde

Department of Electronic and Electrical Engineering

# Design, Analysis, and Implementation
## of
## SRM Drive for Electric Vehicles

by

**Ali A. Abdel-Aziz**

B.Sc., M.Sc.

A thesis presented in fulfilment of the requirements for the degree of

Doctor of Philosophy

2020

This thesis is the result of the author's original research. It has been composed by the author and has not been previously submitted for examination which has led to the award of any degree.

The copyright of this thesis belongs to the author under the terms of the United Kingdom Copyright Acts as qualified by University of Strathclyde Regulation 3.50. Due acknowledgement must always be made of the use of any material contained in, or derived from, this thesis.

Signed: Ali Abdel-Aziz                                                        Date: 30/07/2020

# Acknowledgement

# Contents:

# Abstract

Automobiles are regarded as a major source of greenhouse gases which cause a serious environmental problem, hence researchers are oriented towards transportation electrification. Different types of electrical machines are available for electric vehicle (EV) applications mainly; the permanent magnet synchronous motor, squirrel cage induction motor, and switched reluctance motor (SRM).

The SRM can be a suitable candidate for this function. However, high torque ripple and relatively low power density have been the justification for its non-adoption in EVs. This thesis focuses on tackling these challenges to pave the way for the SRM to penetrate the electrified transportation sector. The thesis considers the machine, the converter, and the control when facing these adoption challenges

In simplistic terms, the current into and out of an SRM (at phase current turn-on and turn-off) can be expressed by $V = L\,{di}/{dt}$. The objective is to force the current into and out of the machine as quickly as possible, that is, through maximizing the ${di}/{dt}$ term, thereby increasing the base-speed, whence output power. The inductive term $L$ is related to the machine design and specifically low $L$ is required (for $V$ fixed) at only phase turn-on (higher $L$ is required at the turn-off to maximize the machine co-energy). This task is accomplished by deploying rotor conducting screens which are basically non-magnetic electrically conducting materials such as aluminium and copper. The screens fill the rotor inter-polar air gaps. When the rotor rotates flux passes through the screen inducing voltage, whence current, which in turn generates flux opposing the original stator flux. As a result, the unaligned inductance is minimised which increases the conversion area and therefore more torque is developed. The material, thickness and shape of the screen are studied to select the optimal design that results in torque improvement. The effect on efficiency is highlighted, being an important factor in EVs. A procedure for calculating the effective value of unaligned inductance for screened motors using the flux tube method is presented. Finite element analysis results for different cases are given to validate the claims.

Another torque improvement approach is to increase ${di}/{dt}$ (at both phase turn-on and turn-off) by effectively increasing the term $V$, in $V = L\,{di}/{dt}$, which is a converter parameter. A brief review

of available power converters is presented A new asymmetric neutral-point diode-clamped converter (NPC) with inherent voltage boosting is presented. The inbuilt NPC clamping capacitors are used for both voltage level clamping and also as dc rail voltage-boosting capacitors to increase motor output power. A detailed design procedure for sizing the boost-capacitors is outlined. Simulation along with experimental results validate the proposed converter.

Different torque ripple (TR) minimization strategies including direct instantaneous torque control, torque sharing function, and current profiling using artificial neural networks are assessed using MATLAB/Simulink. The effect of voltage-boosting on minimizing TR is investigated. A new torque control function (TCF) which fully utilizes the dc link voltage is proposed. It will be substantiated that the new TCF dramatically extends the zero TR speed range, reduces switching losses, and is applicable to any SRM with overlapping phase torques.

# Acronyms

| | |
|---|---|
| AAC | Advance Angle Control |
| ANN | Artificial Neural Network |
| ASHB | Asymmetric half bridge |
| ATC | Average Torque Control |
| BEV | Battery Electric Vehicle |
| BLDC | Brushless DC Machine |
| CCC | Current Chopping Control |
| DITC | Direct Instantaneous Torque Control |
| DSP | Digital Signal Processor |
| emf | Electromotive Force |
| EV | Electric Vehicle |
| FEA | Finite Element Analysis |
| FLT | Full Load Torque |
| FPM | Ferrite Permanent Magnet |
| HBCC | Hysteresis Band Current Controller |
| HBTC | Hysteresis Band Torque Controller |
| HEV | Hybrid Electric Vehicle |
| ICE | Internal Combustion Engine |
| ILC | Iterative Learning Control |
| LUT | Look-Up Table |
| MMC | Modular Multi-Level Converter |
| MOO | Multi-Objective Optimization |
| MPC | Model Predictive Controller |
| NPC | Neutral-Point Diode-Clamped |
| pf | Power Factor |
| PM | Permanent Magnet |
| PMSM | Permanent Magnet Synchronous Machine |
| PWM | Pulse Width Modulation |

| | |
|---|---|
| SCIM | Squirrel Cage Induction Machine |
| SG | Smart Grid |
| SRM | Switched Reluctance Machine |
| SynRel | Synchronous Reluctance Machine |
| TCF | Torque Control Function |
| TR | Torque Ripple |
| TSF | Torque Sharing Function |

# List of symbols

| | |
|---|---|
| a | Neural Network Input |
| A | Cross-Sectional Area |
| A | Constant of the Current c/cs Equation |
| B | Flux Density |
| b | Neural Network Bias |
| $B_{fric}$ | Coefficient of Friction |
| $b_{ry}$ | Rotor Back Iron |
| $b_{sy}$ | Stator Back Iron |
| c | Neural Network Weight |
| $C_d$ | Dump Capacitor |
| $C_{eq}$ | Equivalent Capacitance |
| $dW_e$ | Incremental Increase in Input Electrical Energy |
| $dW_f$ | Change in Stored Field Energy |
| $dW_f'$ | Change in Coenergy |
| $dW_m$ | Part of Energy Converted into Mechanical Energy |
| d | Rotor Outer Diameter |
| D | Stator Outer Diameter |
| $D_{sh}$ | Shaft Diameter |
| e | Induced Voltage |
| f | Neuron Transfer Function |
| F | Set of Pareto Frontier |
| $f_s$ | Sampling Frequency |
| $f_{sw}$ | Switching Frequency |
| $h_r$ | Rotor Pole Height |
| $h_s$ | Stator Pole Height |
| i | Current |
| $I_p$ | Phase Winding Initial Current |

| | |
|---|---|
| J | Rotor Inertia |
| k | Number of objectives in MOO problems |
| K | Constant Representing the Product of Electrical and Magnetic Loading of SRM |
| $K_d$ | SRM Duty cycle |
| l | Magnetic Flux Path Length |
| $l_g$ | Air Gap Length |
| $L_{axial}$ | SRM Axial Length |
| $L_{end}$ | Coil End Length |
| $L_s$ | Stack Length |
| L | Phase Winding Inductance |
| $L_0, L_1, L_2$ | Coefficients for Calculating Inductance |
| $L_A, L_B, ...$ | Bifilar Winding Inductances |
| $L_a$ | Aligned Inductance |
| $L_d$ | Dump Inductor |
| $L_m$ | Half Way Inductance |
| $L_u$ | Unaligned Inductance |
| m | Number of Phases |
| n | Number of Phases Conducting Simultaneously |
| N | Number of Turns per Stator pole |
| $N_s$ | Number of Stator Poles |
| $N_r$ | Number of Rotor Poles |
| p | Pole of the Current Characteristic Equation |
| P | Power |
| Q | Number of Solutions |
| r | Net Input |
| R | Phase Winding Resistance |
| $R_d$ | Dump Resistor |
| $R_{eq}$ | Equivalent Resistance |
| $R_g$ | Air Gap Reluctance |

| | |
|---|---|
| $R_{rp}$ | Rotor Pole Reluctance |
| $R_{ry}$ | Rotor Back Iron Reluctance |
| $R_{sp}$ | Stator Pole Reluctance |
| $R_{sy}$ | Stator Back Iron Reluctance |
| s | Neural Network Output |
| T | Individual Phase Torque |
| $T_e$ | Total Developed Torque |
| $T_L$ | Load Torque |
| $T_{dem}$ | Demand Torque |
| $t_{off}$ | SRM Winding Current Decay Time |
| U | Set of Solutions |
| $V_{DC}$ | DC link Voltage |
| y | Number of Inequality Constraints in MOO |
| z | Number of Equality Constraints in MOO |
| α | Duty Cycle |
| $\beta_r$ | Rotor Pole Arc |
| $\beta_s$ | Stator Pole Arc |
| δ | Weight factor |
| η | Efficiency |
| μ | Permeability of Air |
| $\mu_r$ | Relative Permeability of Fe |
| θ | Rotor Position |
| $\theta_a, \theta_u$ | Aligned/Unaligned Rotor Position |
| $\theta_{off}, \theta_{on}$ | Turn Off, Turn On Angle |
| $\theta_{ov}$ | Overlap Angle |
| $\theta_r, \theta_s$ | Rotor/Stator Pole Pitch |
| $\theta_{stroke}$ | Stroke Angle |
| λ | Flux Linkage |
| φ | Flux |
| $\omega, \omega_n$ | Rotor Speed, rad/s and rpm |

# *Chapter 1*

## *Introduction*

---

This chapter presents a brief overview to the thesis, highlighting the motivation behind the research. An introduction to electric vehicles points out the requirements to be satisfied when selecting an electric motor for propulsion. Based on this specification, the switched reluctance machine is selected. The last section summaries the structure of the thesis.

### 1.1    Background and motivation

The global climate change crisis has caused researchers to explore cleaner energy systems. The transportation sector is second placed in carbon emission. Hence, researchers are oriented towards transportation electrification. The penetration of electric vehicles (EVs) could drastically reduce the greenhouse emissions resulting in a greener environment [1-1]. Fig. 1.1 shows the expected reduction in greenhouse gas emissions between 2020 and 2030 by electrification of transportation system. More than 500 Megatons $CO_2$ equivalent is anticipated to be removed [1-2].
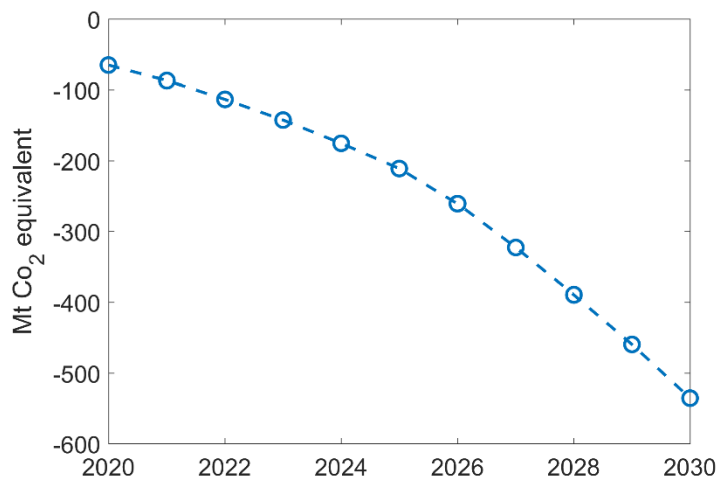
Fig. 1.1 Avoided greenhouse gases emissions forecast

An EV could solely depend on a battery as a power source, whence it is termed a battery electric vehicle (BEV). Alternatively, and predominately, the EV could be equipped with an internal combustion engine (ICE) and a battery source, termed a hybrid electric vehicle (HEV). In BEV, the vehicle range covered depends on the storage magnitude of the battery which limits the range to about 500km [1-3]. The absence of ICE in BEVs offers lower noise with much lower pollution, as opposed to HEV. Hence, BEVs are better suited for urban cycles. Fig. 1.2 shows the main components comprising a BEV. In simplistic form, BEV consists mainly of a battery, an on/off-board battery charger, a power converter, and the propulsion motor.
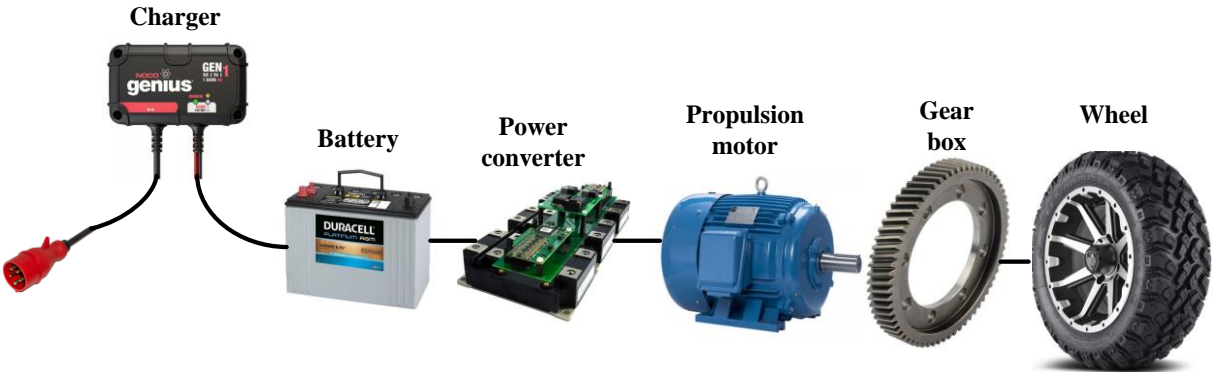


Fig. 1.2 Main components in BEV
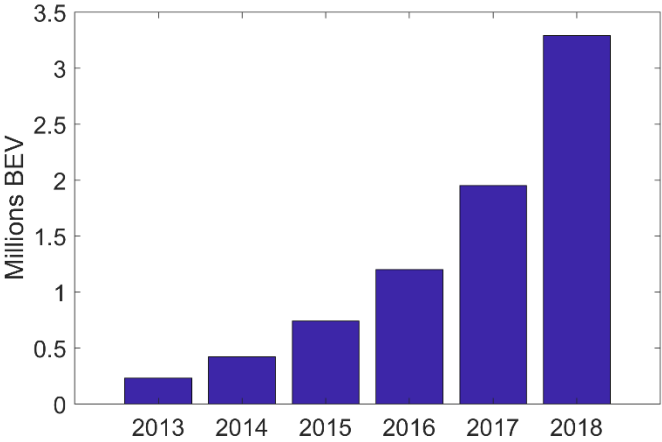


Fig. 1.3 BEV utilization worldwide between 2013 and 2018

Fig. 1.3 shows the penetration of BEVs worldwide over five years between 2013 and 2018. The deployment of BEV in 2018 is almost 13 times that in 2013. These results show that BEVs are

2

gaining much interest in the market. Moreover, it is expected that passenger low-duty BEVs will reach about 150 million by 2030 as illustrated in Fig. 1.4.
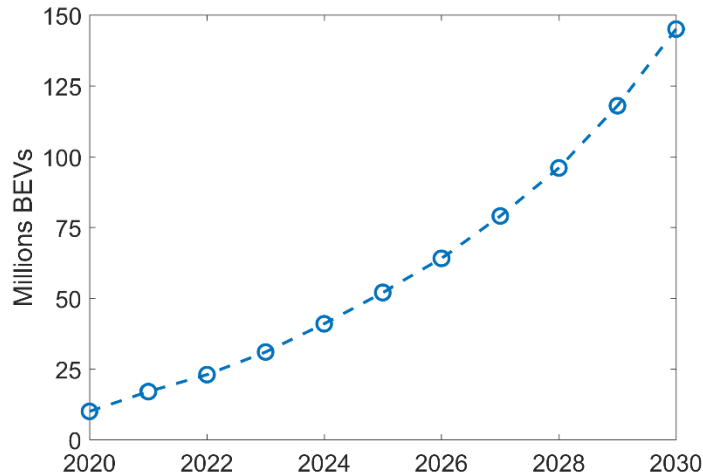


Fig. 1.4 Passenger low-duty BEV forecast

A merit aiding the penetration of EVs is that they could be integrated into smart grids (SGs), thus representing a portable storage system. EVs could be charged during off peak periods and then used as a power source during peak periods.

Apart from using batteries as the main power source, fuel cells could be used to provide the required power [1-4]. The chemical reaction between hydrogen and oxygen generates electricity to drive the propulsion motor. Any excess energy is stored in batteries or ultra-capacitors. Water, which is the by-product of the chemical reaction, is ejected through tailpipes.

Generally, three levels of charging are available for charging EVs [1-5]. Level 1 charging, which represents the slow mode, is available from single-phase 230V outlets (usually takes place in private garages overnight). However, no special power outlets are needed and an on-board charger is sufficient. A three-phase 400V ac power supply is used for the level 2 charging mode, which provides a faster and shorter charging time. For rapid EV charging (level 3 - about half an hour), 600V DC is deployed. Both level 2 and 3 charging require an off-board battery charger. Fig. 1.5 shows battery charger installations in the world between 2013 and 2018, where more than 5 million

battery chargers were installed by 2018. Although private slow chargers hold the lions share, slow and fast public chargers are gaining interest.
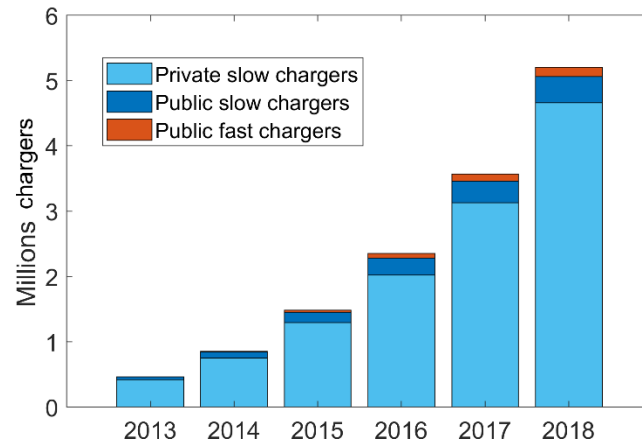


Fig. 1.5 Battery charger installations worldwide between 2013 and 2018

## 1.2    Electric motor for vehicle propulsion

The electric motor is the core of the EV, hence it should satisfy certain specifications, namely;

- High power density (W/kg and W/$m^3$).
- High torque density (N.m/kg and N.m/$m^3$).
- High torque to inertia ratio.
- High efficiency.
- Compact size and low weight.
- Low cost.
- Robust and fault-tolerant.
- Wide constant torque/speed range.
- Low vibration and acoustic noise.

Different types of electrical machines are available for EV applications [1-6]. In the following subsections the merits and limitations of each machine are highlighted.

4

### 1.2.1    DC motor

DC motor, which is one of the old members in the family of electrical machines, could perform the EV task due to its torque-speed profile that fits with the traction requirements in addition to its simple speed control. Citroen Berlingo is an EV which utilizes the DC machine. However, it has a large heavy structure, low efficiency and reliability. The need for brush maintenance reduces its competitiveness in the EV market.

### 1.2.2    Squirrel cage induction motor (SCIM)

Power electronics breakthroughs paved the way for AC machines to set foot in industry and hence propulsion applications. The squirrel cage induction motor (SCIM) has a rugged, simple construction, with low cost and low maintenance and is one of the most developed competitors in EV market. Nevertheless, it has a narrow torque-speed characteristics due to its breakdown torque characteristics. Its cooling process is complicated as heat is generated in the rotor copper bars. Also, the IM has low fault tolerance due to magnetic coupling between distributed stator windings. Low efficiency and low power factor especially at light loads, along with low inverter utilization are major shortcomings that are yet to be resolved. Renault Kangoo, Chevrolet Silverado, Dodge Durango and BMW X5 are examples of IM-based EVs [1-7].

### 1.2.3    Permanent magnet synchronous motor (PMSM)

One salient feature of the permanent magnet synchronous motor (PMSM) is its high power density due to the inherent PM excitation which is not present in the SCIM. The PMSM offers a wide torque-speed range with high efficiency. Hence, it is considered the first-choice traction motor [1-8]. The PMSM is adopted as the propulsion motor in the Nisan leaf, Hyundai Sonata, Honda Accord and Toyota Prius which is one of the best-selling EVs. However, PMs are prone to demagnetization, thereby it has low fault tolerance. Supply limitations and escalating rare-earth material prices for the PMSM has forced the market to search for suitable electrical machine alternatives. Ferrite permanent magnets do not represent an alternative to rare-earth magnets. They only offer one third of the residual flux, can be easily demagnetized, and have a lower torque density than rare earth PMs [1-9]. Consequently, research is focusing on magnet-free machines.

### 1.2.4    Synchronous reluctance motor (SynRel)

Using the synchronous reluctance motor (SynRel) as the main drivetrain is possible as this type of motor, generally, does not contain permanent magnets (PM) in its construction [1-10]. However, this motor is characterized by low pf (which increases the converter VA), high core loss, high torque ripple, low efficiency, and low torque density [1-11]. Improving torque density of SynRel machines is possible with the aid of PM as in BMW i3 and the tesla model 3.

### 1.2.5    Switched reluctance motor (SRM)

The switched reluctance motor (SRM) is a dark horse in this arena [1-12]. It has advantages of a stable, robust and simple structure with low cost. Its fault-tolerant capability, high torque, and wide constant power range are some SRM merits. The absence of PMs (which do not result in a mechanically, thermally, and environmentally stable rotor) and rotor windings simplifies the motor geometry; thus, facilitating the cooling process as most heat is generated in the stator. Moreover, this allows the motor to operate in harsh environments and at high rotor temperatures [1-13]. The Holden Commodore is an example of EVs utilizing SRM.

Recent developments in the design of high power SRM for EV are promising [1-14]. Using a low-loss super core significantly improves the efficiency of the SRM to be equal, if not better than, an equivalent sized PMSM. However, the low-loss material has lower saturation flux density which reduces the torque density implying some geometrical optimization to improve the efficiency without sacrificing the torque density. The new designs are competitive with the PMSM with respect to power density, efficiency and torque-speed range [1-15].

Fig. 1.6 shows some commercial EVs, while Table 1.1 gives a brief comparison between the SCIM, PMSM and SRM.

| (a) Citroen (DC) | (b) Dodge (SCIM) | (c) Toyota (PMSM) | (d) BMW (SynRel) | (e) Holden (SRM) |
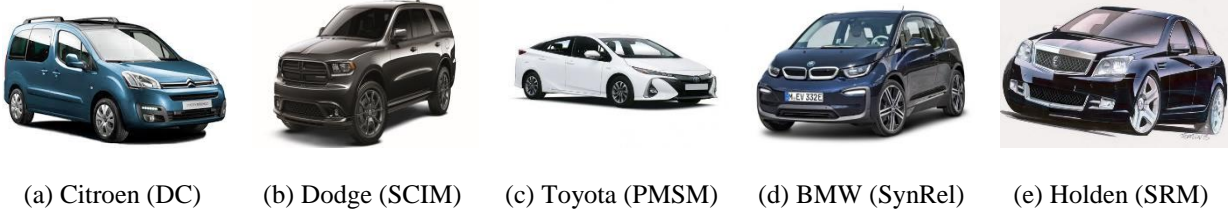
Fig. 1.6 Commercial EVs

Table 1.1 COMPARISON BETWEEN DIFFERENT PROPULSION MOTORS

|  | SCIM | PMSM | SRM |
| --- | --- | --- | --- |
| Size | Moderate | Moderate | Compact |
| Weight | Moderate | Moderate | Low |
| Cost | Low | High | Low |
| Ruggedness | High | Low | High |
| Power density | Moderate | High | Moderate |
| Constant torque speed range | Moderate | Wide | Wide |
| Efficiency | Low | High | Moderate |
| Permanent magnets | No | Yes | No |
| Power factor | Low | High | Low |
| Cooling | Complicated | Moderate | Simple |
| Fault tolerance | Low | Low | High |
| Torque ripple | Low | Low | High |
| Noise and vibration | Low | Low | High |
| Power converter | Modular | Modular | Specific |

Despite the merits of the SRM, there are still some limitations which hamper the rapid penetration of SRMs in the EV market. The main drawbacks are lower power density when compared with equivalent sized PMSM and highly non-linear characteristics, resulting in high torque ripple (TR) which in turn generates undesirable vibration [1-16]. All EVs need a power converter but that for the SRM differs from the conventional EV converter, whether SCIM or PMSM based.

## 1.3     Objectives of the thesis

The aim of the thesis is to develop an SRM drive, as illustrated in Fig. 1.6, to be competitive with an equivalent PMSM drive, for EV applications. The proposed drive should satisfy the mentioned specifications where the SRM drawbacks must be alleviated.
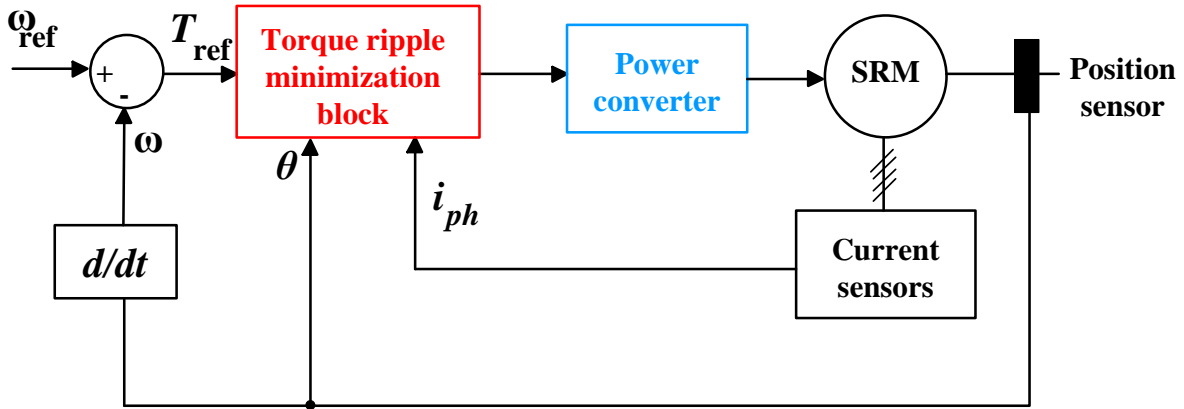
Fig. 1.7 SRM drive

The main components of an SRM drive are: the electrical machine (motor/generator) for electromechanical energy conversion, a reversible power converter to appropriately energize the phase windings, and finally a torque controller (incorporating ripple minimization). The thesis covers all the major parts of the drive. The motor design aspect is studied, where rotor conducting screens are employed to improve the torque density of the motor. A power converter is proposed which increases the base speed of the SRM, and hence extends the constant power region and increases the SRM power density. Also, the problem of torque ripple is studied. A new torque control function (TCF) is proposed to extend the zero TR speed range.

## 1.4    Outlines of the thesis

The thesis is composed of nine chapters, which are briefly summarized as follows:

➤ *Chapter 1* gives a brief introduction on EVs and the available motors used for propulsion. Justification of why this SRM research needs to be conducted is presented.

➤ *Chapter 2* highlights the construction and salient electromagnetic features of the SRM. A guide on designing SRMs is presented. Control methods below and above base speed are demonstrated.

➤ *Chapter 3* reviews available SRM power converters. The merits and drawbacks of each converter are given. Emphasis is given to power converters which can enhance the power capability of the SRM by increasing the base speed.

8

➢ *Chapter 4* proposes a new asymmetric neutral-point diode-clamped converter with inherent dc link voltage-boosting for SRM drives. Analysis of different modes of converter operation, along with design equations for sizing the voltage-boosting capacitors, are detailed. Simulation and experimental results will validate the effectiveness of the proposed converter.

➢ *Chapter 5* studies the concept of rotor conducting screens for torque density improvement of the SRM. A procedure for calculating the unaligned inductance for screened SRM using the flux tube method is detailed. Finite element analysis (FEA) results confirm the validity of the proposed method.

➢ *Chapter 6* explores the effect of thickness, material, and shape of rotor conducting screens on SRM performance. A multi-objective optimization (MOO) problem based on the concept of non-dominated sorting is formulated to elicit the optimal screen with respect to the developed torque, efficiency and weight of added material. FEA results for different screens are presented. Finally, a section is devoted to investigate SRM performance with rotor conducting screens fed by the dc link voltage-boost converter.

➢ *Chapter 7* represents analysis and a survey of the different approaches and methods for reducing SRM torque ripple. Two main categories are highlighted namely; the machine design approach and the control approach. Some control methods are selected, discussed and assessed using simulations.

➢ *Chapter 8* presents a new TR minimization approach for SRM drives. The new approach is based on maximum utilization of available dc link voltage (either with or without voltage-boosting). The new method extends significantly the zero TR speed range. Moreover, the concept is generalized to allow more than two phases conducting simultaneously.

➢ *Chapter 9* highlights the main conclusions, contribution, and gives insight into possible future SRM research for EV applications.

## References

[1-1] S. Habib, M. Khan, F. Abbas, L. Sang, M. Shahid, and H. Tang, "A Comprehensive Study of Implemented International Standards, Technical Challenges, Impacts and Prospects for Electric Vehicles," in *IEEE Access*, vol. 6, pp. 13866-13890, 2018.

[1-2]   IEA (2019), Global EV Outlook 2019, IEA, Paris https://www.iea.org/reports/global-ev-outlook-2019.

[1-3]   F. Un-Noor, S. Padmanaban, L. Mihet-Popa, M. Mollah, and E. Hossain, "A Comprehensive Study of Key Electric Vehicle (EV) Components, Technologies, Challenges, Impacts, and Future Direction of Development," *Energies* 2017, 10, 1217.

[1-4]   C. Chan, "The State of the Art of Electric, Hybrid, and Fuel Cell Vehicles," in *Proceedings of the IEEE*, vol. 95, no. 4, pp. 704-718, April 2007.

[1-5]   S. Alshahrani, M. Khalid, and M. Almuhaini, "Electric Vehicles Beyond Energy Storage and Modern Power Networks: Challenges and Applications," in *IEEE Access*, vol. 7, pp. 99031-99064, 2019.

[1-6]   E. Bostanci, M. Moallem, A. Parsapour, and B. Fahimi, "Opportunities and Challenges of Switched Reluctance Motor Drives for Electric Propulsion: A Comparative Study," in *IEEE Transactions on Transportation Electrification*, vol. 3, no. 1, pp. 58-75, March 2017.

[1-7]   M. Zeraoulia, M. E. H. Benbouzid, and D. Diallo, "Electric Motor Drive Selection Issues for HEV Propulsion Systems: A Comparative Study," in *IEEE Transactions on Vehicular Technology*, vol. 55, no. 6, pp. 1756-1764, Nov. 2006.

[1-8]   P. Ramesh, and N. C. Lenin, "High Power Density Electrical Machines for Electric Vehicles—Comprehensive Review Based on Material Technology," in *IEEE Transactions on Magnetics*, vol. 55, no. 11, pp. 1-21, Nov. 2019.

[1-9]   A. Chiba, and K. Kiyota, "Review of research and development of switched reluctance motor for hybrid electrical vehicle," 2015 *IEEE Workshop on Electrical Machines Design, Control and Diagnosis (WEMDCD)*, Torino, 2015, pp. 127-131.

[1-10] N. Bianchi, S. Bolognani, E. Carraro, M. Castiello, and E. Fornasiero, "Electric Vehicle Traction Based on Synchronous Reluctance Motors," in *IEEE Transactions on Industry Applications*, vol. 52, no. 6, pp. 4762-4769, Nov.-Dec. 2016.

[1-11] G. Kumar, C. Chuang, M. Lu, and C. Liaw, "Development of an Electric Vehicle Synchronous Reluctance Motor Drive," in *IEEE Transactions on Vehicular Technology*.  DOI 10.1109/TVT.2020.2983546.

[1-12] K. Rahman, B. Fahimi, G. Suresh, A. Rajarathnam, and M. Ehsani, "Advantages of switched reluctance motor applications to EV and HEV: design and control issues," in *IEEE Transactions on Industry Applications*, vol. 36, no. 1, pp. 111-121, Jan.-Feb. 2000.

[1-13] S. Wang, Q. Zhan, Z. Ma, and L. Zhou, "Implementation of a 50-kW four-phase switched reluctance motor drive system for hybrid electric vehicle," in *IEEE Transactions on Magnetics*, vol. 41, no. 1, pp. 501-504, Jan. 2005.

[1-14] A. Chiba, K. Kiyota, N. Hoshi, M. Takemoto, and S. Ogasawara, "Development of a Rare-Earth-Free SR Motor With High Torque Density for Hybrid Vehicles," in *IEEE Transactions on Energy Conversion*, vol. 30, no. 1, pp. 175-182, March 2015.

[1-15] K. Kiyota, T. Kakishima, and A. Chiba, "Comparison of Test Result and Design Stage Prediction of Switched Reluctance Motor Competitive With 60-kW Rare-Earth PM Motor," in *IEEE Transactions on Industrial Electronics*, vol. 61, no. 10, pp. 5712-5721, Oct. 2014.

[1-16] M. Takeno, A. Chiba, N. Hoshi, S. Ogasawara, M. Takemoto, and M. A. Rahman, "Test Results and Torque Improvement of the 50-kW Switched Reluctance Motor Designed for Hybrid Electric Vehicles," in *IEEE Transactions on Industry Applications*, vol. 48, no. 4, pp. 1327-1334, July-Aug. 2012.

# *Chapter 2*

# *SRM Fundamentals*

---

This chapter introduces the construction and theory of operation of the SRM. The principle of torque production is discussed along with the machine equivalent circuit. SRM control methods are demonstrated over the entire speed range. Finally, SRM design steps are detailed.

## 2.1 Construction

The SRM is one of the oldest members in the family of electrical machines. The first SRM can be traced back in Glasgow, Scotland in 1838. Simply, it is a double salient machine (both the stator and rotor have salient poles usually made of laminated silicon steel) with a concentrated winding on the stator poles, and neither windings nor permanent magnets on the rotor poles. Each two opposite stator poles are connected either in series or in parallel forming a phase. When the proper stator poles are excited, rotor poles tend to rotate (align with stator poles) to minimize the reluctance of the flux path. Proper, and sequential excitation of stator poles allows continuous rotation of the rotor.

Different combinations for the number of stator and rotor poles ($N_s$, and $N_r$ respectively) are available, some of the researched combinations are summarized as follows [2-1], where *m* is number of phases:

- Single-phase (*m*=1φ) SRM: 2/2
- Two-phase (*m*=2φ) SRM: 4/2
- Three-phase (*m*=3φ) SRM: 6/4, 6/8, 12/8, 18/12, 24/16
- Four-phase (*m*=4φ) SRM: 8/6, 8/10, 16/12, 24/18
- Five-phase (*m*=5φ) SRM: 10/8, 10/12
- Six-phase (*m*=6φ) SRM: 12/10, 12/14

Fig. 2.1 shows a cross section of a 4φ 8/6 SRM having a stack length $L_s$. $D_{sh}$, $d$, $D$ are the shaft diameter, rotor diameter, and outer stator diameter respectively. $h_s$, $h_r$ are the stator and rotor pole

heights respectively. $b_{sy}$, $b_{ry}$ are the stator and rotor back iron respectively. $\beta_s$, $\beta_r$ are the stator and rotor pole arcs respectively. $l_g$ is the air gap length. Number of turns per stator pole is $N$.
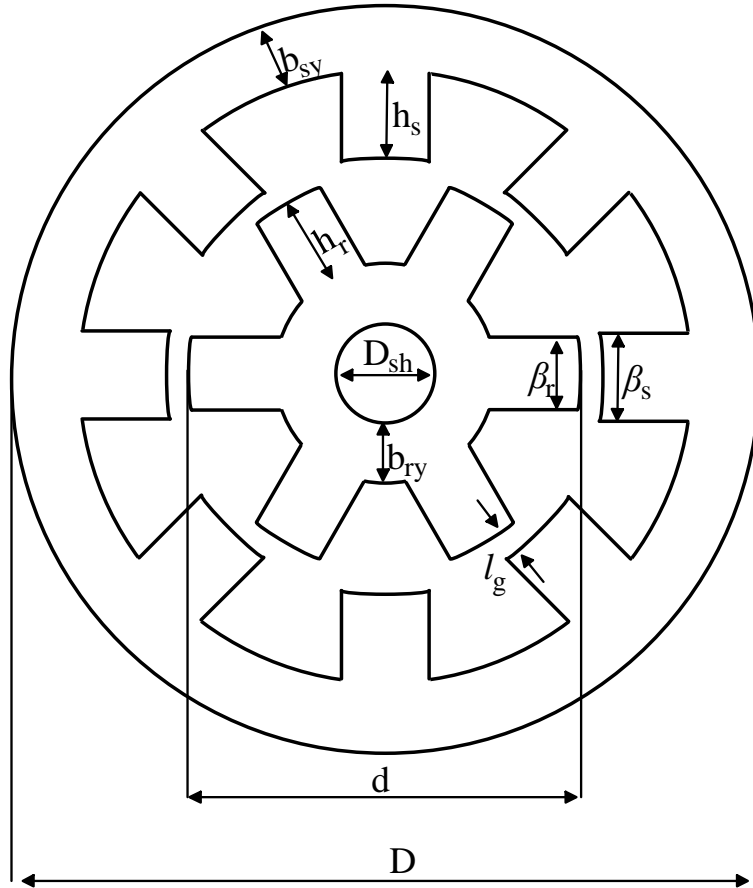


Fig. 2.1 Cross section of 4 8/6 SRM

## 2.2   SRM Torque production

Since SRM is a double salient machine, then phase winding inductance is dependent on rotor position and current excitation level. Torque is produced by the tendency of a rotor pole to align with the excited stator pole so that the reluctance of the magnetic flux path is minimum. The basics of electromechanical energy conversion are sufficient to explain the process of SRM torque production [2-2]. Fig. 2.2 shows the flux linkage – current, $\lambda$–$i$, characteristics for two rotor positions namely; the aligned and unaligned positions. The reluctance of air gap dominates the unaligned reluctance; thus, the $\lambda$-$i$ characteristic is linear, but the reluctance of the core cannot be neglected for the aligned position and therefore the $\lambda$-$i$ characteristic becomes non-linear.
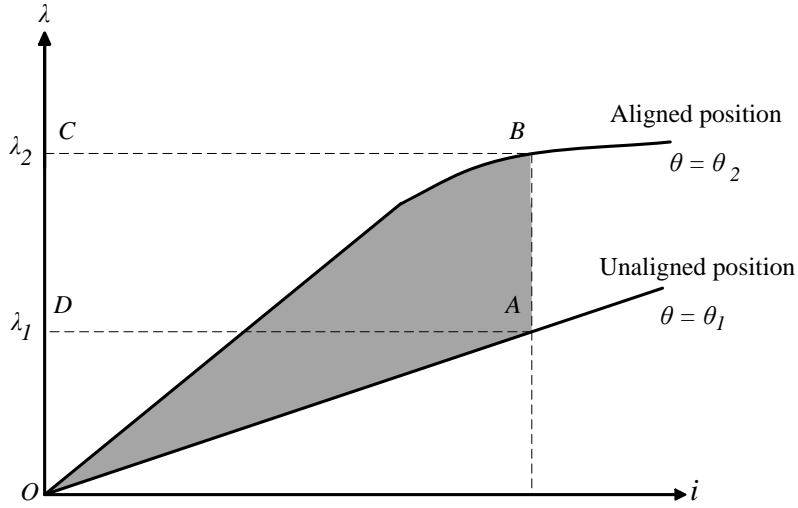
Fig. 2.2 Flux linkage - current ($\lambda$-$i$) characteristics

The energy balance equation for the electromechanical system is given by (2.1).

$$\text{Electrical } i/p = \text{mechanical } o/p + \text{increase in stored field energy} + \text{losses} \qquad (2.1)$$

Considering a differential time $dt$ and ignoring system losses, (2.2) holds.

$$dW_e = dW_m + dW_f \qquad (2.2)$$

where

$dW_e$ represents the incremental increase in input electrical energy in time interval $dt$

$dW_m$ represents the part of energy converted into mechanical energy in time interval $dt$

$dW_f$ represents the change in stored field energy in time interval $dt$

When the rotor moves from the unaligned position to the aligned position, thereby minimizing the reluctance of the flux path, the incremental change in input electrical power is given by:

$$dW_e = \int ei\, dt = \int_{\lambda_1}^{\lambda_2} i\, d\lambda = area\ ABCD \qquad (2.3)$$

The change in stored field energy is given by:

$$dW_f = area\ OBC - area\ OAD \qquad (2.4)$$

The change in mechanical energy is calculated using (2.2) - (2.4) and given by (2.5)

$$dW_m = area\ OAB = dW_f' \qquad (2.5)$$

The area OAB is the increase in co-energy from the unaligned to aligned positions. If $T$ is the torque causing the differential angular displacement $d\theta$, then the torque can be defined as:

$$T = \frac{\partial W_f'}{\partial \theta} \qquad (2.6)$$

where the co-energy is obtained from (2.7).

$$W_f' = \int_0^i \lambda\, di \qquad (2.7)$$

If saturation is neglected (which is not the practical case, but for simplification) the $\lambda$-$i$ characteristics is linear and the flux linkage $\lambda$ can be expressed in terms of inductance $L$ as defined by (2.8).

$$\lambda = Li \qquad (2.8)$$

The torque equation is then simplified to:

$$T = \frac{1}{2} i^2 \frac{\partial L}{\partial \theta} \qquad (2.9)$$

Although (2.9) is a simplified version of the torque equation, some useful conclusions are:

- Torque production depends on current squared. This feature allows controlling each phase winding with a single switch since the current need not be bipolar. Hence, an economical power converter is possible, especially for home appliance applications. Also, the SRM develops a high starting torque, as with DC series motors.

15

- The rate of change of inductance with rotor position determines the sign of the torque. Thus negative (generating/braking) torque is possible enabling four-quadrant operation of the machine.

- The torque production is a discrete process which gives rise to undesirable torque ripple. A mutual effect between phase windings is minimal; Hence, may be neglected without affecting the fidelity of the SRM model.

- SRM winding independence increases machine fault tolerance. Therefore, operation is possible even with a faulted winding.

- One outstanding SRM feature is that there need be no converter shoot-through failure mode (as opposed to conventional 3φ motors fed by a DC-AC inverter) even when there is a power switch short circuit.

Fig. 2.3 shows a typical inductance profile (inductance is assumed to vary linearly with rotor position, that is, core saturation is ignored).

where $\theta_r$ is the rotor pole pitch $= {}^{2\pi}/N_r$ and $L_u$ and $L_a$ are the unaligned and aligned (unsaturated) inductances respectively.
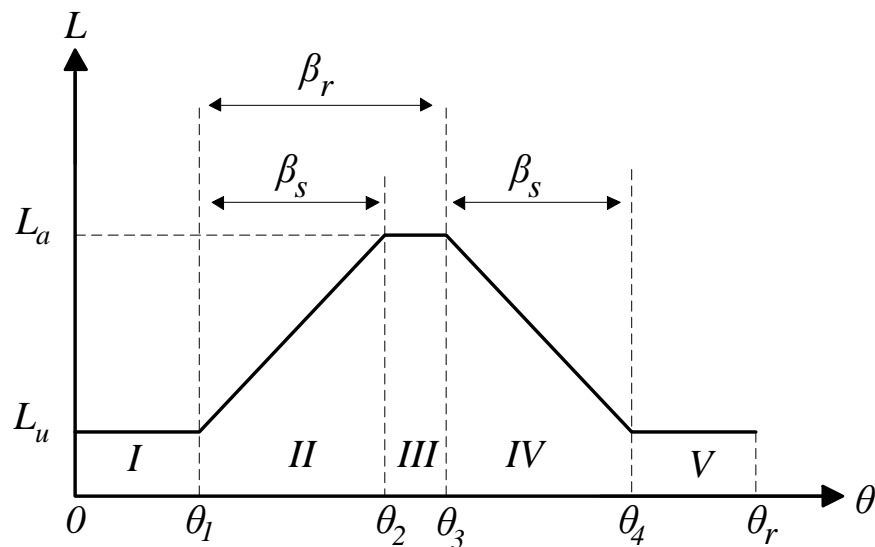


Fig. 2.3 Typical inductance profile

The relevant angles in Fig. 2.3 are defined by

16

$$\theta_1 = \frac{1}{2}(\theta_r - \beta_r - \beta_s) \tag{2.10}$$

$$\theta_2 = \theta_1 + \beta_s \tag{2.11}$$

$$\theta_3 = \theta_2 + \beta_r - \beta_s \tag{2.12}$$

$$\theta_4 = \theta_3 + \beta_s \tag{2.13}$$

The SRM inductance profile is divided into five regions as follows:

i.  $0 - \theta_1$: In this region, the inductance is a minimum, which is the unaligned inductance. No torque can be produced as the inductance is fixed, that is, no change in inductance with respect to rotor position- as per (2.9).

ii.  $\theta_1 - \theta_2$: Overlap between stator and rotor poles takes place, the inductance starts to increase from its minimum unaligned value to the maximum aligned value. Since the rate of change of inductance with respect to rotor position is positive, that is, $\frac{\partial L}{\partial \theta} > 0$, the SRM is operating in the motoring mode producing positive torque if current is injected into the phase winding.

iii.  $\theta_2 - \theta_3$: Complete overlap between stator and rotor poles occurs and the inductance is the aligned value. With no change in inductance with respect to rotor position, no torque is developed. This region depends on the ratio between stator and rotor pole arcs. This region does not exist if both the stator and rotor have the same pole arc.

iv.  $\theta_3 - \theta_4$: The rotor pole moves away from the stator pole decreasing their overlap area. Hence the rate of change of inductance with respect to rotor position is negative, producing a negative (generating/braking) torque provided that current exists in the machine winding.

v.  $\theta_4 - \theta_r$: This region is as the first region and it does not contribute to torque production.

## 2.3   SRM Equivalent circuit and model

Since the interaction between SRM phase windings is minimal, the mutual effect between different phases is ignored, and the voltage equation is expressed by (2.14).

$$V_{DC} = iR + \frac{d\lambda}{dt} \tag{2.14}$$

where $V_{DC}$ is the dc link voltage and $R$ is the phase resistance.

17

The rate of change of flux linkage can be divided into two parts, and then the voltage equations is defined by:

$$V_{DC} = iR + L\frac{di}{dt} + i\omega\frac{dL}{d\theta} \tag{2.15}$$

where $\omega$ is the rotor speed (rad/s).

The three terms on the right-hand side in (2.15) represent the winding resistive voltage drop, the inductive voltage drop, and back electromotive force (emf) of the SRM respectively. Fig. 2.4 shows the equivalent circuit for a single phase of the SRM.
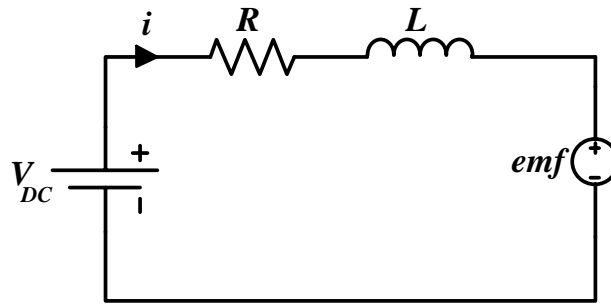


Fig. 2.4 Single phase equivalent circuit for SRM

The total developed torque, $T_e$, is the summation in time of all phase torques and defined by (2.16).

$$T_e = \sum_{1}^{m} T(i,\theta) \tag{2.16}$$

Finally, the equation of mechanical motion is:

$$T_e = J\frac{d\omega}{dt} + B_{fric}\omega + T_L \tag{2.17}$$

where $J$ is the rotor inertia, $B_{fric}$ is the coefficient of friction, and $T_L$ is the load torque.

Due to the high non-linearity of the SRM, developing a mathematical model is a tedious task. Hence, 2D look-up tables (LUTs) are used to store $\lambda$-$i$-$\theta$ characteristics and $T$-$i$-$\theta$ characteristics. These facilitate an accurate model that accounts for non-linearity and avoids a sophisticated

18

mathematical model. The data used to create the look-up tables is obtained either experimentally or from FEA. The simulation diagram for a single phase of an SRM using LUTs is shown in Fig. 2.5.
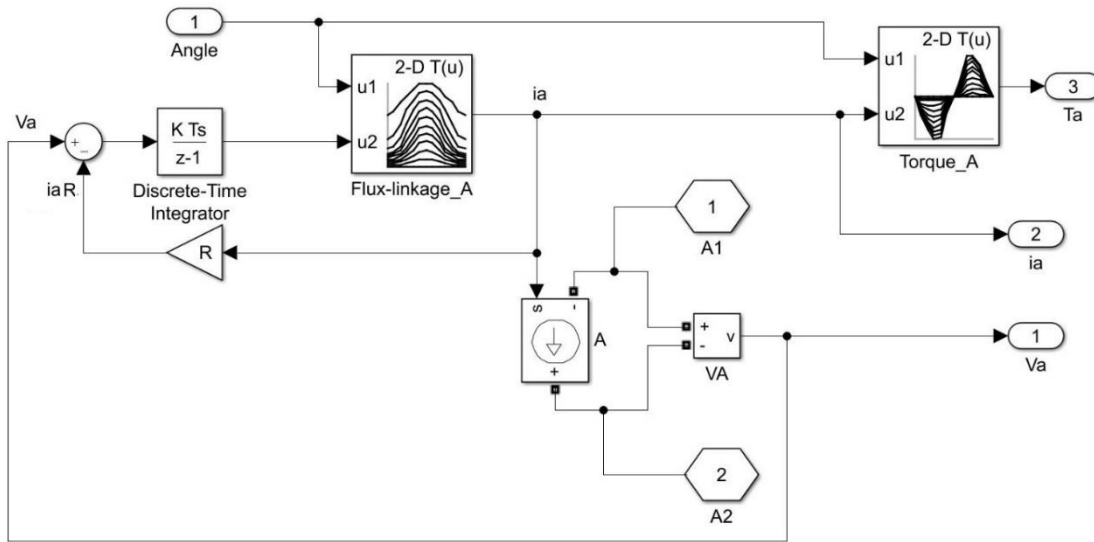


Fig. 2.5 Simulation diagram for a single phase of an SRM

## 2.4    SRM control

The control method depends on the motor speed [2-3]. Below the motor base speed (the speed at which the back emf equals the dc link voltage), current chopping control (CCC) is used. With this control technique, the motor develops its rated torque, and the speed is controlled from zero to base speed by controlling the phase currents either using a hysteresis band current controller (HBCC) or pulse width modulation (PWM). Above base speed, the phase currents cannot be controlled, and the motor enters the single pulse mode. The motor speed is controlled by adjusting the turn on and turn off angles. Hence, this mode is referred to as advance angle control (AAC). Above base speed, the motor cannot produce rated torque. However, controlling the turn on/off angles allows the motor to operate at constant power ($P=T x \omega$). Fig. 2.6 shows the torque-speed characteristics highlighting both control modes.

19
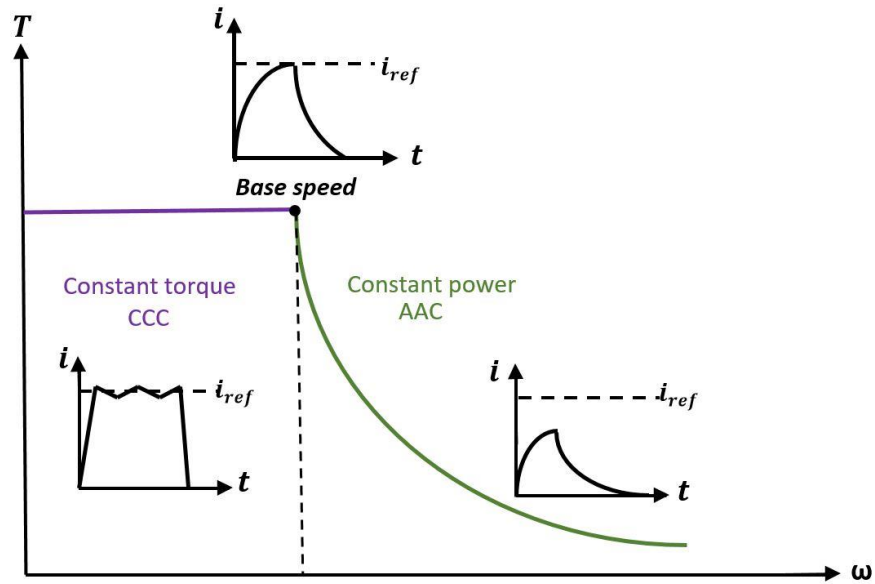
Fig. 2.6 Torque/Speed characteristics

## 2.5 SRM Design

Unfortunately, SRM design, especially for EV applications, is not a straight forward task. The double salient structure increases the saturation effect in the pole tips. Fringing is not insignificant. In addition, the design should account for different specifications including torque density, efficiency over wide speed range, and vibration and acoustic noise. The design process starts by initializing the machine dimensions using analytical formulas. FEA is then used to fine tune the initial design. This section gives a brief description on the basics for SRM initialization [2-4].

Due to the available space constraints for the propulsion motor in EVs, an SRM with high torque density is required. Improving the machine torque density implies improving the electrical and magnetic loading of the machine. Magnetic materials with high saturation flux density will enhance SRM magnetic loading thereby improving the torque density. However, core losses will increase reducing SRM efficiency. Cobalt iron material which is characterized by high saturation flux density and low core loss is available but with high cost [2-5]. Hence, selecting a suitable magnetic material requires trade-off between cost, efficiency and torque density.

The air gap length plays a crucial role in torque density. A small air gap enhances SRM torque density. However, very small air gaps are not practical in EV applications due to road conditions.

The electrical loading of the machine could be improved by utilizing rectangular wires which increases the slot fill factor (ratio between area of conductor and slot area). Cooling techniques as with water jacket cooling also improve SRM electrical loading and thereby the torque density.

### 2.5.1    *Selecting number of phases and poles*

The first step in SRM design is to choose the number of phases, stator poles, and rotor poles. The selection is generally based on the application. For instance, in low cost high speed applications, where performance could be sacrificed in favour of cost, like small home appliances, usually a single-phase or a two-phase SRM is selected. The single-phase SRM cannot inherently reliably self-start. Increasing the number of SRM phases reduces the torque ripple, improve the fault tolerance capability and improves SRM performance, at the expense of converter costs.

The switching frequency for a phase of the SRM is calculated using (2.18):

$$f_{sw} = \frac{\omega}{2\pi} N_r \tag{2.18}$$

Considering (2.18), if the number of rotor poles is increased (while keeping the number of phases unchanged) [2-6] torque ripple will be reduced, and an economical converter could be used. Coil end winding will be smaller allowing increased stack length while maintaining the overall machine axial length unchanged. Hence, torque density will be improved but the switching frequency will increase, resulting in higher core losses.

If the number of rotor poles is increased (while keeping the number of stator poles unchanged) [2-7] the interpolar rotor air gaps will be narrower. Hence, the unaligned inductance will be significantly higher than that of the conventional SRM. The unaligned inductance increase will reduce the energy conversion area thus decreasing the developed torque. Additionally, the current rise time at phase turn on is prolonged as a consequence of higher unaligned inductance which implies using higher dc link voltages to increase the current rate of rise.

### 2.5.2    Sizing stack length, stator and rotor diameters, and air gap

The output torque equation is defined by (2.19)

$$T_e = KL_s d^2 \tag{2.19}$$

where $K$ is a constant in the range of 10.3 to 34.5 kNm/m$^3$ representing the product of electrical and magnetic loading of the SRM. Using (2.19) and for the required output torque, the product of the stack length and the square of the rotor diameter is known. A unity ratio between the stack length and rotor diameter $L_s/d$ is advised in [2-8]. Hence, the stack length and the rotor diameters are initialized. The ratio between the stator diameter and rotor diameter $D/d$ is 1.5~1.8. Thus, the stator diameter is initialized. Mechanically (inertia), for higher speeds, the rotor diameter should be minimised.

Reducing the SRM air gap increases the torque density of the SRM. A typical SRM air gap length for SRM is between 0.25mm and 1mm. A rule of thumb given in [2-9] proposes the air gap to be 0.5% of the rotor diameter. Small air gaps are not suitable in EV applications, since, the drivetrain is affected by road conditions which may produce severe vibration and mechanical stress [2-10].

### 2.5.3    Sizing stator and rotor pole arcs

Selecting adequate stator and rotor pole arcs is of prime importance. Miscalculations could lead to self-starting problems. Hence, to assure torque production at all rotor positions, the stator pole arc is calculated using (2.20).

$$\beta_s \geq \frac{2\pi}{mN_r} \tag{2.20}$$

Usually, the stator pole arc is selected slightly smaller than the rotor pole arc to allow more stator slot area to accommodate the winding. For a complete unaligned position to be achieved, (2.21) should be satisfied.

$$\beta_s + \beta_r < \frac{2\pi}{N_r} \tag{2.21}$$

### 2.5.4 Sizing stator and rotor back iron widths, and pole heights

Fig. 2.7 shows a cross-sectional view of a stator pole, accommodated a winding. The coil end length can be approximated using (2.22). Then the total axial length is calculated using (2.23).

$$L_{end} = \frac{\pi}{2N_s}\left(\tfrac{1}{2}D - b_{sy}\right) \tag{2.22}$$

$$L_{axial} = L_s + 2L_{end} \tag{2.23}$$

The optimal ratio between the stator diameter and the total axial length $D/_{L_{axial}}$ is 2.46, as suggested in [2-11]. Hence, the stator back iron is initialized. A large stator back iron is desirable to reduce vibration, increase mechanical strength, and ease saturation. However, an excessively large value will reduce the available space for the stator winding [2-12].

The stator pole height is calculated by:

$$h_s = \tfrac{1}{2}D - \tfrac{1}{2}d - l_g - b_{sy} \tag{2.24}$$

The rotor pole height should be several times larger than the air gap to increase the conversion area (by reducing the unaligned inductance). The rotor back iron has the same constraint as the stator back iron regarding saturation. Hence, the rule of thumb in (2.25) gives an initial value for the rotor pole height and back iron.

$$h_r, b_{ry} > \tfrac{1}{2}d \, \sin \tfrac{1}{2}\beta_r \tag{2.25}$$

Finally, the shaft diameter is given by (2.26)

$$D_{sh} = \tfrac{1}{2}d - h_r - b_{ry} \tag{2.26}$$
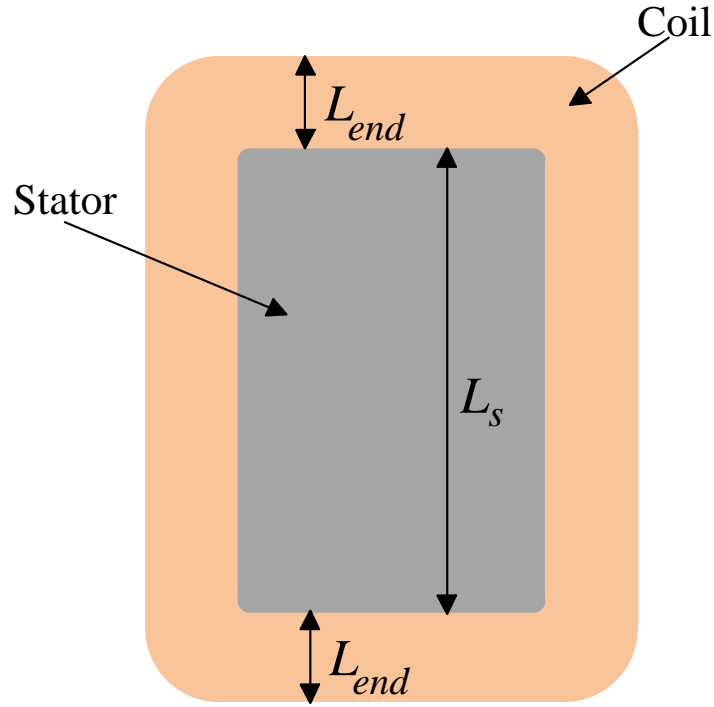
Fig. 2.7 Cross-sectional view of stator pole

### 2.5.5  *Estimating number of turns and current density*

Using (2.14), and neglecting stator phase winding resistance, the maximum flux linkage per pole at speed ω (assuming the conduction angle for each phase is the stroke angle $\frac{2\pi}{mN_r}$ ) is given by (2.27).

$$N\varphi_{max} = \frac{2\pi V_{DC}}{mN_r\omega} \tag{2.27}$$

The maximum flux is defined by:

$$\varphi_{max} = \frac{N_s}{m} B_s L_s \big(d + 2l_g\big) \sin\tfrac{1}{2}\,\beta_s \tag{2.28}$$

where, $B_s$ is the saturation flux density (typically 1.7T)

Combining (2.27) and (2.28), the number of series turns per pole is calculated from:

$$N = \frac{2\pi \, V_{DC}}{\omega N_r N_s B_s L_s \left(d + 2l_g\right)\sin\frac{1}{2}\beta_s} \quad (2.29)$$

Determining SRM current density is of prime importance as it is related to the cooling method adopted. In CCC the current level is maintained at the peak value defined by (2.30).

$$I_p = \frac{P}{n\eta k_d V_{DC}} \quad (2.30)$$

where $P$ is the motor output power ($T_e X \omega$), $n$ is the number of phases conducting simultaneously, $\eta$ is the motor efficiency, and $k_d$ is the SRM duty cycle.

Assuming the conduction angle for each phase is equal to the stroke angle, then the rms phase current is defined by:

$$I_{rms} = \frac{I_P}{\sqrt{m}} \quad (2.31)$$

The current density is directly related with the phase rms current using (2.32).

$$J_{rms} = \frac{NI_{rms}}{k_s \, {A_s}/_2} \quad (2.32)$$

where, $A_s$ is the slot area and $k_s$ is the slot fill factor (ratio between copper winding and slot areas).

The slot fill factor depends on the conductor shape and the slot form. Increasing the value of $k_s$ is desirable to reduce the current density. The slot fill factor is low (40%) if loosely bundled conductors are used. This value increases to 60% if rectangular conductors are used. Finally, the slot fill factor could be improved to reach 80%, if the conductors are customized to fit the slot shape.

If the SRM is designed to be totally enclosed, then the current density should not exceed 5A/mm². This value increases to 10A/mm² for fan cooling, and with liquid cooling the current density should be less than 30A/mm².

## 2.6 Acoustic noise and torque ripple reduction

SRM electromagnetic attraction forces are divided into two components namely; tangential and radial components. The former is directly related to the developed torque of the machine. That is maximizing this component is one of the goals while designing the SRM, but the radial component does not contribute to the process of rotational torque production. It is the main reason for vibration, stator deformation and acoustic noise. Hence, eliminating, or at least minimizing, this component will improve SRM performance. It is shown in [2-13] that skewing the stator and the rotor of a three-phase 12/8 SRM reduces vibration and acoustic noise. A simple solution proposed in [2-14] uses stator spacers, which are nonmagnetic materials as ceramics inserted between the stator poles, to reduce stator vibration and thereby the acoustic noise.

The problem of rotational torque ripple arises due to the discrete nature of torque production. This topic will be studied in detail in chapters 7 and 8.

## 2.7 Summary

This chapter presented the SRM structure highlighting the most common stator/rotor pole number configurations. The process of torque production, based on principles of electromechanical energy conversion, was discussed. SRM operation either in motoring or generating modes was demonstrated based on an approximate inductance profile. Although the SRM has a simple equivalent circuit, LUTs for flux and torque (for different excitation levels and rotor positions) are needed to reflect the severe non-linearity of the machine. Controlling the SRM below and above base speed was illustrated, highlighting the difference between CCC and AAC. Finally, detailed design steps for initializing SRM dimensions were presented.

## References

[2-1]   P. Desai, M. Krishnamurthy, N. Schofield, and A. Emadi, "Novel Switched Reluctance Machine Configuration With Higher Number of Rotor Poles Than Stator Poles: Concept to Implementation," in *IEEE Transactions on Industrial Electronics*, vol. 57, no. 2, pp. 649-659, Feb. 2010.

[2-2]   R. Krishnan, *Switched Reluctance Motor Drives: Modelling, Simulation, Analysis, Design and Applications*. Boca Raton, FL, USA: CRC Press, 2001.

[2-3]  T. Husain, A. Elrayyah, Y. Sozer, and I. Husain, "Unified Control for Switched Reluctance Motors for Wide Speed Operation," in *IEEE Transactions on Industrial Electronics*, vol. 66, no. 5, pp. 3401-3411, May 2019.

[2-4]  K. Chau, "Switched Reluctance Motor Drives," in *Electric Vehicle Machines and Drives: Design, Analysis and Application*, IEEE, 2015, pp.108-146.

[2-5]  K. Rahman, and S. Schulz, "Design of high-efficiency and high-torque-density switched reluctance motor for vehicle propulsion," in *IEEE Transactions on Industry Applications*, vol. 38, no. 6, pp. 1500-1507, Nov.-Dec. 2002.

[2-6]  A. Chiba *et al.*, "Torque Density and Efficiency Improvements of a Switched Reluctance Motor Without Rare-Earth Material for Hybrid Vehicles," in *IEEE Transactions on Industry Applications*, vol. 47, no. 3, pp. 1240-1246, May-June 2011.

[2-7]  I. Husain, "Minimization of torque ripple in SRM drives," in *IEEE Transactions on Industrial Electronics*, vol. 49, no. 1, pp. 28-39, Feb. 2002.

[2-8]  R. Krishnan, R. Arumugan, and J. F. Lindsay, "Design procedure for switched-reluctance motors," *in IEEE Transactions on Industry Applications*, vol. 24, no. 3, pp. 456-461, May-June 1988.

[2-9]  S. Shoujun, L. Weiguo, D. Peitsch, and U. Schaefer, "Detailed design of a high speed switched reluctance starter/generator for more/all electric aircraft," *Chin. J. Aeronaut.*, 2010, 23, (2), pp. 216–226.

[2-10] B. Bilgin, A. Emadi, and M. Krishnamurthy, "Design Considerations for Switched Reluctance Machines With a Higher Number of Rotor Poles," in *IEEE Transactions on Industrial Electronics*, vol. 59, no. 10, pp. 3745-3756, Oct. 2012.

[2-11] K. Kiyota, S. Nakano, and A. Chiba, "A Fast Calculation Method of Optimal Ratio of Outer Diameter and Axial Length for Torque Improvement in Switched Reluctance Motor," *in IEEE Transactions on Industry Applications*, vol. 54, no. 6, pp. 5802-5811, Nov.-Dec. 2018.

[2-12] K. Kiyota, and A. Chiba, "Design of Switched Reluctance Motor Competitive to 60-kW IPMSM in Third-Generation Hybrid Electric Vehicle," in *IEEE Transactions on Industry Applications*, vol. 48, no. 6, pp. 2303-2309, Nov.-Dec. 2012.

[2-13] C. Gan, J. Wu, M. Shen, S. Yang, Y. Hu, and W. Cao, "Investigation of Skewing Effects on the Vibration Reduction of Three-Phase Switched Reluctance Motors," in *IEEE Transactions on Magnetics*, vol. 51, no. 9, pp. 1-9, Sept. 2015.

[2-14] P. Rasmussen, J. Andreasen, and J. Pijanowski, "Structural stator spacers-a solution for noise reduction of switched reluctance motors," in *IEEE Transactions on Industry Applications*, vol. 40, no. 2, pp. 574-581, March-April 2004.

# *Chapter 3*

# *Review of Power Converters for the SRM*

This chapter classifies and reviews the most common power converters used to feed the SRM. The difference between hard and soft switching converters is demonstrated. The main merits and drawbacks of each topology are highlighted. Finally, a comparison between the power converters is presented to elect the most suitable converter for EV applications.

## 3.1    Introduction

The SRM cannot be connected directly to any ac or dc supply but, needs a suitable power converter for its operation. The main task of the converter is to appropriately energize and de-energize each phase winding to assure continuous rotation of the SRM. Various types of converters have been proposed for SRM drives. The type of converter chosen plays a crucial role in cost, size and performance of the drive. The converter must be able to fulfil the following requirements in order to improve SRM drive performance [3-1]:

- **Fast magnetization and de-magnetization of SRM phases:** Fast magnetization allows the current in the phase winding to reach the reference within a short time, thus increasing the SRM base speed. Decreasing the de-magnetization time by extinguishing the phase current quickly eliminates the current tail and prevents the SRM from entering the negative torque production region. To best perform this task, the dc supply voltage can be boosted during the magnetization and de-magnetization periods.

- **Phase overlap:** The converter must be able to energize the incoming phase and de-energize the outgoing phase simultaneously.

- **High efficiency:** To increase SRM drive efficiency, the de-magnetization energy should be efficiently returned to the supply or better, stored and used to energize the next phase instead of being dissipated as heat energy in the winding resistance.

- **Minimum cost:** A converter is economic if it can provide excellent performance with a minimum number of switching devices. Decreasing the number of switches reduces the switching losses, number of gate drive circuits, and the overall cost of the converter.

- **Fault tolerance:** A high reliability converter must be considered for critical applications which allows continuous SRM rotation even after a phase failure.

- **Low complexity:** Simple design and control algorithm are preferred for the SRM converter.

## 3.2    Classification of power converters for the SRM

Generally, there are two criteria for classifying SRM converter types; the first classification is based on the number of converter switching devices, while the second classification depends on the method of commutation [3-2]. Classifying converter types according to the number of switching devices does not reflect the strengths and weaknesses of each converter. Thus the second criterion, which classifies the types of converters regarding the commutation method, is adopted as shown in Fig. 3.1. Other converter topologies exist, however, this chapter only reviews the common converters.
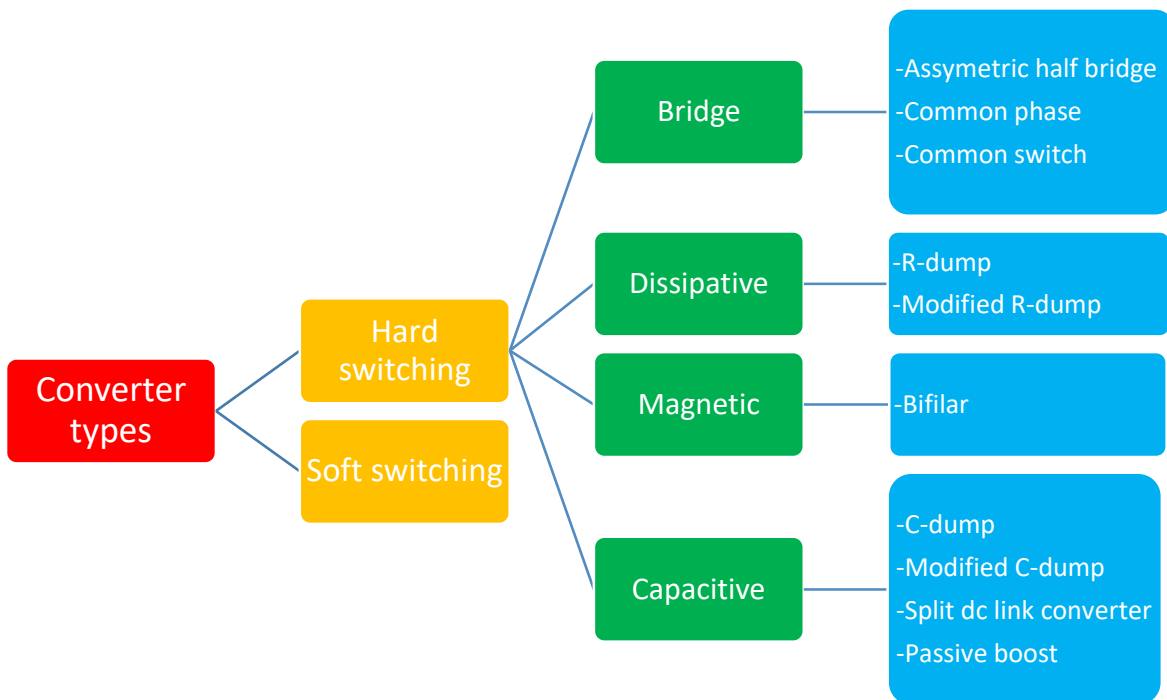


Fig. 3.1 Classification of power converters for SRM

29

### 3.3    Hard switching converters

The majority of the used converters are hard switched. Generally, hard-switching converters have simple circuitry which is easier to implement, than soft switching converters. The hard-switching group is composed of four subgroups; bridge, dissipative, magnetic and capacitive.

### 3.3.1    Bridge converters

The bridge converter is the dominant converter type used for SRM drives. Asymmetric half bridge (ASHB), common phase, and common switch converters are the main types of bridge converters.

### 3.3.1i    Asymmetric half bridge (ASHB) based converter

The ASHB based SRM converter is the most common. So, operation of this converter is presented in detail [3-3]. The ASHB converter uses two switches and two diodes for each phase as shown in Fig. 3.2 for a 4φ SRM.
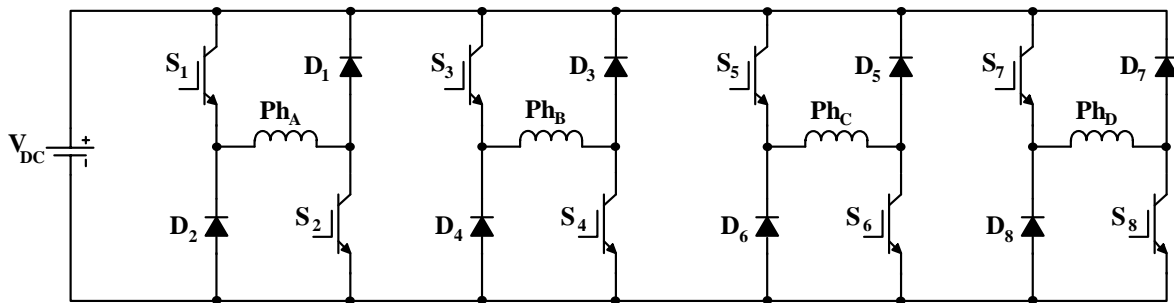


Fig. 3.2 ASHB converter for a 4 phase SRM

Three states are available for operation of the ASHB converter, namely: magnetization, freewheeling, and de-magnetization states, as shown in Fig. 3.3 and described for a given phase, for example $Ph_A$.

*Magnetization, $+V_{DC}$:* This state is obtained by turning on switches $S_1$ and $S_2$ of the phase to be energized, as shown in Fig. 3.3a. The full dc link voltage is applied on the phase, thus the current builds up.

*Free-wheeling, 0V:* Two switch patterns are possible for this voltage level. The first pattern is $S_1$ on, while the other switch, $S_2$, off. The second pattern is $S_2$ on, with $S_1$ off. The two possible patterns are illustrated in Fig. 3.3 parts b and c, respectively, where zero voltage is applied across the phase winding. The two (0V) states can be used alternately to balance losses and heating.

*De-magnetization, $-V_{DC}$:* The last state is with switches $S_1$ and $S_2$ off, as shown in Fig. 3.3d. The de-magnetization energy via the motor winding is pumped back to the dc link, reducing the winding current to zero before the phase enters the negative torque production region.



(a) $+V_{DC}$  (b) $0V$

(c) $0V$  (d) $-V_{DC}$
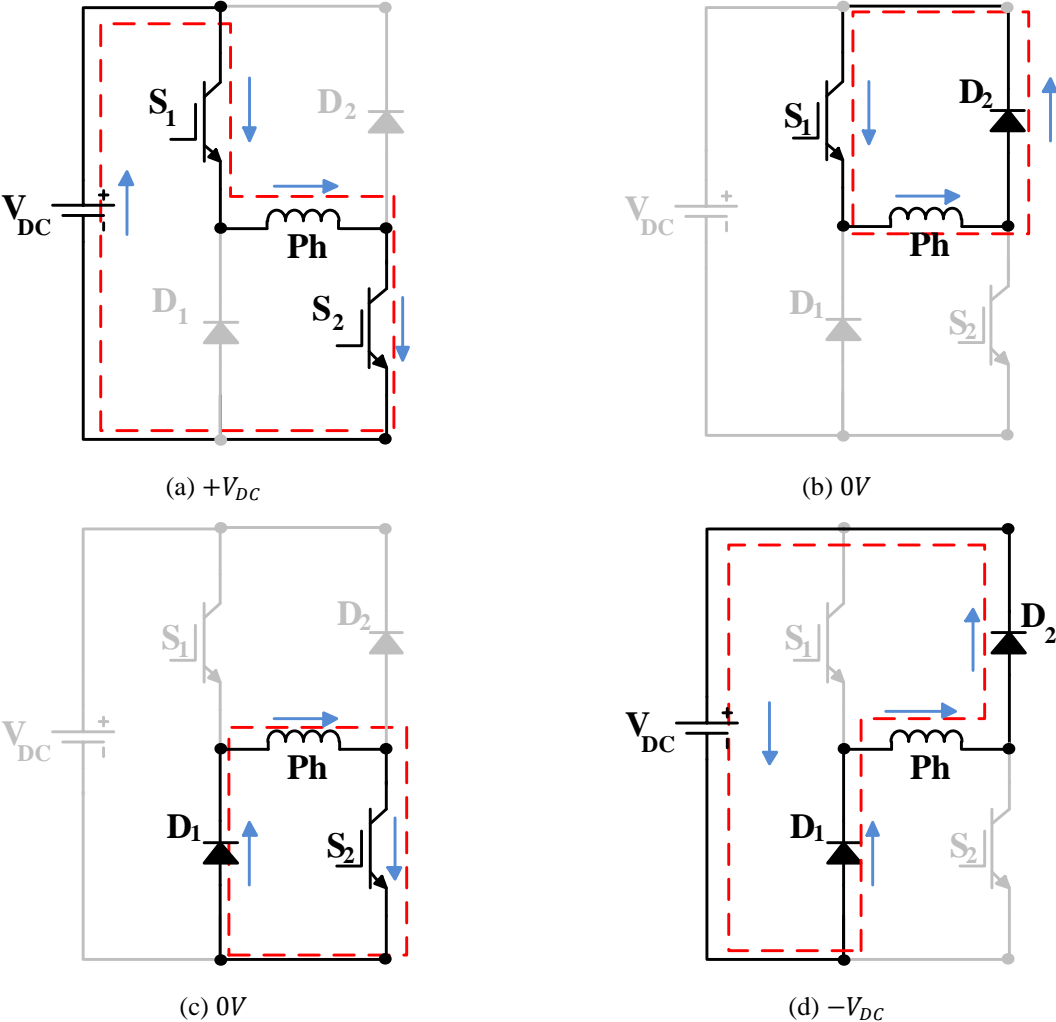
Fig. 3.3 ASHB converter states: (a) Magnetization, (b), (c) Free-wheeling, and (d) De-magnetization

Table 3.1 summarizes the possible converter voltage levels, while Fig. 3.4 illustrates the typical voltage and current waveforms for the three states.

Table 3.1 ASHB CONVERTER STATES

| Level | Fig 3 state | State/KVL |
|-------|-------------|-----------|
| $+V_{DC}$ | 3(a) | $V_{DC}, S_1, S_2$ |
| 0V | 3(b) | $D_2, S_1$ |
|  | 3(c) | $D_1, S_2$ |
| $-V_{DC}$ | 3(d) | $V_{DC}, D_1, D_2$ |
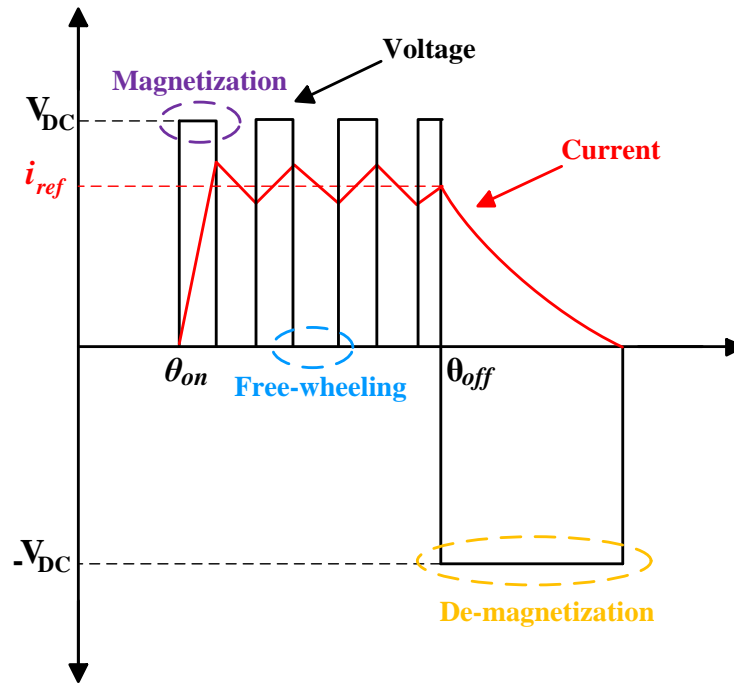


Fig. 3.4 Typical voltage and current waveforms using ASHB

Advantages:

- Independent control of each phase without overlap.
- Three voltage levels are available namely; $+V_{DC}, 0V, -V_{DC}$.
- Low complexity.
- High fault tolerance.
- High efficiency as stored magnetic energy in phase winding is fed back to the dc link during de-magnetization.

32

Drawbacks:

- Increase in the number of semiconductor devices as each phase requires two switches and two diodes.
- More conduction loss since two semiconductors connected in series with the conducting phase winding.
- The relatively low magnetization and demagnetization voltage, limits motor base speed.

The SRM requires a specific converter as opposed to AC motors requiring an off-the-shelf 3φ inverter. Table 3.2 gives a brief comparison between the ASHB and 3φ inverter. Although the ASHB is not commercially available, is has the outstanding feature of the absence of shoot through fault. The use of commercially available semiconductor modules is not an advantage in EV applications, since proprietary modules are viable given the high volume of EV. The number and rating of the semiconductors within the package dominate the relative module cost.

Table 3.2 COMPARISON BETWEEN 3Φ INVERTER AND ASHB

|  | 3φ inverter | ASHB |
| --- | --- | --- |
| Modularity | Modular | Non-modular |
| Number of switches | 6 | 2m |
| Voltage rating of switches | $V_{DC}$ | $V_{DC}$ |
| rms current rating | $I_p/\sqrt{2}$ | $I_p/\sqrt{m}$ |
| Number of diodes | 6 | 2m |
| Utilization of dc link voltage | $V_{DC}/2$ | $V_{DC}$ |
| Shoot through failure | Present | Not present |

3.3.1ii    Common phase converter

The common phase converter [3-4] is an improved version of the ASHB based converter. It has the same advantages as the ASHB converter but with a reduced number of switches (1.5 switches per phase). Fig. 3.5 shows the common phase converter for a 4φ SRM.

The converter uses the double bridge topology with phases A and C in one bridge, sharing a common leg incorporating switch $S_{AC}$. The other two phases, B and D, are in an independent bridge with a common switch $S_{BD}$. This sharing is possible since the two phases sharing the same switch (in the same bridge) are $90^0$ (electrical) out of phase. Hence, no conduction overlap will occur.

The main drawback of this topology is that it is only effective for SRM with an even number of phases. The converter fault tolerance is reduced. (that is, for a fault in the common switch in either of the two bridges, the phases incorporated in that bridge will be lost).
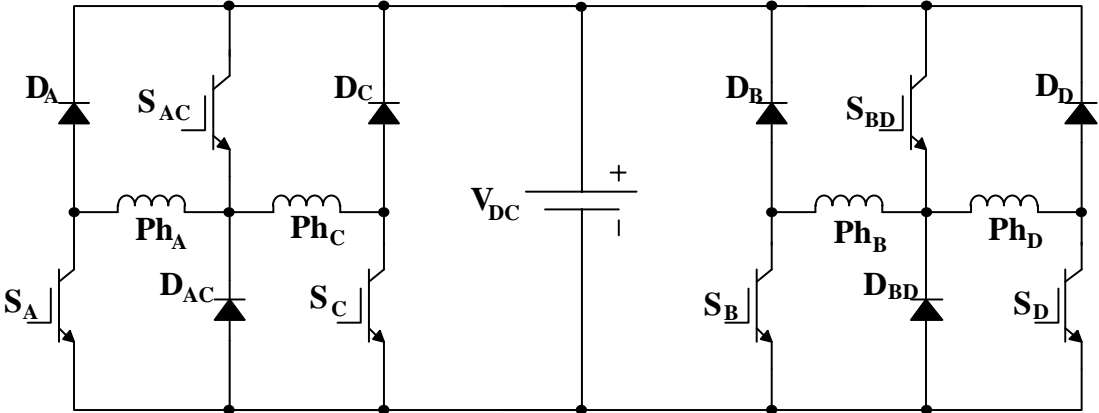


Fig. 3.5 Common phase converter, for a four phase SRM

### 3.3.1iii Common switch converter

To further reduce the number of semiconductor devices in the ASHB converter (hence reduce converter cost and volume), the common switch converter was proposed [3-5] as in Fig. 3.6.
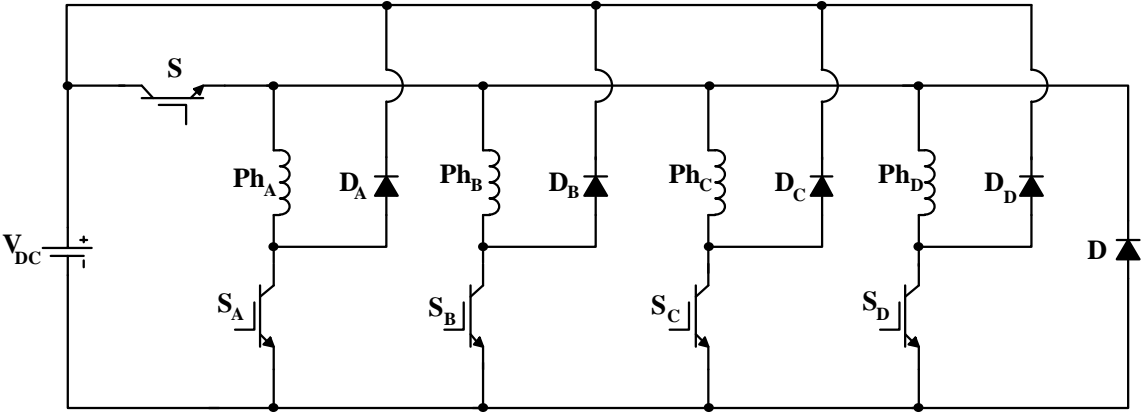


Fig. 3.6 Common switch converter, for a four phase SRM

In this topology, each phase has an independent switch. A main switch, *S,* is shared between all the phases which reduces the switch count to $m + 1$. Despite, the low converter cost compared to the ASHB based converter, the fault tolerance of the converter is much reduced. This topology offers good performance only at low speeds. At high speeds the off-going phase cannot be de-magnetized quickly (as the common switch is turned on) which increases the current tail, thereby producing negative phase torque, which subsequently reduces the total developed torque.

### 3.3.2 *Dissipative converters*

The dissipative converter is considered the simplest SRM converter. It utilizes the minimum number of switches. Only one switch per phase is sufficient. The energy stored in the phase winding is dissipated in a dump resistor instead of being returned to the supply. Thus, it is not an energy efficient converter and cannot be used for high power application. Two versions are available namely; the R-dump [3-6] and the modified R-dump [3-7].

### 3.3.2i    R-dump converter

Fig. 3.7 shows the R-dump converter, where the energy stored in the phase winding is dissipated in the dump resistor, $R_d$. This topology has low efficiency, and requires special cooling for the dump resistor. Hence, it is suitable for low power, low cost applications.
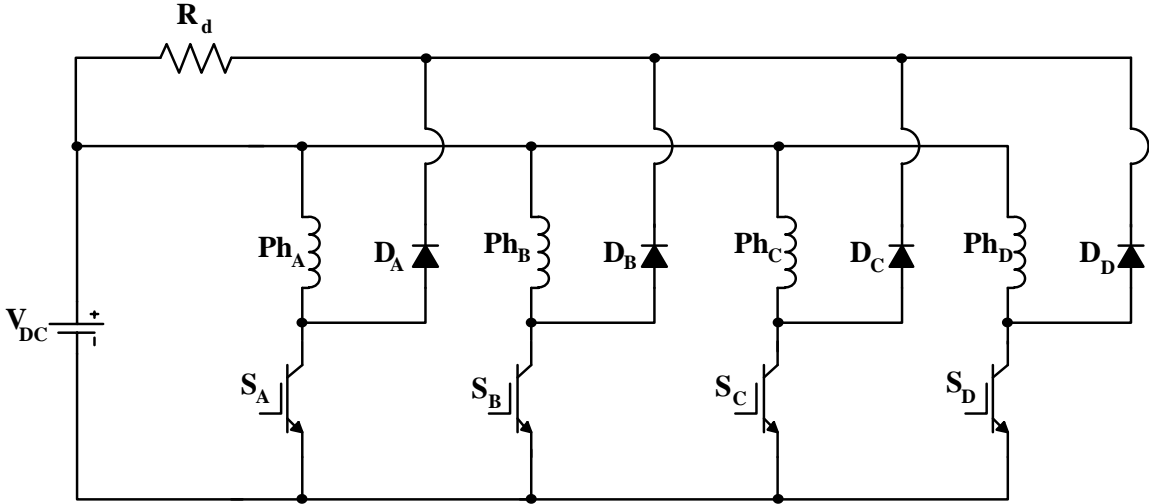


Fig. 3.7  R-dump converter, for a four phase SRM

35
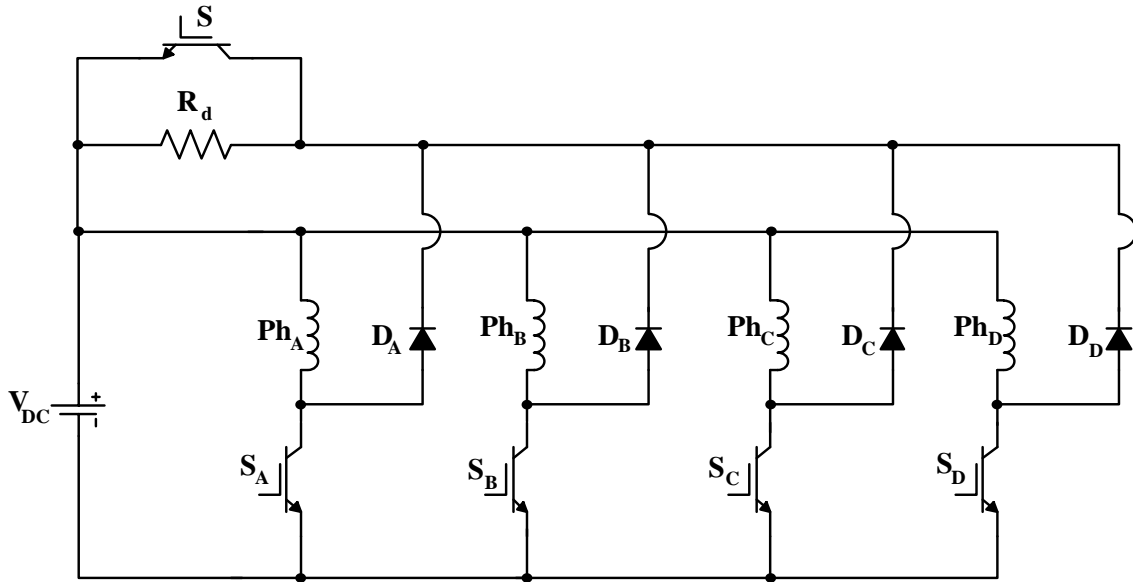
Fig. 3.8 Modified R-dump converter

### 3.3.2ii  Modified R-dump

A modified version of the R-dump converter is illustrated in Fig. 3.8, where an extra switch, *S*, is connected in parallel with the dump resistor. The time constant for current decay is $\frac{L}{R+(1-\alpha)R_d}$. Decreasing the duty cycle, $\alpha$, will increase the effective value of dump resistance for rapid current extinction. Increasing the duty cycle will decrease the effective value of dump resistance improving the efficiency during current switching.

### *3.3.3  Magnetic converters*

The idea of a magnetic converters is to transfer the magnetic stored energy in the SRM phase to coupled winding. The transferred energy is then returned to the supply, or used to energize the next incoming phase. Fig. 3.9 illustrates the connection of a bifilar converter [3-8], which uses a single switch per phase, which is the main advantage. Only two modes are available viz; magnetization, and de-magnetization modes. The 0V free-wheeling mode is not possible with this configuration.
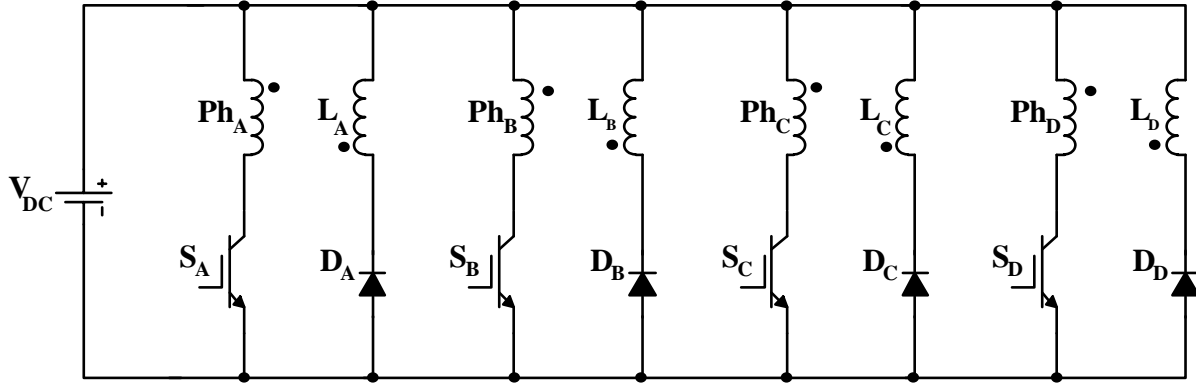
Fig. 3.9 Bifilar converter, for a four phase SRM

$L_A, L_B, L_C, and\ L_D$ are the bifilar windings inductances.

This converter does not dissipate the de-magnetization energy but re-uses it. However, it has limitations. The main drawback is that each SRM phase must be coupled with another winding which increases SRM manufacturing complexity and reduces the copper area for the stator winding. Imperfect coupling between the SRM bifilar windings results in voltage spikes during phase turn-off, implying the use of snubber circuits and an increase in semiconductor voltage ratings.

### 3.3.4   Capacitive converters

The capacitive type converter uses a dump capacitor to store the de-magnetization energy. The stored energy is returned back to the supply or used to energize the next incoming SRM phase winding. C-dump, modified C-dump, split dc link, and passive boost are types of capacitive converters, as follows.

3.3.4i    C-dump converter

Fig. 3.10 shows a C-dump converter, which belongs to the $m + 1$ family (that is, the number of semiconductor switches equals the number of SRM phases, plus one) [3-9].
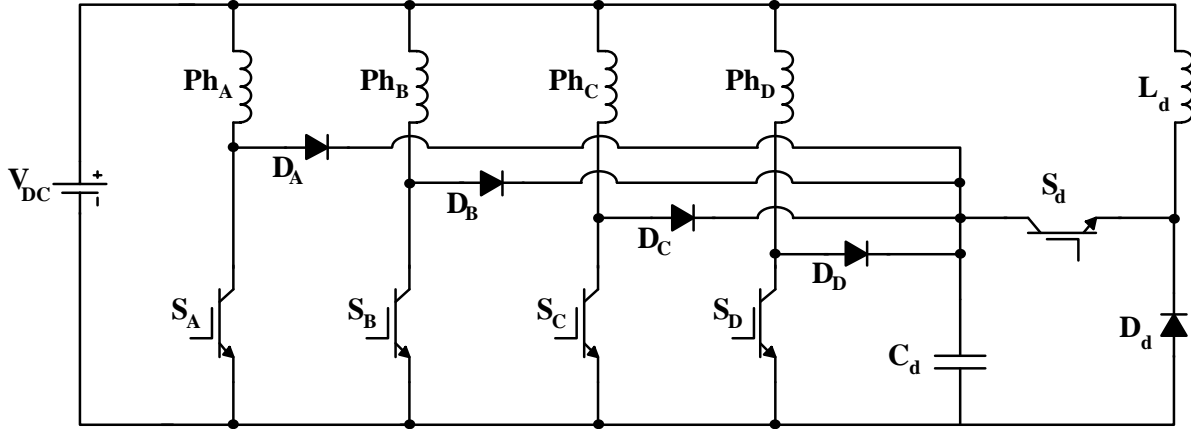
Fig. 3.10 C-dump converter, for a four phase SRM

The stored energy in the SRM phase winding is dumped into the capacitor $C_d$. The capacitor voltage is maintained at twice the supply voltage $2V_{DC}$, in order to apply $-V_{DC}$ on the outgoing phase for rapid current extinguishing. The dumped energy is returned back to the dc link using the buck circuit composed of $S_d, D_d, and\ L_d$.

The main disadvantages of this topology is the need of a bulky capacitor, and a buck converter (which includes a large inductor). The rating of the semiconductor devices is double the dc link voltage, $2V_{DC}$. To maintain the dump capacitor voltage at $2V_{DC}$, the switching frequency of $S_d$ will be high, increasing switching losses.

3.3.4ii   Modified C-dump converter

An attempt to improve the performance of C-dump converter was shown in [3-10], where the inductor in the buck circuit is omitted. The energy stored in the dump capacitor is directly used to energize the next incoming phase instead of being returned to the dc link. Fig. 3.11 show the modified C-dump converter.

Although omitting the inductor and reducing the switching frequency of $S_d$, the rating of the switches remains $2V_{DC}$, as with the C-dump converter. Circuit control is complicated, with poor performance at high speeds.
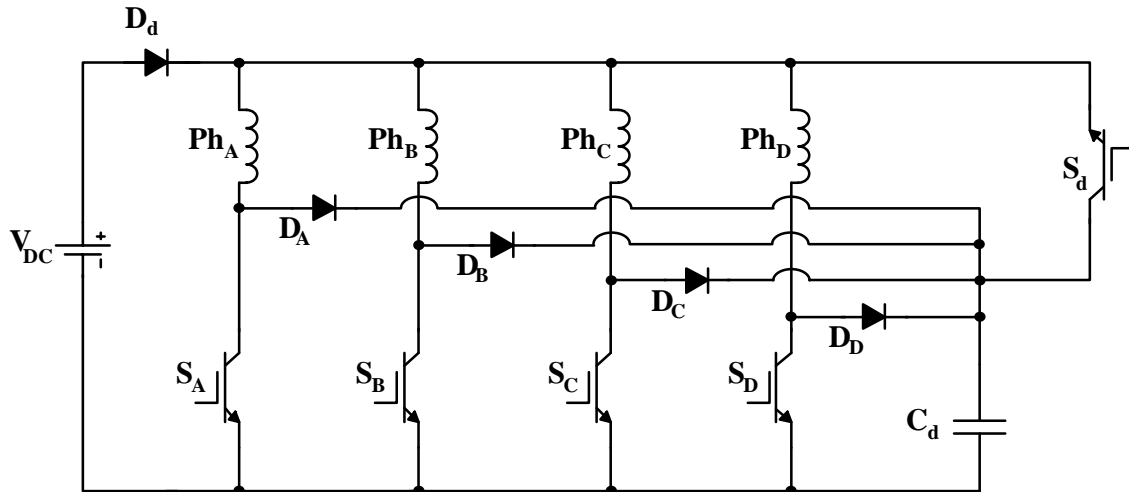
Fig. 3.11 Modified C-dump converter, for a four phase SRM

### 3.3.4iii   Split dc link converter

The split dc link converter has one switch per phase which reduces the switch count [3-11].
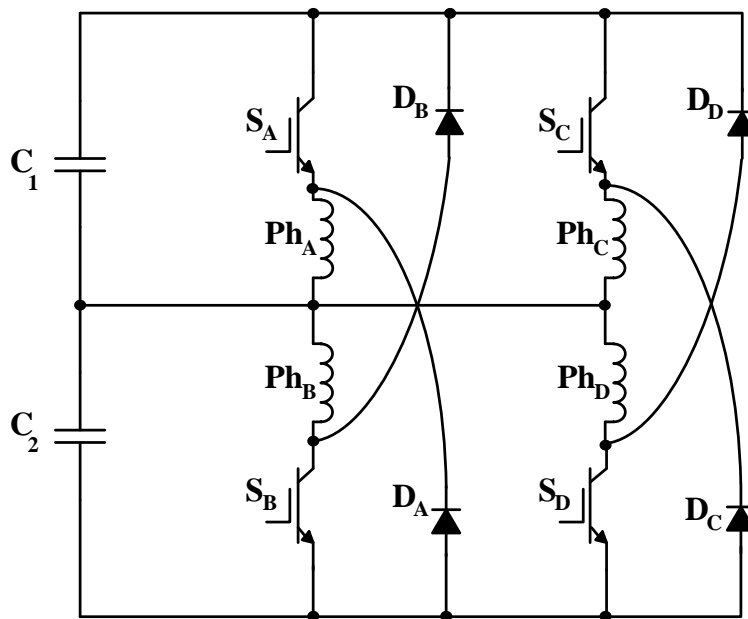


Fig. 3.12 Split dc link converter, for a four phase SRM

However, it requires an SRM with even number of phases. Only half the dc link voltage is utilized for magnetization and de-magnetization, of incoming and outgoing phases respectively, which

prevents the current from building up and decaying quickly. This reduces the base speed of the motor. The converter does not tolerate any phase failure or phase imbalance. Fig. 3.12 shows the conventional split dc link converter.

3.3.4iv   Passive boost converter

Enhancing SRM performance at high speeds is presented in [3-12]. A boost-capacitor with a blocking diode are inserted within the dc link.  The de-magnetization energy of the outgoing phase is stored in the boost-capacitor. The resultant increasing voltage decreases the current fall time thereby effectively extending the positive torque production range, before operating in the negative torque region. The stored energy (which increases the dc link voltage) then feeds the next incoming phase, thus allowing faster current build-up which increases the motor base speed. Fig. 3.13 shows a common phase converter with boost-capacitors.
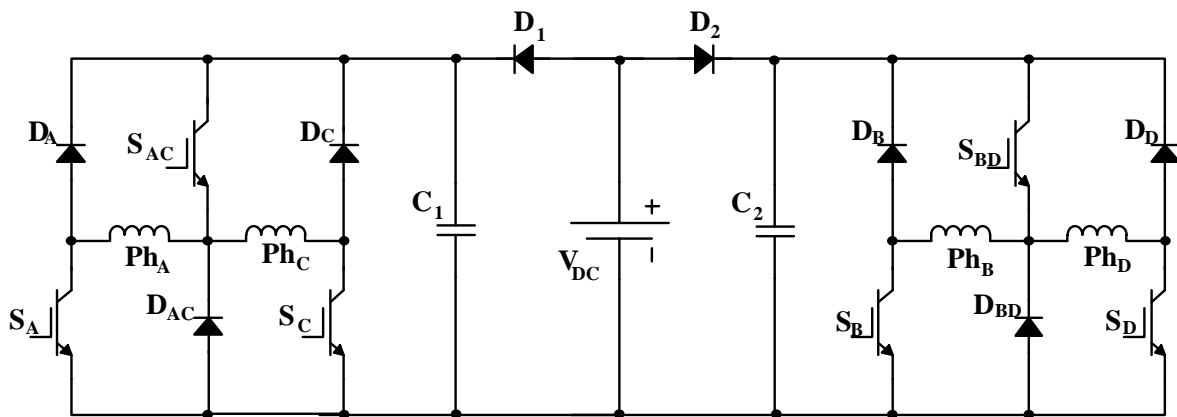


Fig. 3.13 Common phase converter with boost-capacitors, for a four phase SRM

The converter uses the double bridge topology with phases A and C in one bridge, sharing a common leg incorporating switch $S_{AC}$. The other two phases, B and D, are in an independent bridge with a common switch $S_{BD}$. The dc link blocking diodes and capacitors allow boosting of the dc link voltage by forcing recovered current to charge the capacitors to voltages in excess of the dc source $V_{DC}$. The two-independent bridge topology allows better voltage boosting (since no phase overlap occurs in each bridge) with a minimal number of switches.  The drawback of this topology is that it requires semiconductor devices with ratings above the dc link voltage (the ratings depend

on the boost-voltage). Because of the dc link blocking diodes, circuit modification is need for regenerative braking.

## 3.4 Soft chopping converters

To improve SRM performance, the converter's switching frequency is increased. Raising the switching frequency results in higher switching losses and more electromagnetic interference. Soft switching techniques using resonant circuits are proposed for high switching applications [3-13]. Converter complexity and cost makes it impractical for EV applications, hence is not pursued.

## 3.5 Comparing power converters

In this chapter, several converters have been presented covering the most common used power converters in SRM drives. This section compares these different topologies to select the 'best' converter for EV applications. Table 3.2 evaluates some of the available converters in terms of the number and ratings of switches, converter control complexity, the need for SRM design modifications, fault tolerance (ability of SRM to continue rotation after switch failure), performance at low and high speeds, rate of current building up and decay, efficiency, available voltage levels, the need of snubber circuits, and constraints on number of SRM phases.

Table 3.3 COMPARISON BETWEEN DIFFERENT POWER CONVERTERS

|  | Bifilar | R-dump | C-dump | Split dc link | Shared phase + boost |
|---|---|---|---|---|---|
| Number of switches | $m$ | $m$ | $m+1$ | $m$ | $m+2$ |
| Rating of switch | $V_{DC}^+$ | $V_{DC}$ | $2V_{DC}$ | $V_{DC}$ | $V_{DC}^*$ |
| Control complexity | simple | Simple | Complex | Simple | Simple |
| SRM modification | Yes | No | No | No | No |
| Fault-tolerance | High | High | Low | Low | Moderate |
| Performance | Medium | Low | High | Medium | High |
| Current build up and decay | Medium | Slow | Medium | Slow | Fast |
| Efficiency | Medium | Low | High | High | High |
| Voltage levels | $+V_{DC}, -V_{DC}$ | $+V_{DC}, 0V$ | $+V_{DC}, 0V, -V_{DC}$ | $+\frac{1}{2}V_{DC}, -\frac{1}{2}V_{DC}$ | $V_{DC}^*, 0V, -V_{DC}^*$ |
| Snubber circuits | Yes | No | No | No | No |
| Number of phases | Any | Any | Any | Even | Even |
| $V_{DC}^+ = Slightly\ higher\ rating\ than\ V_{DC}$ | | | $V_{DC}^* = V_{DC} + V_{boost}$ | | |

From the analysis in Table 3.2, the converter with shared phase and voltage-boosting (Fig. 3.13) is a promising power converter for SRM drives.

## References

[3-1]   S. Vukosavic, and V. Stefanovic, "SRM inverter topologies: a comparative evaluation," in *IEEE Transactions on Industry Applications*, vol. 27, no. 6, pp. 1034-1047, Nov.-Dec. 1991.

[3-2]   O. Ellabban, and H. Abu-Rub, "Switched reluctance motor converter topologies: A review," *2014 IEEE International Conference on Industrial Technology (ICIT)*, Busan, 2014, pp. 840-846.

[3-3]   Y. Hu, T. Wang, and W. Ding, "Performance Evaluation on a Novel Power Converter With Minimum Number of Switches for a Six-Phase Switched Reluctance Motor," in *IEEE Transactions on Industrial Electronics*, vol. 66, no. 3, pp. 1693-1702, March 2019.

[3-4]   C. Pollock, and B. W. Williams, "Power converter circuits for switched reluctance motors with the minimum number of switches," in *IEE Proceedings B - Electric Power Applications*, vol. 137, no. 6, pp. 373-384, Nov. 1990.

[3-5]   Do-Hyun Jang, I. Husain, and M. Ehsani, "Modified (n+1) switch converter for switched reluctance motor drives," *Proceedings of PESC '95 - Power Electronics Specialist Conference*, Atlanta, GA, USA, 1995, pp. 1121-1127 vol.2.

[3-6]   R. Krishnan, and P. N. Materu, "Analysis and design of a low-cost converter for switched reluctance motor drives," in *IEEE Transactions on Industry Applications*, vol. 29, no. 2, pp. 320-327, March-April 1993.

[3-7]   M. Ehsani, I. Husain, K. Ramani, and J. H. Galloway, "Dual-decay converter for switched reluctance motor drives in low-voltage applications," in *IEEE Transactions on Power Electronics*, vol. 8, no. 2, pp. 224-230, April 1993.

[3-8]   T. Miller, "Converter Volt-Ampere Requirements of the Switched Reluctance Motor Drive," in *IEEE Transactions on Industry Applications*, vol. IA-21, no. 5, pp. 1136-1144, Sept. 1985.

[3-9]   S. Mir, I. Husain, and M. E. Elbuluk, "Energy-efficient C-dump converters for switched reluctance motors," in *IEEE Transactions on Power Electronics*, vol. 12, no. 5, pp. 912-921, Sept. 1997.

[3-10] A. Hava, V. Blasko, and T. Lipo, "A modified C-dump converter for variable-reluctance machines," in *IEEE Transactions on Industry Applications*, vol. 28, no. 5, pp. 1017-1022, Sept.-Oct. 1992.

[3-11] Hong-Je Ryoo, Won-Ho Kim, Geun-Hie Rim, Wook Kang, Ji-Ho Park, and Chung-Yuen Won, "A new split source type converter for SRM drives," *PESC 98 Record. 29th Annual IEEE Power Electronics Specialists Conference (Cat. No.98CH36196)*, Fukuoka, 1998, pp. 1290-1294 vol.2.

[3-12] Y. Dessouky, B. Williams, and J. Fletcher, "A novel power converter with voltage-boosting capacitors for a four-phase SRM drive," in *IEEE Transactions on Industrial Electronics*, vol. 45, no. 5, pp. 815-823, Oct. 1998.

[3-13] D. Cabezuelo, J. Andreu, I. Kortabarria, E. Ibarra, and I. Garate, "SRM converter topologies for EV application: State of the technology," *2017 IEEE 26th International Symposium on Industrial Electronics (ISIE)*, Edinburgh, 2017, pp. 861-866.

*Chapter 4*

*A Neutral-Point Diode-Clamped Converter*

*with Inherent Voltage-Boosting for a Four-Phase SRM Drive*

This chapter proposes a new asymmetric neutral-point diode-clamped (NPC) multilevel converter for a four-phase switched reluctance machine drive. The inbuilt NPC clamping capacitors are used for both voltage level clamping and also as dc rail voltage-boosting capacitors to increase the output power of the motor, particularly for high-speed EV applications. The new converter allows regenerative energy to be recovered back to the dc supply for rapid machine braking, thus increasing overall drive efficiency. Analysis of the different modes of converter operation, along with design equations for sizing the voltage-boosting capacitors, are detailed. The effect of capacitance on boost voltage and increased motor base-speed is presented. Simulation and experimental results will confirm the effectiveness of the proposed converter.

## 4.1   Introduction

As with the PMSM, the SRM cannot be connected directly to any ac or dc supply but, needs a suitable power converter for operation. Chapter three reviewed common converters used with the SRM. Among these converters, the asymmetric half bridge (ASHB) converter based on two switches and two diodes per phase is the most popular converter for SRM drives. Recent developments in EVs involve increasing the dc link voltage from around 400V dc to 800V-1000V dc [4-1]. Hence, the voltage rating of the converter must increase. Higher voltage rated power semiconductor devices not only imply slower response with lower overall efficiency but also higher cost and size. Thus, multilevel inverters become a viable solution [4-2].

In [4-3], a five-level neutral-point diode-clamped (NPC) converter and an asymmetric modular multilevel converter (MMC) were compared for high voltage, high power applications. However, only the full dc link voltage is utilized. Hence, SRM performance at different voltage levels is not exploited. In [4-4], a fault tolerant converter based on the NPC topology was proposed. However,

the main drawback is half the switches withstand the full dc link voltage. In [4-5] the performance of a three-level NPC converter was compared with the conventional ASHB converter. With the same overall rating, the NPC has the advantage of lower losses and current ripple, and lower machine noise. However, motor performance (Nm/A) is improved only at low speeds (below base speed). Since the SRM can be deployed for high-speed applications, its performance (W/kg) must be enhanced at higher speeds. Also, the NPC converter requires large dc link capacitances.

Enhancing single-phase SRM performance at high speeds is presented in [4-6], [4-7]. A boost-capacitor with a parallel diode is inserted in series with the dc link. The boosting-voltage provided by the capacitor aids the winding current to rapidly build-up and decrease thus, increasing the motor base-speed. The application of the boost-capacitor is extended to poly-phase SRM in [4-8] - [4-11]. But current overlap between incoming and outgoing phases reduces the boosting-voltage effect.

In [4-12], a new converter, with comparable performance as the ASHB converter, is presented. The converter uses half the number of diodes, however the same number of switches is required. A ring converter is proposed in [4-13]. However, the converter is only suitable for a six-phase SRM and severe distortion in the phase currents is present. In addition, the fault-tolerance of the converter is inferior. Two off-the-shelf inverters are exploited in [4-14] and [4-15] to enhance SRM fault-tolerance. The converter uses 12 switches which drastically increases converter cost, plus the converter is only suitable for three-phase SRMs. In [4-16], standard six-pack plus dual modules are integrated for a three-phase SRM. Since the converter is based on commercial power components it is more economical than ASHBs. To allow phase overlap between successive phases, only half the dc link voltage is utilized for magnetization and de-magnetization. A three-phase inverter is used in [4-17] to feed a six-phase SRM. Although the inverter is commercially available, the six-phase SRM uses a different winding configuration which imposes limitations in the fabrication of the SRM drive. In [4-18], a new stator winding configuration is presented which allows higher voltages during de-magnetization, but the SRM needs winding reconfiguration which increases production costs. Also, the higher voltage is only applied at phase turn off (that is, the performance at phase turn on is not enhanced).
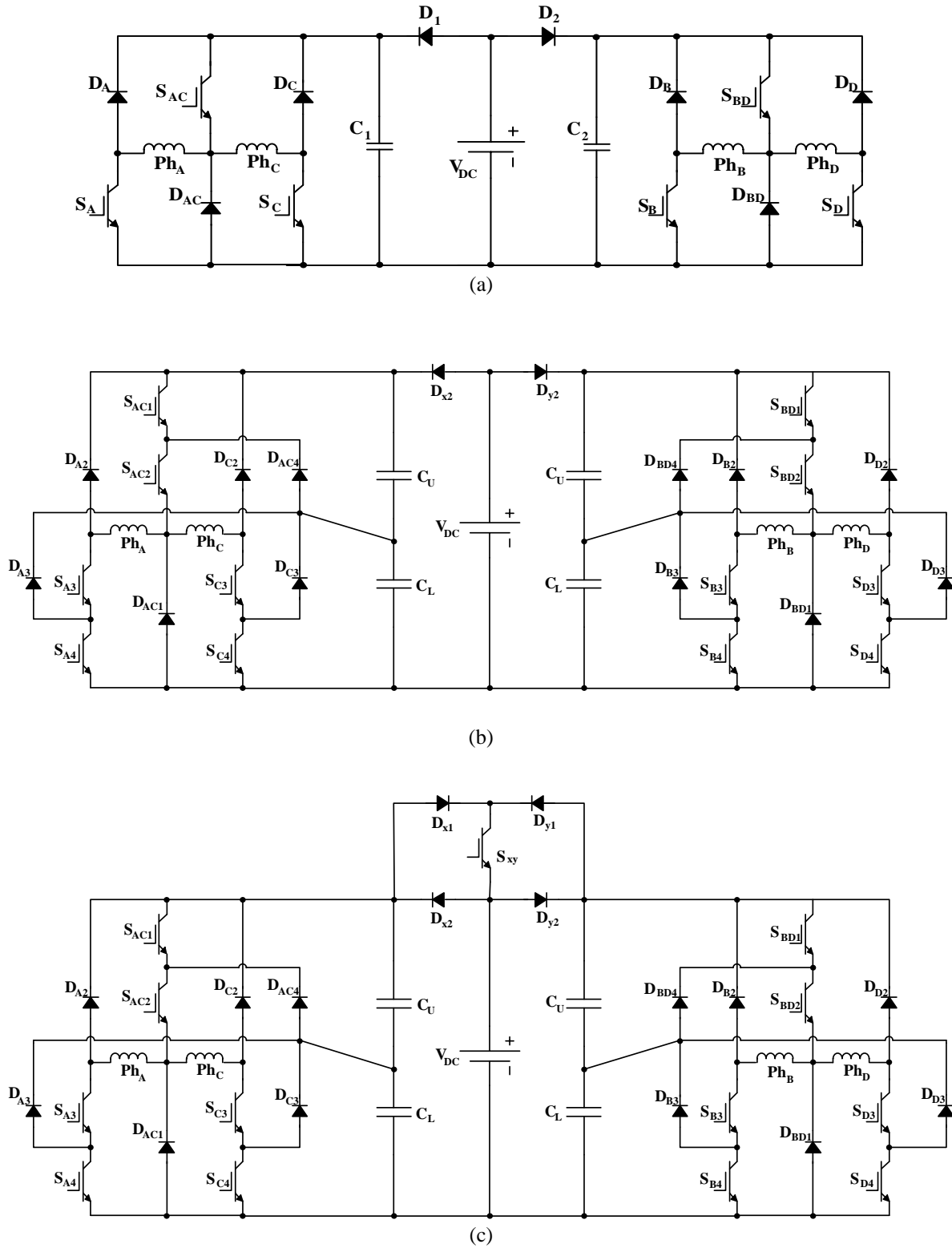
Fig. 4.1 Four-phase SRM converter topologies: (a) Common phase converter with voltage-boosting (Fig.3.13), (b) New NPC converter with voltage-boosting, and (c) New NPC converter with voltage-boosting and regenerative braking circuitry.

The use of commercially available semiconductor modules is not an advantage in EV applications, since proprietary modules are viable given the high volume of EV. The number and rating of the semiconductors within the package dominate the relative module cost.

In this chapter, a new asymmetric NPC converter, shown in Fig 4.1b, with inherent voltage-boosting, is introduced for a four-phase SRM. It is based on the passive boost converter in Fig 4.1a, as introduced in 3.3.4iv, Fig 3.13, which uses the double arm, common switch topology for better voltage boosting with a minimum number of switches. Fig 4.1c shows the extra dc link circuitry necessary for regenerative operation, which is also applicable to the boost circuit in Fig. 4.1a.

In the proposed NPC converter, inter-rail voltage levels are transient (dwelled at for few microseconds, sufficient to ensure switch voltage sharing). Small sized capacitors are deployed instead of the large capacitances normally associated with the conventional NPC converter. The de-magnetization energy of the outgoing phase is stored in the NPC converter split dc link capacitors, hence decreasing the current fall time thereby effectively extending the positive torque production range, before operating in the negative torque region.
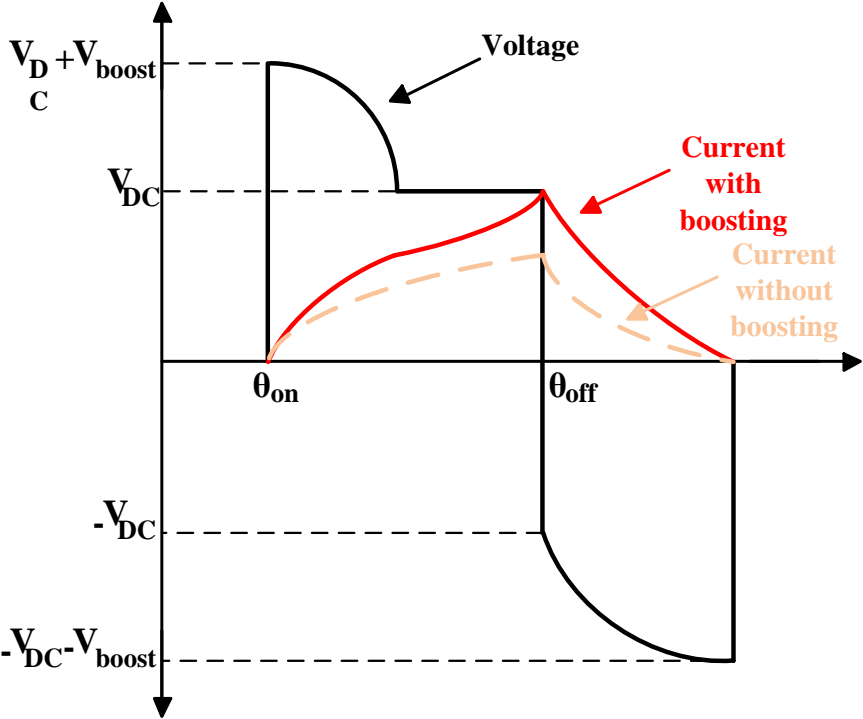


Fig. 4.2 Voltage and current waveforms in single-pulse mode

The stored energy (which increases the dc link voltage) then feeds the next incoming phase, thus allowing faster current build-up which increases the motor output power. The typical voltage and current waveforms are illustrated in Fig. 4.2 for single-pulse mode of operation (at and above base speed). The new converter (Fig. 4.1c) also allows regeneration energy to be fed back to the supply, instead of being dissipated, for rapid machine regenerative braking, thus increasing overall drive efficiency.

## 4.2   Asymmetric NPC converter with voltage-boosting capacitors

The new converter in Fig. 4.1b (as with the circuit in Fig. 4.1a) uses the double bridge topology with phases A and C in one bridge, sharing a common leg incorporating series connected switches $S_{AC1}$ and $S_{AC2}$. The other two phases, B and D, are in an independent bridge with common series connected switches $S_{BD1}$ and $S_{BD2}$.

The dc link blocking diodes and capacitors allow boosting of the dc link voltage by forcing recovered current to charge the capacitors to voltages in excess of the dc source $V_{DC}$. The two-independent bridge topology allows better voltage-boosting (since no phase overlap occurs in each bridge) with a minimal number of switches. In Fig. 4.1c the dc link switch $S_{xy}$ (and diodes $D_{x1}$ and $D_{y1}$) is for regeneration where the stored energy in the phase winding is not dissipated, but returned to the dc link.

The NPC converter switch voltage clamping feature is used to exploit series connection of switches. When changing switch states, the NPC rule of an outer switch is always first off and last on, is retained. The analysis of this converter in the motoring and braking modes is presented in the following subsections.

### 4.2.1   Motoring mode

In the motoring mode of operation, the dc link switch $S_{xy}$ is off and link diodes $D_{x2}$ and $D_{y2}$ conduct. Current is injected into the appropriate phase winding during the increasing inductance region for motoring action. According to the states of the phase switches, the converter offers five voltage levels, as shown in Fig. 4.3 and described in the following text for a given phase, $Ph_A$.
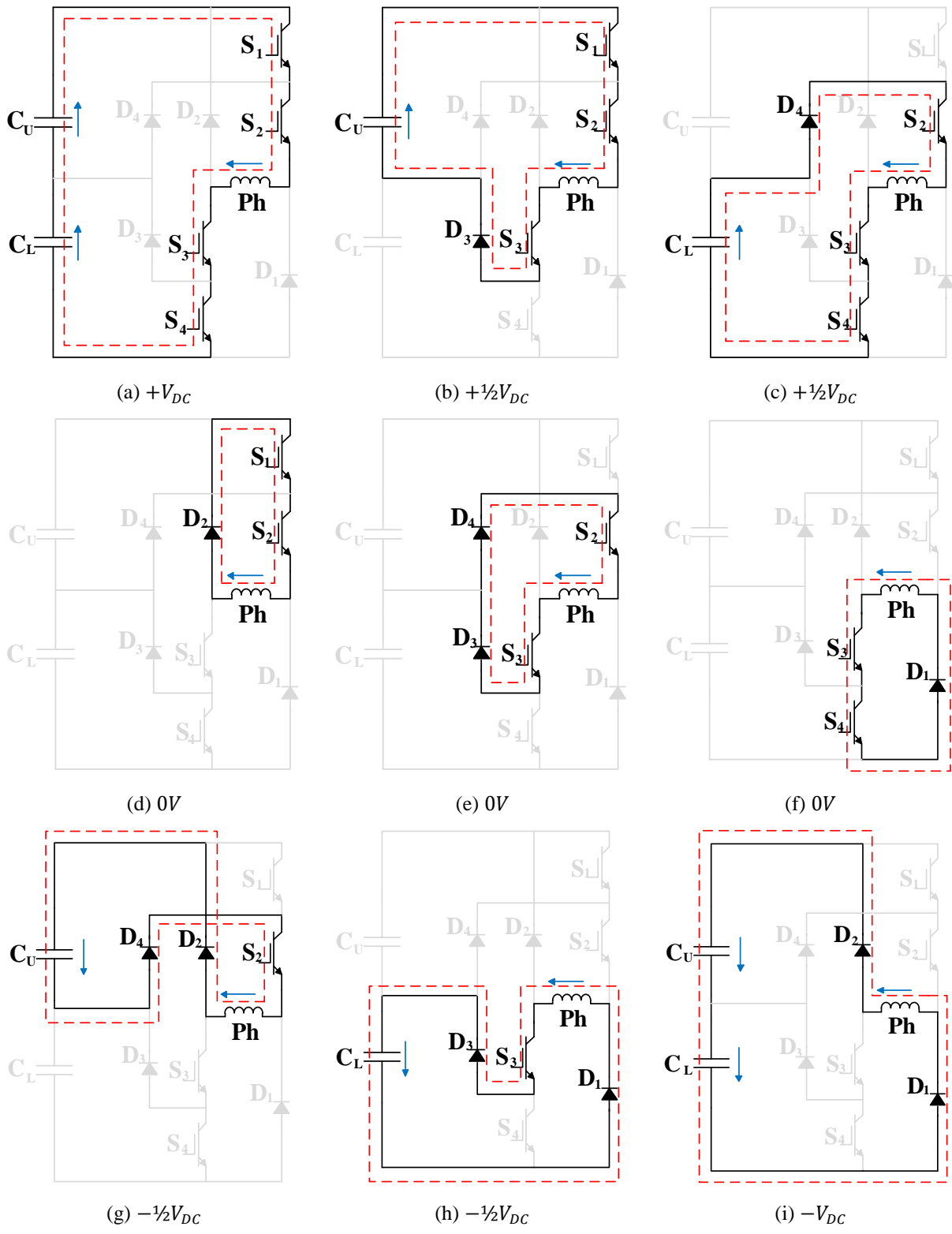
(a) $+V_{DC}$
(b) $+\frac{1}{2}V_{DC}$
(c) $+\frac{1}{2}V_{DC}$

(d) $0V$
(e) $0V$
(f) $0V$

(g) $-\frac{1}{2}V_{DC}$
(h) $-\frac{1}{2}V_{DC}$
(i) $-V_{DC}$

Fig. 4.3 New NPC converter voltage states

*First voltage level,$+V_{DC}$:* This voltage level is obtained by turning on the four switches $S_1, S_2, S_3$ and $S_4$ of the phase to be energized as shown in Fig. 4.3a. Any capacitor boosting effect helps the current in the phase winding to build up quickly reaching the desired reference value, thus increasing the motor output power. The dc link capacitors discharge so that the voltage on the motor winding falls and equals the dc source voltage $V_{DC}$.

*Second voltage level,$+½V_{DC}$:* The second voltage level is realized by two possible switch combinations. The first is with $S_1, S_2$ and $S_3$ on while $S_4$ is off. The second combination is with $S_2, S_3$ and $S_4$ on with $S_1$ off. These two states are demonstrated in Fig. 4.3 parts b and c, respectively. Assuming that the boost capacitors are discharged to $V_{DC}$, the dc link voltage source, only half the dc link voltage $+½V_{DC}$ is applied on the phase winding. This is a transient (dwell) state and alternation between these two states enables NPC capacitor voltage balancing.

*Third voltage level, $0V$:* Three switch patterns are possible for this zero voltage level. The first pattern is $S_1$ and $S_2$ on while the other two switches, $S_3$ and $S_4$, are off. The second pattern is $S_2$ and $S_3$ on with $S_1$ and $S_4$ off. The final pattern is $S_3$ and $S_4$ on while the other two switches $S_1$ and $S_2$ are off. The three possible patterns are illustrated in Fig. 4.3 parts d, e and f respectively, where zero voltage is experience by the phase winding. The boost-capacitors are unaffected.

*Fourth voltage level, $-½V_{DC}$:* This voltage level involves two switch patterns. The first pattern is $S_2$ on while the other three switches $S_1, S_3$ and $S_4$ are off. The second pattern is $S_3$ on while $S_1, S_2$ and $S_4$ are off. Fig. 4.3 parts g and h illustrate the two patterns, where $-½V_{DC}$ is applied across the phase winding and alternation between the two patterns enables capacitor voltage balancing. This transient state ensures switch voltage sharing.

*Fifth voltage level, $-V_{DC}$:* The last voltage level is with all the switches $S_1, S_2, S_3$ and $S_4$ off, as shown in Fig. 4.3i. The de-magnetization energy via the motor winding charges the boost-capacitors in series, to a voltage greater than $+V_{DC}$, reducing the winding current to zero before the phase enters the negative torque production region.

Table 4.1 summarizes the possible voltage levels of the proposed converter, where alternation of the transient half voltage states $±½V_{DC}$ allows boost-capacitor voltage balancing.

Table 4.1 PROPOSED NPC CONVERTER OUTPUT VOLTAGE STATES

| Level | Fig. 4.3 state | State/KVL | dc link initial voltage | dc link final voltage | Capacitor voltage |
|---|---|---|---|---|---|
| $+V_{DC}$ | 3(a) | $S_3, S_4, C_L, C_U, S_1, S_2$ | $+V_{DC} + V_{Boost}$ | $+V_{DC}$ | $C_U\downarrow C_L\downarrow$ |
| $+\frac{1}{2}V_{DC}$ | 3(b) | $S_3, D_3, C_U, S_1, S_2$ | $V_{DC}$ | $V_{DC}$ | $C_U\downarrow C_L\uparrow$ |
| | 3(c) | $S_3, S_4, C_L, D_4, S_2$ | | | $C_U\uparrow C_L\downarrow$ |
| $0V$ | 3(d) | $D_2, S_1, S_2$ | $V_{DC}$ | $V_{DC}$ | $C_U\leftrightarrow C_L\leftrightarrow$ |
| | 3(e) | $S_3, D_3, D_4, S_2$ | | | |
| | 3(f) | $S_3, S_4, D_1$ | | | |
| $-\frac{1}{2}V_{DC}$ | 3(g) | $D_2, C_U, D_4, S_2$ | $V_{DC}$ | $V_{DC}$ | $C_U\uparrow C_L\downarrow$ |
| | 3(h) | $S_3, D_3, C_L, D_1$ | | | $C_U\downarrow C_L\uparrow$ |
| $-V_{DC}$ | 3(i) | $D_2, C_U, C_L, D_1$ | $V_{DC}$ | $V_{DC} + V_{Boost}$ | $C_U\uparrow C_L\uparrow$ |

Table 4.2 NPC CONVERTER OUTPUT VOLTAGE STATE SEQUENCES

Two Quadrant Operation

(one direction of rotation)

| | | Increasing L — Motoring with $S_{xy}$ off | | | Decreasing L — Braking/Regenerating with $S_{xy}$ on when $V_{boost} = 0$ | | |
|---|---|---|---|---|---|---|---|
| | | First +V | Center +V and 0V | Pulse End -V | First +V (energize) | Center -V and 0V | Pulse End -V |
| Below base speed | | $\Delta\Rightarrow0V\Rightarrow+V$<br><br>$\Delta\Rightarrow(e)\Rightarrow(a)$ | $+V\rightarrow\frac{1}{2}V\rightarrow0V\rightarrow\frac{1}{2}V\rightarrow+V$<br><br>$(a)\rightarrow(b)\rightarrow(d)\rightarrow(b)\rightarrow(a)$<br>alternating with<br>$(a)\rightarrow(c)\rightarrow(f)\rightarrow(c)\rightarrow(a)$ | $0V\rightarrow-\frac{1}{2}V\rightarrow-V$<br>$(d)\rightarrow(g)\rightarrow(i)$<br>or<br>$(f)\rightarrow(h)\rightarrow(i)$<br><br>$+V\Rightarrow0V\Rightarrow-V$<br>$(a)\Rightarrow(e)\Rightarrow(i)$ | $\Delta\Rightarrow0V\Rightarrow+V$<br>$\Delta\Rightarrow(e)\Rightarrow(a)$<br>then<br>$+V\rightarrow\frac{1}{2}V\rightarrow0V$<br>$(a)\rightarrow(b)\rightarrow(d)$<br>$(a)\rightarrow(c)\rightarrow(f)$ | $-V\rightarrow-\frac{1}{2}V\rightarrow0V\rightarrow-\frac{1}{2}V\rightarrow-V$<br><br>$(i)\rightarrow(g)\rightarrow(d)\rightarrow(g)\rightarrow(i)$<br>alternating with<br>$(i)\rightarrow(h)\rightarrow(f)\rightarrow(h)\rightarrow(i)$ | $0V\rightarrow-\frac{1}{2}V\rightarrow-V$<br>$(d)\rightarrow(g)\rightarrow(i)$<br>or<br>$(f)\rightarrow(h)\rightarrow(i)$<br><br>-V<br>(i) |
| Above base speed | | $\Delta\Rightarrow0V\Rightarrow+V$<br>$\Delta\Rightarrow(e)\Rightarrow(a)$ | na | $V\Rightarrow0V\Rightarrow-V$<br>$(a)\Rightarrow(e)\Rightarrow(i)$ | $\Delta\Rightarrow0V\Rightarrow+V$<br>$\Delta\Rightarrow(e)\Rightarrow(a)$ | na | $V\Rightarrow0V\Rightarrow-V$<br>$(a)\Rightarrow(e)\Rightarrow(i)$ |

States in brackets – as per Fig. 4.3     When changing switch states, an outer switch is always first off and last on

$\Delta$ is tri-state, all switches off, state (i)    Dwell state (always for $\pm\frac{1}{2}$V), <1μs, state is shown in red italics

$\rightarrow$ single state changed    $\Rightarrow$ two states simultaneously changed    **bold** state – one of two alternating states

Table 4.2 summarizes the sequence of states during motoring below and above base speed and during regeneration. The half voltage states are transitional, and dwelling is long enough to ensure switch voltage clamping (sharing). The allowable state transitions are shown in Fig.4.4.
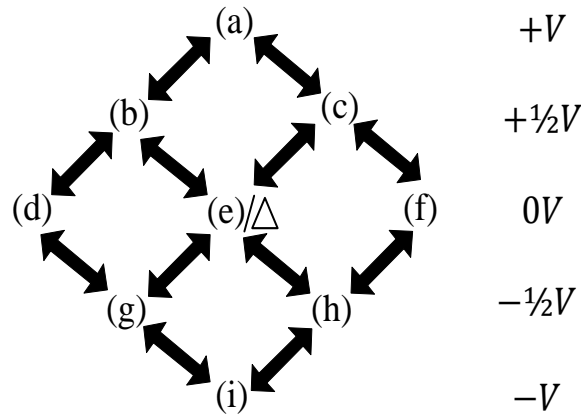


$$+V$$
$$+\tfrac{1}{2}V$$
$$0V$$
$$-\tfrac{1}{2}V$$
$$-V$$

Fig. 4.4 Converter switch states and allowable single and simultaneous double state transitions.

### 4.2.2   Braking mode

Fig. 4.5 shows converter operation in the braking mode (zero voltage states are Fig. 4.3 (d) (e) (f)). Regenerative braking does not involve the boost capacitors.

Any current in a phase during the decreasing inductance period produces a negative (reversing) torque. Current is injected into the phase winding with all switches $S_1, S_2, S_3$ and $S_4$ on (Fig. 4.5a which is similar to state 4.3(a) but the boost-capacitors are not involved), thus producing negative (reverse hence braking) torque. In this mode, the dc link switch $S_{xy}$ is turned on after the boost capacitors discharge to $V_{DC}$. By turning off all four switches, (the state in Fig 4.5b, which is similar to state 4.3(i), except the boost-capacitors are not involved), braking with regeneration occurs, with current fed back into $V_{DC}$ via the dc link switch $S_{xy}$ and diodes $D_{x1}$ and $D_{y1}$. The braking (current) requirement and limit is controlled by interposing zero voltage states, 4.3(d), (e), (f), within the -V state.

The current should reach zero before the start of the increasing inductance. Stored energy in the motor associated with that pole is fed back to the dc supply thus providing efficient and fast regenerative braking action, without the voltage on each boost-capacitor increasing above $\tfrac{1}{2}V_{DC}$.

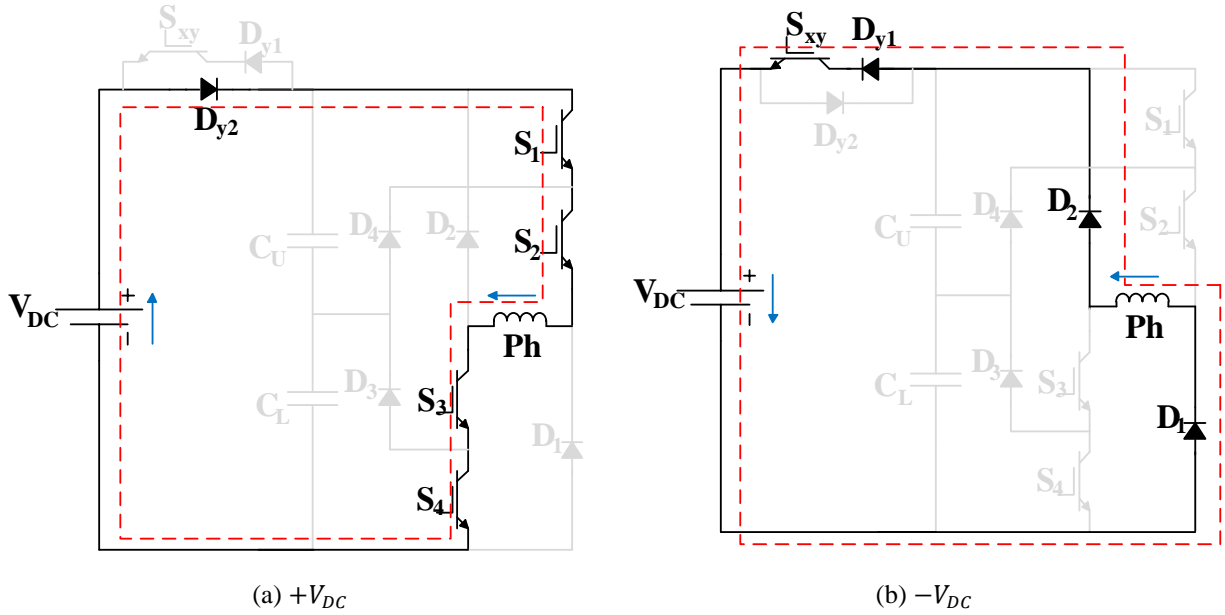(a) $+V_{DC}$             (b) $-V_{DC}$

Fig. 4.5 Regenerative braking mode: (a)Magnetization, and (b) De-magnetization

## 4.3 Sizing of the boost capacitors

Each boost-capacitor voltage rating is half the maximum dc link voltage expected after boosting. The dc link capacitance in this application is not based on the normal NPC converter requirement of providing full load energy at the intermediate voltage levels $\pm$ ½$V_{DC}$. Capacitance is based on the boosting property of the proposed topology. Relatively low capacitance will result in an excessive over voltage, necessitating higher voltage rated devices. Relatively large capacitance results in no significant boost voltage (as with the conventional NPC converter). In [4-6], and [4-11] a formula facilitates sizing of the boost-capacitors. SRM magnetic non-linearity is neglected, with a linear model being adopted. In [4-9] and [4-10], no direct formula is presented to size the boost-capacitors. Also, phase-current overlap crucially affects boosting behaviour. In the following section, a design approach for sizing the boost-capacitors is presented that accounts for SRM magnetic non-linearity. The proposed double arm topology eliminates the problem of phase-current overlap. Fig. 4.6 shows an *RLC* circuit modelling the SRM during de-magnetization at the end of the torque producing period.
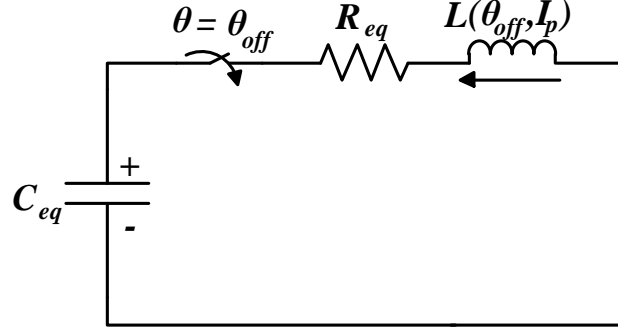
53

Fig. 4.6 Equivalent RLC circuit for the NPC based SRM drive during the de-magnetization period

The equivalent capacitor initial voltage at the beginning of the de-magnetization period is the dc link voltage $V_{DC}$, while the initial current in the phase winding is given by [4-19]:

$$I_p = \frac{P}{n\eta k_d V_{DC}} \tag{4.1}$$

where $P$ is the motor power, $n$ is the number of phases conducting simultaneously, $\eta$ is the motor efficiency, and $k_d$ is the SRM duty cycle.

The equivalent resistance and capacitance are calculated using (4.2) and (4.3) respectively.

$$R_{eq} = R + \omega_{rated} \frac{dL(\theta_{off}, I_p)}{d\theta} \tag{4.2}$$

$$C_{eq} = \tfrac{1}{2} C \tag{4.3}$$

The phase inductance is defined by (4.4) which accounts for SRM magnetic non-linearity [4-20].

$$L(\theta, i) = L_0(i) + L_1(i) \cos(N_r\theta) + L_2(i) \cos(2N_r\theta) \tag{4.4}$$

The coefficients $L_0(i)$, $L_1(i)$ and $L_2(i)$ are defined by:

$$L_0(i) = \tfrac{1}{2}\{\tfrac{1}{2}(L_a(i) + L_u) + L_m(i)\} \tag{4.5}$$

$$L_1(i) = \tfrac{1}{2}\{L_a(i) - L_u\} \tag{4.6}$$

$$L_2(i) = \tfrac{1}{2}\{\tfrac{1}{2}(L_a(i) + L_u) - L_m(i)\} \tag{4.7}$$

where

$L_u$ is the unaligned inductance - current independent.

$L_a(i)$ is the aligned inductance - calculated at current $I_p$.

$L_m(i)$ is the halfway inductance - calculated at current $I_p$.

The inductances can be calculated using FEA or experimentally.

Applying KVL for the *RLC* circuit in Fig. 4.6, assuming constant inductance at the instant of phase turn off:

$$R_{eq}i + L\frac{di}{dt} + \frac{1}{C_{eq}}\int_{-\infty}^{t} idt = 0 \tag{4.8}$$

With the initial conditions given by (4.9) and (4.10):

$$i(\theta_{off}) = I_p \tag{4.9}$$

$$\frac{di}{dt}(\theta_{off}) = -\frac{1}{L}(R_{eq}I_p + V_{DC}) \tag{4.10}$$

The current expression is defined by (4.11) for the overdamped case (normally $C_{eq} > \frac{4L}{R_{eq}^2}$).

$$i(t) = A_1 e^{p_1 t} + A_2 e^{p_2 t} \tag{4.11}$$

where $p_1$ and $p_2$ represent the poles of the characteristic equation, defined by:

$$p_{1,2} = -\frac{R_{eq}}{2L} \pm \sqrt{\left(\frac{R_{eq}}{2L}\right)^2 - \frac{1}{LC_{eq}}} \tag{4.12}$$

Using the initial conditions, $A_1$ and $A_2$ are defined by (4.13) and (4.14) respectively:

$$A_1 = \frac{I_p\left(p_2 + \frac{R_{eq}}{L}\right) + \frac{V_{DC}}{L}}{p_2 - p_1} \tag{4.13}$$

$$A_2 = \frac{I_p\left(p_1 + \frac{R_{eq}}{L}\right) + \frac{V_{DC}}{L}}{p_1 - p_2} \tag{4.14}$$

The time for the motor winding current to decay, is denoted by $t_{off}$ and calculated using:

$$t_{off} = \frac{\ln\left(-\frac{A_2}{A_1}\right)}{p_1 - p_2} \tag{4.15}$$

When the current in the motor winding decays to zero after time $t_{off}$, the voltage on the capacitor $V_{cap}(= V_{DC} + V_{boost})$ is:

$$V_{cap}(t = t_{off}) = \frac{1}{C_{eq}}\left(\frac{A_1}{p_1}e^{p_1 t_{off}} + \frac{A_2}{p_2}e^{p_2 t_{off}}\right) \tag{4.16}$$

Solving (4.16), the boost-capacitance is determined in terms of the boost voltage (dc link voltage in excess of $V_{DC}$).

Although the scope of the chapter is to exploit the series connection of switches, exploiting the multilevel feature would allow reduced current ripple, hence noise, especially at low speeds. In this case, the capacitance should be adequate to supply significant energy to the motor phase. Equation (4.17) describes capacitor voltage ripple.
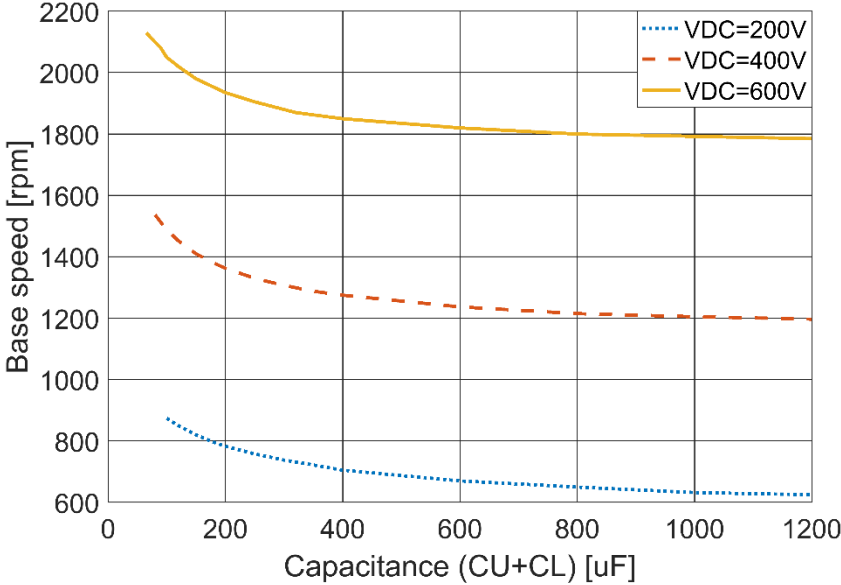
$$i = C\frac{\Delta V}{\Delta t} \tag{4.17}$$

For 5% voltage ripple, the capacitance is:
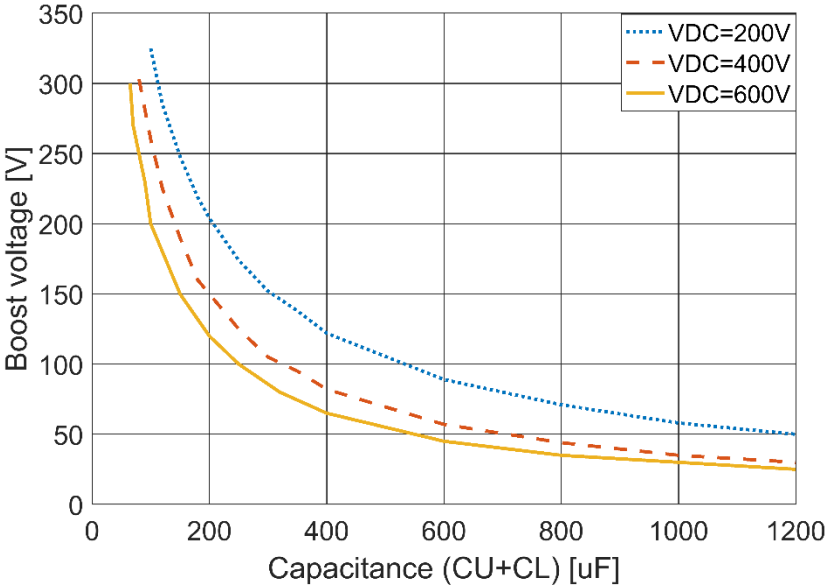
$$C = \frac{I_p}{0.05 V_{DC} f_s} \tag{4.18}$$

where $f_s$ is the sampling frequency.

56

Equations (4.16) and (4.18) could be used to size the capacitor to improved performance at both low and high speeds.
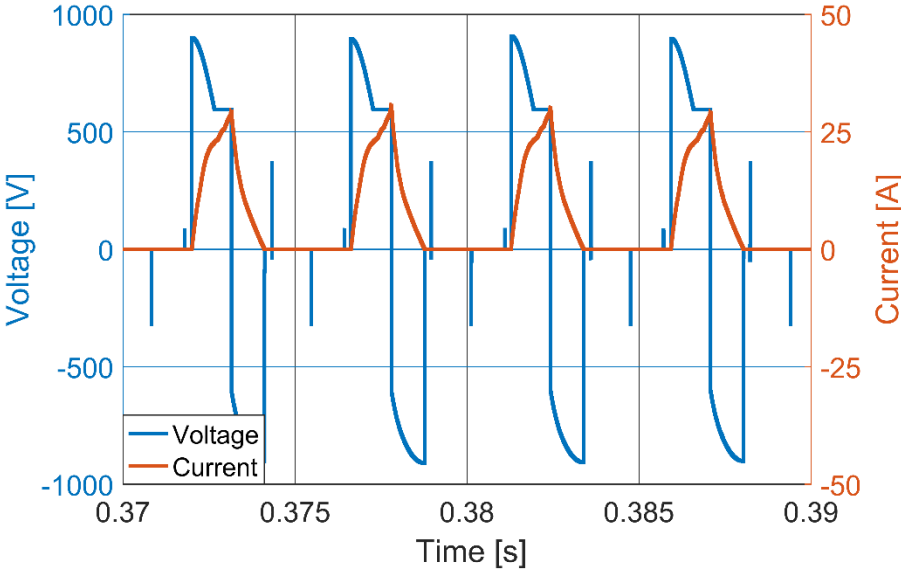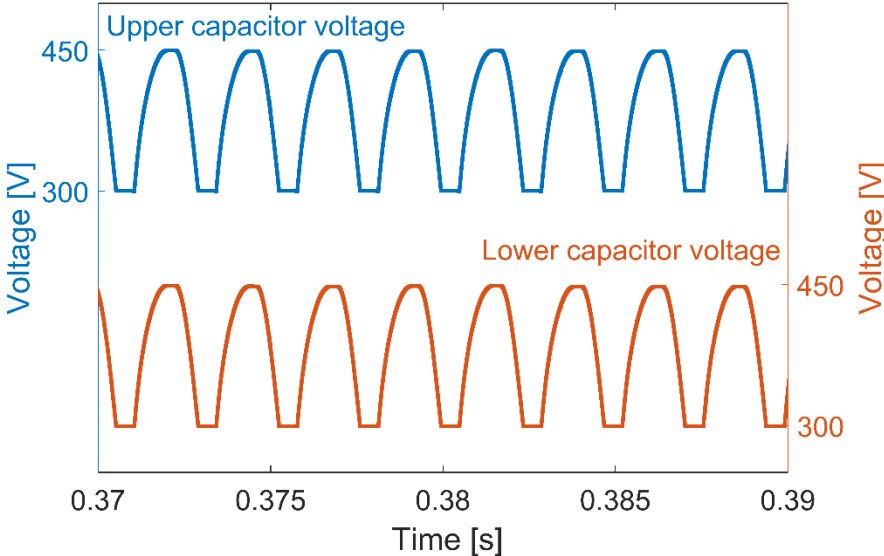
## 4.4    Simulation Results



(a)



(b)

Fig. 4.7 Variation of (a) base-speed and (b) boost-voltage with capacitance.

The 25Nm 1500rpm SRM specifications used in the FEA, MATLAB\Simulink simulations and experimentation are given in Appendix A. The sampling frequency used for simulation is 40kHz, and the motor drives a constant load of 25Nm.



(a)



(b)

Fig. 4.8 SRM waveforms with 65μF boost-capacitors: (a) phase voltage and current at base speed and (b) boost-capacitors, $C_U$ and $C_L$ voltages.

Fig. 4.7 shows the variation of base-speed and boost-voltage with dc link capacitance (upper + lower capacitance for one arm) at different dc link voltages. The motor base-speed and hence output power (power = torque x speed) increase using boost capacitors.

For 300V boost-voltage, based on Fig. 4.7, 65µF, >450V dc capacitors are selected. The dc link voltage is fixed to 600V. The voltage and current waveforms for one motor phase using the selected capacitance are shown in Fig. 4.8a and the balanced boost-capacitor voltages are shown in Fig. 4.8b. Because two phases share a common central converter leg, small currents flow in the decreasing inductance regions, (due to voltage spikes in Fig 4.8a).

Fig. 4.9 shows the voltage and current waveforms below base speed, at 1825rpm. Half the dc link voltage $+\frac{1}{2}V_{DC}$ (which is alternated between states 4.3(b) and 4.3(c)) is used only for 1µs as a transient state to ensure voltage sharing between phase switches thus the clamping diodes $D_3$ and $D_4$ are only transient current rated if switch state 4.3(e) is not employed.
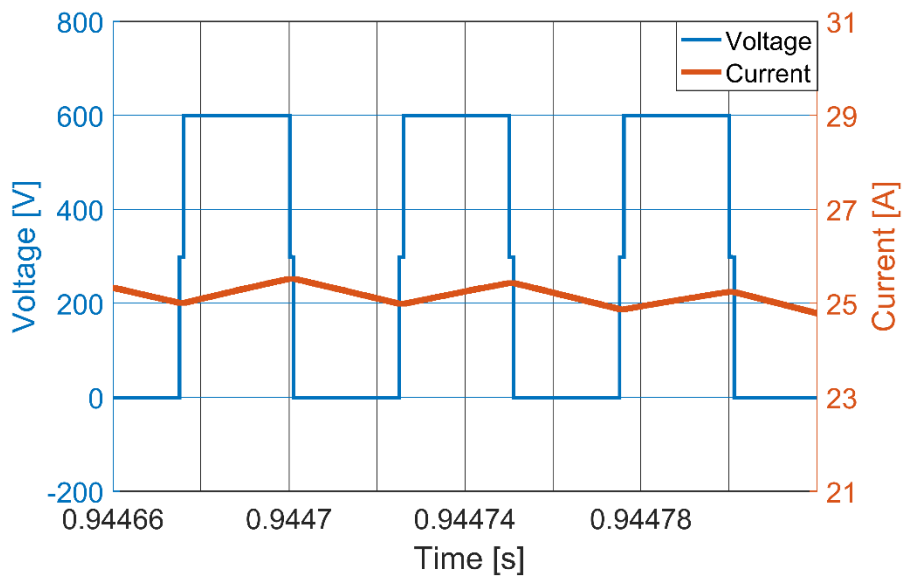


Fig. 4.9 Phase voltage and current waveforms during excitation at low speed.

The PWM adopted in this control strategy uses only 0% and 100% duty cycles for the switches (that is, at each sampling instant if the error signal in phase current is positive, the appropriate switches are turned on until the next sampling instant. Otherwise, the appropriate switches are

59

turned off) This PWM strategy enables the sampling (phase current) frequency to be twice the switching frequency for more accurate operation with lower switching losses and current ripple noise. Device losses are symmetrical about the central leg (but not uniformly distributed). Capacitor balancing takes precedence over alternating of the $\pm\frac{1}{2}V_{DC}$ states.

SRM torque/speed and output power/speed characteristics with and without boost-capacitors are shown in Fig. 4.10. Below base speed, current chopping control is applied for constant torque operation. Above base speed, the advance angle control method is employed for constant power operation. The proposed voltage-boosting method (50%) increases the motor base speed from 1735rpm to 2130rpm, giving a 23% increase in the output power (W/kg) at base speed. This improvement allows the SRM to compete with PMSM in terms of power density.
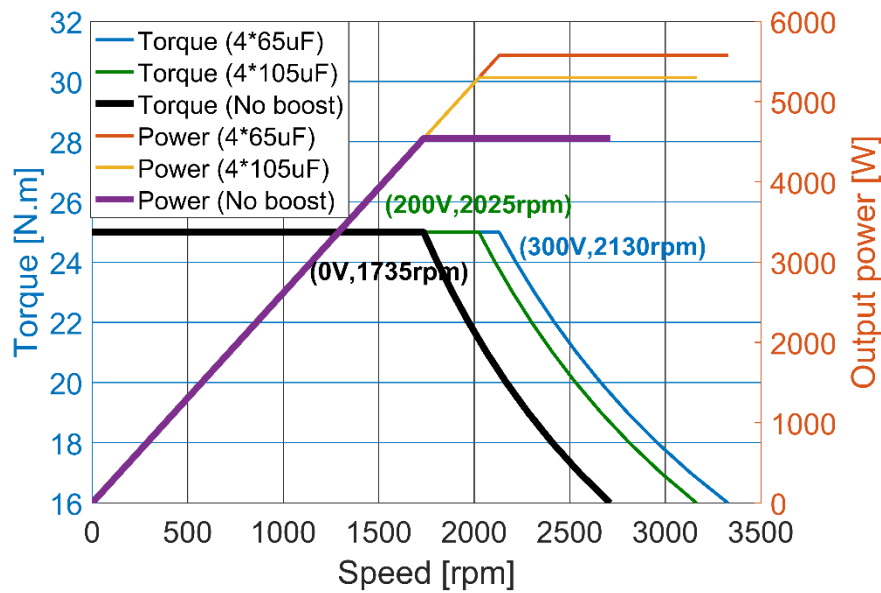


Fig. 4.10 Torque/speed and power/speed characteristics

To assess braking mode performance, the SRM is motored for 0.4s with current injected in the rising inductance region. After receiving a braking command all the phases are briefly turned on (including those switches on, remaining on) simultaneously to allow the boost capacitors to discharge (to $V_{DC}$) into the machine windings and then all the switches are turned off until the current decays. Current is then injected in the falling inductance region (the phase sequence is reversed) to allow regenerative braking as shown in Fig. 4.11a. This is the simplest, but not necessarily the optimal reversing/regeneration method.
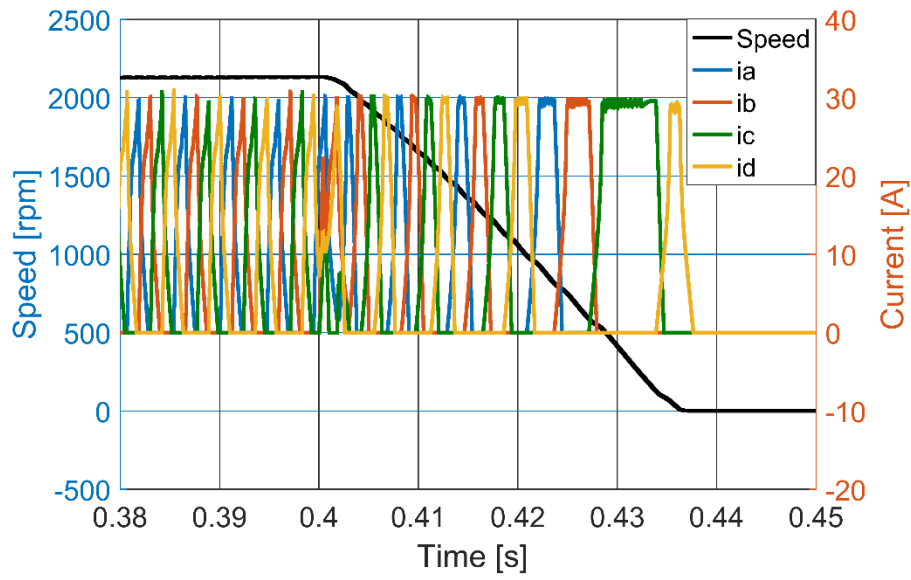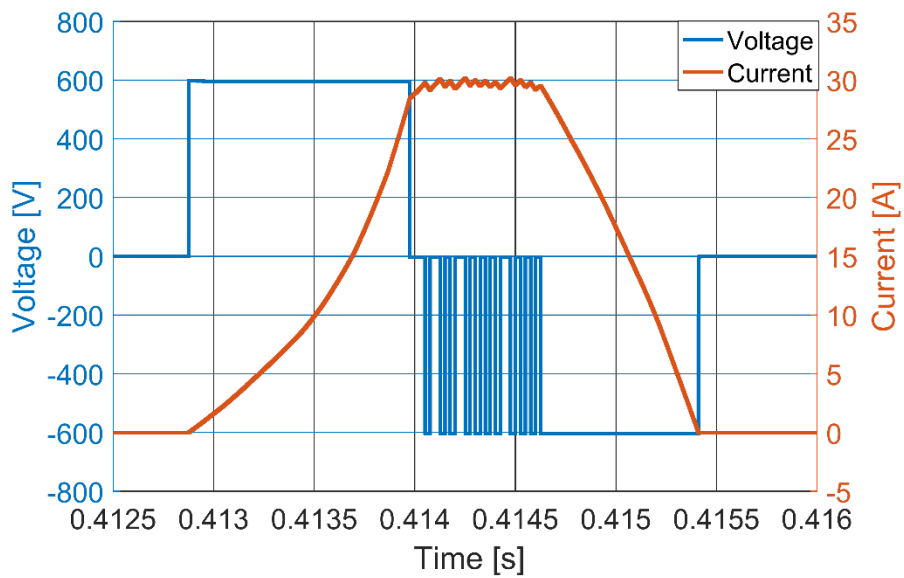
Fig. 4.11 (a) Regenerative braking and (b) Voltage and current waveforms during regenerative braking (soft chopping).

Fast and efficient braking action is achieved without dissipating energy (regeneration). The dc supply is disconnected after the motor comes to rest, otherwise the motor will rotate in opposite direction (reverse). Since the SRM back emf is negative when current is injected in the falling inductance region ($\partial L / \partial \theta < 0$), a soft chopping current control mode (0V, -V) is applied during

motor braking instead of hard chopping current control (+V, -V) as shown in Fig. 4.11b to minimize switching losses during braking.

## 4.5    Experimental Results

Fig. 4.12 shows the experimental test rig used for drive validation. A dc source voltage of 100V is utilized, the boosting capacitors are 75μF ($\pm$10%), and the sampling frequency is 20 kHz. The effect of voltage boosting on SRM performance is compared in two different cases; single pulse mode and current switching mode.
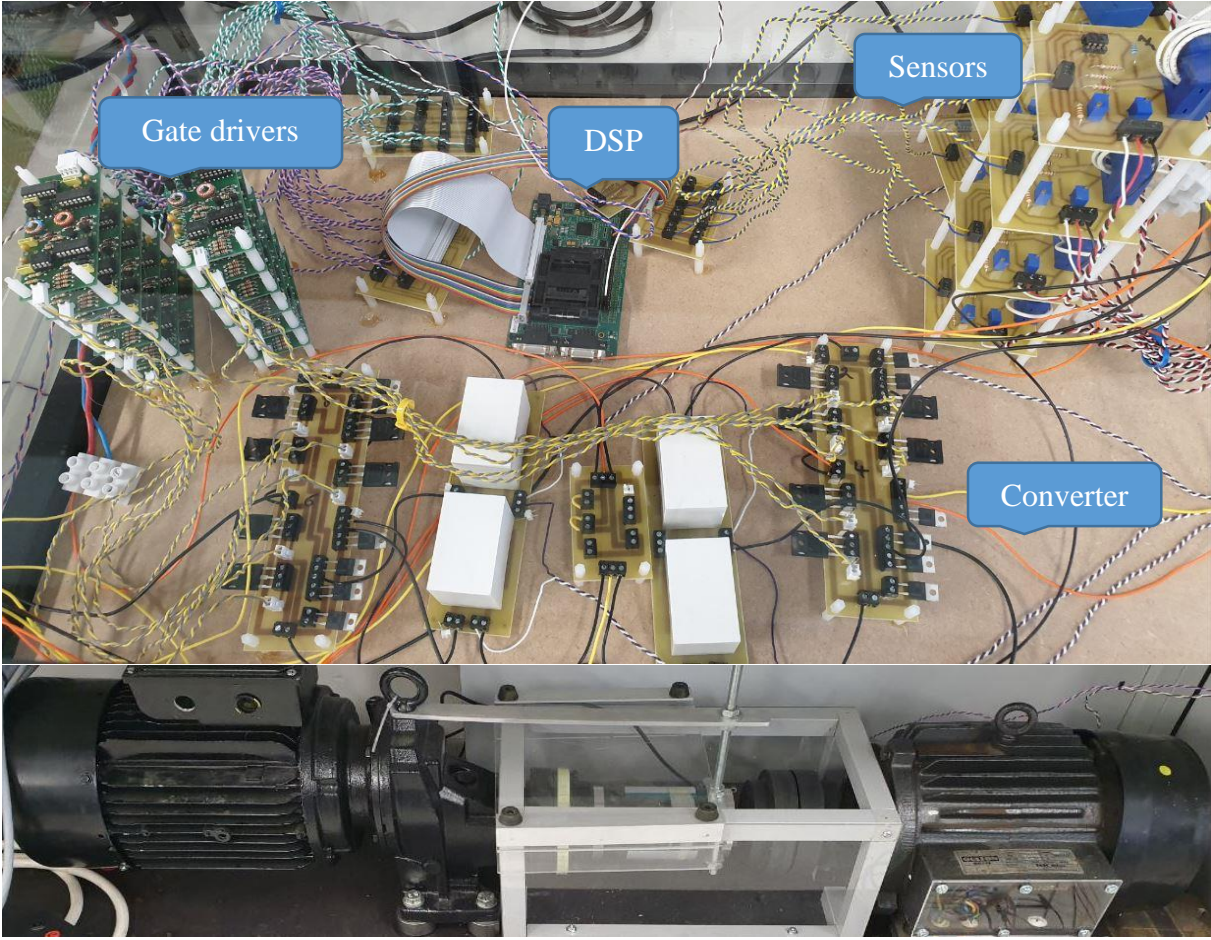


Fig. 4.12 Experimental test rig

Fig. 4.13 shows the phase voltage, current, capacitor voltages, instantaneous torque and speed, in each case. Below base speed (that is, current switching mode), where the torque is constant, the

speed is controlled by adjusting the phase reference current. Allowing the current to build up quickly enables the SRM to operate at higher speed.
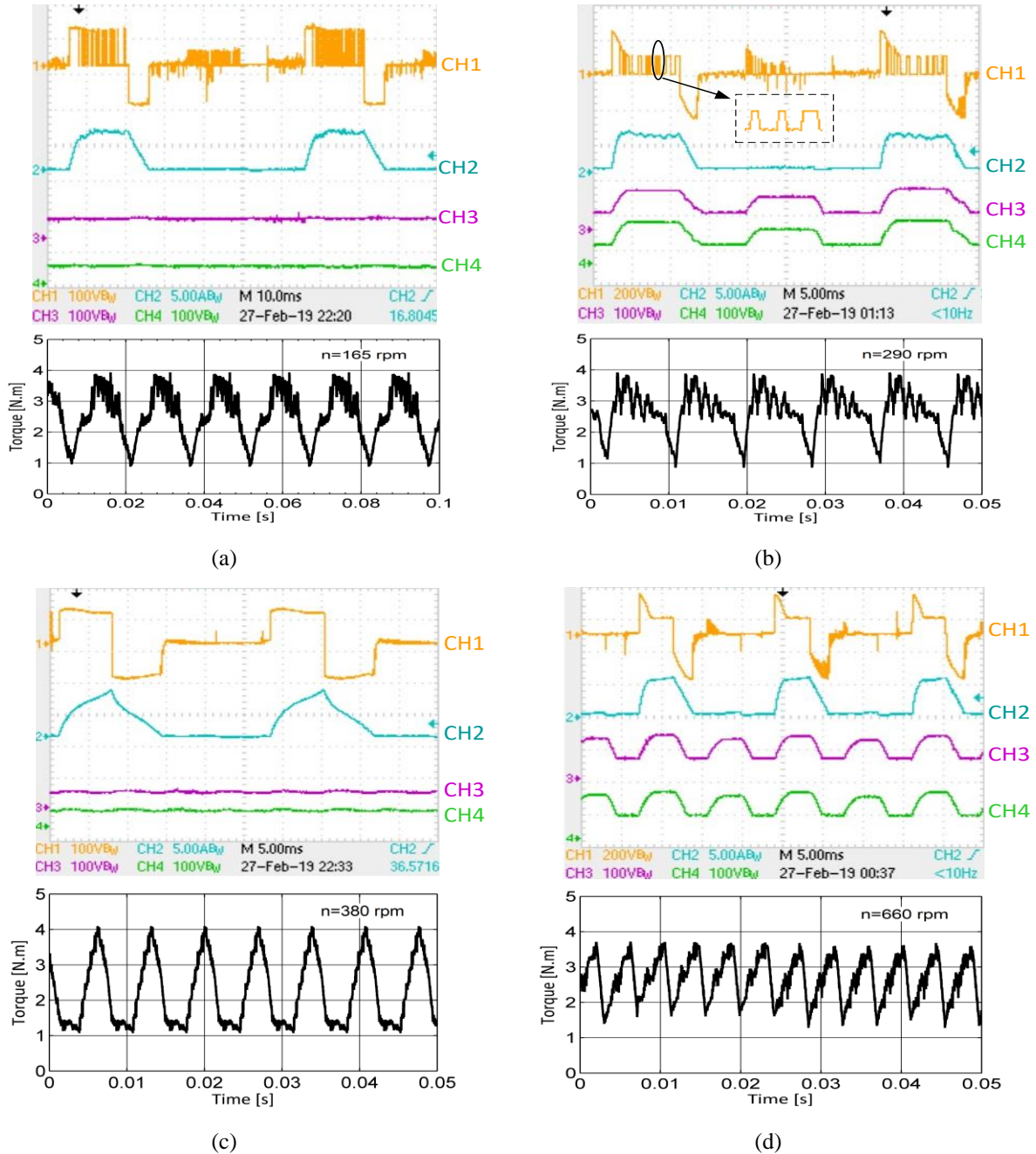


Fig. 4.13 Experimental results: current chopping mode (a) without voltage boosting and (b) with boost-capacitors, single pulse mode (c) without voltage boosting, and (d) with boost-capacitors. Phase voltage (CH1), phase current (CH2), upper capacitor voltage (CH3), lower capacitor voltage (CH4), and instantaneous torque.

63

Fig. 4.13a shows SRM performance without voltage boosting, where the phase voltage is equal to the dc link voltage, while the capacitor voltages are maintained at half the dc link voltage. Since the available dc link (source) voltage (without boost) is insufficient for the current to build up quickly, the speed is 165 rpm.

Fig. 4.13b establishes that motor performance in the current chopping mode is enhanced, since the phase voltage is equal to the dc source voltage (battery) plus boost voltage. The extra voltage supplied by the boost capacitors allows fast current build-up. The speed increases to 290 rpm (from165 rpm without boost) at the same load torque. A 1µs dwell is applied when turning on/off the outer/inner switches to assure equal voltage stress on the switches as presented in Fig. 4.13b.

Above base speed, the speed is controlled by adjusting the turn on/off angles and the SRM operates in the constant power region. Fig. 4.13 parts c and d show SRM performance without and with boosting voltage respectively in the single-pulse mode. The extra voltage offered by the boost capacitors allows the current of the incoming phase to build up quickly, thus increasing the motor speed from 380 rpm to 660 rpm at the same load torque. Also, the outgoing phase current decays faster in the presence of the increasing boost-voltage. The exaggerated improvement in the motor speed obtained experimentally (around 75%) is due to the accentuated boost voltage compared to dc source voltage.

To emphasize the importance of voltage boosting on current build up, the rise time of phase current with/without voltage boosting for the two cases; current chopping mode and single pulse mode, is presented in Fig. 4.14 parts a and b respectively.

The simulated and experimental torque/speed characteristics are compared in Fig. 4.15a, while Fig. 4.15b shows the simulated and experimental output power. The effect of a boosting-voltage is shown to have significant effect on the motor base-speed, meaning the rated torque region is extended, with a corresponding increase in output power. The deviation between the experimental and simulated results is due to the modelling of the SRM using FEA, along with ignoring machine core loss.
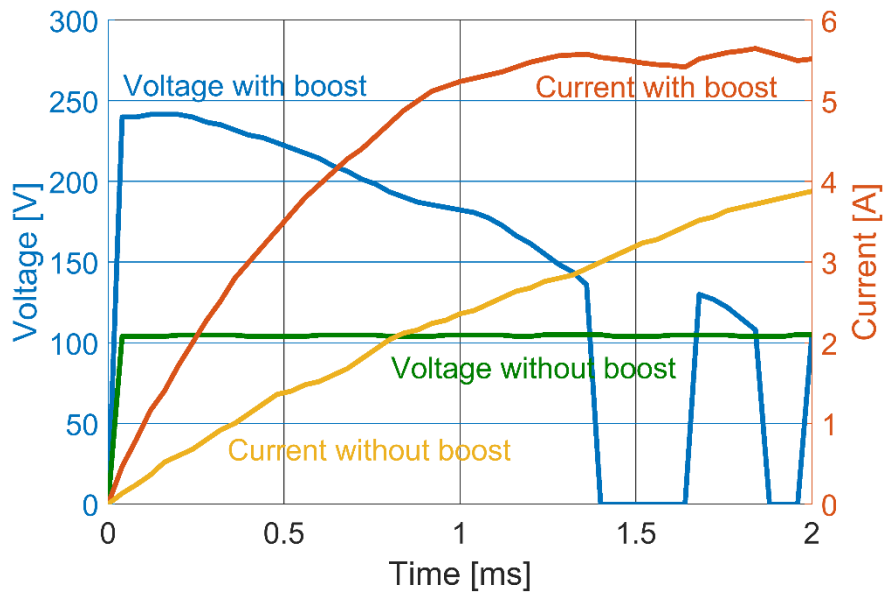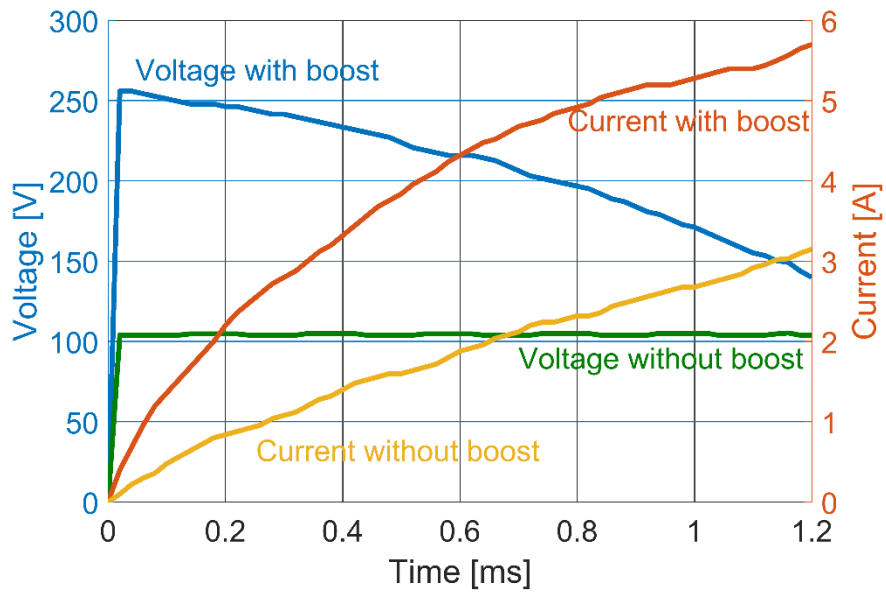
Fig. 4.14 Experimental voltage and current rise time: (a) current chopping mode (with and without voltage boosting) and (b) single pulse mode (with and without voltage boosting)

## 4.6　Machine performance comparison

Two machine types (SRM, and PMSM) are compared in Table 4.3, based on their typical relative power to weight ratio [4-21]. In Table 4.3, the SRM power to weight ratio suffers because of a compromised base speed due to the inability to force sufficient current into (or from) the machine

at higher speeds (power = torque x speed). DC rail voltage boost (50%) increases the speed at which full load torque can be delivered (from 1735rpm to 2130rpm), hence improving the power to weight ratio (by 23%) to be competitive with that of a PMSM, for a given source voltage.
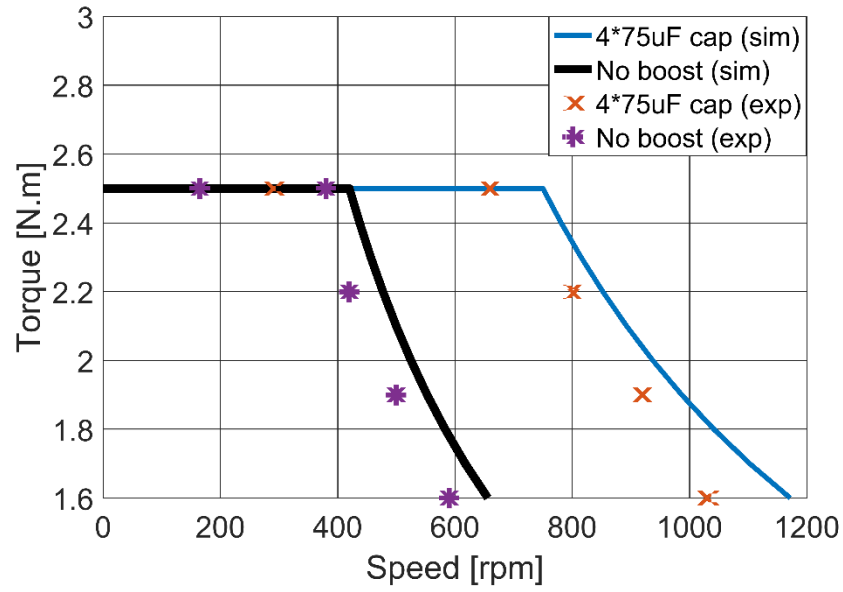


(a)
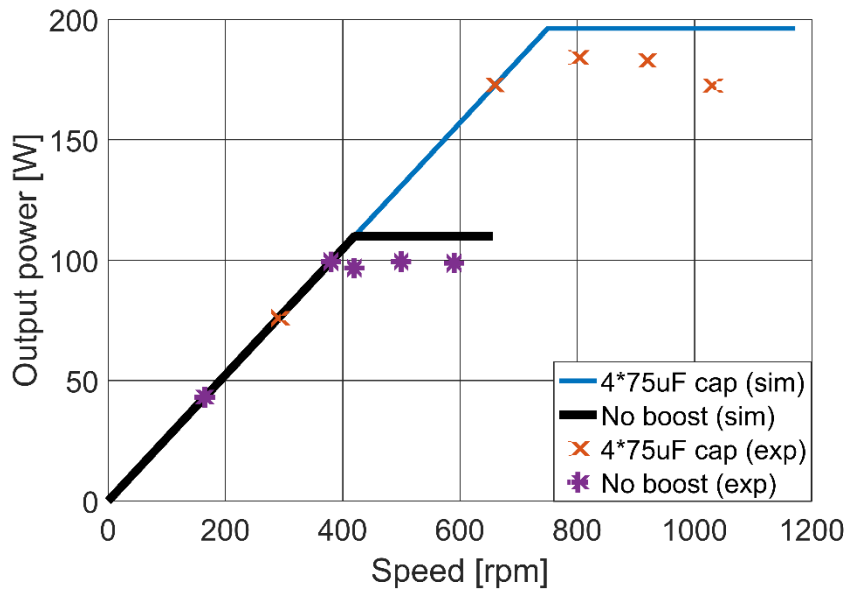


(b)

Fig. 4.15 Experimental versus simulated characteristics with and without dc link voltage boosting: (a) torque/speed and (b) output power/speed.

Table 4.3 RELATIVE PERFORMANCE OF TWO MACHINE TYPES

| Relative pu | PMSM | SRM | SRM + Boost |
|---|---|---|---|
| Power $\left(W/_{kg}\right)$ | 1.0 | 0.8 | 0.93/0.98 |
| SRM power to weight ratio: 200V boost → 0.93pu, 300V boost → 0.98pu | | | |

## 4.7 Converter performance comparison

The proposed topology facilitates lower-rating semiconductor devices, which have the merits of:

- Lower cost.
- Smaller size.
- Higher efficiency.
- Faster response.

The proposed topology, which is based on the NPC, adds minimal cost to the converter when compared with the conventional asymmetric topology (Fig 4.1a with regeneration circuit and Fig 4.1c). The proposed converter utilizes two series dc link capacitors per arm instead of one. However, each capacitor is rated only half the dc link voltage. Thus, the overall cost of the capacitors is near the same since the total energy, whence volume are near the same.

Conventionally, VA is used as a measure to compare the power ratings of semiconductor devices. Since, the proposed topology allows connecting switches in series, each switch is chosen to withstand only half the dc link voltage with the same current rating. Although, the number of switches (and gate drives) increases in the proposed topology, the overall VA does not change. Regarding the main diodes, they block the full voltage, as in the conventional asymmetric topology, with the same current rating. The clamping diodes are additional components. The voltage rating of the clamping diodes is half the dc link voltage and only have a transient current rated. Table 4.4 summarizes a cost comparison between both topologies. The dc link switch and diodes (for regeneration) are excluded as they are the same in both converters.

Extra gate drive circuits and voltage sensors are required with the proposed topology, but the advantages of deploying lower-rating semiconductor devices, especially for high power applications such as EVs mitigate the extra cost.

The PWM adopted in this control strategy (applicable to both converters) uses only 0% and 100% duty cycles for the switches which enables the sampling (phase current) frequency to be twice the switching frequency for more accurate operation with lower switching losses and current ripple noise.

Although the adopted control strategy is more complex, it allows device losses to be symmetrical about the central leg which is a drawback in the prior state of the art converter topology causing asymmetry stress distribution (unless the control strategy is changed, hence losing simplicity).

Table 4.4 COST COMPARISON BETWEEN CONVENTIONAL ASYMMETRIC AND ASYMMETRIC NPC CONVERTERS

| | Conventional asymmetrical converter with voltage-boosting | | | Asymmetrical NPC converter with voltage-boosting | | |
|---|---|---|---|---|---|---|
| | Rating | Quantity | Total | Rating | Quantity | Total |
| Switches | $V_{DC}^*$ x I | 6 | $6V_{DC}^*$ x I | $0.5V_{DC}^*$ x I | 12 | $6V_{DC}^*$ x I |
| Switches total | | | $6V_{DC}^*$ x I | | | $6V_{DC}^*$ x I |
| Main diodes | $V_{DC}^*$ x I | 6 | $6V_{DC}^*$x I | $V_{DC}^*$ x I | 6 | $6V_{DC}^*$ x I |
| Clamp diodes | - | - | 0 | $0.5V_{DC}^*$ x 0.04I* | 6 | $0.12V_{DC}^*$ x I |
| Diodes total | | | $6V_{DC}^*$ x I | | | $6.12V_{DC}^*$ x I |
| Current transducers | | 2 | | | 2 | |
| Voltage transducers | | 2 | | | 4 | |

*I* Transient current rated diode at 40kHz sampling frequency*
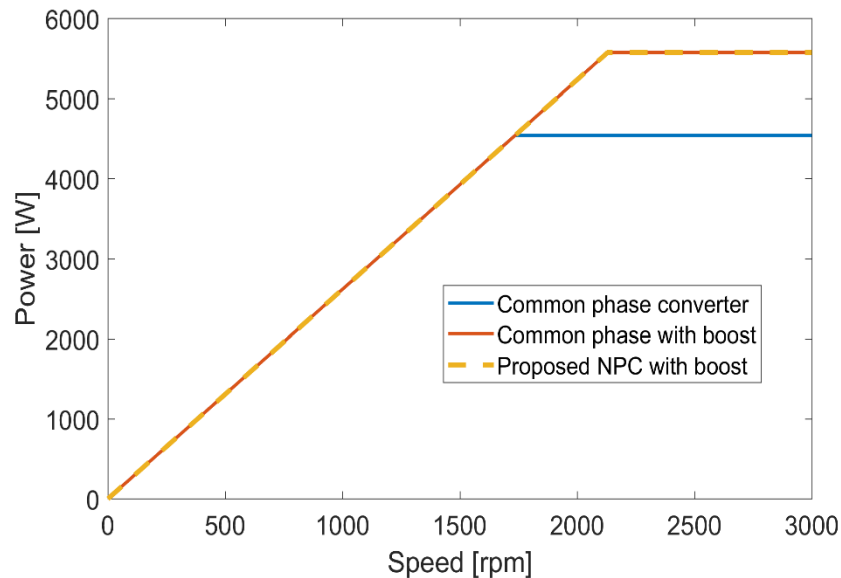$$V_{DC}^* = the\ dc\ link\ voltage + boost$$


Fig. 4.16 SRM output power using three different converters

To further highlight the merits of the proposed converter, a comparison between prior art topologies (either without or with voltage boosting as per Fig. 4.1a) and the proposed converter (as per Fig. 4.1c) is carried out. Fig. 4.16 compares SRM output power at different speeds using the three converters. The effect of voltage-boosting (either in the prior art topology or the proposed NPC converter) is significant and improves the output power by 23% over the prior art topology without voltage-boosting.

Fig. 4.17 compares the conduction and switching losses of the three converters. Semiconductor switches from the same manufacturer (IXYS Semiconductor), with main parameters given in Table 4.5, are deployed for a valid comparison. The main diodes have a forward voltage $V_f = 1.45$. In the proposed topology, fast recovery Schottky diodes with transient current rating are deployed as clamping diodes since the $\pm V_{DC}$ states are transient states dwelled for $1\mu s$ to assure equal voltage stresses on switches.
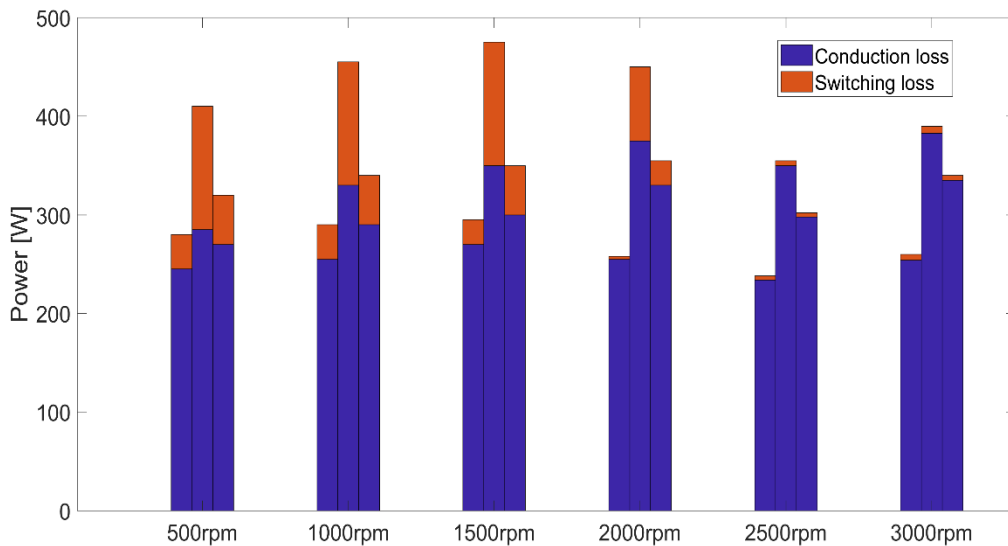


Fig. 4.17 Power loss for three different converters
Left: prior art topology without boost, Middle: prior art topology with boost, and Right: Proposed NPC converter

The prior art topology without voltage-boosting has the lowest conduction and switching losses as the semiconductor devices are rated only at the dc link voltage. However, the proposed topology has lower switching and conduction losses below and above base speed when compared with the

prior art topology with voltage-boosting. The low-rated and fast semiconductor devices significantly improve converter efficiency.

Table 4.5 RATINGS OF SWITCHES

| Point | Common phase without boost | Common phase with boost | Proposed NPC with boost |
|---|---|---|---|
| Switch | IXFK32N80P | IXFB30N120P | IXFR48N60P |
| Voltage rating (V) | 800 | 1200 | 600 |
| Current Rating (A) | 32 | 30 | 32 |
| Turn on resistance ($\Omega$) | 0.27 | 0.35 | 0.15 |
| Turn on rise time (ns) | 24 | 60 | 25 |
| Turn off fall time (ns) | 24 | 56 | 22 |

SRM drive efficiency with the three converters is illustrated in Fig.4.18. The proposed NPC converter with voltage-boosting has better efficiency at all speeds than the prior art topology with voltage-boosting. The proposed converter has better efficiency than the prior art topology without voltage-boosting at high speeds.
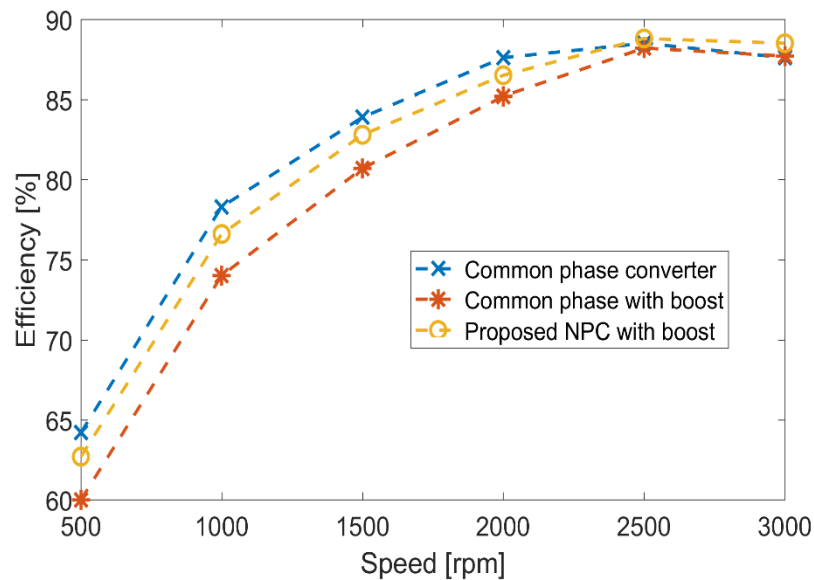


Fig. 4.18 SRM drive efficiency using three different converters

Table 4.6 compares the three different converter topologies.

Table 4.6 COMPARING THE PROPOSED NPC AND PRIOR ART TOPOLOGY CONVERTERS

| Point | Common phase Without boost | Common phase With boost | Proposed topology |
|---|---|---|---|
| Switching stress(about center leg) | Unsymmetrical | Unsymmetrical | Symmetrical |
| Switch efficiency | High | Low | High |
| Switch response | Fast | Slow | Fast |
| Switch size | Medium | Large | Small |
| Current ripple | Low | High | Low |
| Acoustic noise | Low | High | Low |
| Power density | Low | High | High |
| Base speed | Low | High | High |
| Cost of semiconductor devices | Low | Medium | Medium |
| Cost of gate drivers | Low | Low | High |
| Cost of capacitors | - | Similar | Similar |
| Cost of voltage sensors | - | Low | High |
| Control complexity | Low | Low | Higher |

## 4.8    Summary

A novel asymmetric NPC converter with inherent dc link voltage-boosting capacitors for a four-phase SRM drive was presented. Analysis of the proposed converter during motoring and braking resulted in a design approach for sizing the dc link boost capacitors. The proposed converter improves SRM drive performance at low and high speeds. The boost voltage increases the motor base speed, hence output power and efficiency. The SRM power to weight ratio with voltage boosting capability is competitive with the PMSM and has the advantage of a higher torque to weight ratio. Regenerative braking can be deployed for efficient and fast braking action. The new converter allows series connection of fast, low-voltage, efficient switches. Topology penalties are increased number of gate drives and increased control complexity when introducing NPC intermediate dwell states.

## References

[4-1]  C. Jung, "Power Up with 800-V Systems: The benefits of upgrading voltage power for battery-electric passenger vehicles," in *IEEE Electrification Magazine*, vol. 5, no. 1, pp. 53-58, March 2017.

[4-2]  S. J. Watkins, J. Corda and L. Zhang, "Multilevel asymmetric power converters for switched reluctance machines," *2002 International Conference on Power Electronics, Machines and Drives (Conf. Publ. No. 487)*, Sante Fe, NM, USA, 2002, pp. 195-200.

[4-3]   D. Patil, S. Wang and L. Gu, "Multilevel converter topologies for high-power high-speed switched reluctance motor: Performance comparison," *2016 IEEE Applied Power Electronics Conference and Exposition (APEC)*, Long Beach, CA, 2016, pp. 2889-2896.

[4-4]   J. Borecki and B. Orlik, "Novel, multilevel converter topology for fault-tolerant operation of switched reluctance machines," *2017 11th IEEE International Conference on Compatibility, Power Electronics and Power Engineering (CPE-POWERENG)*, Cadiz, 2017, pp. 375-380.

[4-5]   F. Peng, J. Ye and A. Emadi, "An Asymmetric Three-Level Neutral Point Diode Clamped Converter for Switched Reluctance Motor Drives," in *IEEE Transactions on Power Electronics*, vol. 32, no. 11, pp. 8618-8631, Nov. 2017.

[4-6]   S. Chan and H. R. Bolton, "Performance enhancement of single-phase switched-reluctance motor by DC link voltage boosting," in *IEE Proceedings B - Electric Power Applications*, vol. 140, no. 5, pp. 316-322, Sept. 1993.

[4-7]   M. Barnes and C. Pollock, "Power converter for single phase switched reluctance motors," in *Electronics Letters*, vol. 31, no. 25, pp. 2137-2138, 7 Dec. 1995.

[4-8]   A. Dahmane, F. Meebody and F. -. Sargos, "A novel boost capacitor circuit to enhance the performance of the switched reluctance motor," *2001 IEEE 32nd Annual Power Electronics Specialists Conference (IEEE Cat. No.01CH37230)*, Vancouver, BC, 2001, pp. 844-849 vol.2.

[4-9]   D. Lee and J. Ahn, "A Novel Four-Level Converter and Instantaneous Switching Angle Detector for High Speed SRM Drive," in *IEEE Transactions on Power Electronics*, vol. 22, no. 5, pp. 2034-2041, Sept. 2007.

[4-10]  J. Liang, D. Lee, G. Xu and J. Ahn, "Analysis of Passive Boost Power Converter for Three-Phase SR Drive," in *IEEE Transactions on Industrial Electronics*, vol. 57, no. 9, pp. 2961-2971, Sept. 2010.

[4-11]  C. Zhang, K. Wang, S. Zhang, X. Zhu and L. Quan, "Analysis of Variable Voltage Gain Power Converter for Switched Reluctance Motor," in *IEEE Transactions on Applied Superconductivity*, vol. 26, no. 7, pp. 1-5, Oct. 2016.

[4-12]  S. Xu, H. Chen, J. Yang and F. Dong, "Performance Evaluation and Reliability Enhancement of Switched Reluctance Drive System by a Novel Integrated Power Converter," in *IEEE Transactions on Power Electronics*, vol. 34, no. 11, pp. 11090-11102, Nov. 2019.

[4-13]  X. Deng, B. Mecrow, H. Wu, R. Martin and Y. Gai, "Cost-Effective and High-Efficiency Variable-Speed Switched Reluctance Drives With Ring-Connected Winding Configuration," in *IEEE Transactions on Energy Conversion*, vol. 34, no. 1, pp. 120-129, March 2019.

[4-14] Q. Sun, J. Wu, C. Gan and J. Guo, "Modular Full-Bridge Converter for Three-Phase Switched Reluctance Motors With Integrated Fault-Tolerance Capability," in *IEEE Transactions on Power Electronics*, vol. 34, no. 3, pp. 2622-2634, March 2019.

[4-15] Q. Chen, D. Xu, L. Xu, J. Wang, Z. Lin and X. Zhu, "Fault-Tolerant Operation of a Novel Dual-Channel Switched Reluctance Motor Using Two 3-Phase Standard Inverters," in *IEEE Transactions on Applied Superconductivity*, vol. 28, no. 3, pp. 1-5, April 2018.

[4-16] S. Song, Z. Xia, Z. Zhang and W. Liu, "Control Performance Analysis and Improvement of a Modular Power Converter for Three-Phase SRM With Y-Connected Windings and Neutral Line," in *IEEE Transactions on Industrial Electronics*, vol. 63, no. 10, pp. 6020-6030, Oct. 2016.

[4-17] R. Martin, J. D. Widmer, B. C. Mecrow, M. Kimiabeigi, A. Mebarki and N. L. Brown, "Electromagnetic Considerations for a Six-Phase Switched Reluctance Motor Driven by a Three-Phase Inverter," in *IEEE Transactions on Industry Applications*, vol. 52, no. 5, pp. 3783-3791, Sept.-Oct. 2016.

[4-18] M. Abd Elmutalab, A. Elrayyah, T. Husain and Y. Sozer, "Extending the Speed Range of a Switched Reluctance Motor Using a Fast Demagnetizing Technique," in *IEEE Transactions on Industry Applications*, vol. 54, no. 4, pp. 3294-3304, July-Aug. 2018.

[4-19] J. Kim and R. Krishnan, "Novel Two-Switch-Based Switched Reluctance Motor Drive for Low-Cost High-Volume Applications," in *IEEE Transactions on Industry Applications*, vol. 45, no. 4, pp. 1241-1248, July-Aug. 2009.

[4-20] B. Fahimi, G. Suresh, J. Mahdavi and M. Ehsami, "A new approach to model switched reluctance motor drive application to dynamic performance prediction, control and design," *PESC 98 Record. 29th Annual IEEE Power Electronics Specialists Conference (Cat. No.98CH36196)*, Fukuoka, 1998, pp. 2097-2102 vol.2.

[4-21] R. M. Pindoriya, B. S. Rajpurohit, R. Kumar and K. N. Srivastava, "Comparative analysis of permanent magnet motors and switched reluctance motors capabilities for electric and hybrid electric vehicles," *2018 IEEMA Engineer Infinite Conference (eTechNxT)*, New Delhi, 2018, pp. 1-5.

## *Chapter 5*

## *Theory and Operation of the SRM with Rotor Conducting Screens*

This chapter investigates the effect of utilizing rotor electrical conducting screens within an SRM. Conducting, non-magnetic materials such as aluminium or copper are inserted into the interpole regions of the rotor. The effective unaligned inductance decreases which in turn increases the conversion area allowing the SRM to develop more power. A procedure for calculating the effective unaligned inductance for screened motors using the flux tube method is presented. Finite element analysis results establish the validity of the proposed calculation method.

### 5.1   Introduction

In simplistic terms, the current into and out of an SRM (at phase current turn-on and turn-off) can be expressed by

$$V = \pm L \, \frac{di}{dt} \tag{5.1}$$

The objective is to force the current into and out of the machine as quickly as possible, that is, through maximizing the $di/dt$ term, the base-speed, whence output power can be increased. The inductive term $L$ is related to the machine design and specifically low $L$ (for $V$ fixed) at only phase turn-on will increase the conversion area, and hence increase the output power, as shown in Fig 5.1. (Higher $L$ is required at the turn-off to maximize the machine co-energy).

The concept of conducting screens was proposed in [5-1] to increase the output torque. Conducting, non-magnetic materials such as aluminium or copper are inserted in the interpole regions of the rotor. The conducting screens encounter a time-varying flux due to motor rotation, which induces a voltage. The induced voltage produces eddy currents, which in turn produce flux that opposes the original stator pole flux. The opposing flux results in a decrease in the effective unaligned inductance. However, the impact of reducing the unaligned inductance on the developed

torque was not positive. In [5-2]-[5-4], the rotor conducting screens were tested for four-phase (8/6), two-phase (4/2), and single-phase (2/2) SRM, respectively. Although the deployment of rotor conducting screens improved SRM torque per unit volume, the effect of thickness, shape, and material of the conducting screens on SRM performance, including screen loss, was not investigated. Hence, there is no guide available for the optimal selection of the conducting screen to yield good performance at low cost. Also there was no attempt to calculate the effective unaligned inductance for an SRM with conducting screens.

In this chapter a detailed calculation method based on flux tubes is presented to calculate the effective unaligned inductance for a screened SRM. The proposed method (which is based on the flux tube method) [5-5] is validated by FEA using four different SRMs. The dynamic performance and optimal selection of rotor conducting screens are discussed in chapter 6 in detail.

## 5.2    SRM with rotor conducting screens

Torque is dependent on the difference between the aligned and unaligned inductances (which represents the increase in co-energy), and increasing this difference produces more torque and hence, output power as shown in Fig. 5.1.
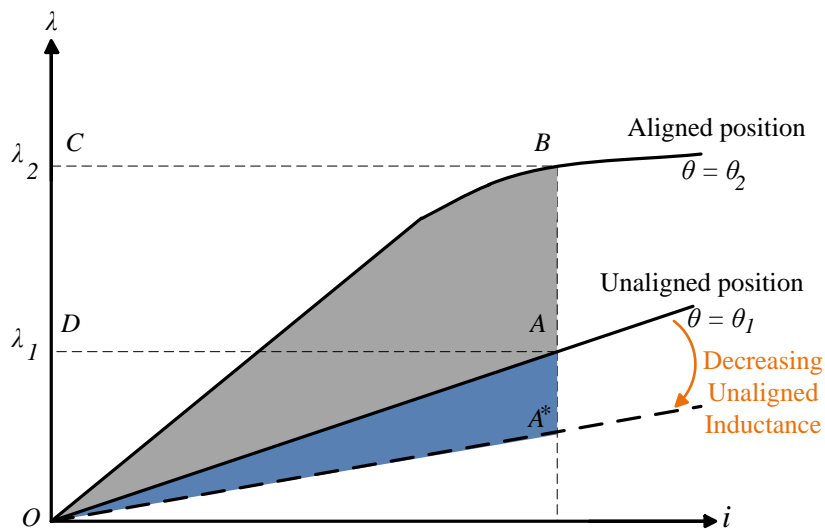


Fig. 5.1 Flux linkage – current $\lambda$ -$i$ characteristics of SRM with and without conducting screens

In order to decrease the unaligned inductance (without affecting the aligned inductance), the spaces between rotor poles can be filled with non-magnetic, electrically conducting material such as aluminium or copper, as shown in Fig. 5.2; this material is referred to as the conducting screen (or flux barrier). The conducting screens are electrically isolated from the rotor and there is no electrical connection between the conducting screens.
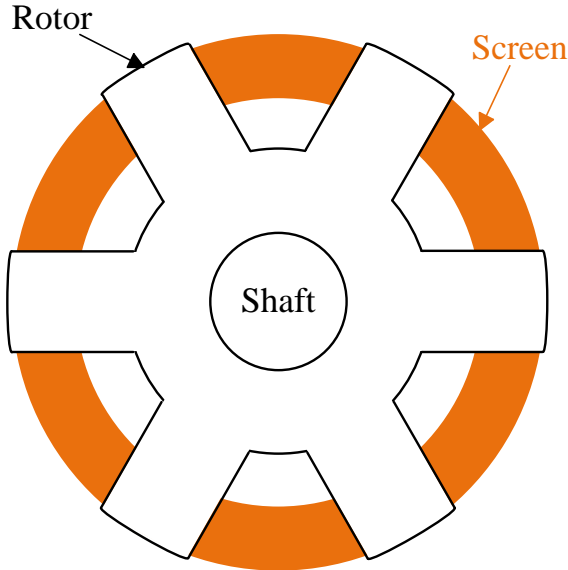


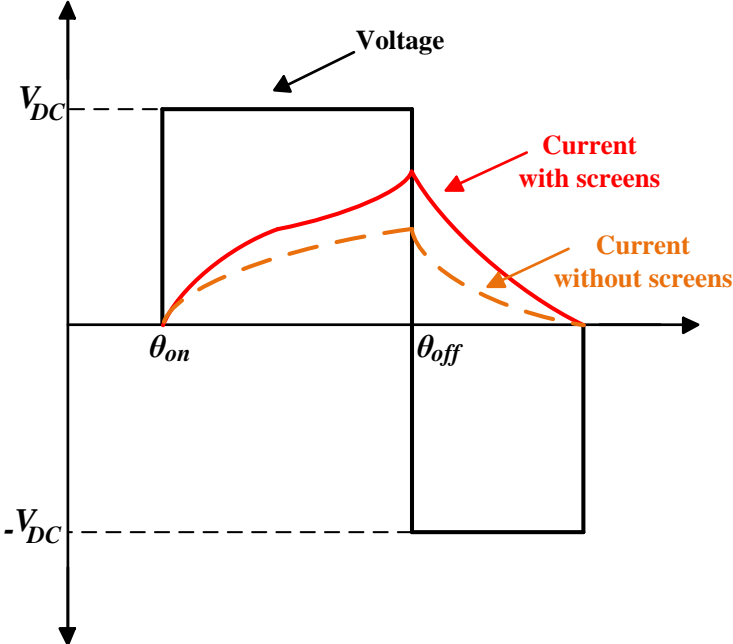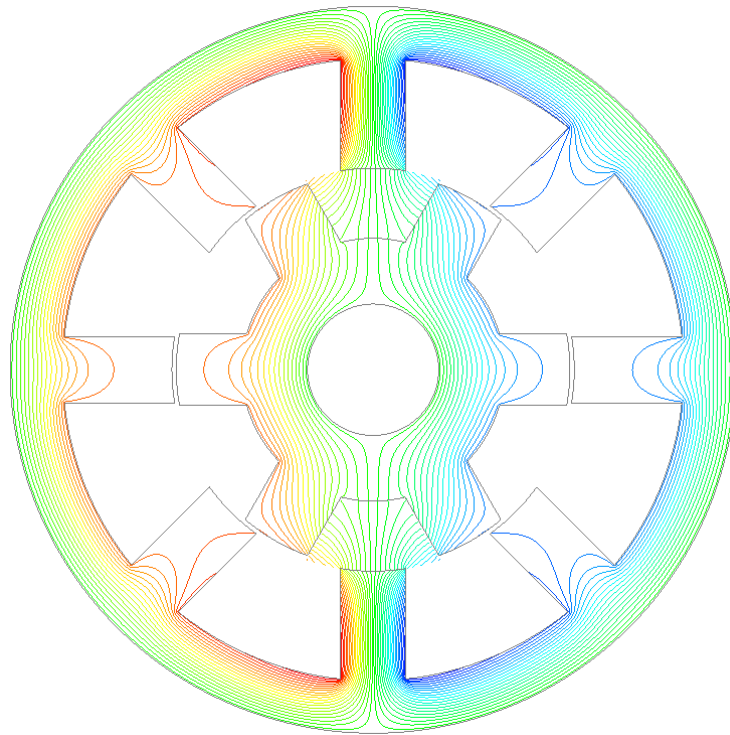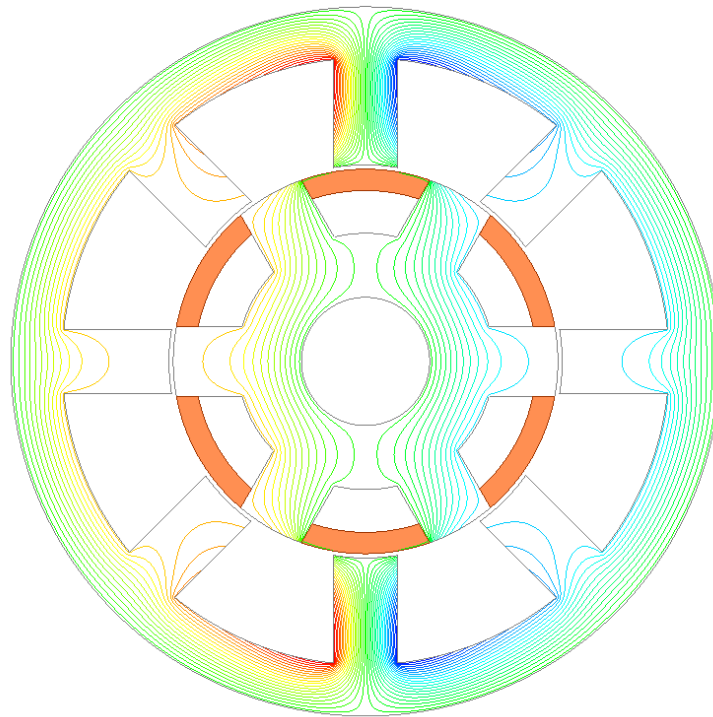Fig. 5.2 Rotor conducting screens, in the interpole regions



Fig. 5.3 SRM voltage and current waveforms with and without conducting screens

(a)



(b)

Fig. 5.4 Magnetic flux lines: (a) Unscreened SRM and (b) Screened SRM

Due to motor rotation along with stator coil excitation, the conducting screens encounter a time-varying flux, which in turn induces voltage ($V \propto d\varphi/dt$). The induced voltage produces circulating eddy currents that produce flux ($i \propto \varphi$). The produced flux opposes the original flux from the stator poles. The opposing flux (which increases the effective flux air path length and reduces the effective area) results in a decrease in the effective unaligned inductance. The decrease in the effective unaligned inductance allows rapid current building up at initial winding excitation, as demonstrated in Fig. 5.3, which increases the motor output torque.

To gain insight into the effect of rotor conducting screens on the SRM performance, Fig. 5.4 parts a and b show the flux path for unscreened and copper screened SRMs, respectively, when one stator phase is excited. Fig. 5.4b shows that the reaction field produced by the eddy current in the copper screen opposes the stator magnetic field, hence preventing the flux lines from crossing through the rotor interpole region, unlike in Fig. 5.4a. The reluctance path length $l$ is increased and the area $A$ is reduced, thus decreasing unaligned inductance $L$, since $L \propto A/l$.

## 5.3    Calculation of effective unaligned inductance for screened SRM

In the early design stage, it is time-consuming to use FEA to predict motor performance. Any change in the motor geometrical dimensions, number of stator/rotor poles, turns number, excitation current or firing angles will dictate a new model to be built and simulated, involving a time consuming process [5-6].  Thus, suitable analytical methods can provide a compromise between accuracy and speed of calculation. The torque depends on the conversion area (area OAB in Fig. 5.1) which is the increase in co-energy when the rotor moves from the unaligned to the aligned position. Reducing the effective unaligned inductance will increase the conversion area, hence increase motor output torque. Generally, the conducting screens will have negligible effect on the aligned inductance, since the rotor pole arc is generally greater than the stator pole arc, so flux fringing and leakage are minimal. But the effective unaligned inductance will be affected significantly. To predict motor performance, the effective unaligned inductance should be known. In this section, the flux tube method [5-7] is used to calculate the effective unaligned inductance. Fig. 5.5 shows the flux paths in the unaligned position, where five flux tubes are sufficient to describe the flux paths.
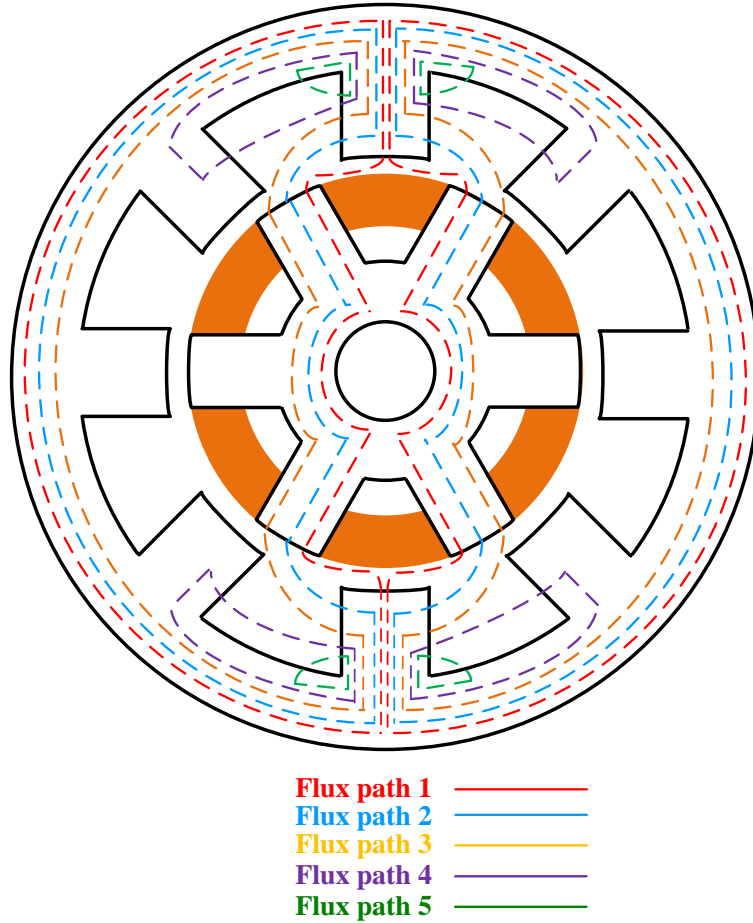
| Flux path 1 | ——— |
| Flux path 2 | ——— |
| Flux path 3 | ——— |
| Flux path 4 | ——— |
| Flux path 5 | ——— |

Fig. 5.5 Flux paths

Fig. 5.6 shows the magnetic equivalent circuit used to calculate the effective unaligned inductance. $R_{sp}, R_g, R_{rp}, R_{sy}$ and $R_{ry}$ are the reluctance paths for the stator pole, air gap, rotor pole, stator back iron, and rotor back iron respectively. The different reluctances are calculated using machine geometrical dimensions.

For nominal current rating, $i$, air gap reluctance dominates the unaligned reluctance resulting in linear flux linkage−current, $\lambda - i$, characteristics; hence, core saturation is not involved, which simplifies the analysis.

Generally, reluctance is defined by

$$R = {l}/{\mu_0 \mu_r A} \tag{5.2}$$

where $l$ is the length of the flux path, $A$ is the cross-sectional area, and $\mu_0$ and $\mu_r$ are the permeability of air and Fe relative permeability respectively. The reluctances for the five flux paths are formulated in the following subsections.
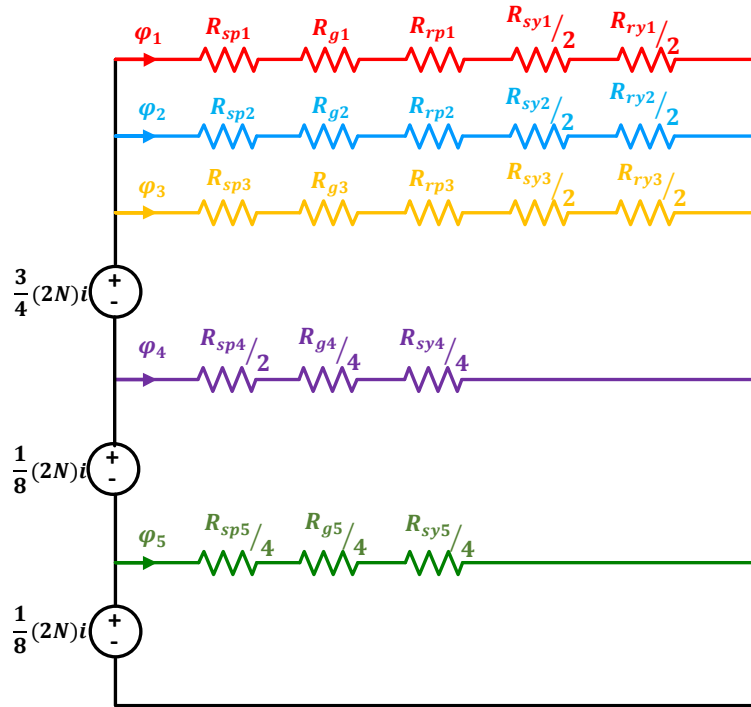


Fig. 5.6 Magnetic equivalent circuit

### 5.3.1   Flux path #1

Fig. 5.7 shows flux path #1 with relevant angles required for derivation. The flux path involves the rotor back iron, the stator back iron, the rotor pole, the stator pole, and the interpolar rotor air gap. Hence, five reluctances are used to complete the flux path. The flux path length and cross-sectional area are calculated as follows. The flux is assumed to leave the stator pole at the tip, and to enter the rotor pole at $\frac{3}{8}\beta_r$ from the pole tip. ($\beta_r$ is rotor pole arc, $\beta_s$ is stator pole arc, and $N$ is the number of turns on one stator pole.)
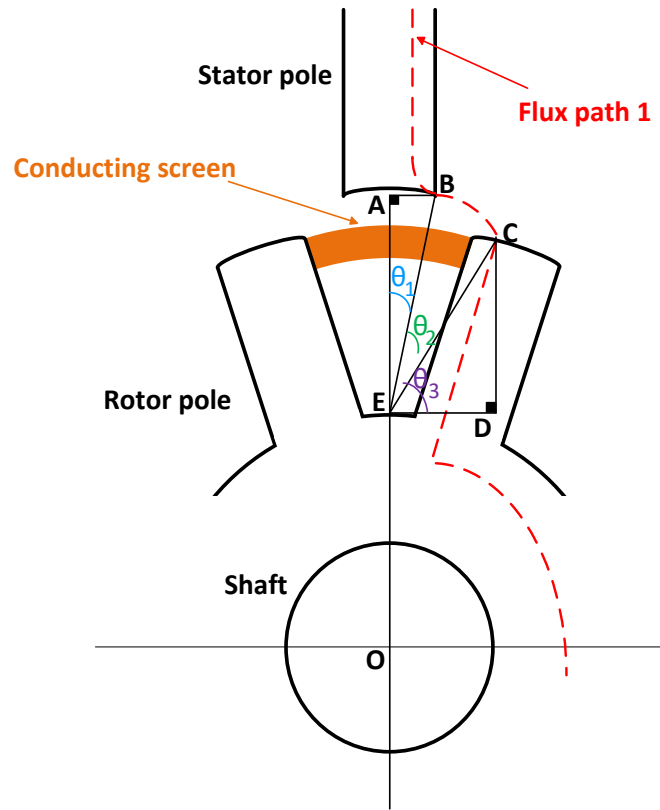
Fig. 5.7 Flux path #1

### 5.3.1i    Air gap reluctance, $R_{g1}$

The length of the air gap flux path is the arc BC, as shown in Fig. 5.7, which is:

$$length = BC = ½(EB + EC)\theta_2^{rad} \tag{5.3}$$

*EB, EC* and $\theta_2$ are calculated using (5.4)-(5.6), respectively.

$$EB = \sqrt{AB^2 + AE^2} \tag{5.4}$$

$$EC = \sqrt{DC^2 + DE^2} \tag{5.5}$$

$$\theta_2^0 = 90^0 - \theta_1^0 - \theta_3^0 \tag{5.6}$$

The angles $\theta_1^0$ and $\theta_3^0$ are defined by (5.7) and (5.8), respectively.

$$\theta_1^0 = \tan^{-1} {AB}/{AE} \tag{5.7}$$

$$\theta_3^0 = \tan^{-1} {DC}/{DE} \tag{5.8}$$

The lengths *AB, AE, DC*, and *DE* are given by (5.9) - (5.12) respectively.

$$AB = \tfrac{1}{2}d \sin \tfrac{1}{2}\beta_s \tag{5.9}$$

$$AE = \tfrac{1}{2}d \cos \tfrac{1}{2}\beta_s - \tfrac{1}{2}D_{sh} - b_{ry} \tag{5.10}$$

$$DC = \left(\tfrac{1}{2}d - l_g\right) \cos\tfrac{1}{2}(\theta_r - \tfrac{1}{4}\beta_r) - \tfrac{1}{2}D_{sh} - b_{ry} \tag{5.11}$$

$$DE = \left(\tfrac{1}{2}d - l_g\right) \sin \tfrac{1}{2}(\theta_r - \tfrac{1}{4}\beta_r) \tag{5.12}$$

The cross-sectional area is the average of the stator and rotor areas. The flux is confined to $\tfrac{1}{4}\beta_s$ of the stator pole arc and to $\tfrac{1}{4}\beta_r$ of the rotor pole arc. Hence, the area is defined as:

$$Area = \tfrac{1}{2}\left\{L_s(\tfrac{1}{8}d\beta_s^{rad}) + L_s\left(\tfrac{1}{2}d - l_g\right)\tfrac{1}{4}\beta_r^{rad}\right\} \tag{5.13}$$

### 5.3.1ii Stator pole reluctance, $R_{sp1}$

The flux travels the length of the stator pole. Hence, the length of the flux path is defined by (5.14), while the area is given by (5.15).

$$length = h_s \tag{5.14}$$

$$Area = \tfrac{1}{8}d\beta_s^{rad}L_s \tag{5.15}$$

### 5.3.1iii Rotor pole reluctance, $R_{rp1}$

Equation (5.16) defines the length of the flux path in the rotor pole, which represents the mean flux path. The area is given by (5.17).

$$length = h_r \tag{5.16}$$

$$Area = L_s\left(\tfrac{1}{2}d - l_g\right)\tfrac{1}{8}\beta_r^{rad} \tag{5.17}$$

5.3.1iv   Stator back iron reluctance, $R_{sy1}$

The length of the flux path in the stator back iron is defined by (5.18), while the area is given by (5.19).

$$length = \tfrac{1}{2}\pi\{D - b_{sy}\} \tag{5.18}$$

$$Area = L_s b_{sy} \tag{5.19}$$

5.3.1v   Rotor back iron reluctance, $R_{ry1}$

The flux path length in the rotor back iron is defined by (5.20) and the area is given by (5.21).

$$length = \tfrac{1}{2}\pi\{D_{sh} + b_{ry}\} \tag{5.20}$$

$$Area = L_s b_{ry} \tag{5.21}$$

After calculating the required reluctances, the inductance for flux path #1, $L_{u1}$ is:

$$L_{u1} = \frac{(2N)^2}{R_{g1} + R_{sp1} + R_{rp1} + \tfrac{1}{2}R_{sy1} + \tfrac{1}{2}R_{ry1}} \tag{5.22}$$

*5.3.2   Flux path #2*

Flux path #2 is illustrated in Fig. 5.8, where the flux is assumed to leave the stator pole at $\tfrac{1}{4}h_s$ from the top of the stator pole, and to enter the rotor pole at the middle.

5.3.2i   Air gap reluctance, $R_{g2}$

The length of the air gap flux path is the arc BC, given by:

$$length = BC = \tfrac{1}{2}(EB + EC)\theta_2^{rad} \tag{5.23}$$

*EB, EC* and $\theta_2$ are calculated using (5.24)-(5.26), respectively.

$$EB = \sqrt{AB^2 + AE^2} \tag{5.24}$$

$$EC = \sqrt{DC^2 + DE^2} \tag{5.25}$$
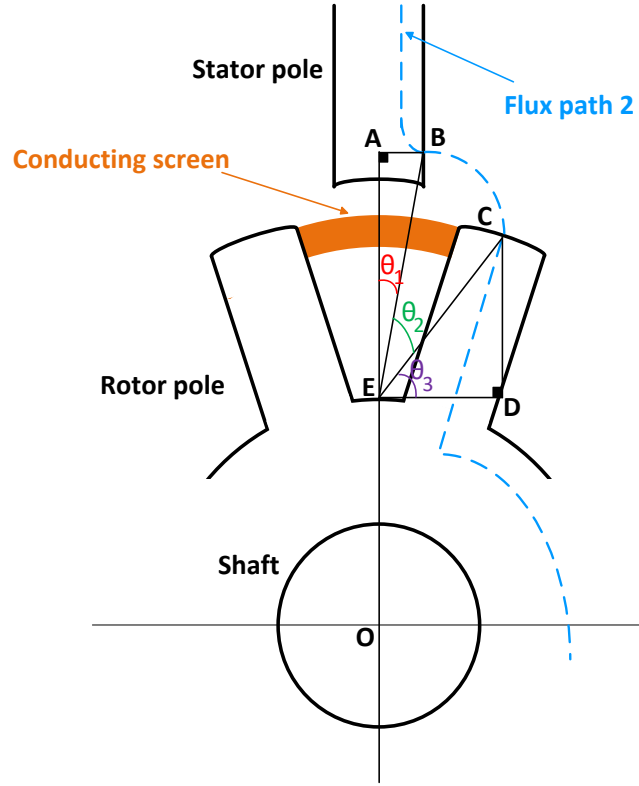
$$\theta_2^0 = 90^0 - \theta_1^0 - \theta_3^0 \tag{5.26}$$



Fig. 5.8 Flux path #2

The angles $\theta_1^0$ and $\theta_3^0$ are defined by (5.27) and (5.28), respectively.

$$\theta_1^0 = \tan^{-1} {AB}/{AE} \tag{5.27}$$

$$\theta_3^0 = \tan^{-1} {DC}/{DE} \tag{5.28}$$

The lengths *AB, AE, DC*, and *DE* are given by (5.29) - (5.32) respectively.

$$AB = \tfrac{1}{2}d \sin \tfrac{1}{2}\beta_s \tag{5.29}$$

$$AE = \tfrac{1}{2}d \cos \tfrac{1}{2}\beta_s + \tfrac{1}{4}h_s - \tfrac{1}{2}D_{sh} - b_{ry} \tag{5.30}$$

84

$$DC = \left(\tfrac{1}{2}d - l_g\right)\cos\tfrac{1}{2}\theta_r - \tfrac{1}{2}D_{sh} - b_{ry} \tag{5.31}$$

$$DE = \left(\tfrac{1}{2}d - l_g\right)\sin\tfrac{1}{2}\theta_r \tag{5.32}$$

The cross-sectional area is the average of the stator and rotor areas. The flux is confined to $\tfrac{1}{3}h_s$ of the stator pole height and to $\tfrac{1}{3}\beta_r$ of the rotor pole arc. Hence, the area is:

$$Area = \tfrac{1}{2}\left\{L_s(\tfrac{1}{3}h_s) + L_s\left(\tfrac{1}{2}d - l_g\right)\tfrac{1}{3}\beta_r^{rad}\right\} \tag{5.33}$$

### 5.3.2ii    Stator pole reluctance, $R_{sp2}$

The flux travels $\tfrac{3}{4}h_s$ of the stator pole, hence the length of the flux path is defined by (5.34), while the area is given by (5.35).

$$length = \tfrac{3}{4}h_s \tag{5.34}$$

$$Area = \tfrac{1}{3}h_s\, L_s \tag{5.35}$$

### 5.3.2iii   Rotor pole reluctance, $R_{rp2}$

Equation (5.36) defines the length of the flux path in the rotor pole, which represents the mean flux path. The area is given by (5.37).

$$length = h_r \tag{5.36}$$

$$Area = L_s\left(\tfrac{1}{2}d - l_g\right)\tfrac{1}{3}\beta_r^{rad} \tag{5.37}$$

### 5.3.2iv   Stator back iron reluctance, $R_{sy2}$

The length of the flux path in the stator back iron is defined by (5.38), while the area is given by (5.39).

$$length = \tfrac{1}{2}\pi\left\{D - b_{sy}\right\} \tag{5.38}$$

$$Area = L_s b_{sy} \tag{5.39}$$

## 5.3.2v  Rotor back iron reluctance, $R_{ry2}$

The length of the flux path in rotor back iron is defined by (5.40) and the area is given by (5.41).

$$length = \frac{1}{2}\pi\{D_{sh} + b_{ry}\} \tag{5.40}$$

$$Area = L_s b_{ry} \tag{5.41}$$

Finally, the inductance for flux path #2, $L_{u2}$ is:

$$L_{u2} = \frac{(2N)^2}{R_{g2} + R_{sp2} + R_{rp2} + \frac{1}{2}R_{sy2} + \frac{1}{2}R_{ry2}} \tag{5.42}$$
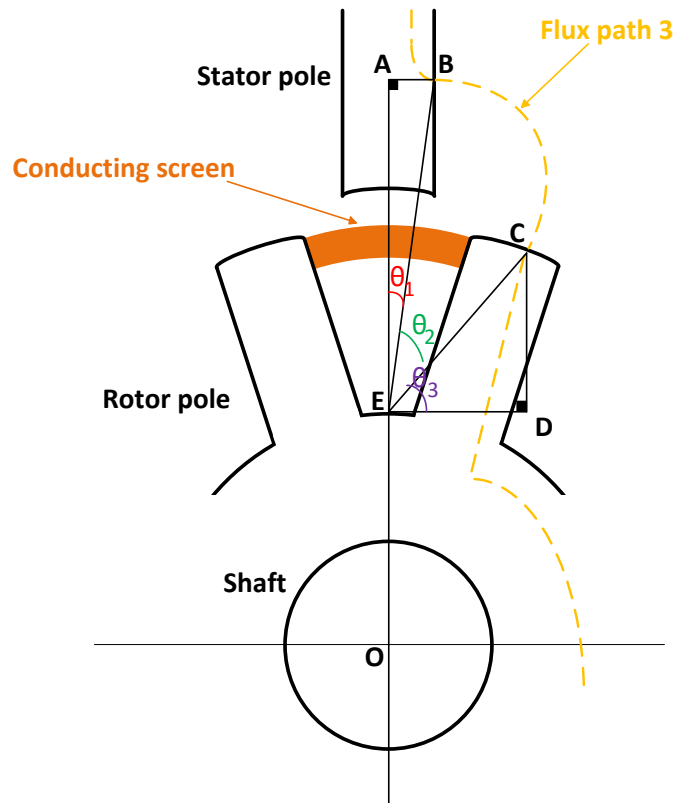
### 5.3.3  Flux path #3



Fig. 5.9 Flux path #3

Fig. 5.9 shows flux path #3 which is similar to path #2 except for some different dimensions. The flux is assumed to leave the stator pole at $\frac{3}{4}h_s$, and to enter the rotor pole at $\frac{5}{8}\beta_r$ from the rotor pole tip.

5.3.3i    Air gap reluctance, $R_{g3}$

The length of the air gap flux path is the arc $BC$, given by:

$$length = BC = \frac{1}{2}(EB + EC)\theta_2^{rad} \tag{5.43}$$

$EB$, $EC$ and $\theta_2$ are calculated using (5.44)-(5.46), respectively.

$$EB = \sqrt{AB^2 + AE^2} \tag{5.44}$$

$$EC = \sqrt{DC^2 + DE^2} \tag{5.45}$$

$$\theta_2^0 = 90^0 - \theta_1^0 - \theta_3^0 \tag{5.46}$$

The angles $\theta_1^0$ and $\theta_3^0$ are defined by (5.47) and (5.48), respectively.

$$\theta_1^0 = \tan^{-1}{AB}/{AE} \tag{5.47}$$

$$\theta_3^0 = \tan^{-1}{DC}/{DE} \tag{5.48}$$

The lengths $AB$, $AE$, $DC$, and $DE$ are given by (5.49) - (5.52) respectively.

$$AB = \frac{1}{2}d \sin \frac{1}{2}\beta_s \tag{5.49}$$

$$AE = \frac{1}{2}d \cos \frac{1}{2}\beta_s + \frac{3}{4}h_s - \frac{1}{2}D_{sh} - b_{ry} \tag{5.50}$$

$$DC = \left(\frac{1}{2}d - l_g\right) \cos \frac{1}{2}(\theta_r + \frac{1}{4}\beta_r) - \frac{1}{2}D_{sh} - b_{ry} \tag{5.51}$$

$$DE = \left(\frac{1}{2}d - l_g\right) \sin\frac{1}{2}(\theta_r + \frac{1}{4}\beta_r) \tag{5.52}$$

The cross-sectional area is the average of the stator and rotor areas. The flux is confined to $\frac{1}{4}h_s$ of the stator pole height and to $\frac{1}{4}\beta_r$ of the rotor pole arc. Hence, the area is:

$$Area = \tfrac{1}{2}\{L_s(\tfrac{1}{4}h_s) + L_s(\tfrac{1}{2}d - l_g)\tfrac{1}{4}\beta_r^{rad}\} \tag{5.53}$$

### 5.3.3ii   Stator pole reluctance, $R_{sp3}$

The flux travels only $\tfrac{1}{4}h_s$ of the stator pole, hence the length of the flux path is defined by (5.54), while the area is given by (5.55).

$$length = \tfrac{1}{4}h_s \tag{5.54}$$
$$Area = \tfrac{1}{4}h_s\,L_s \tag{5.55}$$

### 5.3.3iii   Rotor pole reluctance, $R_{rp3}$

Equation (5.56) defines the length of the flux path in the rotor pole, which represents the mean flux path. The area is defined by (5.57).

$$length = h_r \tag{5.56}$$
$$Area = L_s(\tfrac{1}{2}d - l_g)\tfrac{1}{4}\beta_r^{rad} \tag{5.57}$$

### 5.3.3iv   Stator back iron reluctance, $R_{sy3}$

The length of the flux path in the stator back iron is defined by (5.58), and the area is given by (5.59).

$$length = \tfrac{1}{2}\pi\{D - b_{sy}\} \tag{5.58}$$
$$Area = L_s b_{sy} \tag{5.59}$$

### 5.3.3v   Rotor back iron reluctance, $R_{ry3}$

The length of the flux path in rotor back iron is defined by (5.60) and the area is given by (5.61).

$$length = \tfrac{1}{2}\pi\{D_{sh} + b_{ry}\} \tag{5.60}$$
$$Area = L_s b_{ry} \tag{5.61}$$

The inductance for flux path #3, $L_{u3}$ is:

$$L_{u3} = \frac{(2N)^2}{R_{g3} + R_{sp3} + R_{rp3} + \frac{1}{2}R_{sy3} + \frac{1}{2}R_{ry3}} \tag{5.62}$$

### 5.3.4  *Flux path #4*

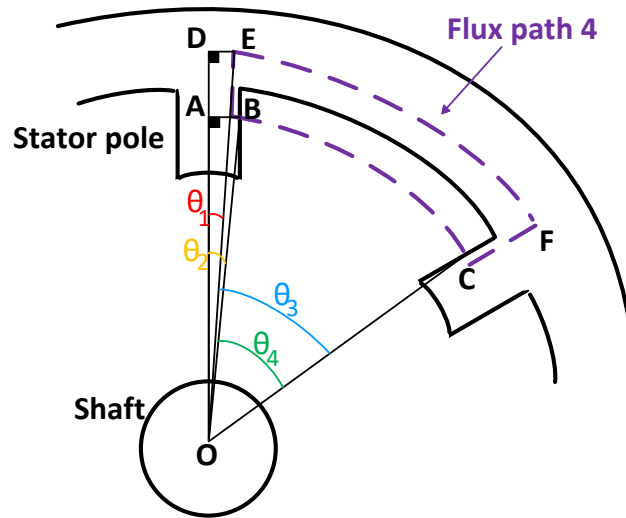The fourth flux path is shown in Fig. 5.10.



Fig. 5.10 Flux path #4

The flux flows from one stator pole to the adjacent stator pole through the air gap and returns via the stator back iron. The rotor is not involved in this flux tube. The three reluctances, $R_{g4}, R_{sp4}$, and $R_{sy4}$, for this flux tube are calculated as follows.

5.3.4i   Air gap reluctance, $R_{g4}$

The length of the air gap flux path is the arc $BC$:

$$length = BC = (OB)\theta_4^{rad} \tag{5.63}$$

*OB* and $\theta_4$ are calculated using (5.64) and (5.65), respectively.

$$OB = \sqrt{AB^2 + AO^2} \tag{5.64}$$

$$\theta_4^0 = \theta_s - 2\theta_2^0 \tag{5.65}$$

where,

$\theta_s$ is the stator pole pitch ($^{2\pi}/_{N_s}$)

$$AB = \tfrac{1}{2}d \sin \tfrac{1}{2}\beta_s \tag{5.66}$$

$$AO = \tfrac{1}{2}d \cos \tfrac{1}{2}\beta_s + \tfrac{1}{4}h_s \tag{5.67}$$

$$\theta_2^0 = \tan^{-1} {AB}/_{AO} \tag{5.68}$$

The cross-sectional area is given by:

$$Area = \tfrac{1}{4}h_s \, L_s \tag{5.69}$$

### 5.3.4ii   Stator pole reluctance, $R_{sp4}$

The flux travels $\tfrac{3}{4}h_s$ of the stator pole. Hence, the length of the flux path is defined by (5.70), while the area is given by (5.71).

$$length = \tfrac{3}{4}h_s \tag{5.70}$$

$$Area = \tfrac{1}{4}h_s L_s \tag{5.71}$$

### 5.3.4iii   Stator back iron reluctance, $R_{sy4}$

The flux path length in the stator back iron is arc *EF* defined by:

$$length = EF = (OE)\theta_3^{rad} \tag{5.72}$$

*OE* and $\theta_3$ are calculated using (5.73) and (5.74), respectively.

$$OE = \sqrt{DE^2 + DO^2} \tag{5.73}$$

$$\theta_3^0 = \theta_s - 2\theta_1^0 \tag{5.74}$$

where,

$$DE = \frac{1}{2}d \sin \frac{1}{2}\beta_s \tag{5.75}$$

$$DO = \frac{1}{2}d \cos \frac{1}{2}\beta_s + h_s + \frac{1}{4}b_{sy} \tag{5.76}$$

$$\theta_1^0 = \tan^{-1} DE/DO \tag{5.77}$$

The cross-sectional area is given by:

$$Area = L_s b_{sy} \tag{5.78}$$

The flux is assumed to link only ¼ of the number of turns per phase (*2N)*. Hence, the inductance for flux path #4, $L_{u4}$ is calculated using:

$$L_{u4} = \frac{(\frac{1}{4})^2 (2N)^2}{\frac{1}{2}R_{sp4} + \frac{1}{4}R_{g4} + \frac{1}{4}R_{sy4}} \tag{5.79}$$

### 5.3.5   *Flux path #5*

The last flux path is illustrated in Fig. 5.11. The flux leaves the stator pole to enter the stator back iron, passing through the air gap. The flux path is assumed to represent the perimeter of a quarter circle with centre at point *A* and radius of a quarter the stator pole height $\frac{1}{4}h_s$. The reluctances are calculated as follows.
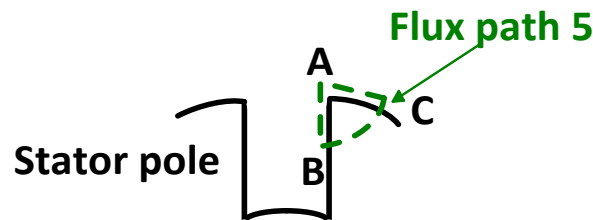


Fig. 5.11 Flux path #5

### 5.3.5i    Air gap reluctance, $R_{g5}$

The length of the air gap flux path is defined by (5.80), which represents the length of arc *BC*. The area is given by (5.81).

$$length = \tfrac{1}{2}\pi \times \tfrac{1}{4}h_s \qquad (5.80)$$

$$Area = \tfrac{1}{8}h_s L_s \qquad (5.81)$$

### 5.3.5ii    Stator pole reluctance, $R_{sp5}$

The length of the flux path in the stator pole is defined by (5.82), and the area is given by (5.83).

$$length = \tfrac{1}{4}(h_s + b_{sy}) \qquad (5.82)$$

$$Area = \tfrac{1}{8}h_s L_s \qquad (5.83)$$

### 5.3.5iii   Stator back iron reluctance, $R_{sy5}$

The length of the flux path in the stator back iron is defined by (5.84), where the area is given by (5.85).

$$length = \tfrac{1}{4}h_s \qquad (5.84)$$

$$Area = L_s b_{sy} \qquad (5.85)$$

The flux is assumed to link only $\tfrac{1}{8}$ the turns per phase (*2N*), hence the inductance for flux path #5, $L_{u5}$ is:

$$L_{u5} = \frac{(\tfrac{1}{8})^2 (2N)^2}{\tfrac{1}{4}R_{sp5} + \tfrac{1}{4}R_{g5} + \tfrac{1}{4}R_{sy5}} \qquad (5.86)$$

Finally, the effective unaligned inductance is the sum of the unaligned inductances for the five flux tubes, calculated using:

$$L_{ueff} = \sum_{k=1}^{5} L_{uk} \qquad (5.87)$$

## 5.4    Validation

Static FEA is used to validate the proposed flux tube method for calculating the effective unaligned inductance of SRM with conducting screens. The proposed method is validated using four different SRMs, shown in Fig 5.12, with specifications given in appendices A and B.
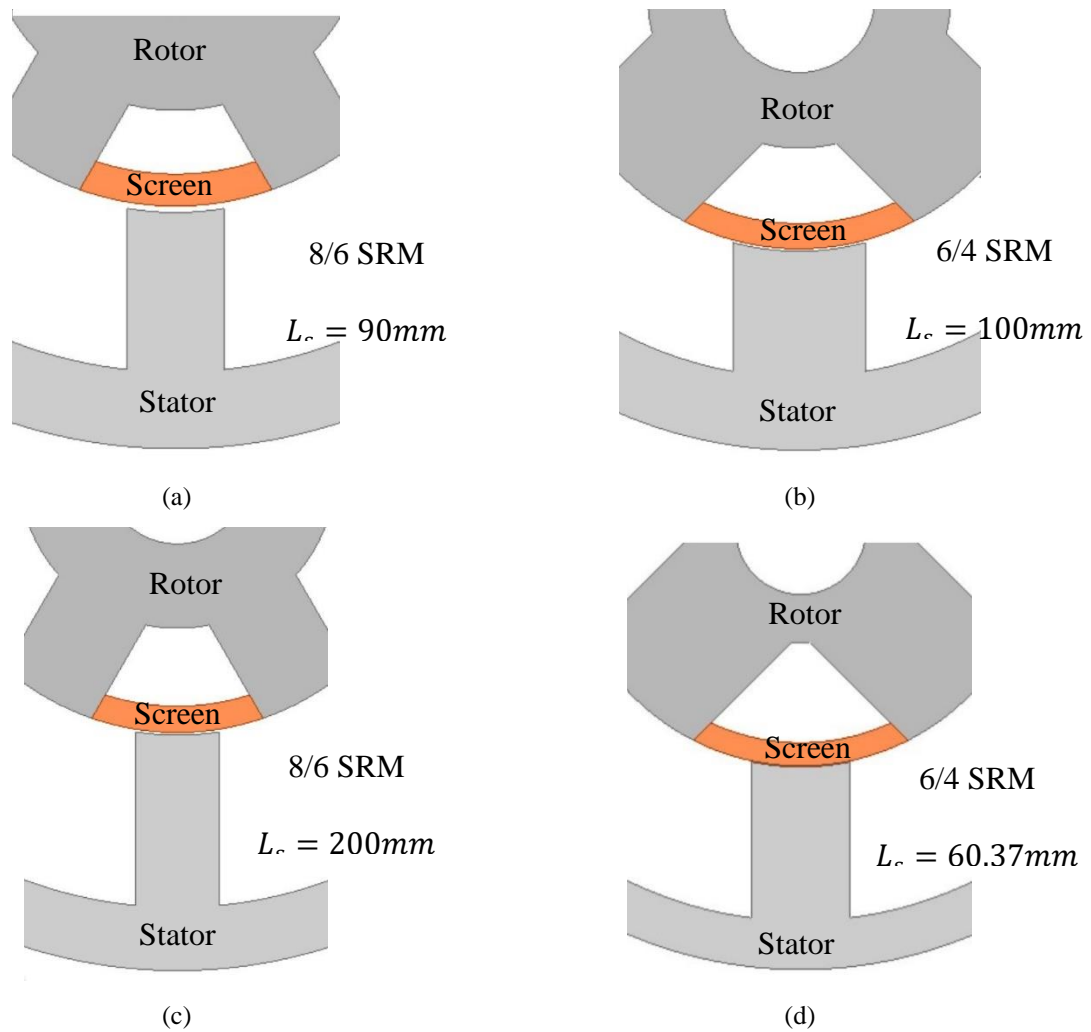


Fig. 5.12 Four SRMs with rotor conducting screens: (a) 4φ, 8/6 SRM, (b) 3φ, 6/4 SRM-1, (c) 4φ, 8/6 SRM-2, and (d) 3φ, 6/4 SRM-3

Table 5.1 compares the value of unaligned inductances obtained using mathematical calculations (as proposed in the previous section) with the values obtained using FEA. A step voltage is applied on the phase winding in the static FEA, hence $d\varphi/dt$ is established and the effect of the screen is observed. Otherwise, (if a constant DC voltage is applied to the phase winding) there will be no rate of change of flux and the screen will not be exploited. The good engineering correlation between the analytical and the static FEA values validates the proposed flux tube method.

Table 5.1 UNALIGNED INDUCTANCE VALUES FOR SCREENED SRMs

|                 | SRM    | SRM-1  | SRM-2  | SRM-3   |
|-----------------|--------|--------|--------|---------|
| Proposed method | 4.66   | 5.95   | 4.62   | 14.9    |
| FEA             | 4.87   | 5.55   | 4.74   | 13.46   |
| % error         | - 4.3% | + 7.2% | - 2.5% | + 10.7% |

## 5.5   Summary

This chapter investigated the effect of utilizing rotor conducting screens to decrease SRM effective unaligned inductance. A detailed analytical method, based on flux tube method, is proposed to calculate the effective unaligned inductance for a screened SRM. The proposed method was assessed on four different SRMs (two 3φ SRMS and two 4φ SRMs), where acceptable agreement between the proposed method and FEA was recorded.

## References

[5-1]   A. J. Hutton and T. J. E. Miller, "Use of flux screens in switched reluctance motors," *1989 4th International Conference on Electrical Machines and Drives* London, UK, 1989, pp. 312-316.

[5-2]   Y. Dessouky, B. Williams, and J. Fletcher, ''Conducting screen utilization in switched reluctance motors,'' *IEEE Transactions Energy Conversion*, vol. 14, no. 4, pp. 946-951, Dec. 1999.

[5-3]   R. Hamdy, J. Fletcher, B. Williams, and S. Finney, ''High-speed performance improvements of a two-phase switched reluctance machine utilizing rotor-conducting screens,'' *IEEE Transactions Energy Conversion*, vol. 17, no. 4, pp. 500-506, Dec. 2002.

[5-4]   M. Mahmoud, J. Fletcher, and B. Williams, ''Evaluation of rotor conducting screens on the rotor of the single-phase switched reluctance machine,'' *IEEE 2nd international conf. on Power Electron., Machines and Drives*, Edinburgh, UK, Mar. 2004, pp. 18-23.

[5-5] R. Krishnan, *Switched Reluctance Motor Drives: Modelling, Simulation, Analysis, Design and Applications*. Boca Raton, FL, USA: CRC Press, 2001.

[5-6] P. Materu and R. Krishnan, "Analytical prediction of SRM inductance profile and steady-state average torque," *Conference Record of the 1990 IEEE Industry Applications Society Annual Meeting*, Seattle, WA, USA, 1990, pp. 214-223.

[5-7] N. K. Sheth and K. R. Rajagopal, "Calculation of the flux-linkage characteristics of a switched reluctance motor by flux tube method," in *IEEE Transactions on Magnetics*, vol. 41, no. 10, pp. 4069-4071, Oct. 2005.

*Chapter 6*

*SRM Power Density Improvement using*

*Rotor Conducting Screens and DC Link Voltage Boosting*

---

This chapter investigates SRM power density enhancement when using rotor conducting screens and dc-link voltage-boosting. The utilization, dynamic operation, and optimal selection of rotor conducting screens are explored. The effect of thickness, material resistivity and shape of the conducting screens on the SRM performance is studied. A multi-objective optimization problem based on the concept of non-dominated sorting is formulated to elicit the optimal screen with respect to the developed torque, efficiency and weight of added material. FEA results for different screens are presented.

## 6.1    Introduction

In the previous chapter, the concept of rotor conducting screens was expounded. It was shown that when filling the rotor interpolar air gaps with electrical conducting, non-magnetic materials (referred as conducting screens) such as aluminium or copper, a voltage is induced in the screens due to flux variation. The induced voltage produces eddy currents, which in turn produce flux that opposes the original stator pole flux. The opposing flux results in a decrease in the effective unaligned inductance. The decrease in the effective unaligned inductance allows a rapid current building up. Hence, an increase in the conversion area and thereby the developed torque is expected.

Fig. 6.1 shows the variation of inductance for half a cycle (from the unaligned to aligned position) for screened and unscreened SRMs, with the SRM specifications in Appendix A. The unscreened SRM has an unaligned inductance of 10.78mH, while this is reduced to 4.87mH in the presence of conducting screens. This 55% decrease in the effective unaligned inductance increases the conversion area (OAB to OA$^*$B) by 18% as shown in Fig. 6.2 thus improving the SRM developed

torque. The aligned inductance decreases by 2%, which is insignificant compared to the reduction in the unaligned value.
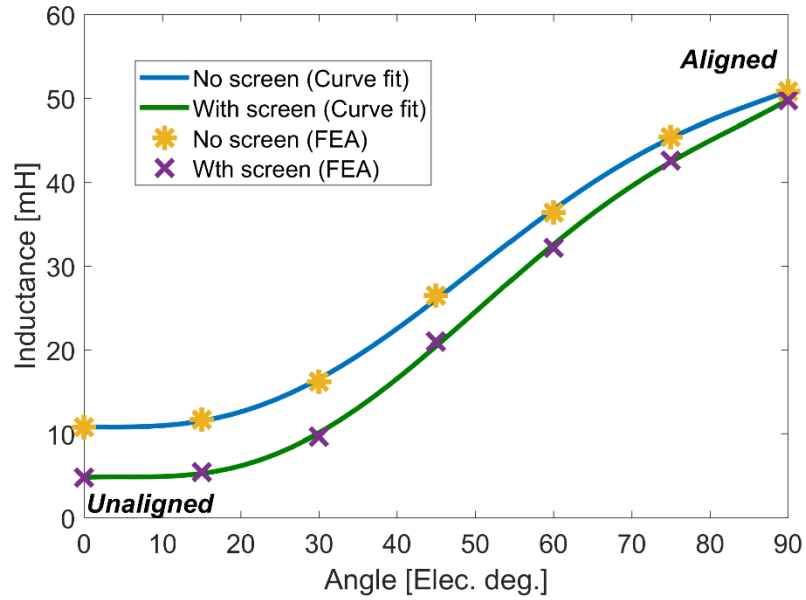


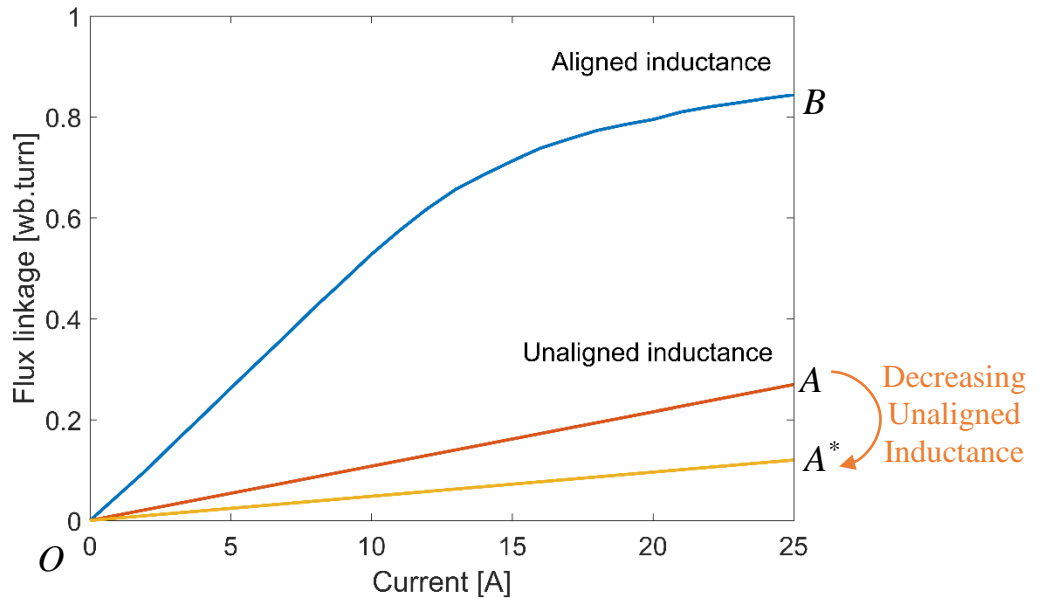Fig. 6.1 Variation of inductance for screened and unscreened SRMs



Fig. 6.2 Flux linkage – current, $\lambda - i$, characteristics

## 6.2 SRM Dynamic performance with rotor conducting screens

In this section, the effect of rotor conducting screens on SRM dynamic performance is explored, over the entire speed range. Varying screen thickness, material conductivity, and screen shape is shown to alter the SRM developed torque. A common phase converter topology (as per Fig. 3.13) is used for all simulations.
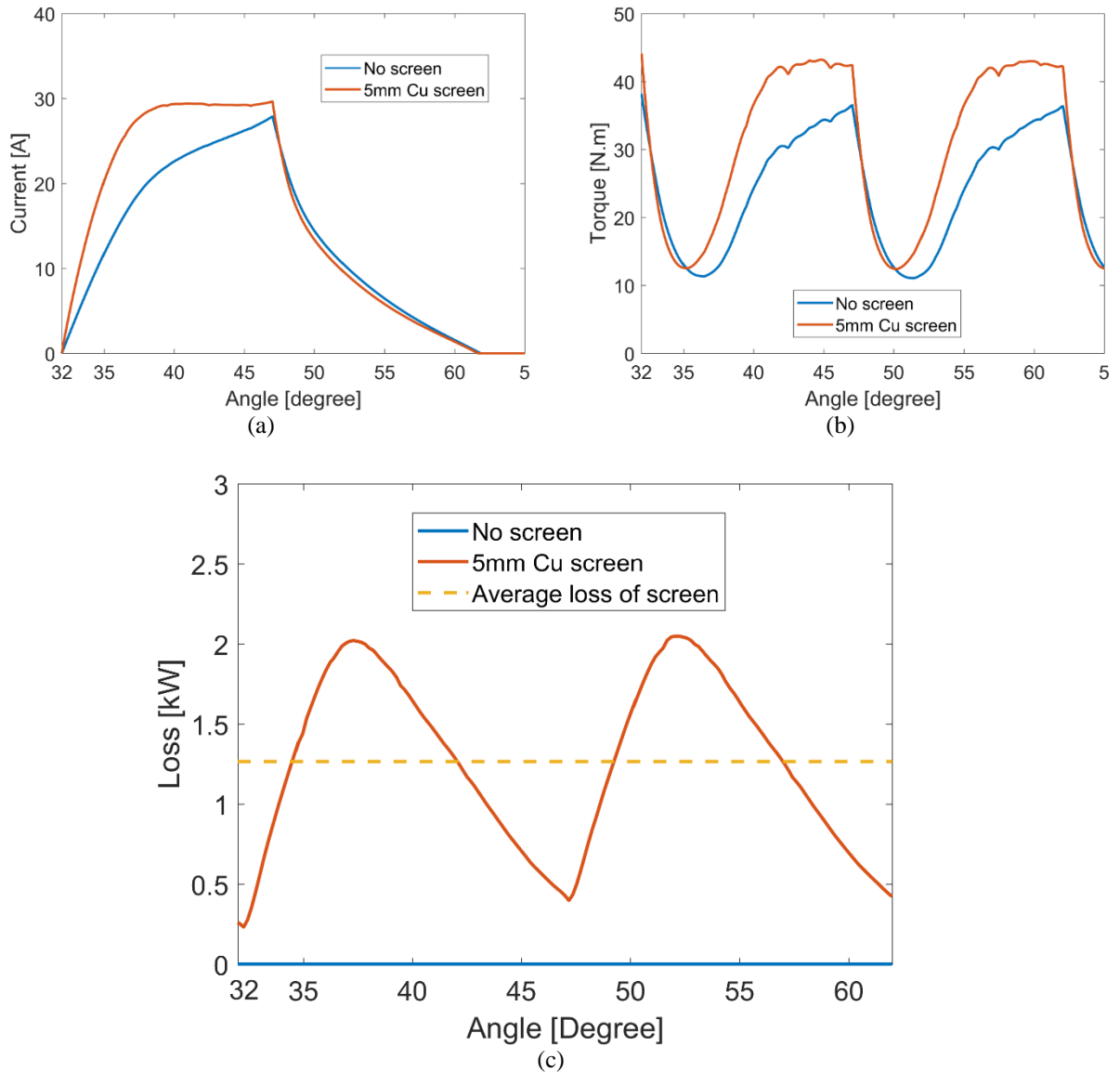


Fig. 6.3 SRM performance (FEA) with and without conducting screens at 1500rpm:
(a) Phase currents, (b) Developed torque, and (c) Screen loss

### 6.2.1 Performance at base speed

Fig. 6.3 compares the performance of an unscreened SRM and a 5mm Cu screen SRM. Both SRMs operate at base speed (1500rpm) with $\theta_{on} = 32^0$ and $\theta_{off} = 47^0$. At base speed, the SRM back emf equals the dc link voltage, hence the SRM operates in single-pulse mode. The unmodified SRM delivers rated load, 24Nm, 4kW.

Fig. 6.3a shows that the reduction in the effective unaligned inductance allows the current in the phase winding to build up quicker for the screened SRM than for the unscreened machine. The rms phase current increases from 11.7A in the unscreened SRM to reach 14A in the screened SRM. This implies an increase in the stator winding ohmic loss.

Fig. 6.3b illustrates that the increase in phase winding current reflects on the developed torque, where a 29% increase in the developed torque is recorded. Since the theory of operation of rotor conducting screens is based on eddy currents, a new loss component (eddy current loss in the screens) occurs, as demonstrated in Fig. 6.3c, specifically 1.3kW in a 4kW machine.

### 6.2.2 Performance above base speed

The performance of 5mm Cu screen SRM against unscreened SRM at 3000rpm is investigated in this subsection with $\theta_{on} = 26^0$ and $\theta_{off} = 44^0$. Fig. 6.4a shows an increase in the phase current due to the reduced effective unaligned inductance. The screened SRM recorded 12.95A rms current, while the unscreened SRM operates at 9.46A rms current. An increased conversion area is observed in the enhancement of the developed torque. The unscreened machine recorded only 12Nm, while the 5mm Cu screen SRM achieved 16.74Nm, as shown in Fig. 6.4b.

### 6.2.3 Performance below base speed

To cover the entire speed range, the effect of conducting screens on SRM performance well below base speed is investigated with $\theta_{on} = 32^0$ and $\theta_{off} = 47^0$.
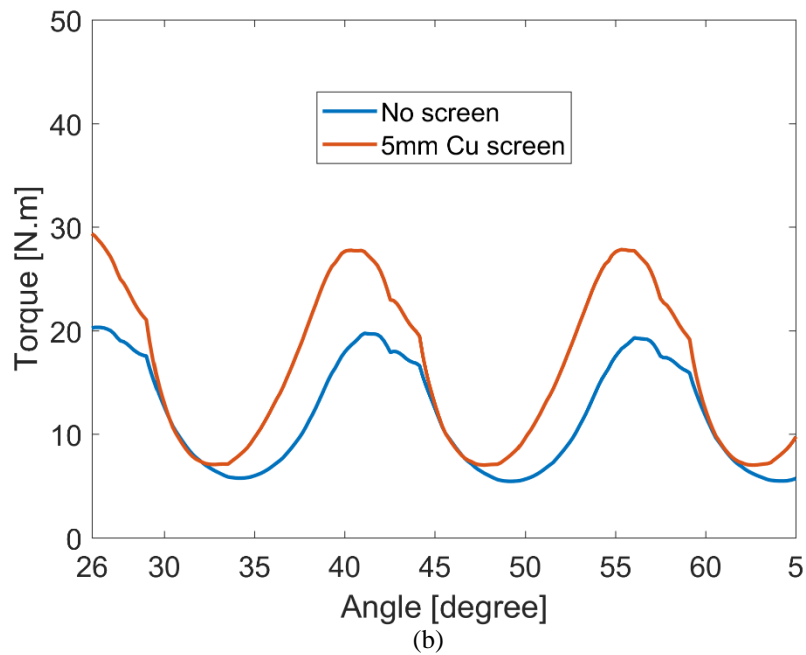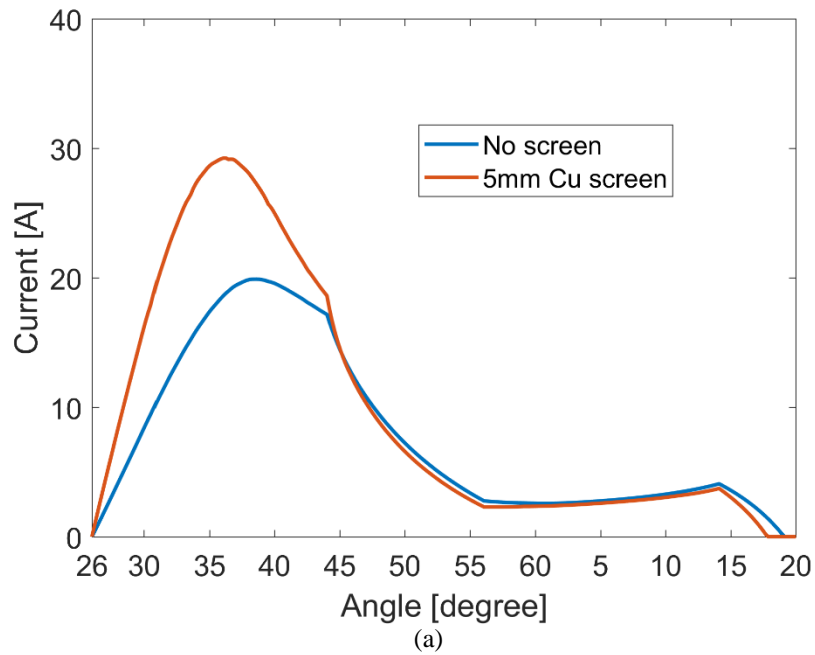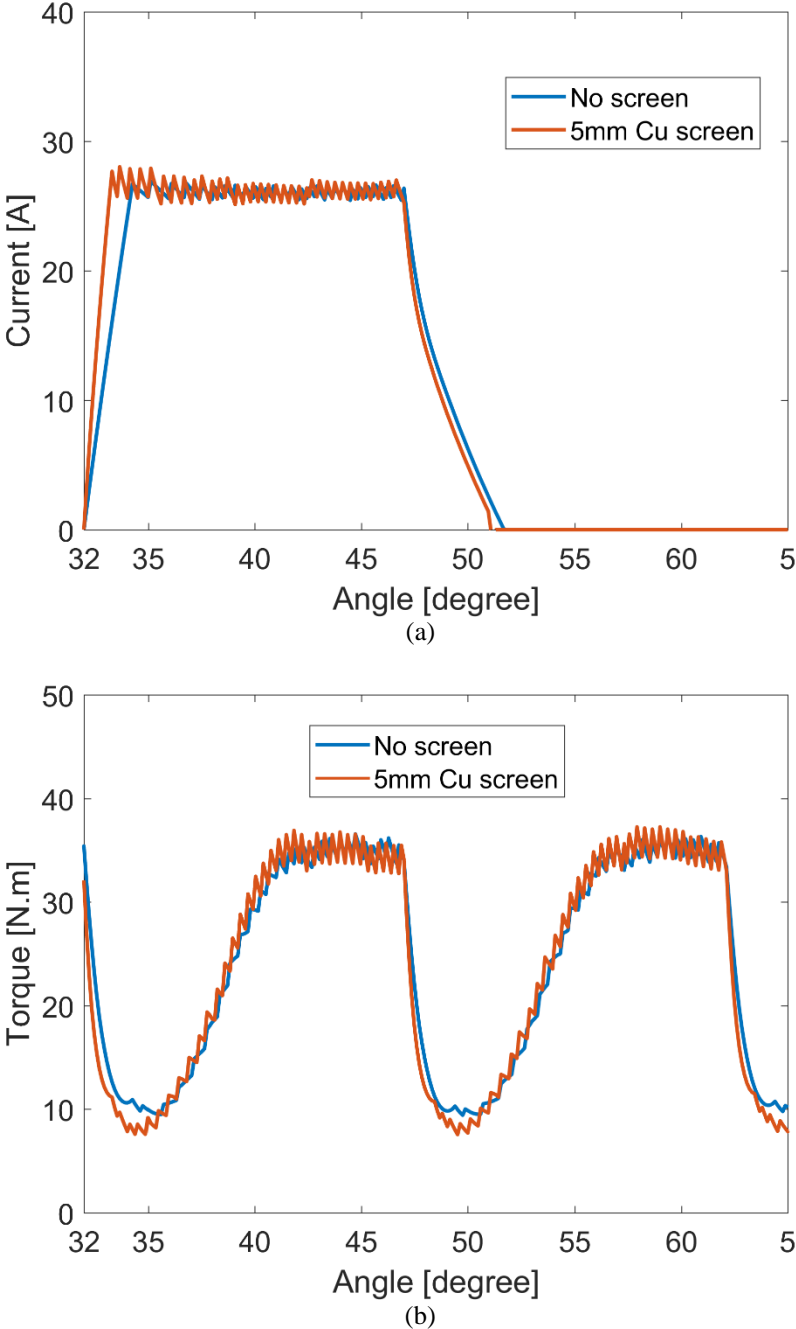
Fig. 6.4 SRM performance with and without conducting screens at 3000rpm:
(a) Phase currents, and (b) Developed torque

Fig. 6.5a shows that 5mm Cu screens assist the phase winding current to reach the chopping period faster. However, there is no benefit to build up the current faster since both SRMs are adjusted to deliver the full load torque of 24Nm as shown in Fig. 6.5b.

From this simple study, it is concluded that conducting screens are beneficial at and above the base speed. But below base speed rotor conducting screens increase the loss without any performance gain.



Fig. 6.5 SRM performance with and without conducting screens at 500rpm:
(a) Phase currents, and (b) Developed torque

### 6.2.4 *Effect of screen material*

Fig. 6.6 compares SRM performance at 1500rpm (base speed) with different thickness copper screens. The turn on/off angles are the same for the screened and unscreened SRMs, where $\theta_{on} = 32^0$ and $\theta_{off} = 47^0$.
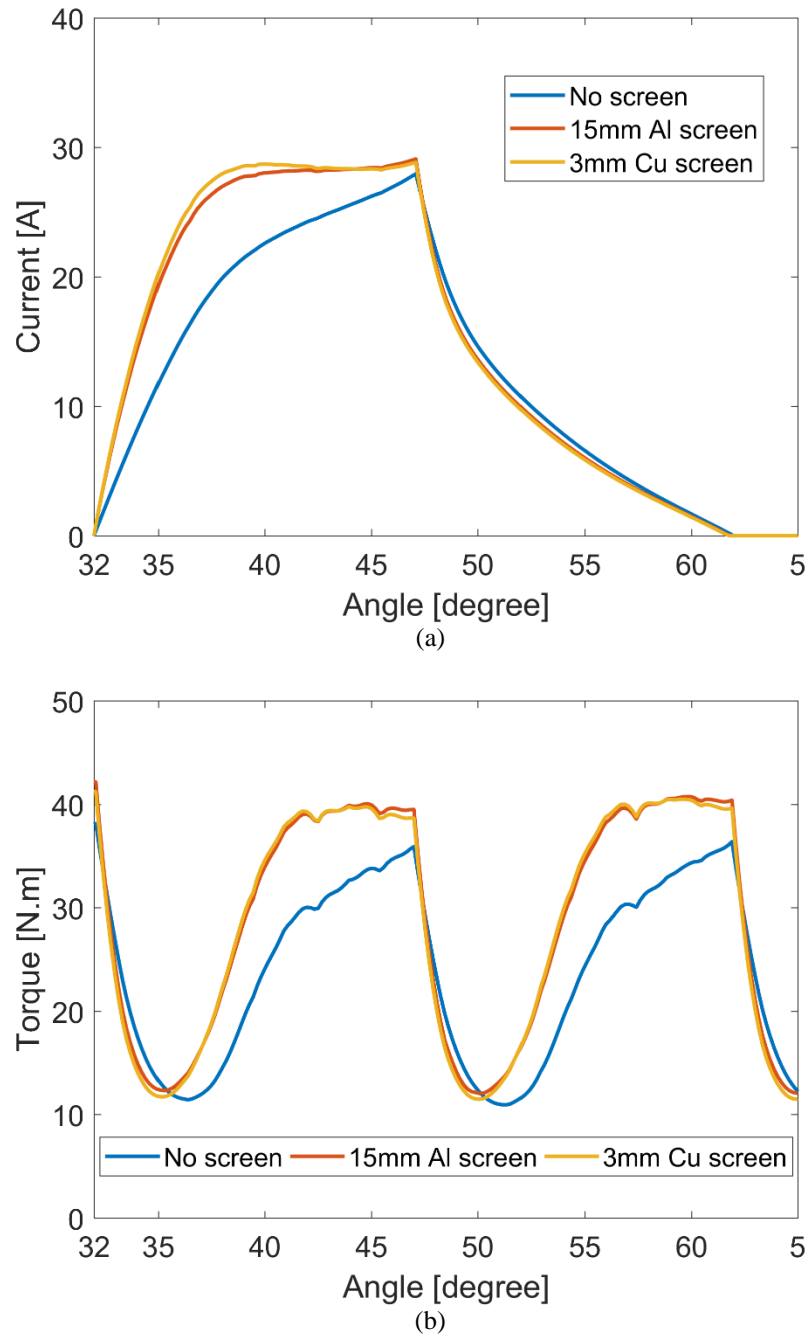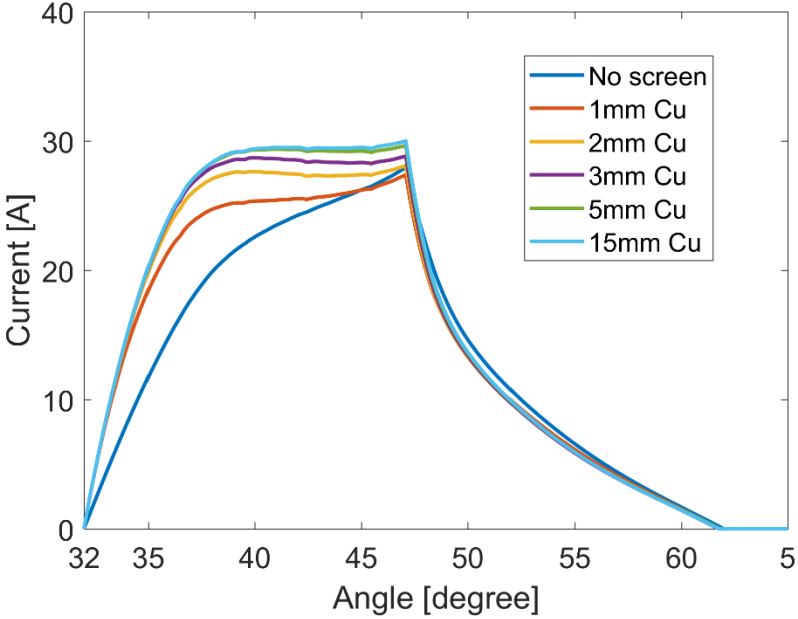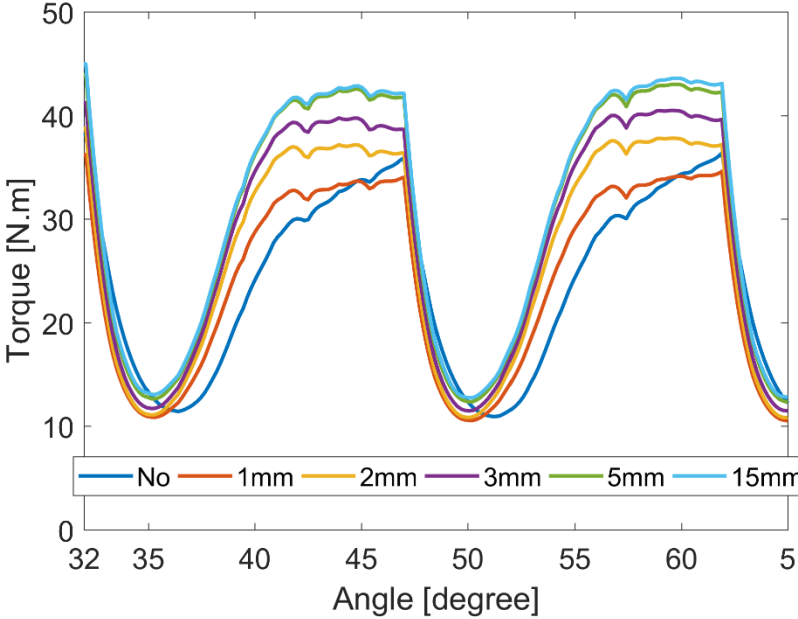


Fig. 6.6 Performance of SRM using different screen materials:
(a) Current waveforms, and (b) torque waveforms.

The first screen is 3mm copper, while the second screen is 15mm aluminium. From Fig. 6.6a, the decrease in the effective unaligned inductance accelerates the process of current building-up.



Fig. 6.7 Performance of SRM using different screen thickness:
(a) Current waveforms and (b) torque waveforms.

As a result, the developed torque increases from 24.1 Nm (unscreened) to reach 29.25 Nm (screened) as illustrated in Fig. 6.6b.

The electrical conductivity of copper is $5.98 \times 10^7 S/m$ with density $8960\ kg/m^3$. The electrical conductivity of aluminum is $3.5 \times 10^7 S/m$ with density $2600\ kg/m^3$. The SRM with 3mm copper screens is able to deliver the same output torque as the 15mm aluminium screen machine. This highlights that electrical conductivity plays an important role in the behaviour of the induced eddy current.

### 6.2.5   Effect of screen thickness

Fig. 6.7 compares SRM performance when different thickness copper screens are deployed. The turn on/off angles are the same for the screened and unscreened SRM where, $\theta_{on} = 32^0$ and $\theta_{off} = 47^0$. The speed is the base speed 1500rpm. Increasing the screen thickness to fill the entire interpole gap yields the best torque enhancement. However, extra copper (implying more weight and cost) is needed.

From this basic study, it is evident that the electrical conductivity of the screen material, along with its thickness, have a significant effect on SRM performance. Using a film screen with low conductivity results in higher resistance to the induced voltage, hence the eddy current is smaller. Increased resistivity does result in a reduced eddy current decay time constant.

### 6.2.6   Effect of screen shape

The theory of rotor conducting screens relies on the eddy current effect, where eddy current loss in the screens is inevitable. Since machine efficiency is of prime importance in applications as EVs, different screen shapes are compared in terms of developed torque, Cu winding loss and screen loss. Results for different Cu screen shapes (of around 3mm-6mm thick) are summarized in Table 6.1, where the rotor rotates at 1500rpm anti-clockwise, with the same turn-on/turn-off angles. The screen shape plays an important role in determining the developed torque and screen loss, as shown in Table 6.1. Trimming the conducting screens (as with shapes 7 in Table 6.1) reduces the screen loss. However, a reduction in the developed torque results.

Table 6.1 RELATIVE FEA PERFORMANCE OF DIFFERENT Cu SCREEN SHAPES AT 1500RPM

| Screen | | Average o/p torque [Nm] | Winding loss [kW] | Screen loss [kW] |
|---|---|---|---|---|
| SRM | | 24.1 | 0.44 | - |
| 1 | | 30.76 | 0.625 | 1.27 |
| 2 | | 30 | 0.6 | 1.04 |
| 3 | | 30.57 | 0.625 | 1.29 |
| 4 | | 30.26 | 0.625 | 1.31 |
| 5 | | 30.46 | 0.63 | 1.3 |
| 6 | | 29.9 | 0.615 | 1.34 |
| 7 | | 27.34 | 0.53 | 0.52 |

## 6.3    Optimal screen selection

From the previous analysis, material, thickness and shape of screen have crucially influenced SRM performance. In this section a multi-objective optimization problem based on the concept of non-dominated sorting is formulated to elicit the optimal screen with respect to the developed torque, efficiency and cost of added material. FEA results for different screens are presented.

### 6.3.1   Multi-objective optimization (MOO)

Generally, optimization means finding a solution that maximizes/minimizes an objective function. When there is more than one objective function the problem is named multi-objective optimization. Usually, in MOO problems, the objective functions are in conflict. Trying to optimize one function may result in a degradation in the other objective functions. Hence, a

compromise between these objectives is desirable. Without loss of generality, the optimization problem is of the form [6-1]:

$$Minimize\ f(x) = [f_1(x), f_2(x), \ldots, f_k(x)] \tag{6.1}$$

$$subject\ to: \begin{cases} g_{ii}(x) \leq 0, & ii = 1, 2, \ldots, y \\ h_{jj}(x) = 0, & jj = 1, 2, \ldots, z \end{cases} \tag{6.2}$$

where $k$ is the number of objective functions, $y$ is the number of inequality constraints, and $z$ is the number of equality constraints.

In MOO problems there is no single optimal solution, but a set of solutions satisfying a predetermined definition of optimality. Hence, a trade-off between the objectives is achieved according to the perspective of the decision maker. A Pareto optimal (non-dominated) solution is a point that improves at least one objective without retrograding the remaining objectives [6-2], as demonstrated in Fig. 6.8.
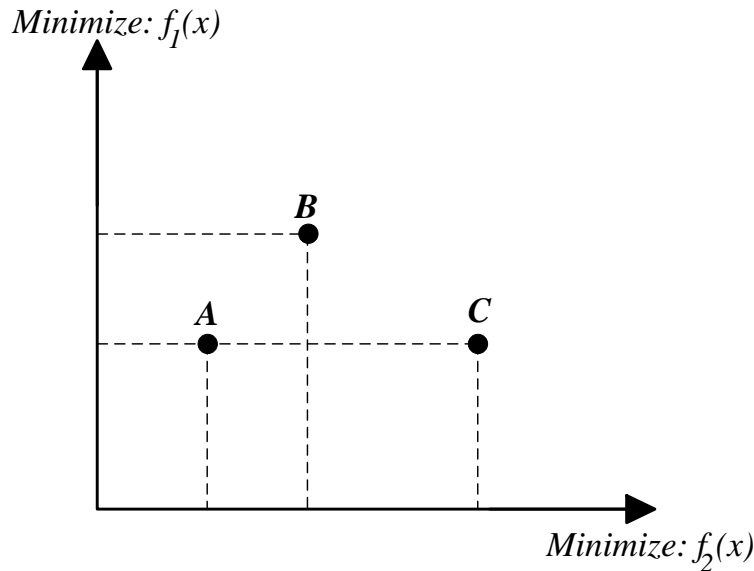


Fig. 6.8 Illustration of dominance

In Fig. 6.8 point A dominates point B as the former has minimum values for both objective functions $f_1$ and $f_2$. Also, point A dominates point C as they both have the same value of $f_1$. However, point A has lower value of $f_2$ than point C.
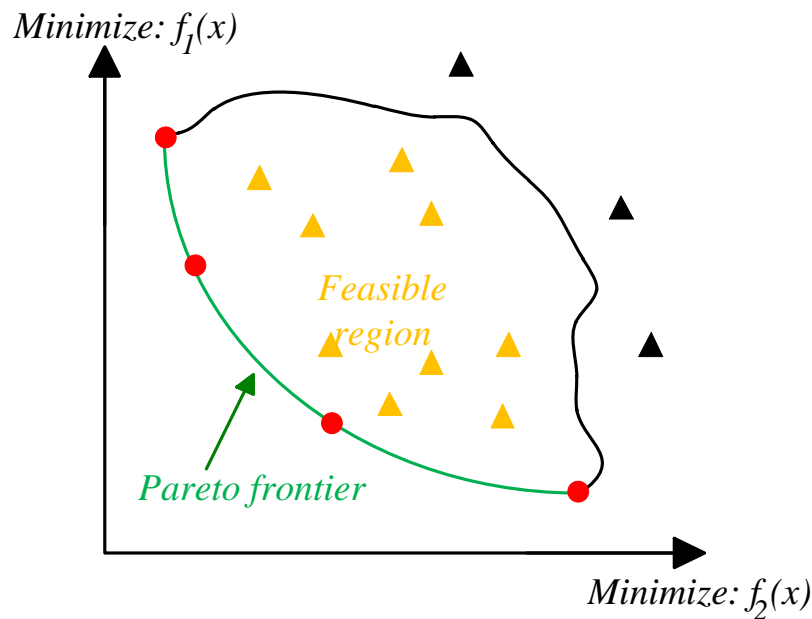
Fig. 6.9 Illustration of Pareto optimal frontier

Finally, when comparing point B with point C, either dominates the other as each point is better than the other in one objective and worse in another. The point which is not dominated by any other point (point A in this case) is termed a non-dominated (Pareto optimal) point.

The set of Pareto optimal solutions is called a Pareto frontier as shown in Fig 6.9. Usually, it is preferable to know all the solutions in the Pareto frontier to allow the designer to select the most adequate solution among different alternatives. The problem of generating the Pareto frontier is based on non-dominated sorting, where all the solutions are compared to select the non-dominated ones. Hence, non-dominated sorting is applied to assess the obtained solutions [6-3], [6-4].

The sequence of applying non-dominated sorting on a set of solutions, $U$, containing $Q$ solutions $(s_1, s_2, \dots, s_Q)$ to generate the Pareto frontier, $F$, can be described as follows:

1. Transfer $s_1$ from $U$ to $F$ to initialize the process.
2. Compare $s_2$ with $s_1$. Three cases can be realized namely; if $s_1$ dominates $s_2$, then $s_1$ stays in $F$ and $s_2$ is deleted. If $s_2$ dominates $s_1$ then $s_2$ is transferred to $F$ and $s_1$ is deleted. Otherwise, both $s_1$ and $s_2$ are non-dominated (they both belong to the Pareto frontier) and they are placed in $F$.

3.  Compare $s_3$ with all the solutions in $F$. If $s_3$ is dominated by any solution in $F$, delete $s_3$. Any solution in $F$ dominated by $s_3$ is deleted. Otherwise, $s_3$ is also non-dominated and is transferred to $F$.

4.  Repeat step 3 until all the $Q$ solutions in $U$ are checked. After completing all comparisons, the solutions in $F$ form the required Pareto frontier.

These steps are summarized in a flow chart as shown in Fig. 6.10.

To illustrate the process of non-dominated sorting, a simple example is considered [6-5]. Five solutions for a three objective minimization problem are given in Table 6.2.

Table 6.2 FIVE SOLUTIONS FOR THE THREE-OBJECTIVE MINIMIZATION PROBLEM (EXAMPLE)

| Solution | $f_1$ | $f_2$ | $f_3$ |
|---|---|---|---|
| 1 | 0.2 | 0.7 | 0.5 |
| 2 | 5 | 1.1 | 0.6 |
| 3 | 1 | 0.7 | 0.5 |
| 4 | 0.1 | 2 | 1.2 |
| 5 | 0.1 | 1.5 | 0.8 |

The procedure for creating the Pareto frontier is summarized in Table 6.3, where solutions 1 and 5 are the non-dominated solutions forming the Pareto frontier $F$.

Table 6.3 PROCEDURE FOR CALCULATING THE PARETO FRONTIER (EXAMPLE)

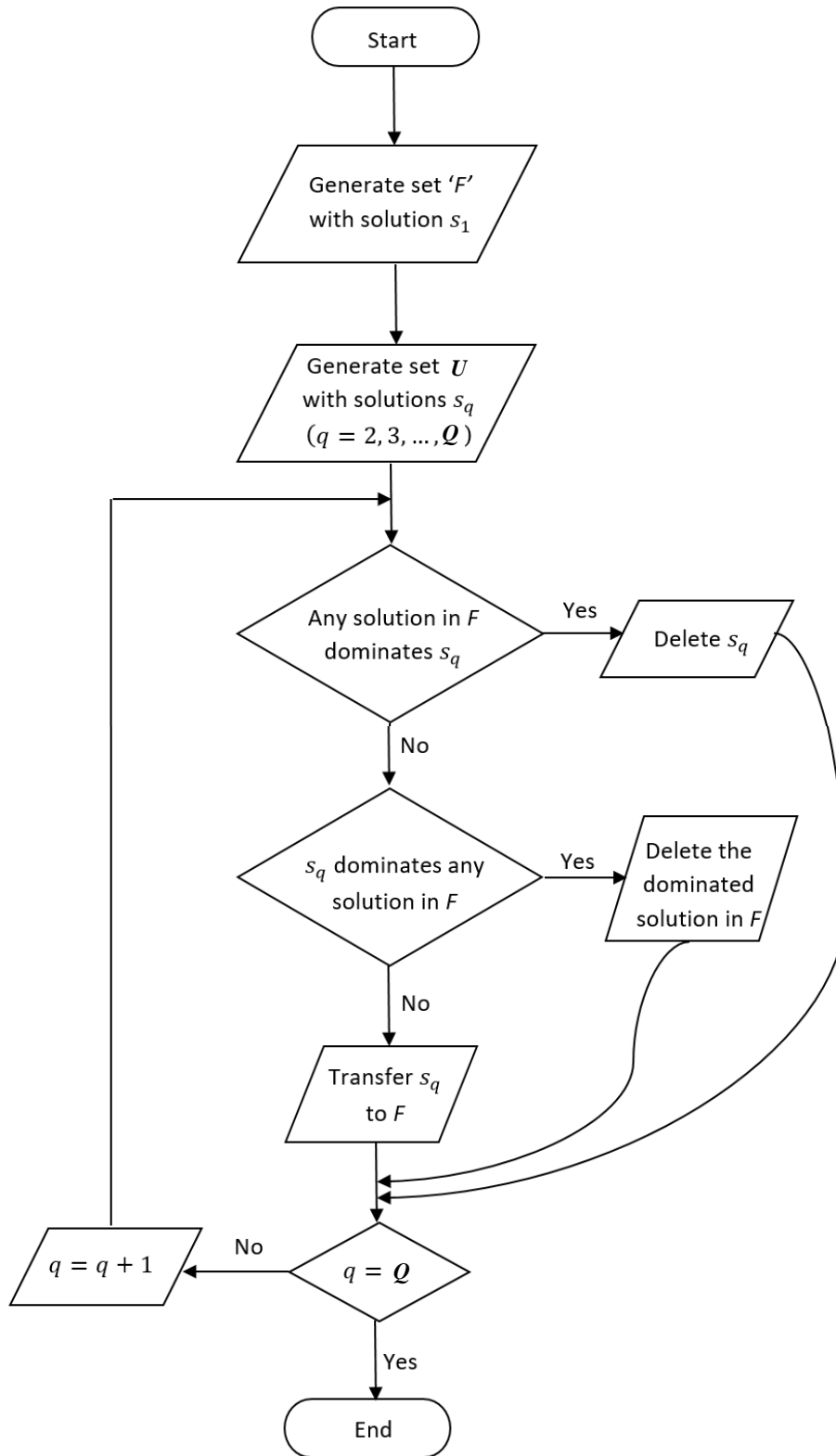| Step | Solutions in $F$ | Solutions in $P$ | Comparisons |
|---|---|---|---|
| 0 | - | 1,2,3,4,5 | - |
| 1 | 1 | 2,3,4,5 | - |
| 2 | 1 | 3,4,5 | 2&1 |
| 3 | 1 | 4,5 | 3&1 |
| 4 | 1,4 | 5 | 4&1 |
| 5 | 1,5 | - | 5&1, 5&4 |

Fig. 6.10 Illustration of non-dominated sorting process

## 6.3.2 FEA results

Since the theory of rotor conducting screens relies on the eddy current effect, screen eddy current loss is inevitable. As machine efficiency is of prime importance, different screen shapes are compared in terms of developed torque, weight of added material, and efficiency to elicit the best screen candidates (generating the Pareto frontier).

More than 100 screens shapes are compared, with rotor 1500rpm anti-clockwise rotation, using the same turn-on/turn-off angles for all cases as in Appendix C. Shapes of screens representing the Pareto frontier are shown in Fig. 6.11 with results summarized in Table 6.4, which only considers screens with at least 10% increase in developed torque.
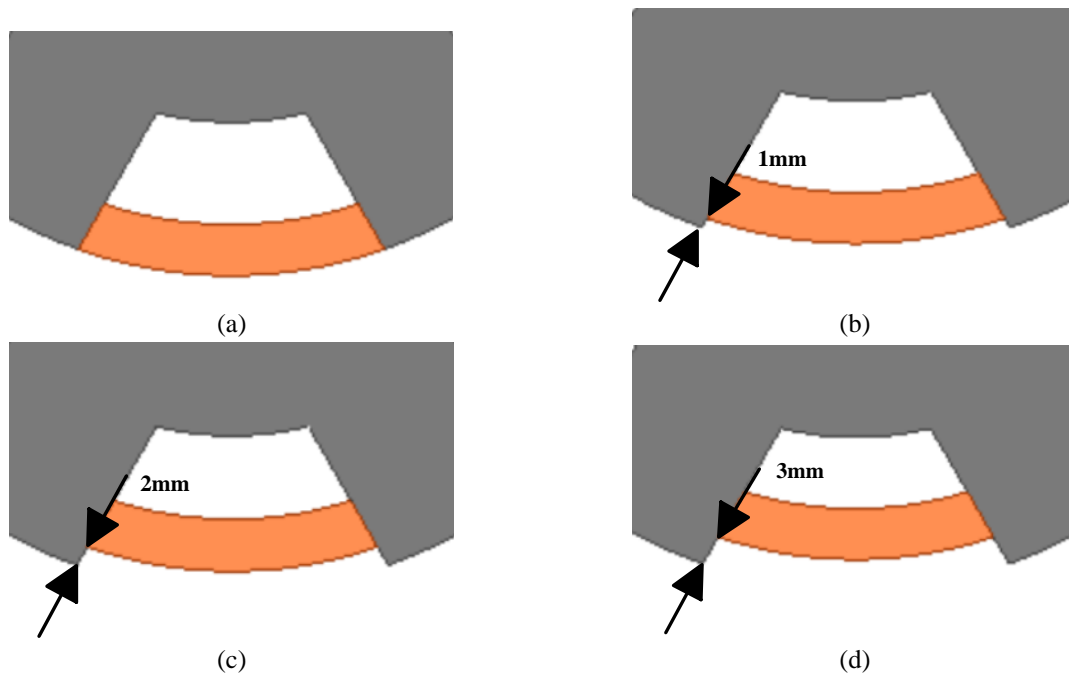


Fig. 6.11 Optimal screen designs: (a) design a, (b) design b, (c) design (c), and (d) design d

The results presented in Table 6.4 represent the optimal screen designs. Each screen is a trade-off between the three objective functions viz., developed torque, weight of added material and efficiency. A 3.5 cost ratio between copper and aluminium suggests that aluminium screens are lighter and cheaper than copper screens. However, torque improvement using aluminium screens is inferior to that of copper screens. Shifting the screen below the rotor pole tip (as in designs 'b', 'c' and 'd') increases the area of the flux path, hence slightly increasing the unaligned inductance compared to design 'a'. This slight increase in the inductance reduces the phase current, hence the

eddy current loss, improving the efficiency. However, this improvement in efficiency (as compared to design 'a') is at the cost of a reduction in the developed torque (that is, design 'a' produces the highest torque with the lowest efficiency). Designs 'b', 'c' and 'd' improve the efficiency of design 'a' with a slight reduction in torque.

Depending on the constraints dictated by the application, the decision maker can choose the adequate screen shape satisfying the application needs. In EV applications, the developed torque and output efficiency are most important. Based on Pareto optimal frontier analysis of the screens in Table 6.4, a 5mm Cu screen of design 'b' is selected and used for the rest of this chapter.

Table 6.4 SCREENS PARETO OPTIMAL FRONTIER

| Screen | Material | Thickness [mm] | Weight of screen [$kg/m$] | Increase in o/p torque [%] | Efficiency [%] |
|--------|----------|----------------|----------------------------|-----------------------------|-----------------|
| SRM | - | - | - | - | 89.56 |
| Sc-a | Al | 3 | 1.36 | 11.75 | 69.0 |
| | | 4 | 1.78 | 15.90 | 70.0 |
| | | 5 | 2.18 | 18.47 | 70.9 |
| | | 6 | 2.57 | 20.00 | 71.5 |
| | | 7 | 2.94 | 20.80 | 71.9 |
| | Cu | 4 | 6.13 | 26.00 | 71.0 |
| | | 5 | 7.53 | 28.20 | 71.9 |
| | | 6 | 8.86 | 29.30 | 72.4 |
| Sc-b | Al | 4 | 1.70 | 12.60 | 73.8 |
| | | 5 | 2.10 | 14.57 | 74.5 |
| | | 6 | 2.47 | 15.57 | 75.0 |
| | Cu | 4 | 5.90 | 20.60 | 74.6 |
| | | 5 | 7.24 | 21.50 | 76.5 |
| Sc-c | Al | 5 | 2.00 | 11.30 | 77.4 |
| | | 6 | 2.37 | 12.10 | 77.8 |
| | Cu | 4 | 5.68 | 15.94 | 77.5 |
| | | 5 | 6.96 | 17.35 | 78.2 |
| Sc-d | Cu | 4 | 5.46 | 12.70 | 80.0 |
| | | 5 | 6.68 | 13.50 | 80.4 |

Screen interpretation example: Sc-b, with reference to Fig. 6.11b, leading edge screen is 1mm below air gap and trailing edge screen is 1mm below air gap.

## 6.4 Power density improvement with rotor conducting screens and dc link voltage-boosting

Fig. 6.12 shows the torque-speed curve for the FEA SRM (with efficiency and pu output power). Rotor conducting screens and dc rail voltage boost (50%, 47.5µF as advised in Chapter 4) increase the speed at which full-load torque can be delivered (from 1500rpm to 1650rpm and 1810rpm, respectively), hence improving the power to weight ratio (by 10% and 21%, respectively) which is comparable to that of a PMSM. Deploying rotor conducting screens along with voltage-boosting increases the base-speed to 1875rpm (25% increase), hence improving the power to weight ratio by 25% to be competitive with an equivalent-volume PMSM. At 3000rpm, the SRM with screens and boost-capacitors increase the developed torque by 55%, but at the expense of efficiency.
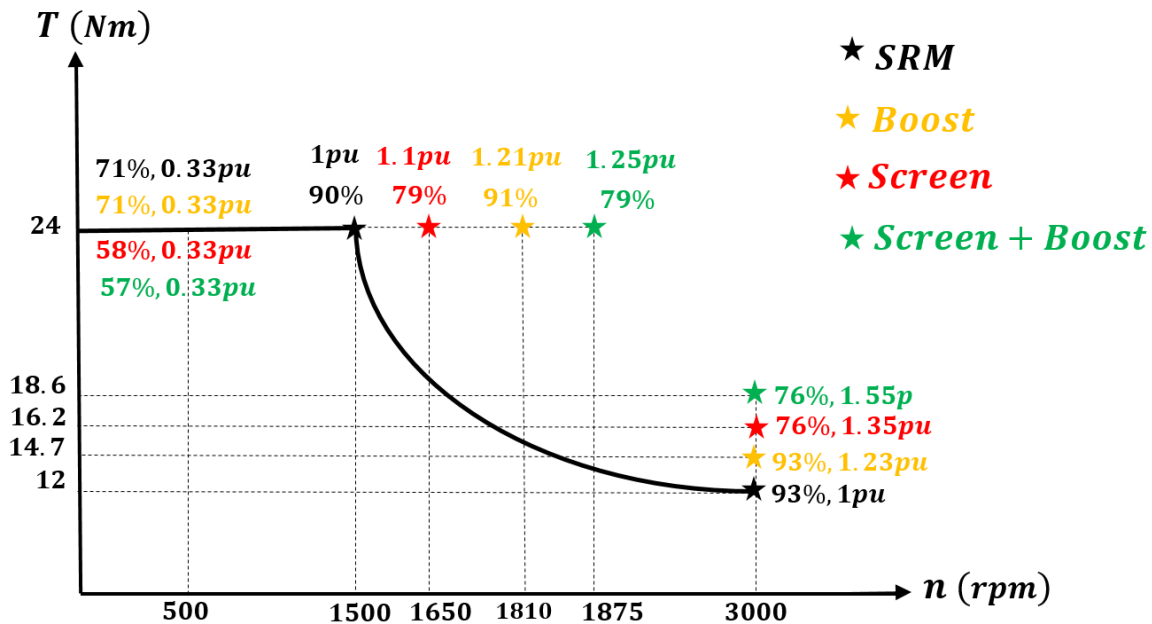


Fig. 6.12 Torque/speed curve with relevant efficiencies and pu output power

The penalty of deploying rotor conducting screens is lower efficiency as a consequence of introducing a screen eddy current loss component.

The penalty of utilizing boost-capacitors (without screens) is high semiconductor voltage stresses as a consequence of using capacitors for high speed performance enhancement, but with improved machine efficiency.

## 6.5 Summary

This chapter studied the effect of utilizing rotor conducting screens along with dc link voltage boosting-capacitors to enhance SRM performance. The effect of using conducting screens of different materials, thicknesses and shape on SRM performance was presented. Using a film screen with low conductivity results in higher resistance to the induced voltage, hence the eddy current is smaller. Increased resistivity results in a reduced eddy current decay time constant.

A multi-objective optimization problem based on non-dominated sorting was formulated to elicit the optimal screen shape. Four designs are advised with respect to the developed torque, efficiency and weight of added material. A 3.5 cost ratio between copper and aluminium suggests that aluminium screens are lighter and cheaper than copper screens. However, torque improvement using aluminium screens is inferior to that of copper screens. Shifting the screen below the rotor pole tip (below the air gap) offers a trade-off between developed torque and efficiency.

DC link voltage boosting improves the power to weight performance but with increased semiconductor voltage stresses as a consequence of boost capacitor voltages in excess of the dc voltage source, which improves high speed performance. An SRM with rotor conducting screens and dc link voltage-boosting improves SRM power to weight ratio to be competitive with an equivalent PMSM, but with the penalty of inevitable screen eddy current loss.

Because drive efficiency is of paramount importance in EV applications, this chapter clearly establishes that the use of rotor conducting screens, which although increases the base speed, is untenable due to the inevitable associated Joules losses. DC link voltage boost is a potential method for SRM performance enhancement in EV applications.

## References

[6-1] Z. Fei, B. Li, S. Yang, C. Xing, H. Chen, and L. Hanzo, ''A survey of multi-objective optimization in wireless sensor networks: metrics, algorithms and open problems,'' *IEEE Communications Surveys and Tutorial,* vol. 19, no. 1, pp. 550-586, First quarter 2017.

[6-2] X. Zhang, Y. Tian, R. Cheng, and Y. Jin, ''An efficient approach to non-dominated sorting for evolutionary multi-objective optimization,'' *IEEE Transactions on Evolutionary Computation*, vol. 19, no. 2, pp. 210–213, Apr. 2015.

[6-3]  K. Deb, A. Pratap, S. Agarwal, and T. Meyarivan, "A fast and elitist multi-objective genetic algorithm: NSGA-II," *IEEE Transactions on Evolutionary Computation*, vol. 6, no. 2, pp. 182–197, Apr. 2002.

[6-4]  K. M. Clymont and E. Keedwell, "Deductive sort and climbing sort: New methods for non-dominated sorting," *Evolutionary Computation*, vol. 20, no. 1, pp. 1–26, 2012.

[6-5]  H. Fang, Q. Wang, Y. Tu, and M. F. Horstemeyer, "An efficient non-dominated sorting method for evolutionary algorithms," *Evolutionary Computation*, vol. 16, no. 3, pp. 355–384, 2008.

# Chapter 7

## *Overview of Torque Ripple Minimization in SRM Drives*

This chapter presents a survey of the different approaches and methods for reducing SRM torque ripple. Two main approaches are highlighted namely; the machine design approach and the control approach. Torque sharing functions, current profiling using artificial neural network, and direct instantaneous torque control are reviewed. Simulations using a four phase 8/6 SRM in MATLAB/Simulink demonstrate the performance of existing approaches.

### 7.1    Introduction

The SRM has many merits, such as robustness, simple construction and low cost. However, its deployment in servo applications is restrained due to the acoustic noise caused by radial vibration [7-1], [7-2]. Also, the discrete nature of torque production along with SRM high nonlinearity can result in severe torque ripple (TR) during commutation (the transfer of torque production from an outgoing phase to an incoming phase). The high torque ripple may cause mechanical vibration stresses (possibly resulting in mechanical resonance effects) and speed oscillations especially at low speeds, which are undesirable in EV applications [7-3].

The object of this thesis is employing the SRM in EV applications, thus the torque (whence torque ripple) requirement specific to that application needs eliciting, particularly due to the torque ripple criticism attributed to the SRM. To sustain a given speed, the developed motor torque must balance opposing vehicle forces, like rolling resistance, drag, drive incline force, etc.

Torque produced by the motor in excess of these resisting forces produces acceleration. In simple terms, as the speed increases, the drag force dominates since that force is proportional to speed squared (power is proportional to speed cubed). Thus, during acceleration ripple is important over the full torque range.

As the vehicle decelerates (without applying the brakes) the SRM torque developed is less than the forces on the vehicle, whence the speed decreases so as to balance the machine force to that

115

imposed physically on the vehicle. Deceleration is applicable over the full speed range, within which operating area, torque ripple is important.
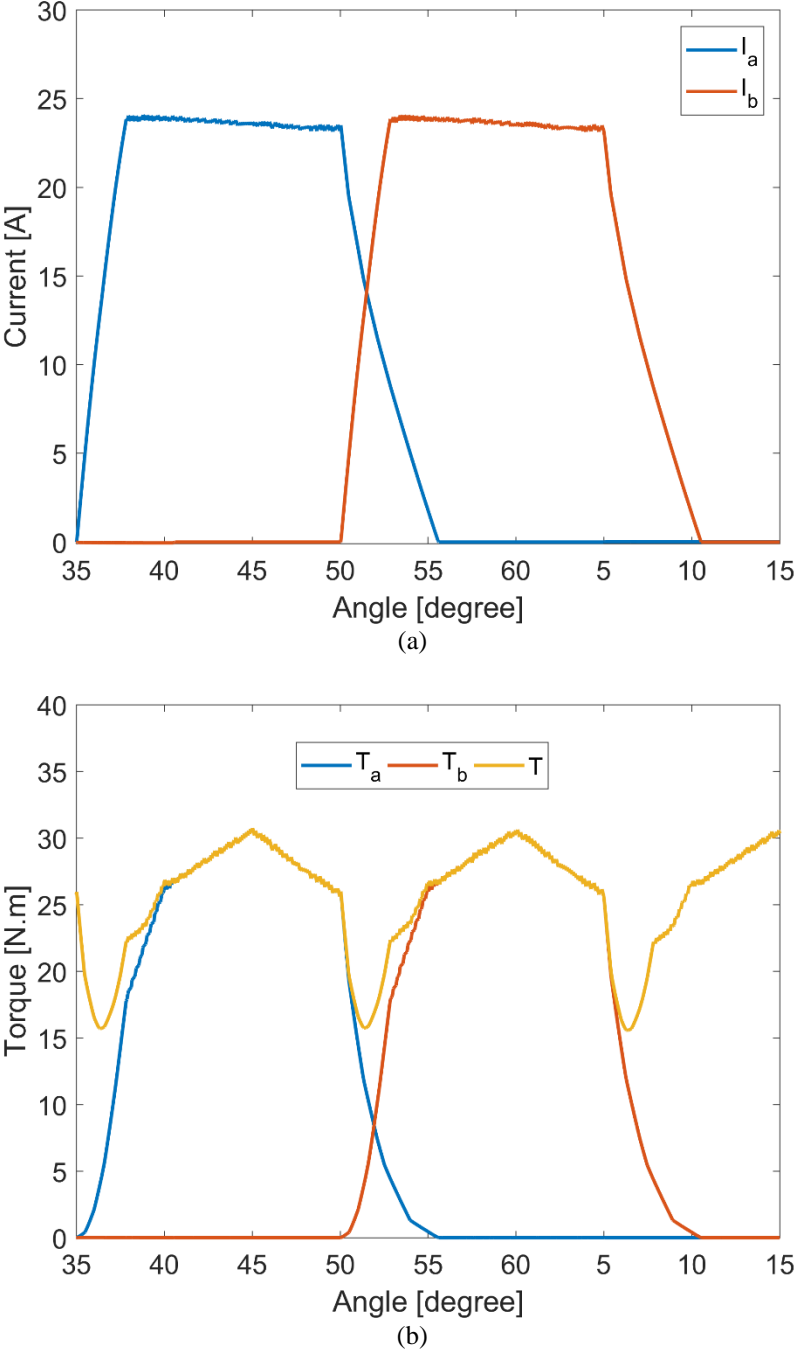


Fig. 7.1 SRM performance in current chopping mode: (a) Current waveforms, and (b) Torque waveforms

116

Therefore, in EV applications, torque ripple must be minimised over the full speed and torque ranges, if this perceive SRM torque ripple limitation in EV is to be addressed.

As a general example of torque ripple, Fig. 7.1 shows SRM performance in the current chopping mode at 750rpm driving full load torque (FLT). The turn on and turn off angles are 35º and 50º respectively (positive torque region is 30º to 60º). Fig. 7.1a shows the currents of two overlapping phases, while, Fig. 7.1b shows the corresponding phase torques along with the overall total developed torque. Severe torque dip is observed during commutation.

## 7.2    Torque ripple minimization approaches

Many solutions have been proposed to alleviate these undesirable SRM features (noise/vibration and TR) [7-4]. This chapter focuses specifically on the minimization of TR. Generally, two main approaches are considered to reduce TR namely; the motor design approach and the control approach [7-5] as illustrated in Fig. 7.2. A brief discussion on prior art of these two approaches is presented in the following sections.
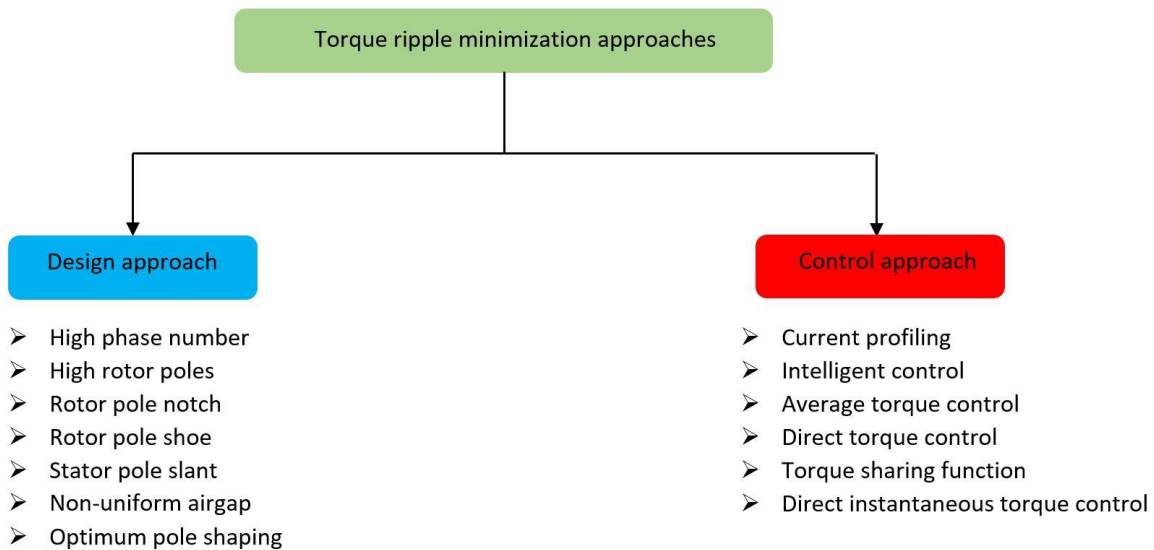


Fig. 7.2 Torque ripple (TR) minimization approaches

## 7.3    Machine design approach to torque ripple reduction

Increasing the number of SRM stator and rotor poles results in overlap of more than two phases during commutation which can minimize torque ripple. However, the increased switching

frequency results in more converter losses and machine losses (corresponding to envisaged EV machine speeds of up to 20,000 rpm). In addition, extra converter switches are required (if number of phases increases), increasing the converter cost [7-6].

A new SRM approach explores an SRM with higher number of rotor poles than stator poles, as presented in [7-7]. The new motor concept ($N_s<N_r$) has lower mass and copper loss than the conventional SRM ($N_s>N_r$). Due to the extra space available in the stator slot area, windings with a higher number of turns and thicker cross-sectional area can be deployed [7-8]. Also, the increased rotor pole number minimizes TR, which is vital for EV application [7-9]. However, since the interpolar rotor airgaps are narrower in the new motor design, the unaligned inductance is significantly higher than that of the conventional SRM. The increase of unaligned inductance reduces the energy conversion area, thus decreases the developed torque [7-10]. Also, the current rise time at phase turn-on is prolonged as a consequence of higher unaligned inductance, which implies using higher dc-link voltages to increase the current rate of rise [7-11].
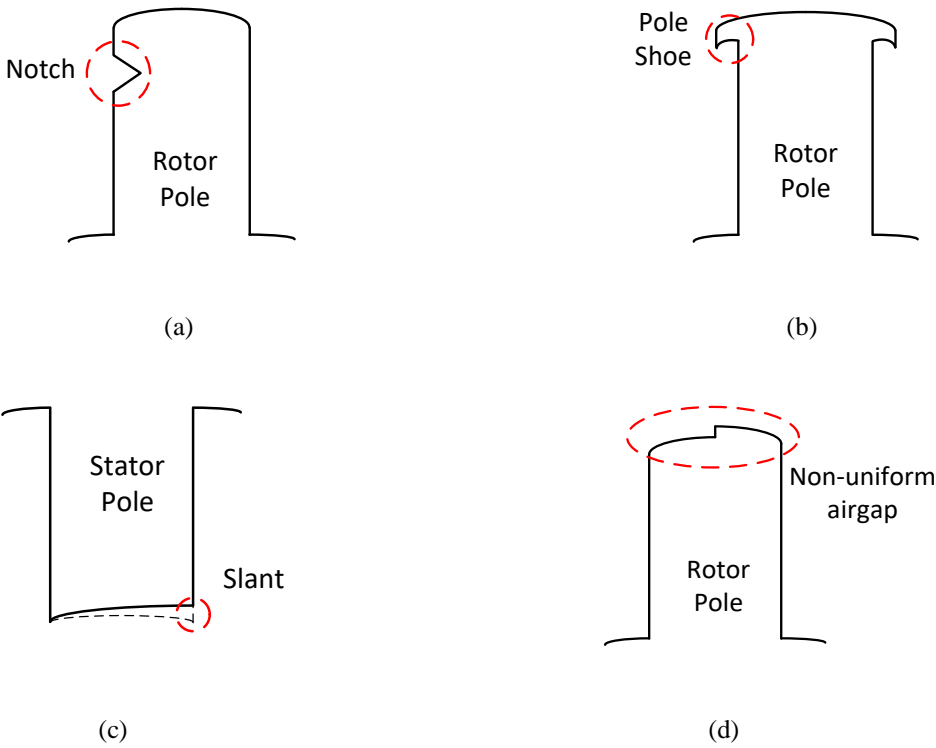


Fig. 7.3 SRM pole design:
(a) Rotor pole notch, (b) Rotor pole shoe, (c) Stator pole slant, and (d) Non-uniform air gap

Introducing a notch in the rotor pole as shown in Fig. 7.3a was presented in [7-12] for TR reduction. This approach was extended in [7-13] for a mutually coupled SRM. The rotor pole shoe shown in Fig. 7.3b is discussed in [7-14]. On the other hand, a stator pole slant, as illustrated in Fig. 7.3c, is demonstrated in [7-15], and the non-uniform air gap in Fig. 7.3d. for a two phase SRM, is presented in [7-16]. All these variations attempt to minimize TR. However, machine torque density is reduced. Increasing the average torque and reducing torque ripple was proposed in [7-17] by optimizing the stator and rotor poles for a four-phase 8/6 SRM. However, the approach of modifying the machine design is limited to a narrow speed range and for rated load conditions.

Changes to the basic rotor/stator design result in reduced power output, which is an unacceptable SRM limitation when being compared to the PMSM in EVs.

## 7.4 Control approaches to torque ripple reduction

As opposed to the machine design approach, the control approach is less expensive, more effective and flexible, and can cover a wide range of speeds [7-18].

Ripple-free torque could be obtained by current profiling [7-19], where optimal current contours, producing constant output torque, are generated using static SRM data. These current profiles are stored using look up tables (LUTs) and current controllers are used to track these profiles [7-20]. However, the main drawback of this approach is that it requires memory to store the current profiles for different speeds, torque demands and dc link voltages. Moreover, a high bandwidth current controller is required to accurately track the stored current profiles [7-21]-[7-23]. Using conventional PWM may result in current tracking errors especially at high speeds [7-24]-[7-27]. The majority of the current controllers are implemented based on analytical modelling of the SRM [7-28]. Hence, inaccuracy is inevitable. In [7-29], [7-30] current profiling along with a new SRM design with a flat torque profile are combined to reduce the torque ripple. Yet, the new machine design has a narrow speed range compared with conventional SRM designs.

Generally, optimal current profiles are generated as discrete points and the intermediate points are found using linear interpolation. Increasing the number of points will improve the accuracy at the expense of time and storage memory in the form of LUTs. In [7-31], harmonic coefficients are used to produce the required current profiles, where interpolation is not required. However, this method is based on the accuracy of the analytical model. Fuzzy logic and neural networks

119

presented in [7-32], [7-33] can generate the required magnetization data without the need of huge memory. But, computational complexity increases significantly. In [7-34], [7-35] a control scheme is developed based on iterative learning control (ILC). The advantage of this method is that it does not depend on model accuracy and does not need large memory to store the magnetization data. Yet, it has slow dynamics with poor response during transients which is not tolerable in EV applications.

Average torque control (ATC) was presented in [7-36], [7-37], where torque is calculated using co-energy derived based on terminal quantities (voltage and current) [7-38]. The method is extended in [7-39] for four quadrant operation at low speeds. However, this method relies on high precision measurement of voltage and current. In addition, the effect of varying the stator resistance (due to temperature change) is not considered which affects co-energy estimation.

The principle of direct torque control (DTC), which is similar to that used for induction motors, was proposed in [7-40], and optimized in [7-41]. The concept is based on controlling the flux which in turn controls the developed torque. Hysteresis controllers are used, hence variable switching frequency is unavoidable which sophisticates the digital implementation of the controller. To overcome this limitation, a deadbeat torque controller was proposed in [7-42] which has a fixed switching frequency. However, the control algorithm is complicated. Improving the torque per ampere ratio, and hence improving the efficiency, was considered in [7-43], [7-44]. A model predictive controller (MPC) was presented in [7-45] to choose the suitable voltage vector. Though, the method relies on the SRM mathematical model which does not reflect machine non-linearity.

## 7.5   Torque sharing function (TSF)

TSF is a good method to minimize SRM drive TR caused by the discrete non-linear nature of torque production [7-46]-[7-48]. TR reduction, specifically in the commutation time when the developed torque is being transferred from one active phase to another, is the most critical issue. The total developed SRM torque at any instant is the sum of individual phase torques, thus the TSF generates reference torque for each individual phase using the total reference torque. The reference phase torque is transformed into a reference current using a LUT depending on rotor position. The reference phase current is compared with actual phase current generating an error

signal, this error is minimised using a high bandwidth current controller. The effect of phase turn-on and turn-off is discussed in [7-49]. Optimizing a TSF with regards to phase rms current and efficiency is studied in [7-50]. A non-linear TSF was reported in [7-51] to account for the SRM magnetic characteristics.

Although the generation of the reference current signal from the individual phase reference torque is possible, but the $T - i - \theta$ LUT inversion is not an easy task [7-52]. Another approach is helpful in this case which is based on obtaining the actual phase torques from the actual phase currents directly using the LUT. The generated reference phase torques and the actual phase torques are then compared and the command torque is regulated by the controller [7-53]. Usually a hysteresis band torque controller (HBTC) is used to handle the error signal. Operation of a TSF method for a four-phase 8/6 SRM is illustrated in Fig. 7.4.
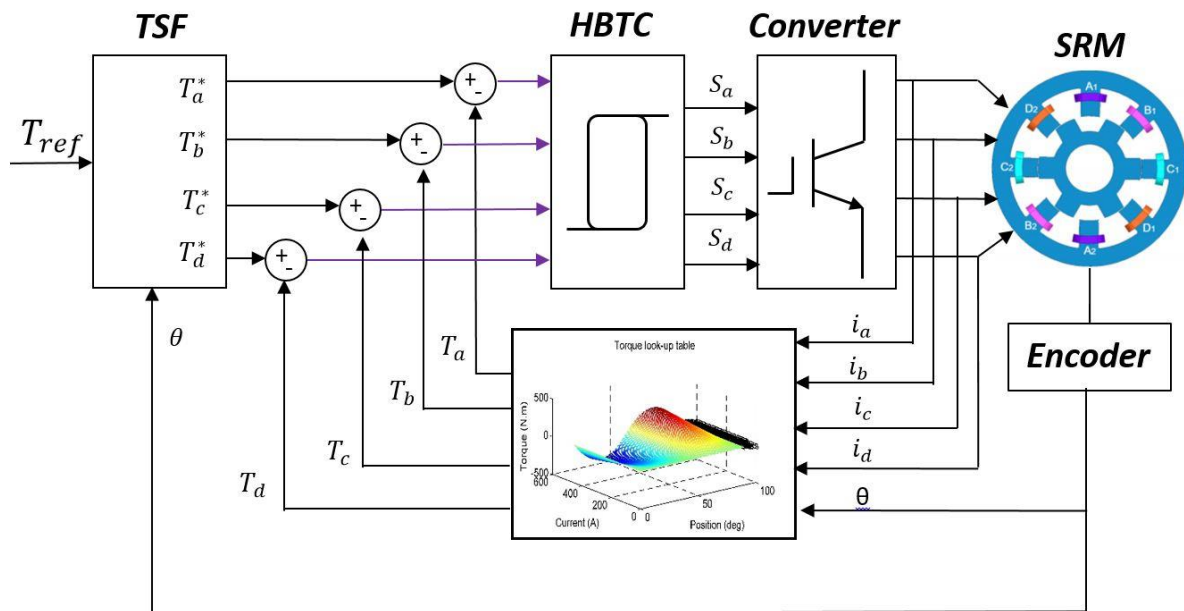


Fig. 7.4 Illustration of a TSF control system

Torque production is divided into two regions; single and double excitation regions (one and two phases conducting). In the single excitation region only one phase produces the total required torque, while in the double excitation region the overall torque developed is shared between two phases, the incoming and outgoing phase, keeping an overall torque value equal to the reference torque value. The method by which the two phases share the torque defines the type of TSF. Mainly

121

two types of TSF are used; linear and non-linear TSF. The non-linear TSFs include; cos, cubic and exponential functions, which are illustrated in Fig. 7.5. The non-linear TSF reflects, to some extent, the non-linearity of SRM, thus is more efficient approach.
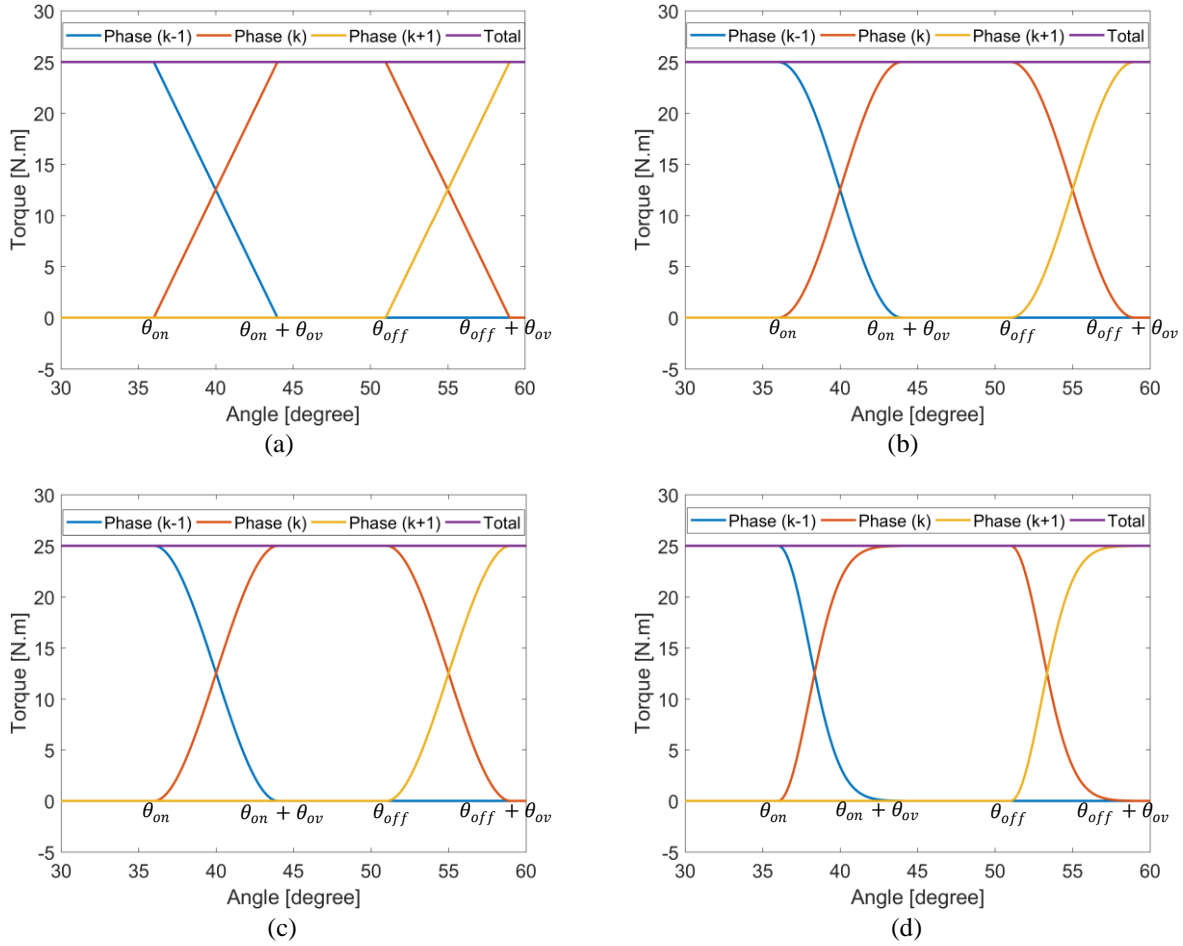


Fig. 7.5 Types of TSF: (a) Linear, (b) Cos, (c) Cubic, and (d) Exponential

Equation (7.1) defines individual torque profile for an arbitrary phase *k*.

$$
T_k^*(\theta) = \begin{cases}
0, & 0 \leq \theta < \theta_{on} \\
T_{dem} x f_{rise}(\theta), & \theta_{on} \leq \theta < \theta_{on} + \theta_{ov} \\
T_{ref}, & \theta_{on} + \theta_{ov} \leq \theta < \theta_{off} \\
T_{dem} x f_{fall}(\theta), & \theta_{off} \leq \theta < \theta_{off} + \theta_{ov} \\
0, & \theta_{off} + \theta_{ov} \leq \theta < \theta_r
\end{cases}
\tag{7.1}
$$

where $\theta_{on}$ is the turn-on angle, $\theta_{off}$ is the turn-off angle, $\theta_{ov}$ is the overlap angle, and $\theta_r$ is the rotor pole pitch. $T_{dem}$ is the demand torque.

The arbitrary phase $k$ is energized depending on rotor position between the turn-on and turn-off angles, for the motoring mode the turn-on and turn-of angles must satisfy (7.2).

$$\begin{cases} \theta_{on} \geq \theta_u \\ \theta_{off} + \theta_{ov} \leq \theta_a \end{cases} \tag{7.2}$$

where $\theta_u$ and $\theta_a$ are the unaligned and aligned rotor position, respectively.

The overlap angle $\theta_{ov}$ represents the interval where the torque is shared between two phases; the incoming and outgoing phases. The maximum overlap angle is calculated using (7.3).

$$\theta_{ov} = \frac{1}{2}\theta_r - \theta_{stroke} \tag{7.3}$$

where $\theta_{stroke}$ is the stroke angle $= \frac{360^0}{mN_r}$ ($15^0$ for 8/6 SRM).

For $30^0$ conduction period (7.1) becomes on the form:

$$T_k^*(\theta) = \begin{cases} 0, & 0 \leq \theta < 30^0 \\ T_{dem} x f_{rise}(\theta), & 30^0 \leq \theta < 45^0 \\ T_{dem} x f_{fall}(\theta), & 45^0 \leq \theta < 60^0 \end{cases} \tag{7.4}$$

During the interval of commutation the function $f_{rise}$ increases from 0 to 1, while the function $f_{fall}$ decreases from 1 to 0. The function $f_{rise}$ and subsequently $f_{fall}$ depend on the type of TSF. The linear, cos, cubic and exponential TSFs are expressed in (7.5) - (7.8) respectively.

$$\text{linear:} \begin{cases} f_{rise} = \frac{\theta - \theta_{on}}{\theta_{ov}} \\ f_{fall} = 1 - \frac{\theta - \theta_{off}}{\theta_{ov}} \end{cases} \tag{7.5}$$

$$\text{cos:} \begin{cases} f_{rise} = \frac{1}{2} - \frac{1}{2}\cos\pi\left(\frac{\theta - \theta_{on}}{\theta_{ov}}\right) \\ f_{fall} = \frac{1}{2} + \frac{1}{2}\cos\pi\left(\frac{\theta - ff}{\theta_{ov}}\right) \end{cases} \tag{7.6}$$

$$cubic: \begin{cases} f_{rise} = 3\left(\frac{\theta - \theta_{on}}{\theta_{ov}}\right)^2 - 2\left(\frac{\theta - \theta_{on}}{\theta_{ov}}\right)^3 \\ f_{fall} = 1 - 3\left(\frac{\theta - \theta_{off}}{\theta_{ov}}\right)^2 + 2\left(\frac{\theta - \theta_{off}}{\theta_{ov}}\right)^3 \end{cases} \quad (7.7)$$

$$Exp: \begin{cases} f_{rise} = 1 - e^{-\frac{(\theta - \theta_{on})^2}{\theta_{ov}}} \\ f_{fall} = e^{-\frac{(\theta - \theta_{off})^2}{\theta_{ov}}} \end{cases} \quad (7.8)$$

## 7.6  Current profiling using artificial neural network (ANN)

ANN is a processing model that mimics the operation of biological neural networks [7-54]. The basic element in the ANN is the neuron which is illustrated in Fig. 7.6, where $a$ is the input, $s$ is the output, b, $c$, $f$, and $r$ are the bias, weight, transfer function, and the net input, respectively.
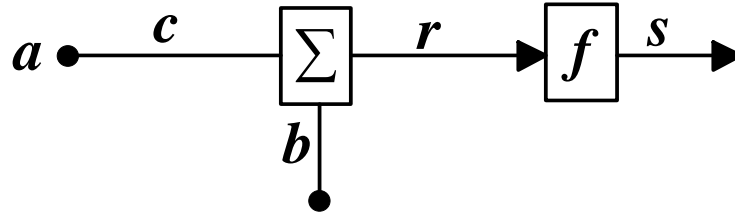


Fig. 7.6 The basic structure of ANN (neuron)

The bias and the weight are scalar values that can be adjusted. The relation between the input and output of the neuron is given by (7.9).

$$s = f(ca + b) \quad (7.9)$$

The transfer function may be linear or non-linear depending on the specifications of the application. Fig. 7.7 describes some of the most common transfer functions used in ANNs namely; linear, hard limit, and log sigmoid [7-55].

Describing the model with only one neuron is not sufficient. Hence, several neurons are connected together in parallel to form a layer. Several layers can be used in series to form the ANN.

$$s = r$$

$$s = \begin{cases} 0, & r < 0 \\ 1, & r \geq 0 \end{cases}$$

$$s = \frac{1}{1 + e^{-r}}$$

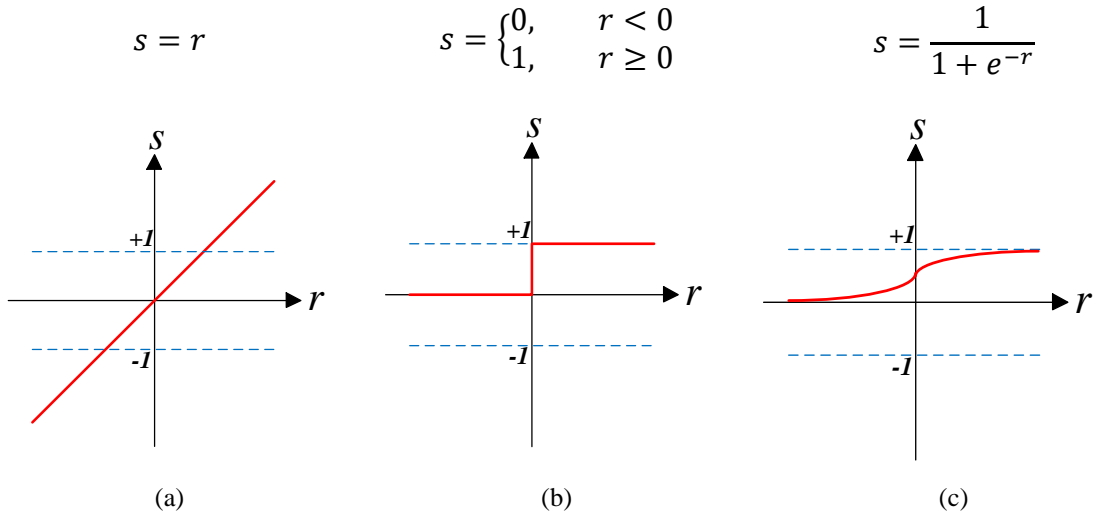(a)                    (b)                    (c)

Fig. 7.7 Common transfer functions: (a) Linear, (b) Hard limit, and (c) Log sigmoid

Fig. 7.8 shows a two layer ANN including the input, one hidden layer, and the output layer. The model has two inputs, the hidden layer is composed of three neurons, and the output layer has only one neuron (since the model has only one output).
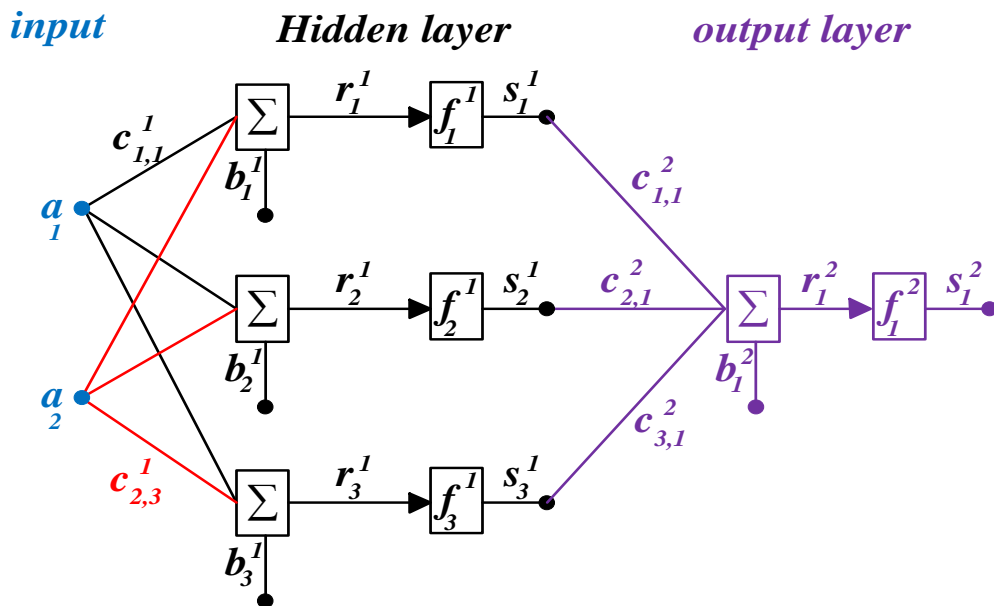


Fig. 7.8 Two layer ANN

ANN could be used to generate the required current profile for each phase [7-56], thus minimizing the generated TR. The inputs to the ANN are the rotor angle $\theta$ and the demand torque $T_{dem}$. The

output of the ANN is the required current profiles. Fig. 7.9 shows the SRM torque ripple minimization control system using ANN. Current is handled using a hysteresis band current controller (HBCC).
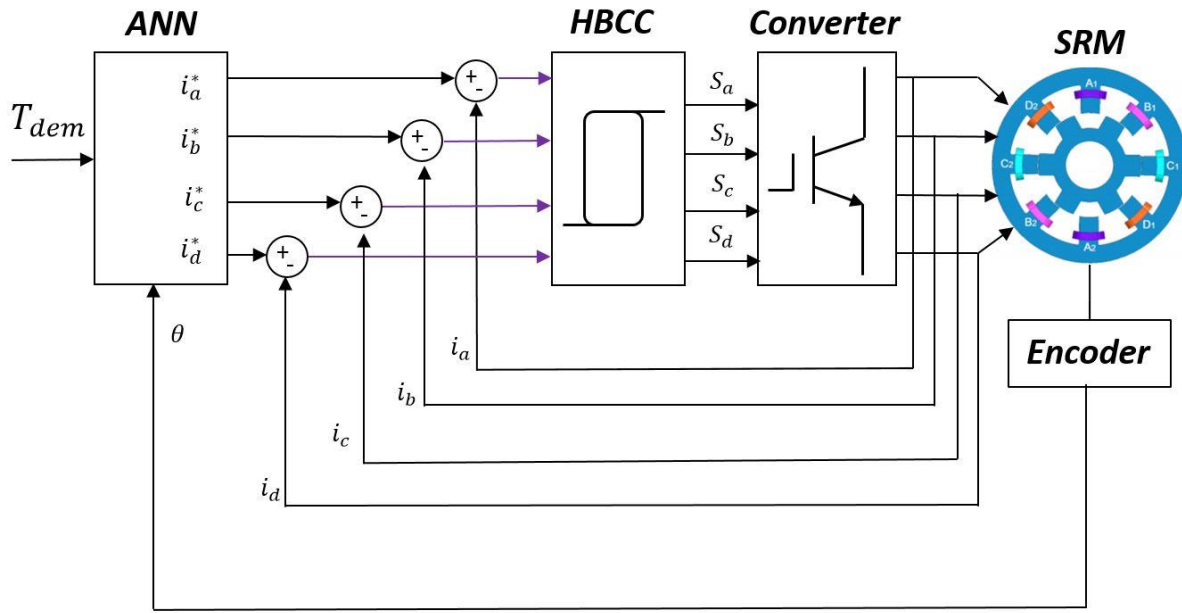


Fig. 7.9 Illustration of current profiling using ANN

## 7.7 Direct instantaneous torque control (DITC)

Due to SRM severe non-linearity, the actual phase torque cannot perfectly follow the reference torque near the unaligned and aligned positions, as in TSFs or current profiling, which results in severe torque dips. Based on this, another method was proposed in [7-57], where the total torque is regarded as the control variable as opposed to the TSF which regards the phase torque as the control variable.

DITC can continuously control the instantaneous value of developed torque, so it significantly minimizes torque ripple. In [7-58], a four quadrant DITC was presented, but the method relies on using a hysteresis controller with variable switching frequency. To overcome this limitation, a predictive PWM was reported in [7-59] with an extension of the scheme for SRMs with more than four phases.

The method is based on measuring the actual phase currents and then converting these currents into phase torques with respect to rotor position using LUTs [7-60], [7-61]. The individual phase torques are added to represent the overall developed torque which is compared with the required reference torque value. HBTC is used to generate the converter switching signals. Fig. 7.10 demonstrates the operation of DITC for four-phase SRM.
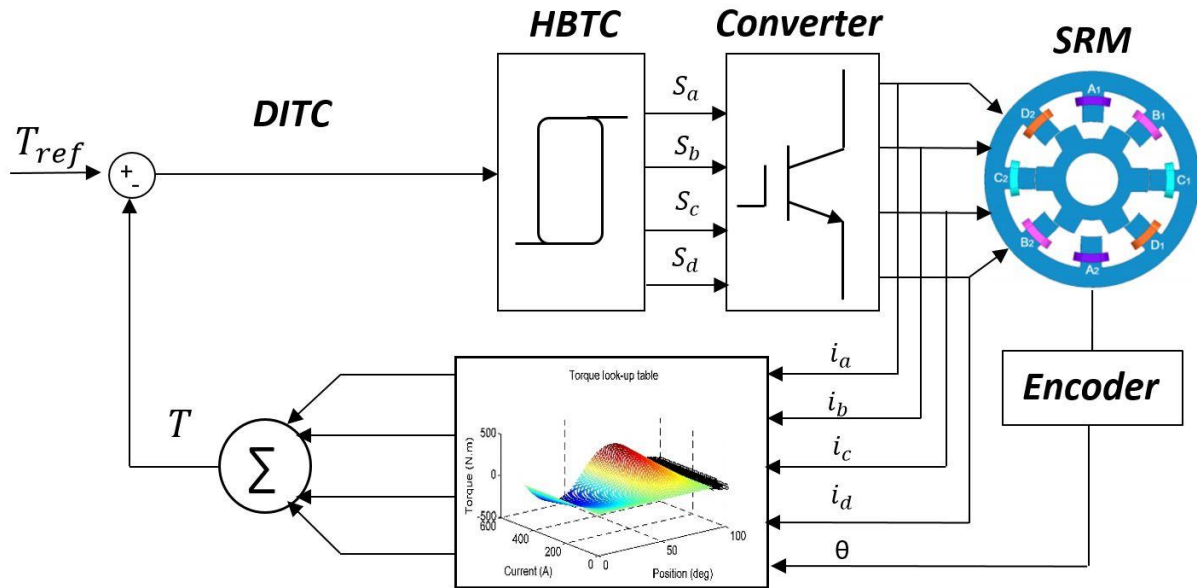


Fig. 7.10 Illustration of DITC

## 7.8 Simulation results

This section presents the simulation results for different torque control techniques namely; TSF, current profiling using an ANN, and DITC. The SRM specifications used for simulation are given in Appendix A. A common-phase converter (as illustrated previously in Fig. 3.13) either with or without voltage-boosting is used. The SRM delivers full load torque (25Nm) and runs at 30% base speed (450rpm). Angles are adjusted for each approach to yield the lowest TR. A 0.4A hysteresis band is used for the current controllers (for TSF and ANN results), while a 1Nm band is used for the torque controller (for DITC).

### 7.8.1 TSF results

In this sub-section the reduction of torque ripple using different TSFs is demonstrated. Fig. 7.11 explores SRM performance under linear TSF, where the SRM is driven by a common-phase converter without voltage-boosting.
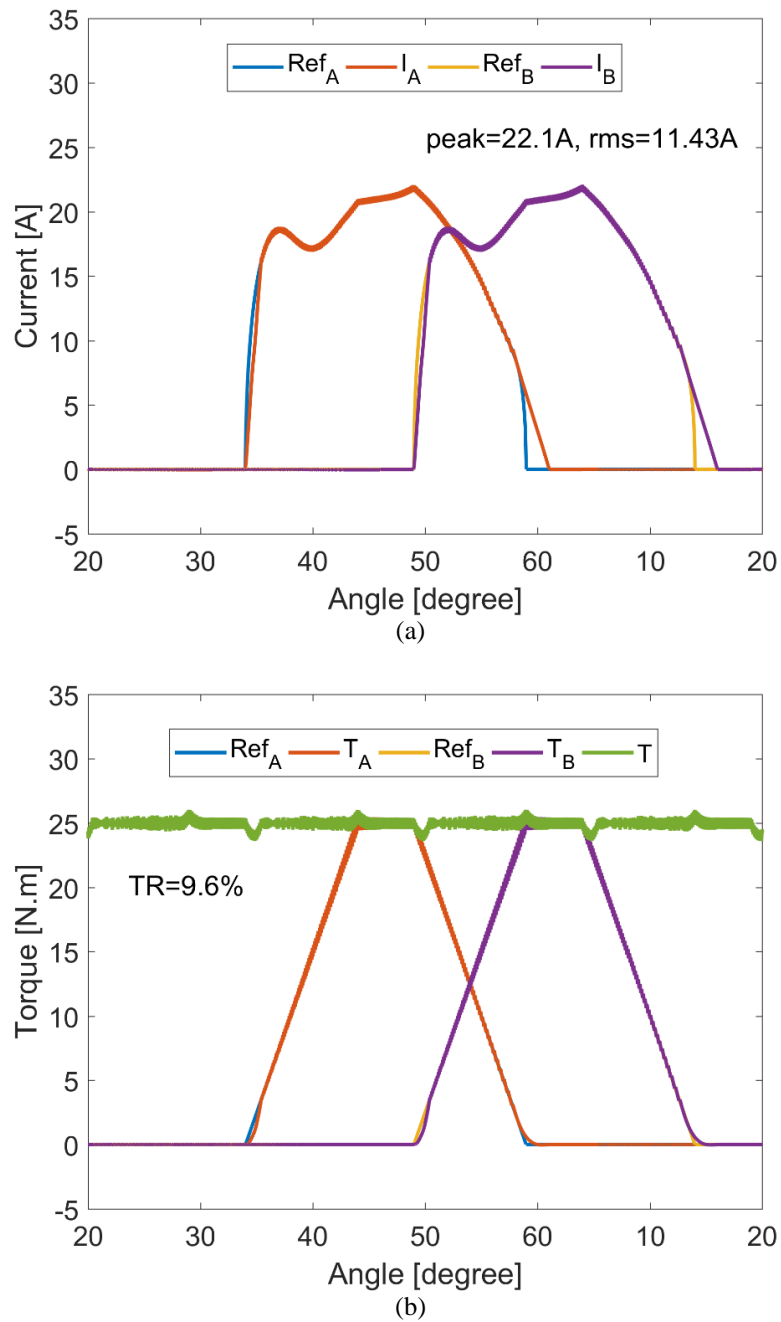


Fig. 7.11 SRM performance with linear TSF without voltage-boosting: (a) Current waveforms, and (b) Torque waveforms
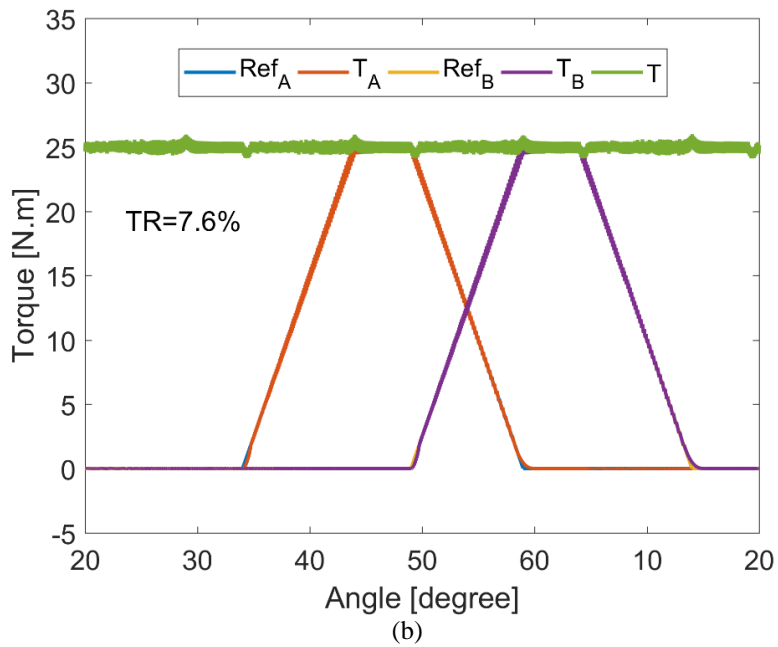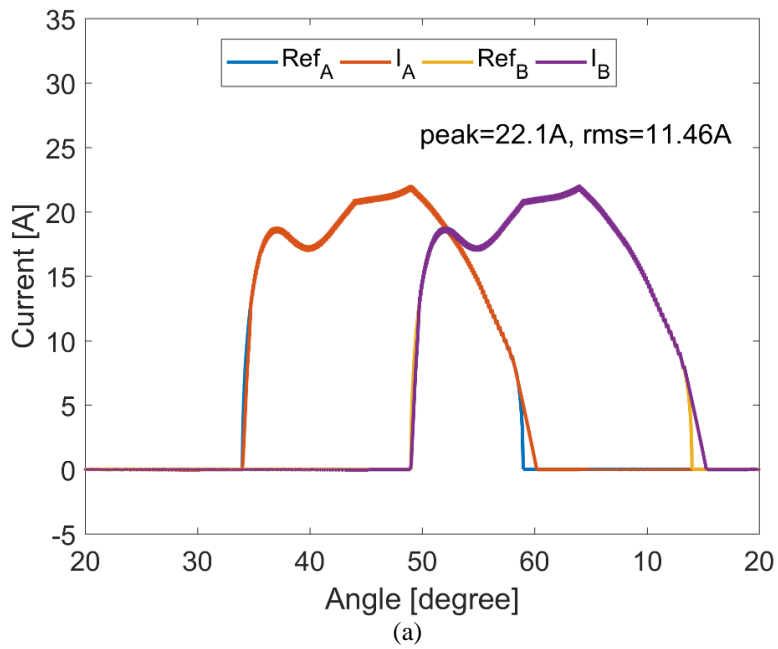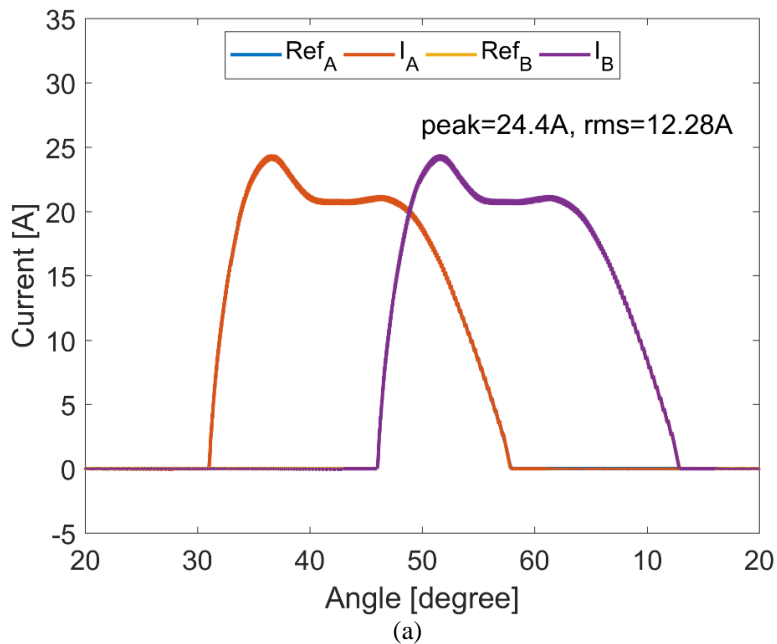
128

Fig. 7.12 SRM performance with linear TSF with voltage-boosting: (a) Current waveforms, and (b) Torque waveforms

Fig. 7.11a shows the current waveforms of two overlapping phases, where the phase winding draws 11.43A rms current with a 22.1A peak. Fig. 7.11b shows the corresponding phase torques along with the total developed torque. The linear TSF does not reflect the SRM non-linearity.

Hence, the actual phase torque struggles to follow the reference during phase turn on/off due to lack of dc link voltage resulting in a 9.6% TR.

The effect of utilizing voltage-boosting for linear TSF is illustrated in Fig. 7.12. The increase in dc link voltage during phase turn on/off aids the winding current to build-up/decay quickly. Hence, the TR is reduced to 7.6%, as in Fig. 7.12b. A linear TSF is not adequate for reducing TR at this torque and speed. However, dc link voltage-boosting has positive impact on reducing TR. Hence, the common phase converter with voltage-boosting is utilized for the remaining results in this chapter.

The non-linear TSF, based on co-sinusoidal phase torque waveforms, is shown in Fig. 7.13. Since the phase torque demand at turn on/off is minimized (as a consequence of using a non-linear TSF), there is no sharp edges in the current waveforms as highlighted in Fig. 7.13a. The rms current is12.28A with a 24.4A peak. The TR is reduced to 4.6% as in Fig. 7.13b. The cubic and exponential based TSFs give similar, but not better TR results as the Cos TSF.
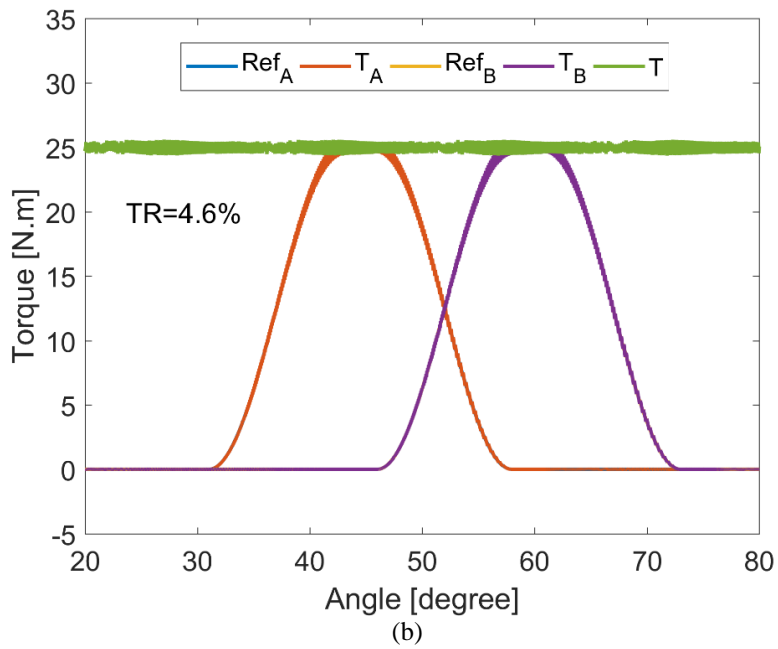


(a)

(b)

Fig. 7.13 SRM performance with cos TSF with voltage-boosting: (a) Current waveforms, and (b) Torque waveforms
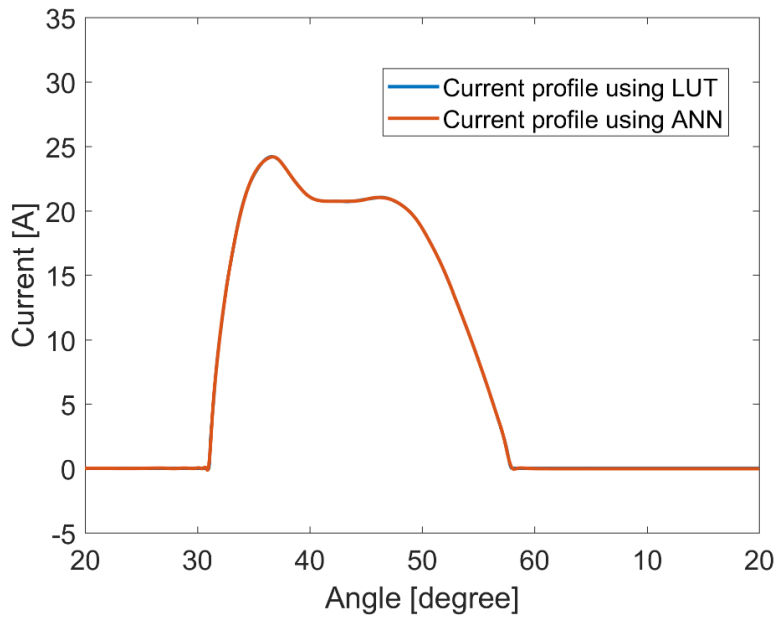


Fig. 7.14 Optimal phase current profile generated by ANN and LUT

131

## 7.8.2 Artificial neural networks results

Fig. 7.14 compares the phase current profiles obtained using an ANN and LUT at FLT, where excellent agreement is achieved.
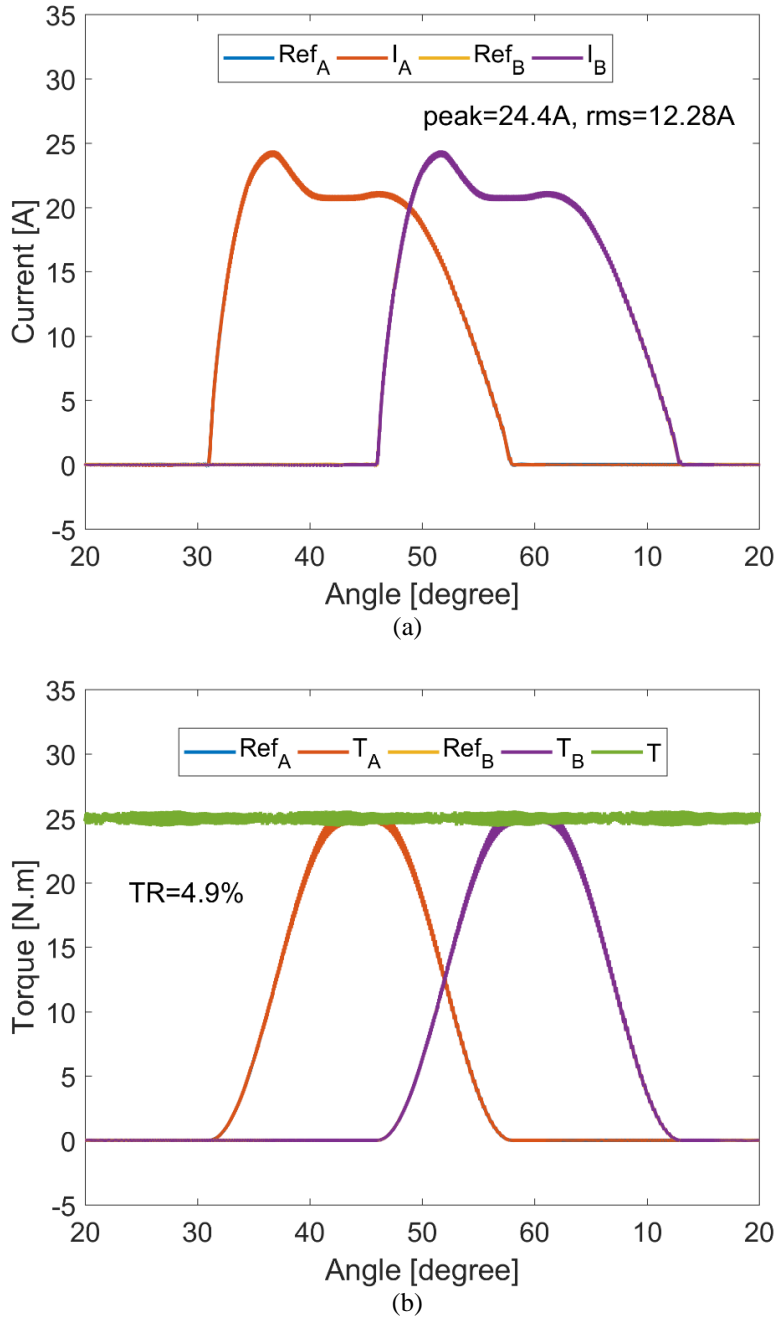


(a)



(b)

Fig. 7.15 SRM performance using ANN with voltage-boosting: (a) Current waveforms, and (b) Torque waveforms

This shows that ANN could be used instead of LUTs to generate the required phase current waveforms. Fig. 7.15 shows the current and torque waveforms in the dynamic condition (at 450rpm FLT) with 12.28A rms and 24.4 peak (identical values as for the Cos TSF case considered in 7.8.1). A 4.9% TR is recorded.
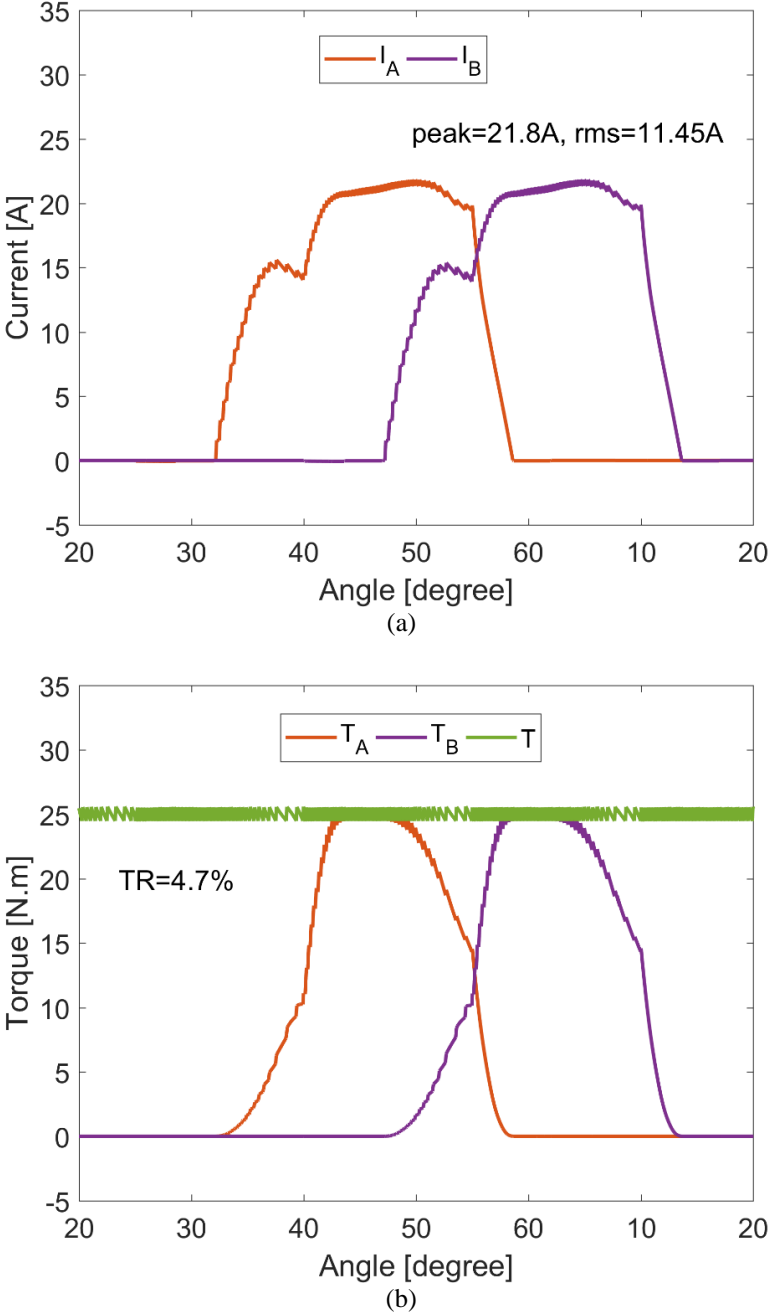


(a)



(b)

Fig. 7.16 SRM performance using DITC with voltage-boosting: (a) Current waveforms, and (b) Torque waveforms

### 7.8.3 Direct instantaneous torque control results

DITC results are presented in this subsection. Fig. 7.16a shows the current waveforms of two overlapping phases with 11.45A rms and 21.8A peak. Fig. 7.16b shows the relevant phase torques, along with the total developed torque. The phase torques non-linearly reduce the current required at phase turn on. The DITC method controls the total torque instead of controlling individual phase torques. Thus, if the incoming phase is not capable of providing the required total torque the shortfall is supplied by the outgoing phase, thereby maintaining the total torque constant. A 4.7% TR is recorded using this method.

## 7.9    Summary

The researched methods referenced have been introduced and simulated. Most methods give low ripple (excluding switching ripple). Voltage-boosting significantly reduces the TR during commutation between two phases, for all torque methods by offering higher voltage during turn on/off. This highlights that optimal utilization of the available dc link voltage will extend the region over which the SRM can operate with zero TR (theoretically).

The TCF (torque control function) method proposed in the next chapter improves TR performance, by better exploiting the dc link voltage, with and without boosting.

**References**

[7-1]   J. Dong, J. Jiang, B. Howey, H. Li, B. Bilgin, A. Callegaro and A. Emadi, ''Hybrid acoustic noise analysis approach of conventional and mutually coupled switched reluctance motors,'' *IEEE Transactions on Energy Conversion*, vol. 32, no. 3, pp. 1042-1051, Sep. 2017.

[7-2]   H. Makino, T. Kosaka, and N. Matsui, ''Digital PWM-control-based active vibration cancellation for switched reluctance motors,'' *IEEE Transactions on Industry Applications*, vol. 51, no. 6, pp. 175-182, Dec. 2015.

[7-3]   Y. Chai and C. Liaw, ''Reduction of speed ripple and vibration for switched reluctance motor drive via intelligent current profiling,'' *IET Electric Power Applications*, vol. 4, no. 5, pp. 380-396, 2010.

[7-4]   C. Gan, Q. Sun, W. Kong, H. Li, and Y. Hu, ''A review on machine topologies and control techniques for low-noise switched reluctance motors in electric vehicle applications,'' *IEEE Access*, vol. 6 pp. 31430-31443, 2018.

[7-5]   I. Hussain, ''Minimization of torque ripple in SRM drives,'' *IEEE Transactions on Industrial Electronics*, vol. 49, no. 1, pp. 28-39, Feb. 2002.

[7-6]  X. Deng, B. Mecrow, H. Wu, and R. Martin, ''Design and development of low torque ripple variable-speed drive system with six-phase switched reluctance motors,'' *IEEE Transactions on Energy Conversion*, vol. 33, no. 1, pp. 420-429, Mar. 2018.

[7-7]  J. Jiang, B. Bilgin, and A. Emadi, ''Three-phase 24/16 switched reluctance machine for a hybrid electric powertrain,'' *IEEE Transactions on Transportation Electrification,* vol. 3, no. 1, pp. 76-85, Mar. 2017.

[7-8]  P. Desai, M. Krishnamurthy, N. Schofield, and A. Emadi, ''Novel switched reluctance machine configuration with higher number of rotor poles than stator poles: Concept to implementation,'' *IEEE Transactions on Industrial Electronics*, vol. 57, no. 2, pp. 649-659, Feb. 2010.

[7-9]  B. Bilgin, A. Emadi, and M. Krishnamurthy, ''Design considerations for switched reluctance machines with a higher number of rotor poles,'' *IEEE Transactions on Industrial Electronics*, vol. 59, no. 10, pp. 3745-3756, Oct. 2012.

[7-10] B. Bilgin, A. Emadi, and M. Krishnamurthy, ''Comprehensive evaluation of the dynamic performance of a 6/10 SRM for traction application in PHEVs,'' *IEEE Transactions on Industrial Electronics*, vol. 60, no. 7, pp. 2564-2575, July 2013.

[7-11] J. Lin, N. Schofield, and A. Emadi, ''External-rotor 6-10 switched reluctance motor for an electric bicycle,'' *IEEE Transactions on Transportation Electrification*, vol. 1, no. 4, pp. 348-356, Dec. 2015.

[7-12] J. Lee, H. Kim, B. Kwon, and B. Kim, ''New rotor shape design for minimum torque ripple of SRM using FEM,'' *IEEE Transactions on Magnetics*, vol. 40, no. 2, pp. 754-757, Mar. 2004.

[7-13] G. Li, J. Ojeda, S. Hlioui, E. Hoang, M. Lecrivain, and M. Gabsi, ''Modification in rotor pole geometry of mutually coupled switched reluctance machine for torque ripple mitigating,'' *IEEE Transactions on Magnetics*, vol. 48, no. 6, pp. 2025-2034, June 2012.

[7-14] Y. Choi, H. Yoon, and C. Koh, ''Pole-shape optimization of switched-reluctance motor for torque ripple reduction,'' *IEEE Transactions on Magnetics*, vol. 43, no. 4, pp. 1797-1800, Apr. 2007.

[7-15] N. Sheth, and K. Rajagopal, ''Torque profiles of a switched reluctance motor having special pole face shapes and asymmetric stator poles,'' *IEEE Transactions on Magnetics*, vol. 40, no. 4, pp. 2035-2037, Jul. 2004.

[7-16] D. Lee, T. Pham, and J. Ahn, ''Design and operation characteristics of four-two pole high-speed SRM for torque ripple reduction,'' *IEEE Transactions on Industrial Electronics*, vol. 60, no. 9, pp. 3637-3643, Sep. 2013.

[7-17] N. Sheth, and K. Rajagopal, ''Optimum pole arcs for a switched reluctance motor For higher torque with reduced ripple,'' *IEEE Transactions on Magnetics*, vol. 39, no. 5, pp. 3214-3216, Sep. 2003.

[7-18] T. Husain, A. Elrayyah, Y. Sozer, and I. Husain, ''Unified control for switched reluctance motors for wide speed operation,'' *IEEE Transactions on Industrial Electronics*, vol. 66, no. 5, pp. 3401-3411, May 2019.

[7-19] D. Schramm, B. Williams, and T. Green, 'Torque ripple reduction of switched reluctance motors by phase current optimal profiling' *in Proc. Power Electronics Specialists Conf.,* Toledo, Spain, May 1992, pp. 857–860.

[7-20] P. Dubravka, P. Rafajdus, P. Makys, and L. Szabo, ''Control of switched reluctance motor by current profiling under normal and open phase operating condition,'' *IET Electric Power Applications*, vol. 11, no. 4, pp. 548-556, 2017.

[7-21] S. Schulz, and K. Rahman, ''High-performance digital PI current regulator for EV switched reluctance motor drives,'' *IEEE Transactions on Industry Applications*, vol. 39, no. 4, pp. 1118-1126, Aug. 2003.

[7-22] R. Gobbi, and K. Ramar, ''Optimization techniques for a hysteresis current controller to minimize torque ripple in switched reluctance motors,'' *IET Electric Power Applications*, vol. 3, no. 5, pp. 453-460, 2009.

[7-23] Z. Lin, D. Reay, B. Williams, X. He, ''High-performance current control for switched reluctance motors based on on-line estimated parameters,'' *IET Electric Power Applications*, vol. 4, no. 1, pp. 67-74, 2010.

[7-24] R. Mikail, I. Husain, Y. Sozer, M. Islam, and T. Sebastian, ''A fixed switching frequency predictive current control method for switched reluctance machines,'' *IEEE Transactions on Industry Applications*, vol. 50, no. 6, pp. 3717-3726, Dec. 2014.

[7-25] J. Ye, P. Malysz, and A. Emadi, ''A fixed-switching-frequency integral sliding mode current controller for switched reluctance motor drives,'' *IEEE Trans. Selected and Emerging Topics in Power Electronics*, vol. 3, no. 2, pp. 381-394, June 2015.

[7-26] X. Li, and P. Shamsi, ''Model predictive current control of switched reluctance motors with inductance auto-calibration,'' *IEEE Transactions on Industrial Electronics*, vol. 63, no. 6, pp. 3934-3941, June 2016.

[7-27] F. Peng, J. Ye, and A. Emadi, ''A digital PWM current controller for switched reluctance motor drives,'' *IEEE Transactions on Power Electronics*, vol. 31, no. 10, pp. 7087-7098, Oct. 2016.

[7-28] X. Zhang, Q. Yang, M. Ma, Z. Lin, and S. Yang, ''A switched reluctance motor torque ripple reduction strategy with deadbeat current control and active thermal management,'' *IEEE Transactions on Vehicular Technology*, vol. 69, no. 1, pp. 317-327, Jan. 2020.

[7-29] R. Mikail, I. Husain, Y. Sozer, M. Islam, and T. Sebastian, ''Torque-ripple minimization of switched reluctance machines using current profiling,*'' IEEE Transactions on Industry Applications*, vol. 49, no. 3, pp. 1258-1267, June 2013.

[7-30] R. Mikail, I. Husain, M. Islam, Y. Sozer, and T. Sebastian, ''Four quadrant torque ripple minimization of switched reluctance machine through current profiling with mitigation of rotor eccentricity problem and sensor errors,'' *IEEE Transactions on Industry Applications*, vol. 51, no. 3, pp. 2079-2104, June 2015.

[7-31] P. Chapman, and S. Sudhoff, ''Design and precise realization of optimized current waveforms for an 8/6 switched reluctance drive,'' *IEEE Transactions on Power Electronics*, vol. 17, no. 1, pp. 76-83, Jan. 2002.

[7-32] L. Henriques, P. Branco, L. Rolim, and W. Suemitsu, ''Proposition of an offline learning current modulation for torque-ripple reduction in switched reluctance motors: Design and experimental evaluation,'' *IEEE Transactions on Industrial Electronics*, vol. 49, no. 3, pp. 665-676, June 2002.

[7-33] Z. Lin, D. Reay, B. Williams, X. He, ''Torque ripple reduction in switched reluctance motor drives using B-spline neural networks,'' *IEEE Transactions on Industry Applications*, vol. 42, no. 6, pp. 1445-1453, Dec. 2006.

[7-34] S. Sahoo, S. Panda, and J. Xu, ''Iterative learning-based high-performance current controller for switched reluctance motors,'' *IEEE Transactions on Energy Conversion*, vol. 19, no. 3, pp. 491-498, Sep. 2004.

[7-35] S. Sahoo, S. Panda, and J. Xu, ''Indirect torque control of switched reluctance motors using iterative learning control,'' *IEEE Transactions on Power Electronics*, vol. 20, no. 1, pp. 200-208, Jan. 2005.

[7-36] R. Inderka, and R. De Doncker, ''High-dynamic direct average torque control for switched reluctance drives,'' *IEEE Transactions on Industry Applications*, vol. 39, no. 4, pp. 1040-1045, Aug. 2003.

[7-37] H. Cheng, H. Chen, and Z. Yang, ''Average torque control of switched reluctance machine drives for electric vehicles,'' *IET Electric Power Applications*, vol. 9, no. 7, pp. 459-469, 2015.

[7-38] K. Wong, K. Cheng, and S. Ho, ''On-line instantaneous torque control of a switched reluctance motor based on co-energy control,'' *IET Electric Power Applications*, vol. 3, no. 4, pp. 257-264, 2009.

[7-39] K. Wong, K. Cheng, and S. Ho, ''Four-quadrant instantaneous torque control of switched reluctance machine at low speed based on co-energy control,'' *IET Electric Power Applications*, vol. 3, no. 5, pp. 431-444, 2009.

[7-40] Cheok, and Y. Fukuda, ''A new torque and flux control method for switched reluctance motor drives,'' *IEEE Transactions on Power Electronics*, vol. 17, no. 4, pp. 543-557, Jul. 2002.

[7-41] X. Ai-de, Z. Xianchao, H. Kunlun, and C. Yuzhao, ''Torque ripple reduction of SRM using optimized voltage vector in DTC,'' *IET Electric Systems in Transportation*, vol. 8, no. 1, pp. 35-43, 2018.

[7-42] W. Zhang, A. Xu, L. Han, and S. Wang, ''Minimizing torque ripple of SRM by applying DB-DTFC,'' *IET Electric Power Applications*, vol. 13, no. 11, pp. 1883-1890, 2019.

[7-43] P. Reddy, D. Ronaki, and P. Perumal, ''Efficiency improvement and torque ripple minimization of four-phase switched reluctance motor drive using new direct torque control strategy,'' *IET Electric Power Applications*, vol. 14, no. 1, pp. 52-61, 2020.

[7-44] N. Yan, X. Cao, and Z. Deng, ''Direct torque control for switched reluctance motor to obtain high torque-ampere ratio,'' *IEEE Transactions on Industrial Electronics*, vol. 66, no. 7, pp. 5144-5152, July 2019.

[7-45] Xu, C. Shang, J. Chen, J. Zhu, and L. Han, ''A new control method based on DTC and MPC to reduce torque ripple in SRM,'' *IEEE Access*, vol. 7, pp. 68584-68593, 2019.

[7-46] J. Ye, B. Bilgin, and A. Emadi, ''An Extended-Speed Low-Ripple Torque Control of Switched Reluctance Motor Drives,'' *IEEE Transactions on Power Electronics*, vol. 30, no. 3, pp. 1457-1470, March 2015.

[7-47] J. Ye, B. Bilgin, and A. Emadi, ''An Offline Torque Sharing Function for Torque Ripple Reduction in Switched Reluctance Motor Drives,'' *IEEE Transactions on Energy Conversion*, vol. 30, no. 2, pp. 726-735, June 2015.

[7-48] H. Li, B. Bilgin, and A. Emadi, ''An Improved Torque Sharing Function for Torque Ripple Reduction in Switched Reluctance Machines,'' *IEEE Transactions on Power Electronics*, vol. 34, no. 2, pp. 1635-1644, Feb. 2019.

[7-49] X. Xue, K. Cheng, and S. Ho, ''Optimization and Evaluation of Torque-Sharing Functions for Torque Ripple Minimization in Switched Reluctance Motor Drives,'' *IEEE Transactions on Power Electronics*, vol. 24, no. 9, pp. 2076-2090, Sept. 2009.

[7-50] V. Vujičić, ''Minimization of Torque Ripple and Copper Losses in Switched Reluctance Drive,'' *IEEE Transactions on Power Electronics*, vol. 27, no. 1, pp. 388-399, Jan. 2012.

[7-51] D. Lee, J. Liang, Z. Lee, and J. Ahn, ''A Simple Nonlinear Logical Torque Sharing Function for Low-Torque Ripple SR Drive,'' *IEEE Transactions on Industrial Electronics*, vol. 56, no. 8, pp. 3021-3028, Aug. 2009.

[7-52] Gan, J. Wu, Q. Sun, S. Yang, Y. Hu, and L. Jin, ''Low-cost direct instantaneous torque control for switched reluctance motors with bus current detection under soft-chopping mode,'' *IET Power Electronics*, vol. 9, no. 3, pp. 482-490, 9 3 2016.

[7-53] Q. Sun, J. Wu, C. Gan, Y. Hu, and J. Si, ''OCTSF for torque ripple minimization in SRMs,'' *IET Power Electronics*, vol. 9, no. 14, pp. 2741-2750, 16 11 2016.

[7-54] M. Hagan, H. Demuth, M. Beale, and O. Jesus ''Neural networks design''

[7-55] M. Beale, M. Hagan, and H. Demuth ''Neural networks toolbox user's guide''

[7-56] D. Reay, T. Green, and B. Williams, "Application of associative memory neural networks to the control of a switched reluctance motor," *in Proc. IECON*, 1993, vol. 1, pp. 200–206.

[7-57] R. Inderka, and R. De Doncker, ''DITC-direct instantaneous torque control of switched reluctance drives,'' *IEEE Transactions on Industry Applications*, vol. 39, no. 4, pp. 1046-1051, July-Aug. 2003.

[7-58] N. Fuengwarodsakul, M. Menne, R. Inderka, and R. De Doncker, ''High-dynamic four-quadrant switched reluctance drive based on DITC,'' *IEEE Transactions on Industry Applications*, vol. 41, no. 5, pp. 1232-1242, Sept.-Oct. 2005.

[7-59] H. Brauer, M. Hennen, and R. De Doncker, ''Control for Polyphase Switched Reluctance Machines to Minimize Torque Ripple and Decrease Ohmic Machine Losses,'' *IEEE Transactions on Power Electronics*, vol. 27, no. 1, pp. 370-378, Jan. 2012.

[7-60] J. Liang, D. Lee, and J. Ahn, ''Direct instantaneous torque control of switched reluctance machines using 4-level converters,'' *IET Electric Power Applications*, vol. 3, no. 4, pp. 313-323, July 2009.

[7-61] H. Zeng, H. Chen, and J. Shi, ''Direct instantaneous torque control with wide operating range for switched reluctance motors,'' *IET Electric Power Applications*, vol. 9, no. 9, pp. 578-585, 11 2015.

*Chapter 8*

*New Off-line SRM Torque Control Function*

*for Torque Ripple and rms Current Minimization*

---

This chapter presents a new torque control function for torque ripple reduction in SRM drives. The new approach is based on maximum utilization of available dc link voltage (either with or without voltage-boosting). The new method extends significantly the zero TR speed range. Moreover, the concept is generalized to cater for more than two phases conducting simultaneously. Simulations are carried on a four phase 8/6 SRM in MATLAB/Simulink and results are demonstrated.

## 8.1 Introduction

TSFs (as illustrated in chapter 7) proved to reliably reduce the TR generated during commutation (when torque production is transferred from an outgoing to an incoming phase). In [8-1] the objective was to optimize linear and sinusoidal TSFs in order to reduce TR along with rms current. However, saturation was neglected and analytical expressions were required to carry out the optimization process. In [8-2], the concept of maximum rate of change of flux linkage was introduced to assess conventional TSFs (linear, sinusoidal, cubic and exponential). It was shown that a low rate of change of flux linkage increases the ripple-free speed range. In addition, optimal values for turn-on and overlap angles were advised. A logical non-linear TSF was proposed in [8-3], with no attention to maximum rate of change of flux linkage. In [8-4], an online TSF was proposed, where the selection between incoming and outgoing phase during commutation is determined based on the value of rate of change of flux linkage. Nevertheless, this method requires a PI controller to compensate the error between the reference and estimated torque. Also, conversion of the torque expression to current expression requires an analytical formula. An offline TSF was presented in [8-5] which offers a trade-off between low rms current and low rate of change of flux linkage. The model requires accurate analytical expressions to derive the current profiles. A DITC based TSF was proposed in [8-6], which requires fewer current sensors. However, the phase current detection accuracy is low. Also, circuit modification along with two

high frequency pwm signals are required for phase current extraction. A hybrid switching mode (a combination between hard and soft switching) was proposed in [8-7] instead of the hard switching mode usually adopted in conventional TSFs. The commutation region is divided into two regions controlled by a torque compensator. In the first region when the incoming phase cannot supply the required torque, the outgoing phase conducts such that the demand torque is met. The opposite is true in the second region. However, there was no illustration of the maximum ripple-free speed range of this method. In [8-8], an off-line TSF based on SRM magnetic characteristics was proposed, where a weighting parameter is adjusted to minimize the rms current, while ensuring that the rate of change of flux linkage is below the dc link voltage, for accurate current tracking.

In the literature, all TSFs have some salient shortcomings which can be summarized as follows:

- All TSFs are limited to one or two phases conducting simultaneously. There was no attempt to investigate TSF performance for more than two phases conducting simultaneously.
- The dc link voltage was not fully exploited which limits the ripple-free speed range.
- Either hard or hybrid switching is required for accurate current tracking, which increases switching losses.
- The methods do not inherently account for the possibility of dc link voltage boosting

To further illustrate these shortcomings, Fig. 8.1 shows the performance of an 8/6 SRM under cos TSF, using a 415 dc link voltage. The motor delivers FLT (25N.m) and rotates at 315rpm. Fig. 8.1a shows the flux linkage waveform, where a heavily non-linear profile is required at phase turn on and off. Fig. 8.1b shows the rate of change of flux linkage which reflects the voltage demand required to generate zero TR. It is clear that at phase turn on and off, and for a short duration, high voltage is required for the current to build up and decay respectively. Fig. 8.1c shows the current profiles which produces zero TR as illustrated in Fig. 8.1d.

Most TSF are inherently based around using that part of the torque-angle profile that produces the highest Nm/A, so as to minimise the rms current, whilst minimising the torque ripple. This high Nm/A region, at low speed, can be used as an assessment basis for comparing the performance of all TSF schemes, as considered in the next section, and forms the basis for the proposed TCF.
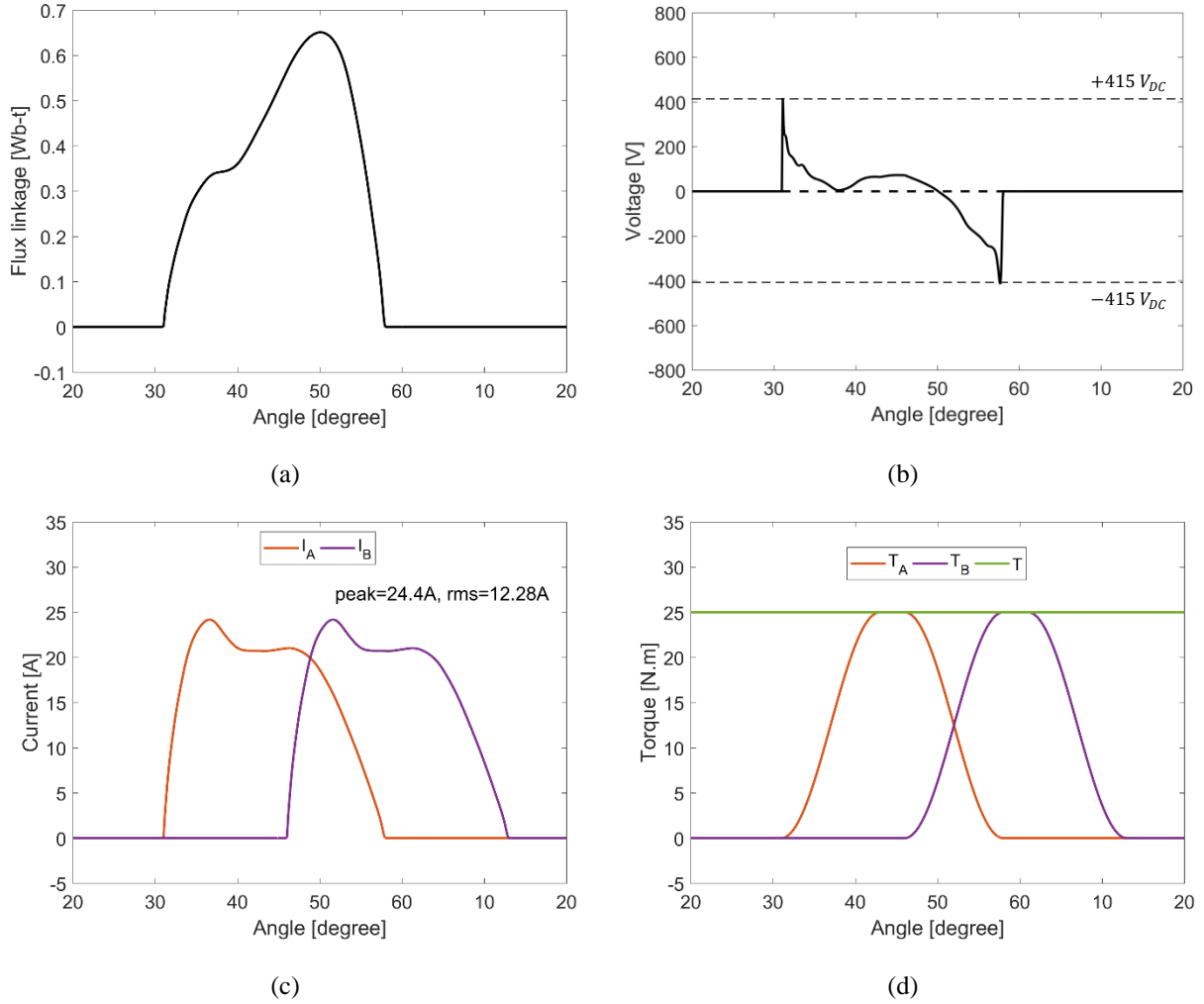
Fig. 8.1 Performance waveforms of SRM at FLT, 415V dc link, and 315 rpm using cos TSF: (a) Flux linkage, (b) Rate of change of flux linkage (voltage demand), (c) Currents, and (d) Torques.

## 8.2   SRM Torque Production Angle Theory

Initially and for the idea case, assume infinite ±V phase terminal voltages are available.

With reference to the 8/6 SRM, specified in Appendix A, positive torque can be produced over a $30^0$ period for each phase, where a $0^0$ to $30^0$ period always over laps sequentially with two adjacent phases, as seen pictorially in Fig. 8.2.

If conduction is decreased from $30^0$ to a continuous $15^0$, $\theta_{0^0}$ to $\theta_{15^0}$, anywhere within the $30^0$ positive torque period, then no phase overlapping torque production occurs and continuous torque

is produced over 360⁰. In Fig. 8.2 phase #1 is followed by phase #2, then phase #3, followed by #4 etc., without any overlap and with contiguous torque.
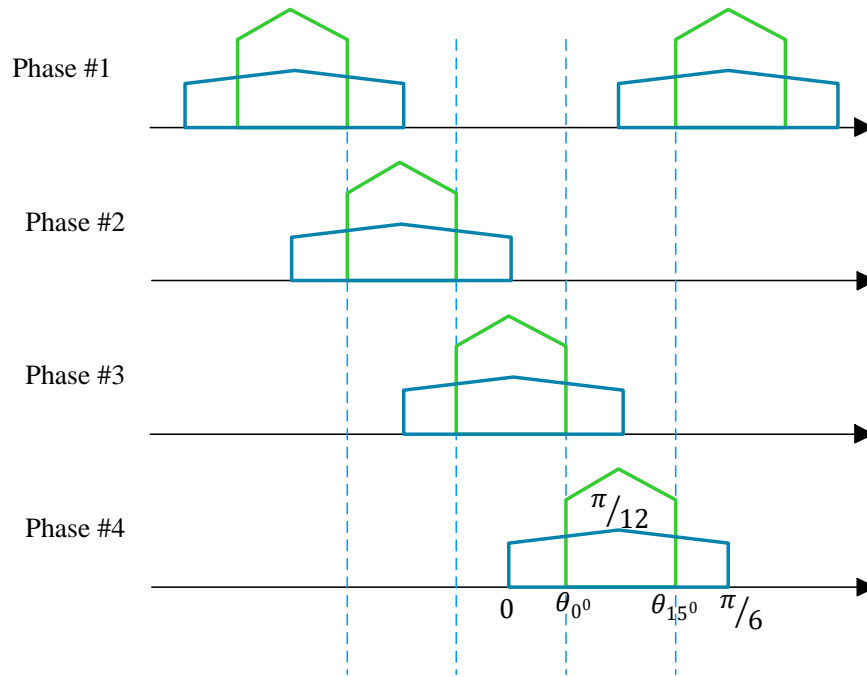


Fig. 8.2 Phase conduction periods, 15⁰ and 30⁰, for positive torque production

If this slide-able 15⁰ period (advance or retard but within 30⁰ positive torque region) is associated with and bounds the region of highest positive Nm/A, typically between 38⁰ and 53⁰ in Fig 8.3, then a given torque is produced with the minimum possible rms current: specifically ripple-free FLT with 11.36A rms, 29.2A peak with the current profile in Fig 8.3c. Being the highest Nm/A region, Fig 8.3c, switching frequency ripple (due to current control of the voltage source converter), will have the highest torque ripple sensitivity, 1 to 1.2 Nm/A at FLT, from Fig 8.3c. This phase current profile is the ideal case, with ideal angles (but infinite voltages). Advancing or retarding the 15⁰ period (away from the optimal angle period) within the 30⁰ positive torque region can still result in continuous ripple free positive torque, although not with minimum rms current.

To create square edged current with infinite $\left|\frac{di}{dt}\right|$ as in Fig 8.3c, with the existence of machine inductance requires infinite voltages, as $V = L\frac{di}{dt}$. But finite available dc link voltage $V_{DC}$ means only trapezoidal type current edges are produced, be they linear, cos, etc. In the cos TSF example in section 8.2, finite voltage, ±415V dc, enabled 315rpm FLT without torque ripple with a phase current of 12.28A rms. As a figure of merit, this 12.28A can be bench marked against

11.36A rms required in the idea square edged case at FLT (11.36A rms is applicable at all speeds). The cos TSF requires an extra 8.1% current, because of realistic voltage constraints. This extra current manifest as 16.9% higher copper losses, whence reduced machine efficiency. This comparison method, 11.36A rms at FLT, 9.4A rms at 0.75FLT, etc. (Fig. 8.3a), will be used to assess the effectiveness of the proposed TCF at all torque levels and at the ripple free rpm limit in each case.
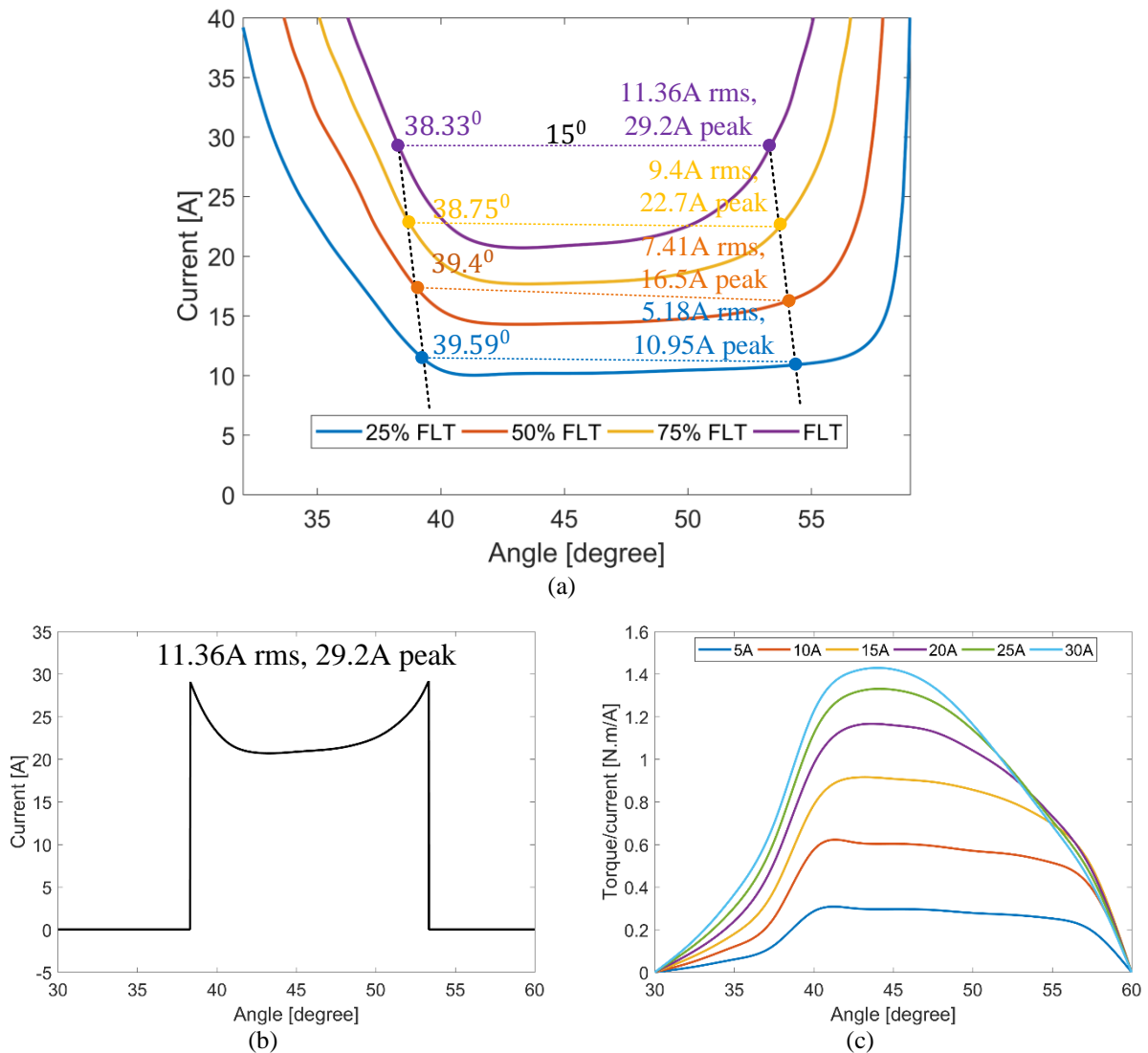


Fig. 8.3 8/6 SRM torque/current characteristics: (a) Current demand at different torque levels, (b) Extracted ideal current for FLT, and (c) Nm/A for different current levels

### 8.3 Proposed off-line torque control function (TCF)

In this section a new offline TCF based on SRM magnetic characteristics is presented. The new TR concept is introduced which divides the torque ripple into two parts, namely;

- Phase commutation torque ripple and
- Switching (PWM/hysteresis) torque ripple.

The proposed TCF for commutation ripple reduction is based on generating a flux linkage profile that fully utilizes the available dc link voltage at both turn-on and turn-off. This flux profile is transformed to a current profile stored in a LUT. The merits of the proposed TCF are:

- The method is suitable for SRM with any number of phases, and stator/rotor pole number.
- The concept of TCF is generalized to include more than two phases conducting simultaneously.
- Maximum utilization of available dc link voltage (either with or without boosting) is achieved at both turn-on and turn-off.
- The SRM maximum speed range with theoretically zero TR (that is, commutation ripple is eliminated, leaving ripple due only to PWM switching) is determined.
- Soft switching control is deployed (as opposed to hard or hybrid switching usually adopted for traditional TSFs), which reduces switching losses.
- The proposed TCF requires switching for only $15^0$ of the conduction period (8/6 SRM), which reduces switching losses.

Two phase conduction modes of SRM operation exist, created to cater for the converter configuration, with three control scenarios within each mode: (8/6 SRM used for illustration)

- Mode #1 - Phase current conduction $\leq 30º$, dependant bridge phase operation as in Fig. 3.5 and/or 3.13: Fig. 8.4 a, b and c.
    - i. Conduction $\leq 30º$ only positive torque, Fig. 8.4a.
    - ii. Conduction $\leq 30º$, turn-on advanced to give initial negative torque, Fig. 8.4b.
    - iii. Conduction $\leq 30º$ turn-on retarded to give final negative torque, Fig. 8.4c.
- Mode #2 - Phase current conduction $> 30º$, four independent phase bridges as in Fig. 3.2: Fig. 8.4 d, e and f.
    - i. Conduction $> 30º$ negative, then positive, then negative torque, Fig. 8.4d.

ii.   Conduction > 30° turn-on advanced, negative, then positive torque, Fig. 8.4e.

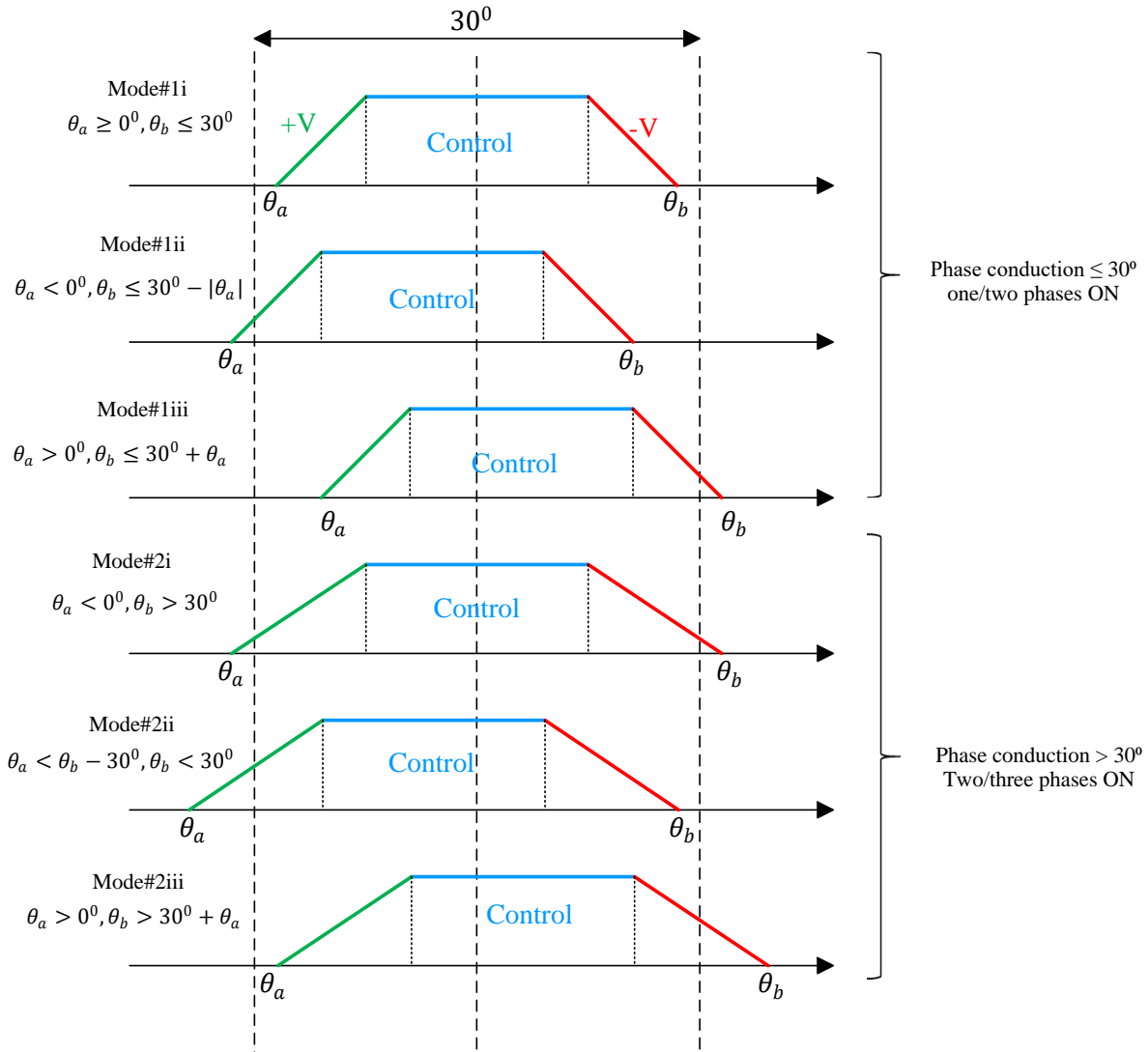iii.   Conduction > 30° turn-on retarded, positive, then negative torque, Fig. 8.4f.



Fig. 8.4 Two current conduction modes giving six conduction possibilities, with one/two phase conduction, ≤30° and two/three phase conduction, >30°, showing periods clamped to +V and -V, and a 15° PWM control region.

In the following sub-sections, the two modes of operation namely; mode 1 and mode 2 are investigated in detail. A four phase 8/6 SRM, with specifications given in Appendix A is used to demonstrate the proposed TCF. The rotor pole pitch and the phase shift for an 8/6 SRM are $60^0$ and $15^0$ respectively. For the SRM under study, the unaligned position is at $30^0$, while the aligned position is at $60^0$, (negative torque 0 to 30°, positive torque 30° to 60°), All the angles are given in mechanical degrees.

146

### 8.3.1 Mode #1 Single/two phase operation

In this mode of operation, either one or two phases (simultaneously) conduct to generate the required torque. A common-phase converter (shown in Fig. 3.13) could be used since the maximum conduction period for each phase is limited, in this mode, to maximum $30^0$. Fig. 8.5 shows the phase torques along with total torque for an arbitrary conduction period ($15^0 < \{\theta_b - \theta_a\} \le 30^0$).
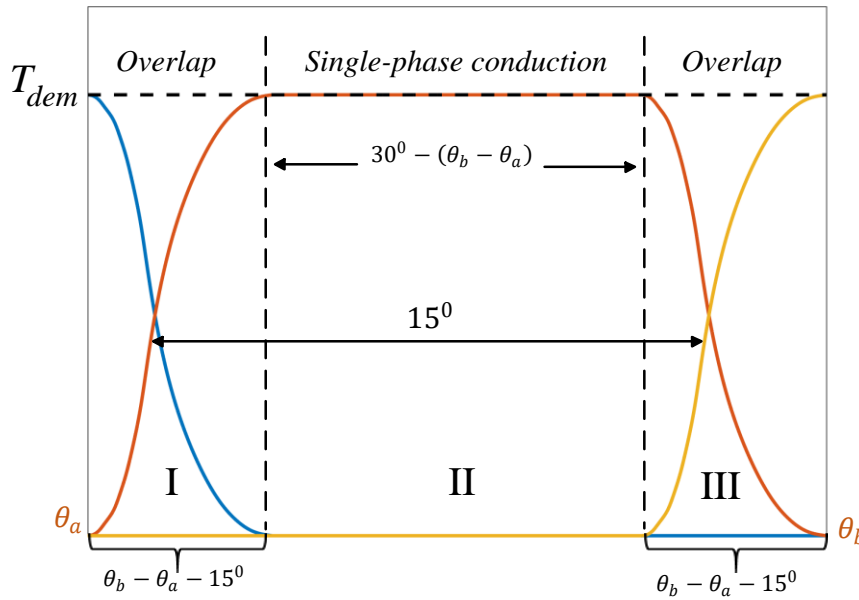


Fig. 8.5 Illustration of the proposed TCF in mode #1

In regions I and III, two phases overlap and produce additively the demand torque, while, in region II only one phase produces the required torque. If the conduction period is $30^0$ (that is, $\theta_a=30^0$ and $\theta_b=60^0$), the second region (II) vanishes and only regions I and III exist. The goal is to generate a phase torque profile which fully utilizes the available dc link voltage, which will offer the widest zero TR speed range. The phase torque profile will be composed of five parts. To illustrate the concept, a numerical example is given with $\theta_a=35^0$ and $\theta_b=55^0$ as shown in Fig. 8.6.

When the incoming phase is at $35^0$, full positive dc link voltage ($+V_{dc}$) is applied (continuously) to this phase for rapid current, and hence torque, build up, portion 1, (in this case the incoming phase is termed the master phase). Simultaneously, the outgoing phase is at $50^0$ (due to a $15^0$

147

phase shift). The outgoing phase generates the rest of the torque so that the torque demand level is reached, portion2, (in this case the outgoing phase is termed the control phase). Thus, the torque profile forming the two portions 1 and 2 is known.
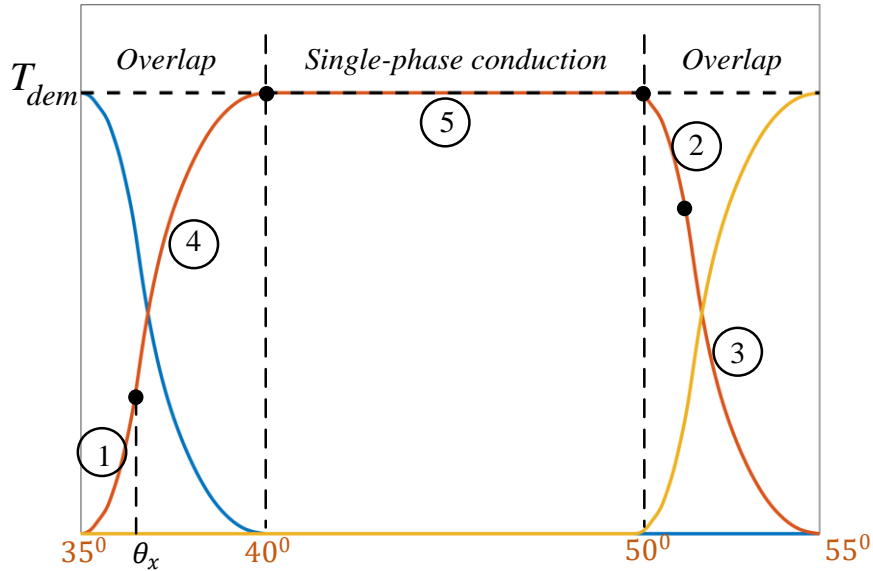


Fig. 8.6 Numerical example Illustrating the proposed TCF in mode #1

When angle $\theta_x$ is reached, the outgoing phase takes precedence, hence the outgoing phase becomes the master phase and full negative dc link voltage $(-V_{dc})$, portion 3, is applied (continuously) for rapid current extinguishing. Simultaneously, the incoming phase becomes the control phase, portion 4, supplies the torque deficiency to maintain the torque demand. Thus, torque portions 3 and 4 are known. Finally, portion 5 is when only one phase conducts to generate the demanded torque. Concatenating the five portions, the phase torque profile is obtained. Table 8.1 demonstrates this process in the overlap region (the single-phase conduction region, 5, is excluded).

Table 8.1 ILLUSTRATION OF PROPOSED TCF DURING OVERLAP

| Phase | Angle | | State | | Voltage | |
|---|---|---|---|---|---|---|
| Incoming | $35^0 \rightarrow 35^0 + \theta_x$ | $35^0 + \theta_x \rightarrow 40^0$ | Master | Control | Fixed $(+V_{dc})$ | Variable |
| Outgoing | $50^0 \rightarrow 50^0 + \theta_x$ | $50^0 + \theta_x \rightarrow 55^0$ | Control | Master | Variable | Fixed $(-V_{dc})$ |

The final step is to calculate the value of $\theta_x^0$ which maximizes the zero TR speed $\omega_n$ $(rpm)$.

Equation (8.1) defines the voltage equation at turn on/off for one SRM phase, neglecting phase winding resistance.

$$\pm V_{dc} = {d\lambda}/{dt} \tag{8.1}$$

where $\lambda$ is the flux linkage. $+V_{dc}$ is applied (continuously) at phase turn-on (portion 1), while $-V_{dc}$ is applied (continuously) at phase turn-off (portion 3).

Integrating (8.1):

$$(\lambda_f - \lambda_i) = \pm V_{dc}t \tag{8.2}$$

where $\lambda_f$, $\lambda_i$ are the final and initial values of flux linkage respectively, while $t$ is time.

At phase turn-on the initial flux linkage of the phase winding is zero. Hence the final flux linkage is calculated by (8.3).

$$\left(\lambda_f\right)_{incoming} = \frac{+V_{dc}(\theta_x^0 - \theta_a^0)}{6\omega_n} \tag{8.3}$$

At phase turn-off the flux linkage must decay to zero at the aligned position. Hence, the final flux linkage is zero and the initial flux linkage is calculated from (8.4).

$$(-\lambda_i)_{outgoing} = \frac{-V_{dc}(\theta_b^0 - 15^0 - \theta_x^0)}{6\omega_n} \tag{8.4}$$

Equations (8.3) and (8.4) are solved iteratively to calculate $\theta_x^0$ and $\omega_n$ ensuring that (8.5) is satisfied.

$$T_{dem} = T\left\{\left(\lambda_f\right)_{incoming}, (\theta_x)\right\} + T\left\{(\lambda_i)_{outgoing}, (15^0 + \theta_x)\right\} \tag{8.5}$$

For the numerical example with demand torque 25Nm, the angle $\theta_x^0$ is 36.65$^0$, $\omega_n$ is 355rpm, $(\lambda_f)_{incoming}$ is 0.32Wb-t and $(\lambda_i)_{outgoing}$ is 0.65Wb-t. The developed phase torques for the incoming and outgoing phases are 10.35Nm and 14.65Nm, respectively, and the rms phase current is 11.63A.

*8.3.2   Mode #2 two/three phase operation*

Fig. 8.7 shows operation in mode #2 were two/three phases conduct simultaneously to produce the required torque.
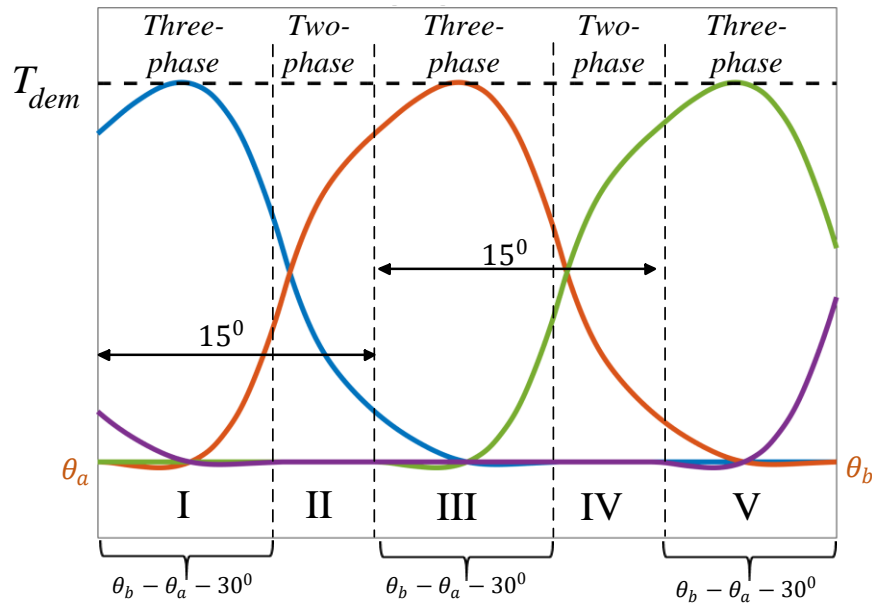


Fig. 8.7 Illustration of the proposed TCF in mode #2

The conduction period is $(30^0 < \{\theta_b - \theta_a\} \le 45^0)$, so periods of negative torque exist. Hence, the common-phase converter (in Fig. 3.13) cannot be deployed and instead a conventional four ASHB converter (in Fig. 3.2) is used. In regions I, III and V three phases conduct simultaneously. In regions II and IV only two phases conduct. A numerical example with $\theta_a$=25$^0$ and $\theta_b$=65$^0$ is given to clarify the concept as shown in Fig. 8.8.

In the three-phase conduction region there are two master phases and one control phase. Full dc link voltage $+V_{dc}$ is applied (continuously) on the incoming phase (Master-1), portion 1, full negative dc voltage $-V_{dc}$ is applied (continuously) on the outgoing phase (Master-2), portion 2. Meanwhile, the middle phase is the control phase which supplies the rest of the demand torque, portion 3. Hence, torque in portions 1, 2 and 3 is determined. The two-phase conduction period gives the remaining portions 4, 5, 6 and 7, specified in mode #1.
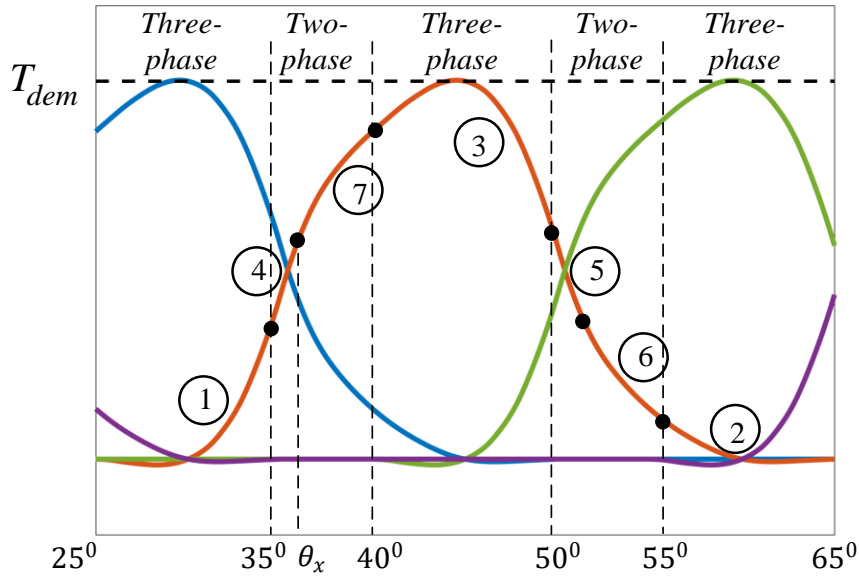


Fig. 8.8 Numerical example Illustrating the proposed TCF in mode #2

For the numerical example with demand torque 25Nm, the angle $\theta_x^0$ is $35.06^0$, $\omega_n$ is 1765rpm, $(\lambda_f)_{incoming}$ is 0.39Wb-t, and $(\lambda_i)_{outgoing}$ is 0.58Wb-t. The developed phase torques for the incoming and outgoing phases are 11.1Nm and 13.9Nm, respectively, and the rms phase current is 14.1A.

## 8.4    Zero TR speed range of the proposed TCF mode #1i

This section investigates the maximum torque ripple-free speed range achieved at different torque demands using the proposed TCF in mode#1i, that is $(15^0 < \{\theta_b - \theta_a\} \le 30^0)$. Results are demonstrated for two cases namely; with and without voltage-boosting.

151

## 8.4.1 Mode #1i without voltage-boosting

A common-phase converter (Fig. 3.13) without voltage boosting is initially deployed. The maximum speed range with zero TR is calculated for 25%, 50%, 75% and 100% FLT.
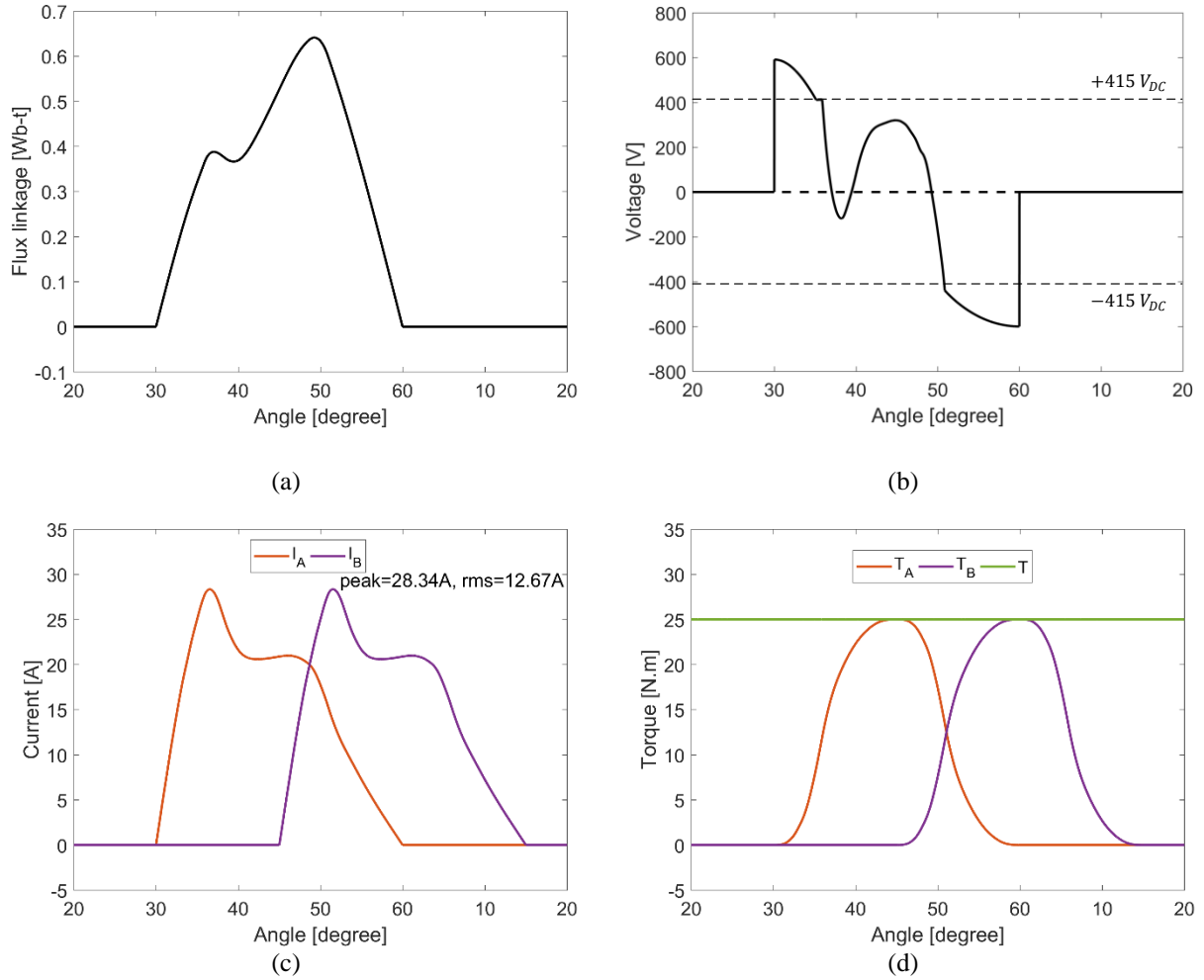


(a)

(b)

(c)

(d)
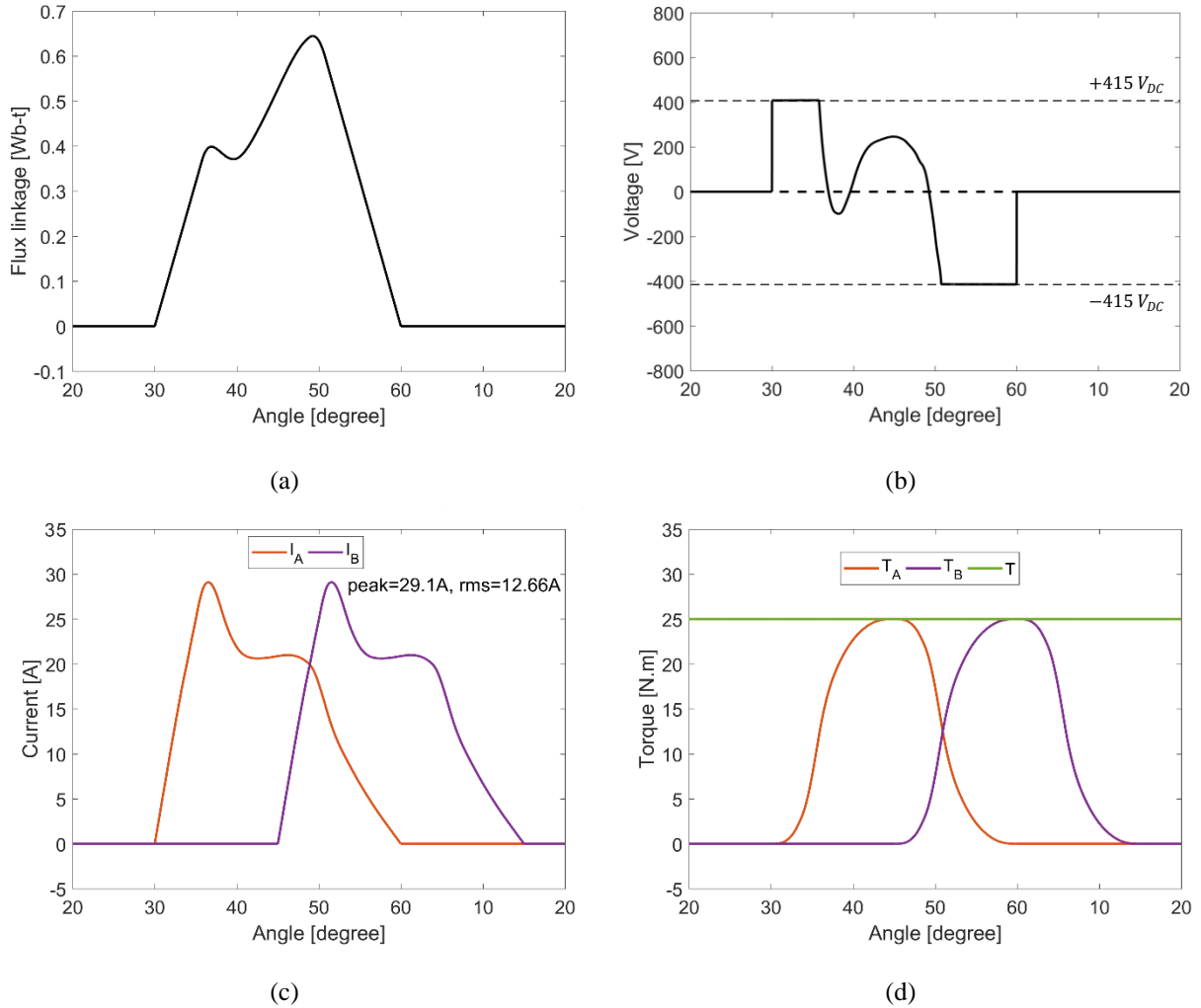
Fig. 8.9 SRM performance at FLT and 1065 rpm using proposed TCF without voltage-boosting:
(a) Flux linkage waveform, (b) Rate of change of flux linkage (voltage demand), (c) Current waveforms, and (d) Torque waveforms.

Fig. 8.9 investigates the proposed TCF at FLT and 1065rpm. The flux linkage profile is shown in Fig. 8.9a, which is linear near the unaligned and aligned positions. This is expected as the full dc link voltage, either positive or negative, is applied (continuously) on the phase winding at turn-on and turn-off respectively, as highlighted in Fig. 8.9b. The full utilization of dc link voltage

improves the zero TR speed range from 315rpm (as in the case of cos TSF) to 1065rpm. The required current profiles are demonstrated in Fig. 8.9c. A slight increase in rms current (12.66A, up from theoretical minimum of 11.36A) is observed (which reflects on the copper loss) as well as an increase in the peak current (which impacts the current rating of semiconductor devices). Finally, torque waveforms are plotted in Fig. 8.9d which shows zero TR operation.

The maximum speed, rms, and peak currents are calculated for different torque demands namely; 25%, 50% and 75% FLT. The results (including FLT) without voltage-boosting are summarized in Table 8.2. The proposed TCF dramatically extends the zero TR speed range at different torque demands. With a FLT base speed of 1500rpm, a zero torque zero ripple FLT at 1065rpm means 71% of the FLT speed range can be torque ripple free. In the case of the cos TSF, at 315rpm, only 21% of the speed range is ripple free.

Not only does the new TCF increase the zero ripple speed, it also reduces the rms current. Fig. 8.13 shows the new TCF requires 11.6A rms for zero ripple at 315rpm while the cos TSF requires 12.28A at the same speed. This represent a 5.5% decrease in rms current, whence a 10.8% decrease in Cu losses at 315rpm.

Table 8.2 PERFORMANCE OF PROPOSED TCF WITHOUT VOLTAGE-BOOSTING AT DIFFERENT TORQUE DEMANDS

| $T_{dem}$ (% FLT) | 100% | 75% | 50% | 25% |
|---|---|---|---|---|
| $\omega_n$ (rpm) | 1065 | 1210 | 1455 | 2045 |
| $I_{rms}$ (A) | 12.66 (11.36) | 10.79 (9.40) | 8.75 (7.41) | 6.18 (5.18) |
| $I_{peak}$ (A) | 29.1 | 24.8 | 20 | 14.25 |
| rms currents in brackets, for comparison, are those theoretically possible with infinite $\pm V_{DC}$ | | | | |

### 8.4.2 *Mode #1i with (45%) voltage-boosting*

Usually the lack of dc link voltage (especially at turn on and off) restrains SRM ripple-free operational speed as highlighted in chapter 7. This sub-section studies the performance limit of the proposed TCF when the SRM is driven by a common-phase converter with voltage-boosting as per Fig. 3.13.
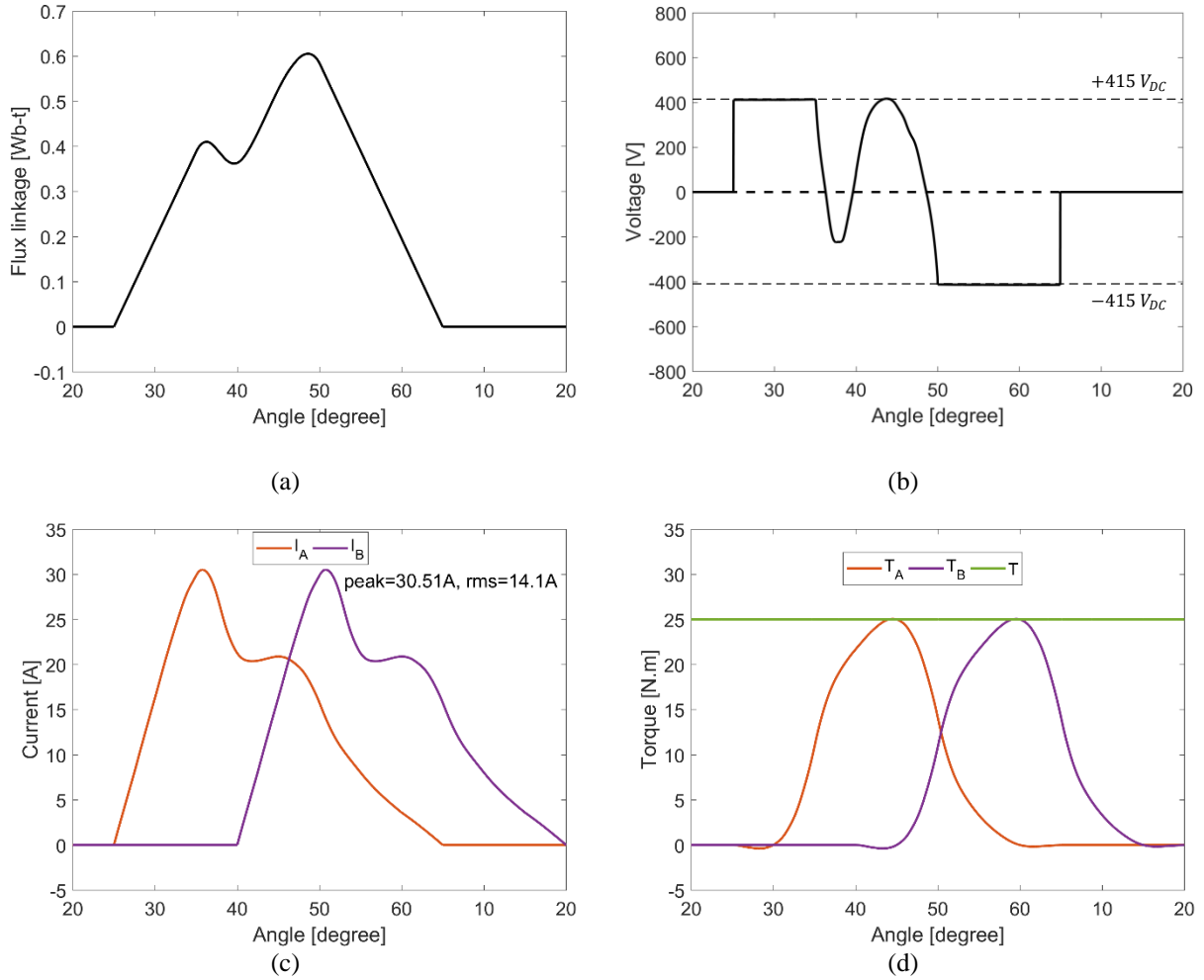
Fig. 8.10 SRM performance at FLT and 1385 rpm using proposed TCF with 45% voltage-boosting:
(a) Flux linkage waveform, (b) Rate of change of flux linkage (voltage demand), (c) Current waveforms, and (d)
Torque waveforms.

Fig. 8.10 highlights SRM TR free performance at FLT and 1385rpm using the proposed TCF with 45% voltage-boosting. The flux linkage profile is shown in Fig. 8.10a. The excess voltage (boost) above the dc link (415V dc), as illustrated in Fig. 8.10b, allows current to build up and decay faster. Hence, the zero TR speed range is improved to 1385rpm. The required current profiles are demonstrated in Fig. 8.10c, while the torque waveforms in Fig. 8.10d shows zero TR operation.

The maximum speed, rms, and peak currents are calculated for different torque demands namely; 25%, 50% and 75% FLT. The results (including the FLT point) are summarized in Table 8.3 for the 45% voltage-boosting case. The proposed TCF significantly extends the zero TR speed range at different torque demands (specifically for FLT: 315rpm for the cos TRF, 1065rpm for the new

154

approach without voltage boost, and 1385rpm with 45% boost). Without voltage boost 71% of the FLT speed range is ripple free, but 45% voltage boosting extends the ripple free range to over 92% (of the non-boost base speed). A vital spin off is the FLT base speed is increase from 1500 rpm (11.6A rms, TR=106%) without voltage boosting to 1790rpm (11.8A rms, TR=90%) with boosting. Torque ripple at base speed (106% versus 90%) is decreased.

Table 8.3 PERFORMANCE OF PROPOSED TCF WITH VOLTAGE-BOOSTING AT DIFFERENT TORQUE DEMANDS

| $T_{dem}$ (% FLT) | 100% | 75% | 50% | 25% |
|---|---|---|---|---|
| $\omega_n$ (rpm) | 1385 | 1520 | 1720 | 2265 |
| $I_{rms}$ (A) | 12.67 (11.35) | 10.79 ( 9.40) | 8.77 (7.41) | 6.18 (5.18) |
| $I_{peak}$ (A) | 28.34 | 24.21 | 19.75 | 14.17 |

rms currents in brackets, for comparison, are those theoretically possible with infinite $\pm V_{DC}$

## 8.5 Zero TR speed range of the proposed TCF mode #2i

To further exploit the proposed TCF, the conduction period can be extended beyond $30^0$, thereby introducing negative torque production. With an increased conduction period, increased rms current can be expected. The common-phase converter (shown in Fig. 3.13) cannot perform this task as each arm incorporates two phases sharing a common switch, so to maintain control of each phase within one bridge, currents should not overlap (conduction ≤ 30º).

To overcome this over-lapping conduction limitation with current conduction of >30º, a four ASHB based converter (shown in Fig. 3.2) is necessary. The ASHB approach offers independent control on each phase for the whole 60º cycle (positive and negative torque periods). Although four ASHBs are required, only two current sensors are needed because of the unique TCF control mode of hard turn-on and turn-off. Specifically the over lapping of current in phases 1 and 3 (2 and 4), with >30º conduction, occurs when no current sensor information is used or needed. The limit of overlap is restricted to a phase conduction period of 45º.

Fig. 8.11 SRM performance at FLT and 1765 rpm using proposed TCF with an ASHB converter:
(a) Flux linkage waveform, (b) Rate of change of flux linkage (voltage demand), (c) Current waveforms, and (d)
Torque waveforms.

Fig. 8.11 shows SRM performance at FLT and 1765rpm. The conduction period is extended to $40^0$. Fig. 8.11a shows the flux linkage waveform, while Fig. 8.11b shows the voltage demand (rate of change of flux linkage). The voltage demand in the control period hits the dc link value which indicates that further improvements in the speed range with zero TR is not possible unless higher dc link voltage is utilized (or dc link voltage-boosting). Due to the conduction period extension (and negative torque), the rms current increases to 14.1A rms as illustrated in Fig. 8.11c. Since, each phase conducts beyond the unaligned/aligned positions, a small negative torque is produced as demonstrated in Fig. 8.11d. The currents are low and the Nm/A is also low around the unaligned position. Consequently, operation can be ripple-free.

156

The maximum speed, rms, and peak currents are calculated for different torque demands namely; 25%, 50% and 75% FLT. The results are summarized in Table 8.4 for operation with an ASHB converter. The zero TR speed range is improved to 1765rpm with a slight increase in rms current.

Table 8.4 PERFORMANCE OF PROPOSED TCF USING ASHB CONVERTER AT DIFFERENT TORQUE DEMANDS

| $T_{dem}$ (% FLT) | 100% | 75% | 50% | 25% |
|---|---|---|---|---|
| $\omega_n$ (rpm) | 1765 | 1785 | 2040 | 2600 |
| $I_{rms}$ (A) | 14.1 (11.36) | 11.7 (9.40) | 9.4 (7.41) | 6.5 (5.18) |
| $I_{peak}$ (A) | 30.51 | 26.2 | 21 | 14.75 |

rms currents in brackets, for comparison, are those theoretically possible with infinite $\pm V_{DC}$

The 4 bridges can be used and controlled with 2 current sensors, because commutating phases can be held hard on or off. But although commutation ripple free operation can be produced up to 1765rpm, the incurred control restrictions undesirably increase the rms current from 12.67 A (with 4 current transducers, in Table 8.4) to 20.5A rms.

When the SRM operates at low speeds, the dc link voltage does not pose any limitation on SRM ripple-free operation. Hence, it is necessary to produce a current profile which minimizes the rms current.
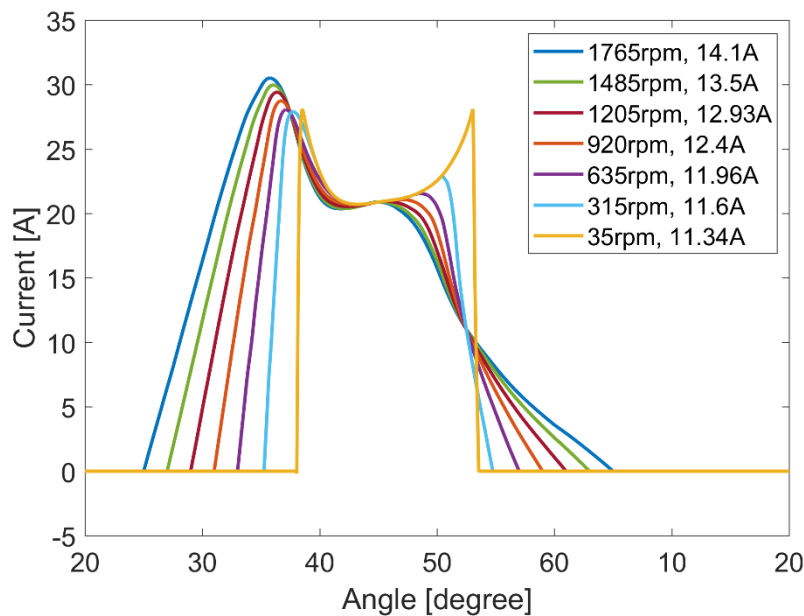


Fig. 8.12 Current profiles at FLT and different speed limits

157
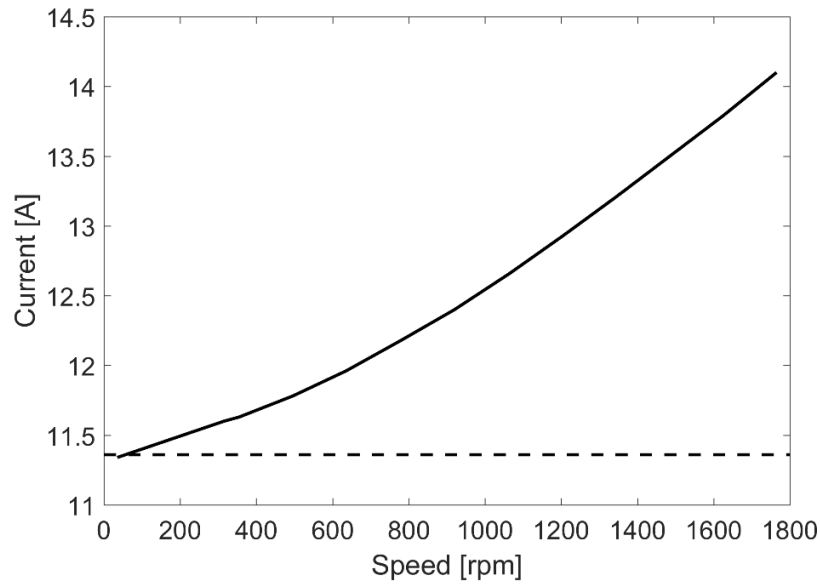
Fig. 8.13 Current (rms) at different speeds
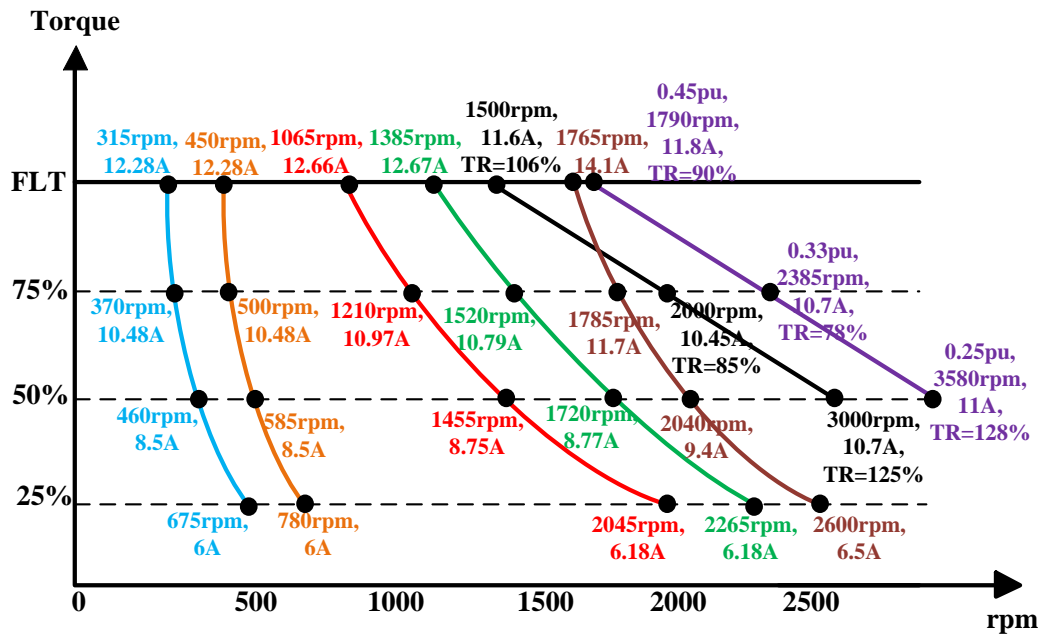


Fig. 8.14 SRM torque/speed characteristics:
Cos TSF, No boost 415Vdc   Cos TSF, Boost 415Vdc + 185Vdc
Proposed TCF, No boost 415Vdc   proposed TCF, Boost 415V dc+185Vdc
Proposed TCF, ASHB, No boost 415V dc
SRM standard control, No boost 415Vdc   SRM standard control, Boost 415V+185V dc

158

Fig. 8.12 shows different current profiles for different zero TR speed ranges, where each current profile satisfies specific discrete FLT operating speeds. Importantly as speed decreases the conduction period decreases toward 15º, the wave shape (315rpm in Fig 8.12) asymptotes to the idea squared-edged reference current shown in Fig. 8.3b, with an rms value of 11.36A.

Any rms current convergence error is due to the different ways of utilizing and interpolating the discrete data produced by FEA of the SRM. As speed increases, the conduction period is extended resulting in an increase in rms current as shown in Fig. 8.13. Improvements in the zero TR speed range and base speed are summarized (from previous tables in this chapter) in Fig. 8.14.

## 8.6    Simulation results

In the previous sections, a new TCF was proposed which eliminates TR during phase commutation. The results were produced using an ideal current source (no semiconductor switching). However, when tracking the generated current profiles with a voltage source converter, another form of TR appears due to switching which produces current ripple (whence torque ripple which will be termed switching $TR_{sw}$, as opposed to commutation $TR_{com}$). In this section, SRM dynamic performance using the proposed TCF is investigated and the effect of voltage switching (current ripple) on the generated TR is discussed. The current is sampled at 200kHz and the hysteresis band is 0.3A (specification parameters well within the bounds of flux gate current measurement technology).

Fig. 8.3 indicates that the torque sensitivity is in excess of 1Nm/A in the high torque producing region of the 30º period. Within the 0.3A hysteresis band, ripple torque (peak to peak) of in excess of 0.3Nm can be expected. At 25Nm, this represents 1.2% ripple, but lower torque levels, 0.3Nm of switching ripple may not be insignificant, particular given the rotation torque being produced is ripple free.

### 8.6.1    *SRM in-circuit performance using proposed TCF mode #1i without voltage-boosting*

In this subsection, results of the proposed TCF without voltage-boosting are presented at FLT and 25% of FLT. Fig. 8.15 represents the performance at FLT and 1065rpm. The rate of change of flux linkage (voltage demand) is illustrated in Fig. 8.15a along with the actual phase voltage.  During

turn-on and turn-off there is no switching since the voltage is in continuous $\pm V_{DC}$ modes. Hence, switching ripple is zero and advantageously, no switching losses occur. Prior knowledge of the required voltage demand allowed using soft switching control. When the voltage demand is positive, the upper switch is on and the lower switch is controlled (switched). On the other hand, when the voltage demand is negative, the upper switch is off while the lower switch is controlled (switched). This further reduces the switching action. In conventional TSFs, where the voltage demand is not determined, hard/hybrid switching is a must to guarantee good current tracking.



(a)

(b)

(c)
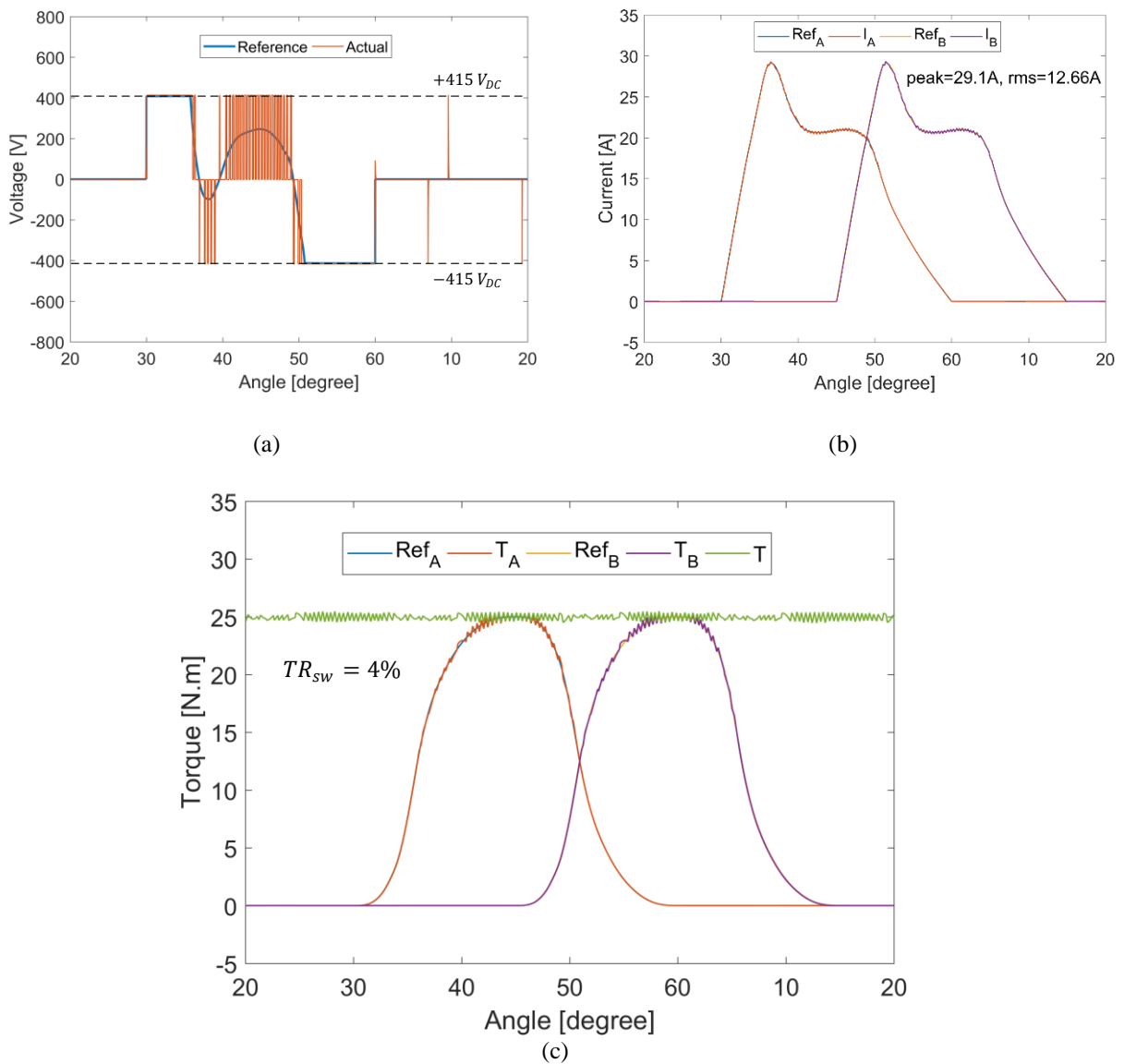
Fig. 8.15 SRM performance at FLT and 1065rpm using proposed TCF without voltage-boosting:
(a) Rate of change of flux linkage (voltage demand), (b) Current waveforms, and (c) Torque waveforms

Fig 8.15b demonstrates the actual and reference phase currents showing excellent tracking at the unaligned and aligned positions. The phase torques along with the total developed torque are illustrated in Fig. 8.15c. A 4% $TR_{sw}$ is recorded, solely due to switching ($TR_{com}$ due to commutation is completely eliminated).

SRM performance using the proposed TCF without voltage-boosting can be assessed at lower torque demands, specifically 25% FLT and 2045rpm, as highlighted in Fig. 8.16.



(a)

(b)

(c)
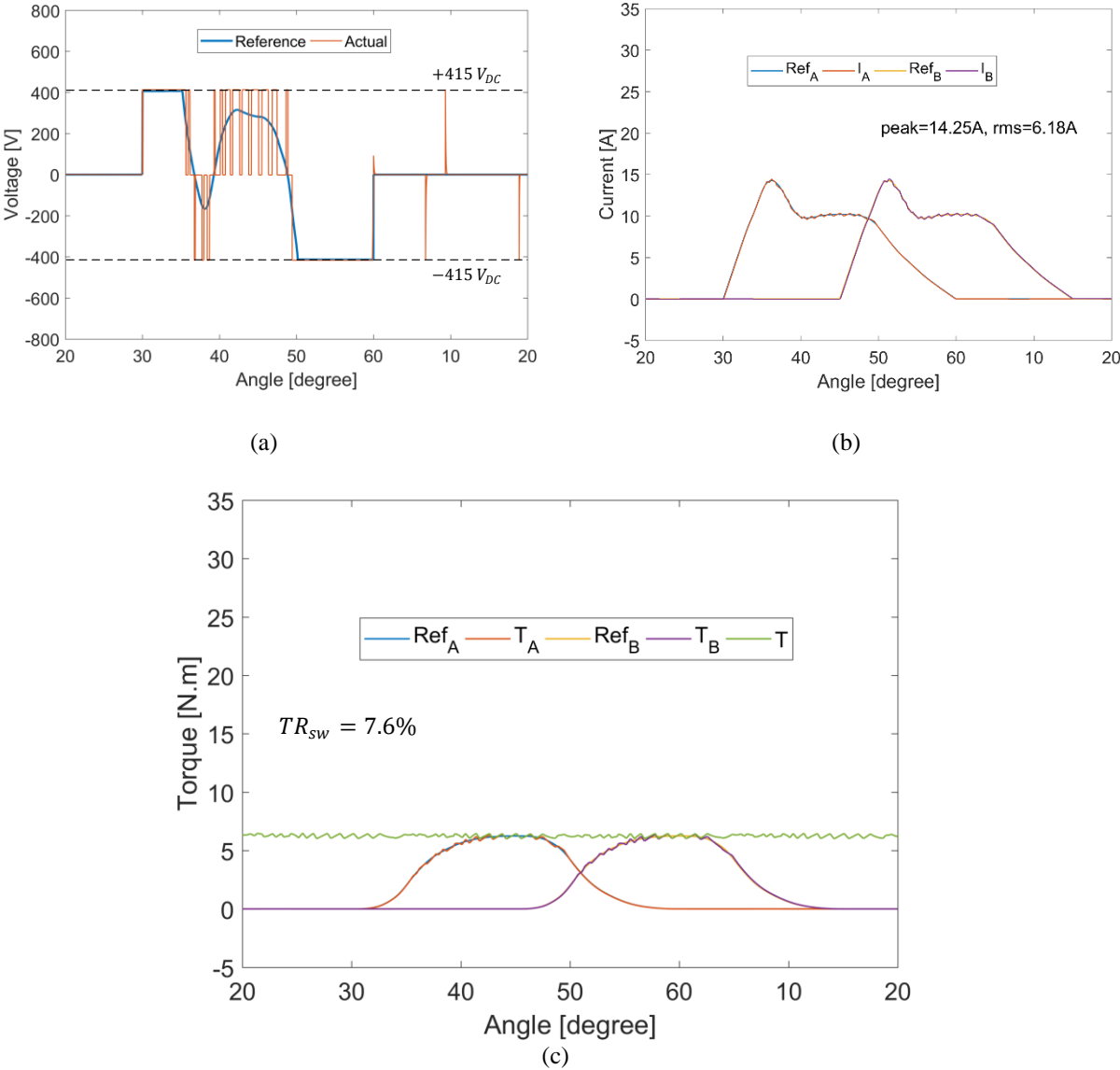
Fig. 8.16 SRM performance at 25% FLT and 2045rpm using proposed TCF without voltage-boosting:
(a) Rate of change of flux linkage (voltage demand), (b) Current waveforms, and (c) Torque waveforms

161

Reducing the torque demand to 25% FLT results in around 50% reduction in current level. Hence, the selected 0.3A band is wide for this low torque demand which reflects on the $TR_{sw}$ recording being 7.6%, shown in Fig. 8.16c.

## 8.6.2    *SRM in-circuit performance using proposed TCF mode #1i with 45% voltage-boosting*



(a)

(b)

(c)
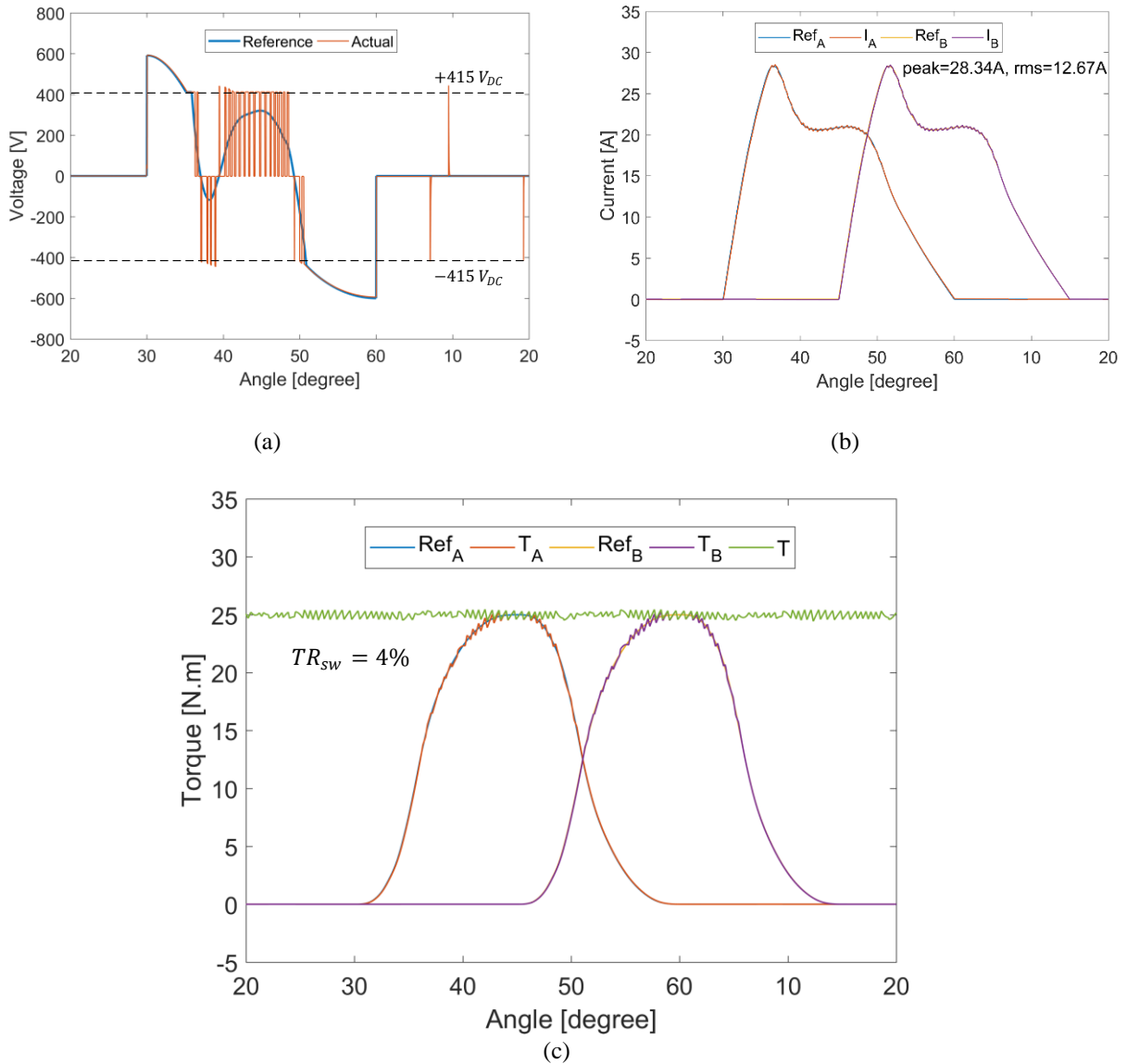
Fig. 8.17 SRM performance at FLT and 1385rpm using proposed TCF with 45% voltage-boosting:
(a) Rate of change of flux linkage (voltage demand), (b) Current waveforms, and (c) Torque waveforms

SRM performance using the proposed TCF, and the common-phase converter with voltage-boosting, with FLT at 1385rpm gives the results in Fig. 8.17. Boost-capacitors of 47.5μF, giving 45% boost-voltage, are deployed. Fig. 8.17a shows the demand voltage along with actual voltage, where the boost-voltage is observed. Current waveforms are demonstrated in Fig. 8.17b, while the torque waveforms in Fig. 8.17c shows a 4% $TR_{sw}$.



(a)



(b)



(c)
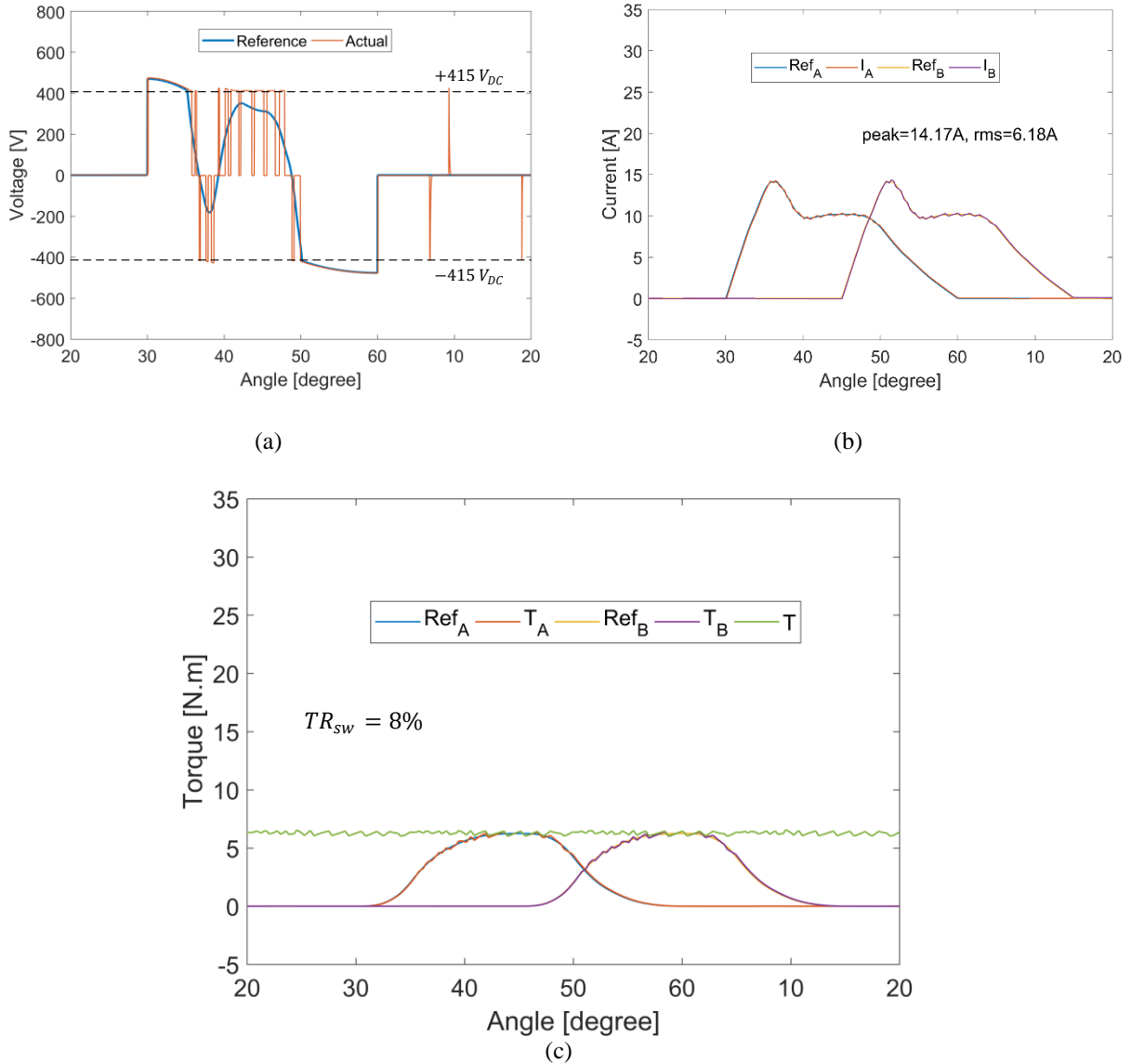
Fig. 8.18 SRM performance at 25% FLT and 2265rpm using proposed TCF with 15% voltage-boosting: (a) Rate of change of flux linkage (voltage demand), (b) Current waveforms, and (c) Torque waveforms

163

Performance at 25% FLT and 2265rpm is shown in Fig. 8.18. Since the torque demand, and hence the phase current level, is reduced, the increase in boost-voltage is limited to only 15% (as opposed to 45% in case of FLT) as shown in Fig. 8.18a. Relevant current and torque waveforms are illustrated in Fig. 8.18 parts b and c respectively, showing 8% $TR_{sw}$.

### 8.6.3   *SRM in-circuit performance using proposed TCF mode #2i (ASHB converter)*



(a)

(b)

(c)
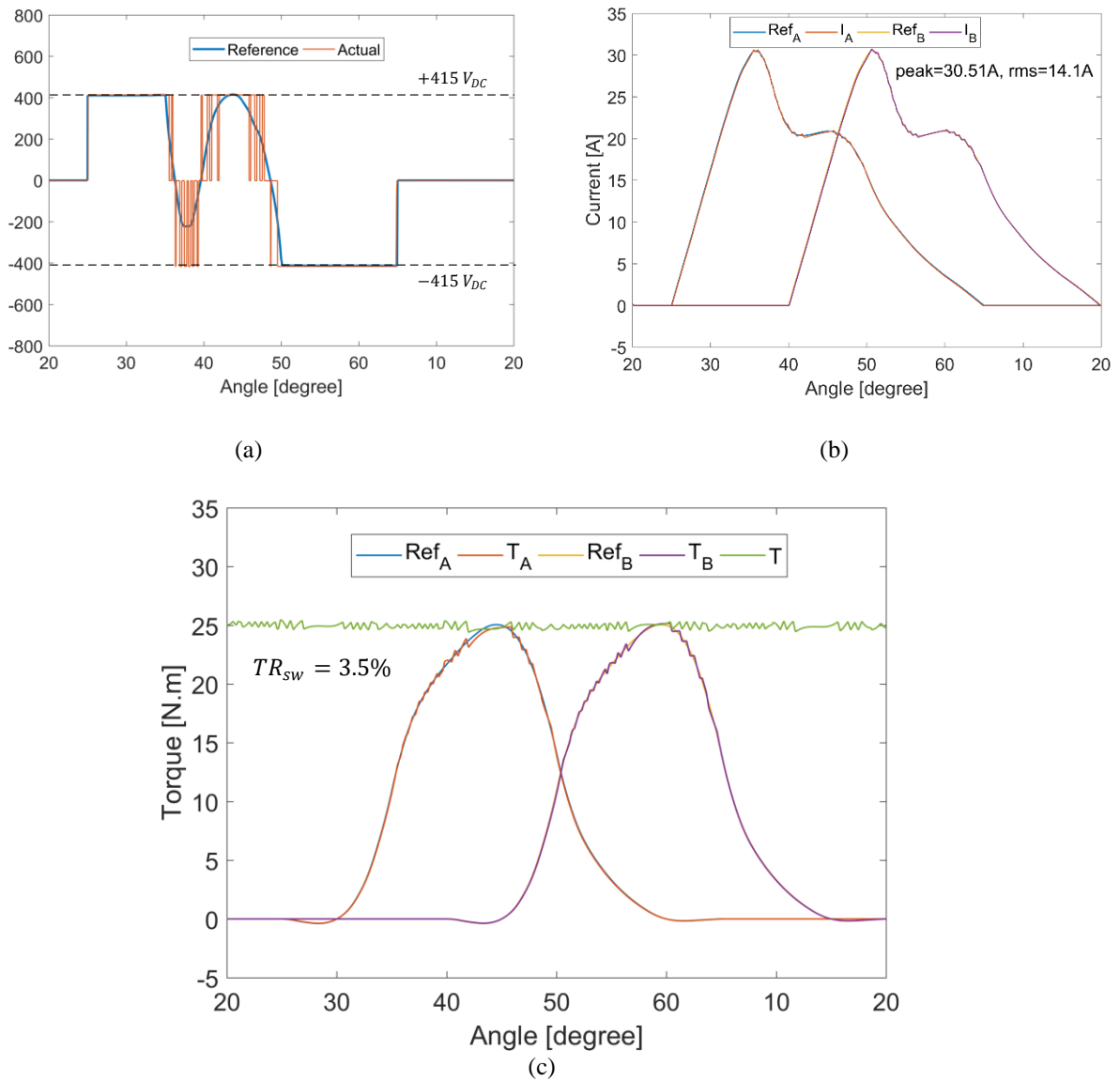
Fig. 8.19 SRM performance at FLT and 1765rpm using proposed TCF, ASHB:
(a) Rate of change of flux linkage (voltage demand), (b) Current waveforms, and (c) Torque waveforms

164

As indicated in section 8.5, a conduction period beyond $30^0$ can significantly extend the zero $TR_{com}$ speed range, but at the expense of higher RMS phase currents. The common-phase converter cannot be used and instead the conventional four ASHB converter is used. In this subsection the performance at FLT and at 25% FLT is investigated. Fig. 8.19 shows SRM performance at FLT and 1765rpm (where $TR_{com}$ is zero).



(a)

(b)



(c)
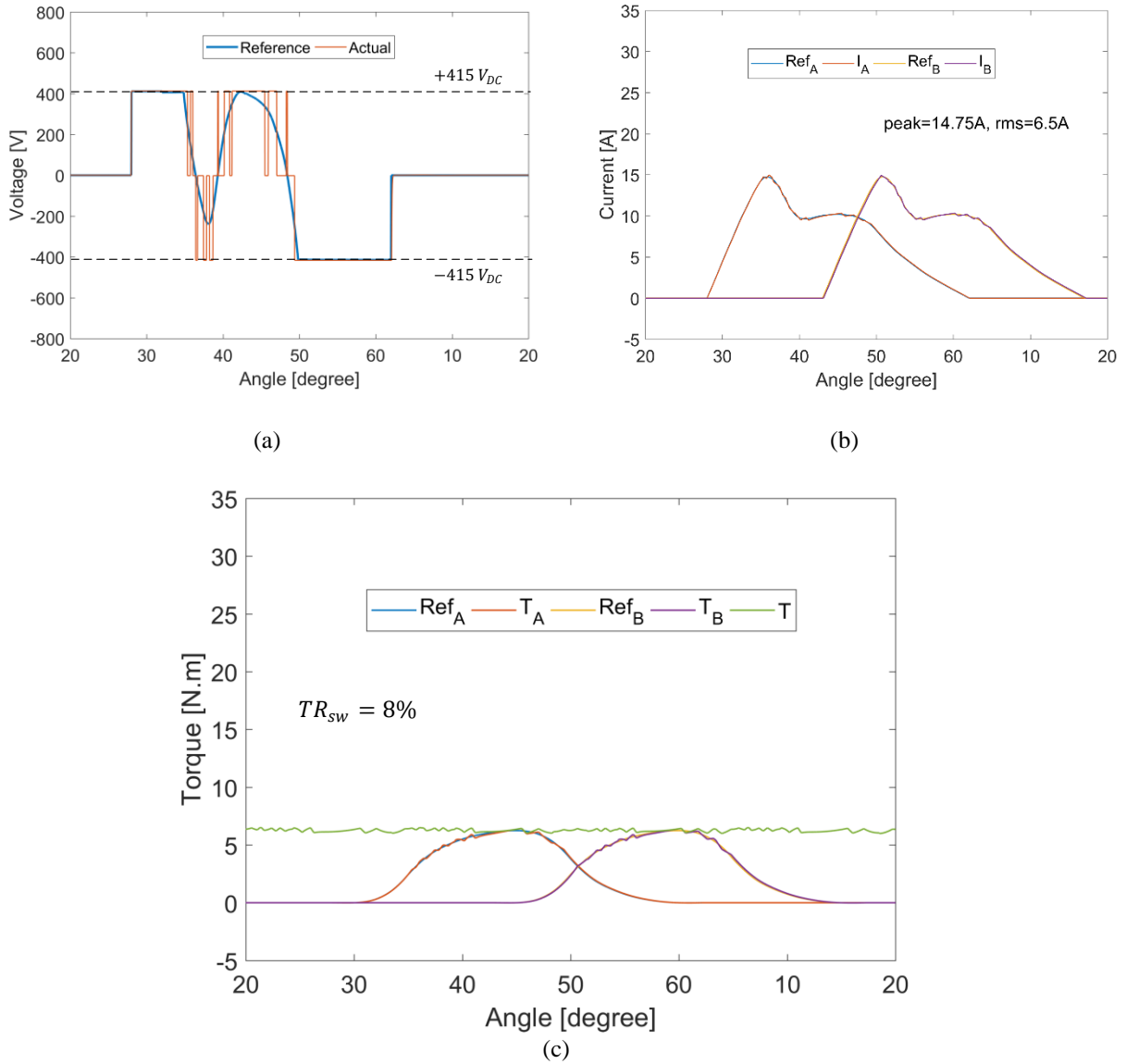
Fig. 8.20 SRM performance at 25% FLT and 2600rpm using proposed TCF, ASHB:
(a) Rate of change of flux linkage (voltage demand), (b) Current waveforms, and (c) Torque waveforms

The voltage demand in the control region reaches the dc link voltage level as shown in Fig. 8.19a revealing that further improvement in zero TR requires higher dc link voltage. Switching in the control region is reduced, thereby decreasing switching losses. Current and torque waveforms are demonstrated in Fig. 8.19 parts a and b respectively showing 3.5% $TR_{sw}$.

Finally, SRM performance at 25% FLT and 2600rpm (at zero $TR_{com}$) is illustrated in Fig. 8.20, with 8% $TR_{sw}$. The relatively high values of switching torque ripple at low torque levels, indicate the importance of a narrow hysteresis band. Flux gate current transducers offer 0.01% accuracy and linearity, with the necessary 1dB bandwidth, but at a financial cost.

## 8.7 Discussion

The study presented in the previous sections focused on the operation of the proposed TCF in modes 1i and 2i (that is the conduction period is centered at $45^0$). The selection of this specific position was intuitive, given that $45^0$ has the highest N.m/A at rated condition as in Fig. 8.3c. Moreover, $45^0$ is the midway between unaligned and aligned position, so for $30^0$ conduction period the operation will be confined in the positive torque production region. However, the operation in modes ii, and iii (that is advancing or retarding the conduction period) was not investigated which may result in degradation/improvement in performance regarding the maximum zero TR speed range and peak/rms phase current.

In addition, the calculated zero $TR_{com}$ speed limits calculated in the previous sections was based on neglecting the stator phase winding resistance. Nevertheless, the account for resistance (especially at FLT, whence maximum current) would impact the available voltage (due to resistive voltage drop). Hence, affecting the maximum zero $TR_{com}$ speed limit.

Moreover, the operation of the proposed TCF above the maximum zero $TR_{com}$ speed range up to the base speed was not investigated.

Finally, when conventional square wave current profiles are used at low speeds (that is in CCC mode), the SRM suffers from commutation torque ripple. However, the average developed torque will be higher than the developed torque obtained using the proposed current profile (provided the square wave current profile and the proposed current profile have the same rms value). The gain

in the average developed torque along with the generated torque ripple are assessed and compared with the proposed results. This section covers all these four aspects.

### 8.7.1 *Effect of turn on angle (advancing/retarding the conduction period)*

The maximum speed in section 8.4 employed a 30º conduction period between 30º and 60º, that is mode #1i, with a 12.66A rms phase current at 1065rpm and FLT.
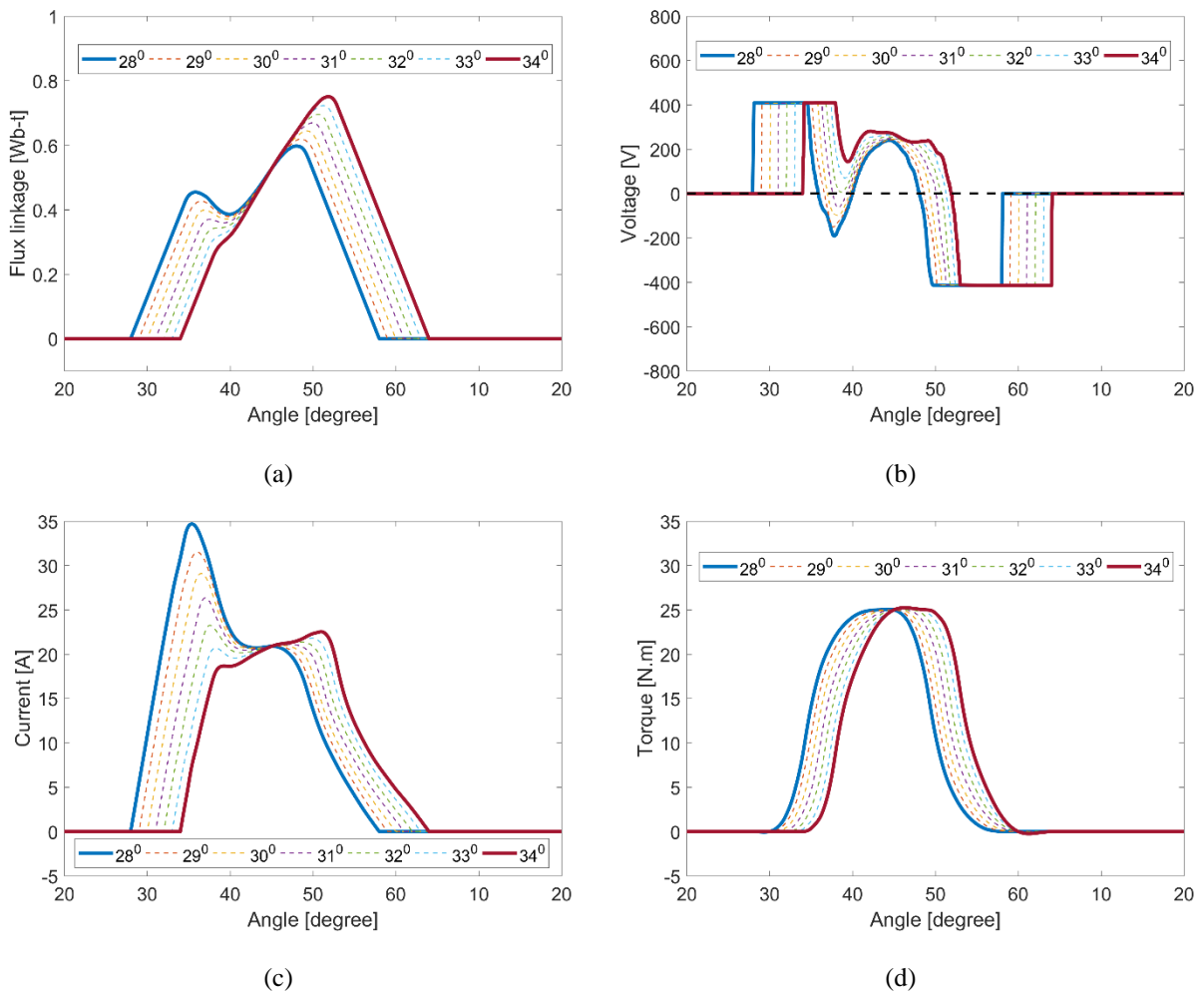


(a)

(b)

(c)

(d)

Fig. 8.21 Effect of turn on angle: (a) Flux linkage waveform, (b) Rate of change of flux linkage (voltage demand), (c) Current waveforms, and (d) Torque waveforms

Table 8.5 RESULTS FOR $30^0$ PHASE CONDUCTION WITH DIFFERENT TURN ON ANGLES

| $\theta_{on}$ ($^0$) | Speed (rpm) | rms (A) | Peak (A) | Current at $60^0$ (A) |
|---|---|---|---|---|
| 28 | 1055 | 14.2 | 34.7 | 0 |
| 29 | 1055 | 13.35 | 31.5 | 0 |
| 30 | 1065 | 12.66 | 29.1 | 0 |
| 31 | 1065 | 12.1 | 26.4 | 1.22 |
| 32 | 1065 | 11.65 | 23.25 | 2.42 |
| 33 | 1060 | 11.4 | 21.8 | 3.6 |
| 34 | 1055 | 11.29 | 22.55 | 4.77 |

By advancing and retarding the 30º conduction period, negative torque production is introduced as shown in Fig. 8.21d, but as Table 8.5 and Fig. 8.21c show, with a 2º retard of turn-on angle, the same zero ripple speed limit of 1065rpm at FLT can be reached, but with the rms phase current reduced from 12.66A to 11.65A (and with a reduced peak current, from 29.1A to 23.25A). This rms current reduction represents a copper loss reduction of 16%. The current at alignment (shown in Table 8.5), represents a component adding to radial forces. Moreover, Fig. 8.21c shows that advancing the turn on angle results in a slight reduction in maximum zero $TR_{com}$ speed with a significant increase in peak/rms current. Finally, retarding the turn on angle shifted the voltage demand in the control region above 0V as demonstrated in Fig. 8.21b. Hence, soft switching only between 0V and $+V_{DC}$ is required. (no $-V_{DC}$ loop is required).

### 8.7.2 Effect of phase winding resistance

This sub-section investigates the impact of accounting for the phase winding resistance on the performance of SRM under the proposed TCF. Fig. 8.22 compares the results with and without resistance at FLT, $30^0$ conduction without voltage-boosting.

Ignoring phase winding resistance results in a 1065rpm maximum zero $TR_{com}$ speed limit as in section 8.4i. However, when accounting for copper winding resistance this limit reduces to 1045rpm. This 2% speed reduction is due to the resistive voltage drop which slightly reduces the applied phase voltage during the continuous applied voltage periods, as illustrated in Fig. 8.22b. Other waveforms (flux linkage, current and phase torque) are almost identical as shown in Fig. 8.22. parts a, c and d respectively.

(a)

(b)

(c)

(d)
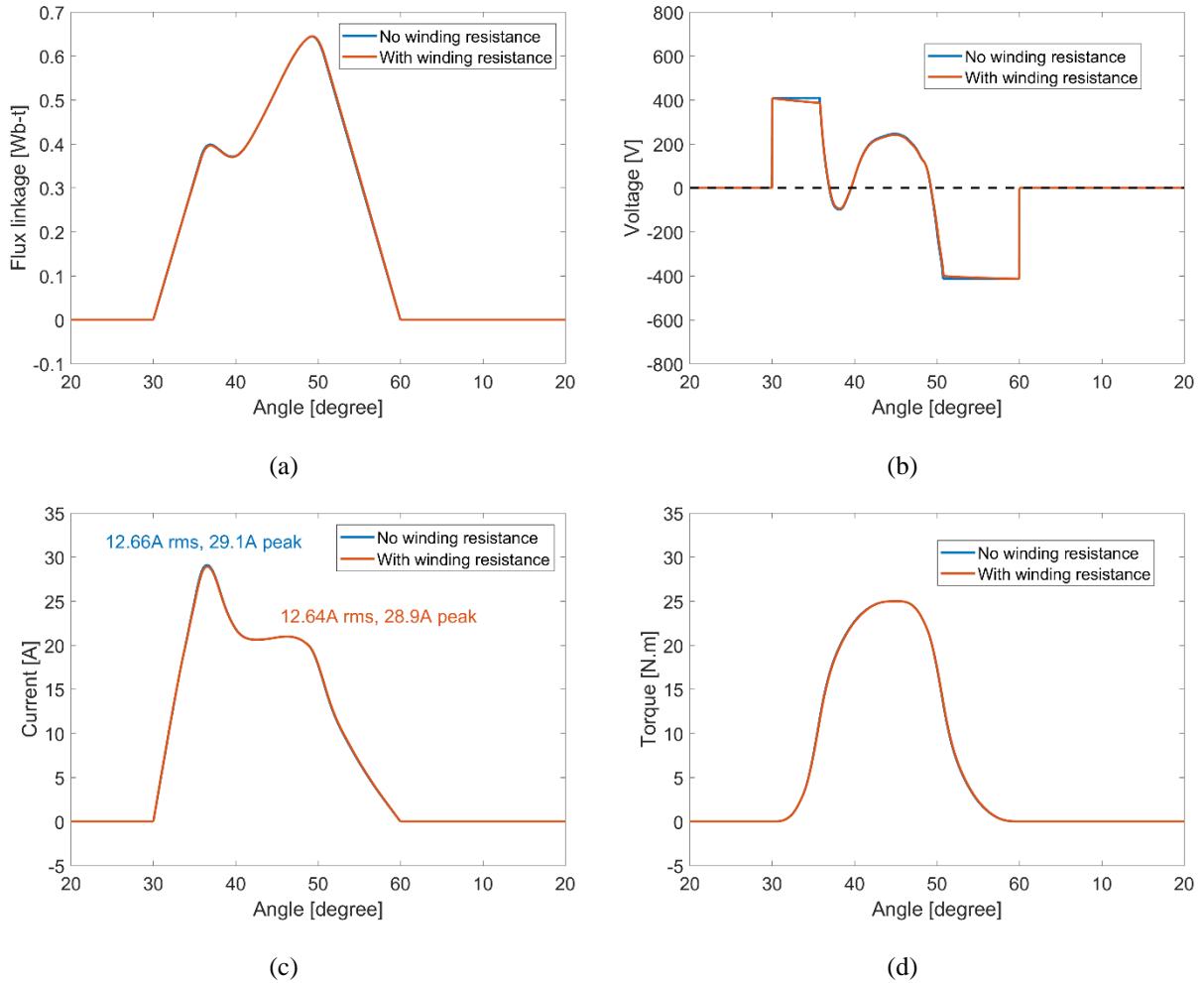
Fig. 8.22 Effect of phase winding resistance: (a) Flux linkage waveform, (b) Rate of change of flux linkage (voltage demand), (c) Current waveforms, and (d) Torque waveforms

### 8.7.3   *Operation between maximum zero $TR_{com}$ speed limit and base speed*

The SRM can have ripple-free operation from zero up to the maximum zero $TR_{com}$ speed limit using the proposed TCF as presented in the previous sections. However, the performance between the maximum ripple-free speed and the base speed should be explored. This sub-section discusses this aspect. The maximum ripple-free speed limit at FLT, without voltage-boosting and with $30^0$ conduction is 1065rpm (as given in sub-section 8.4i). The generated current profile is used to feed the SRM when operating at base speed (1500rpm). A high switching frequency is used to exclude the switching ripple.
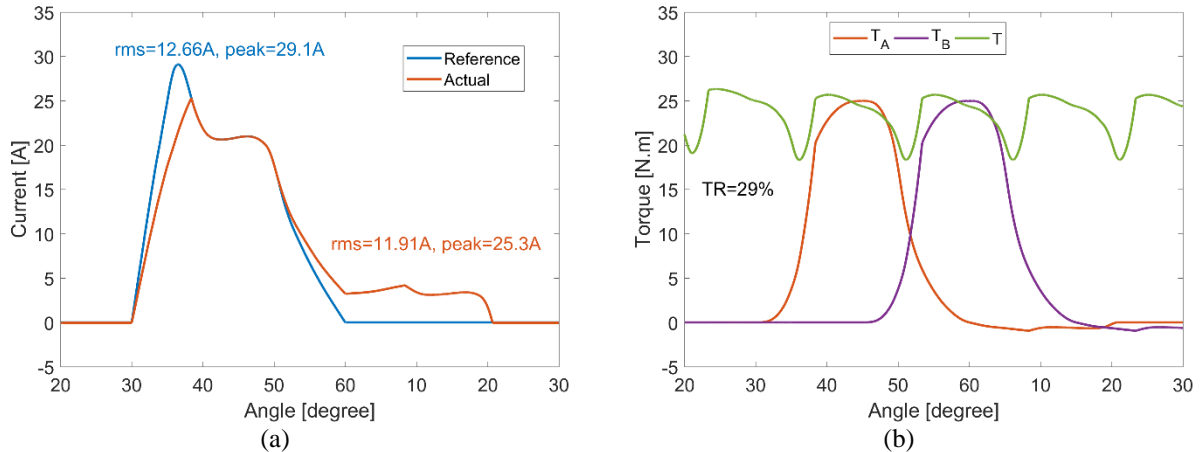
Fig. 8.23 Performance of SRM at base speed using proposed TCF: (a) Current waveforms, and (b) Torque waveforms

Fig. 8.23 demonstrates SRM performance in this case. Fig. 8.23a shows that phase current is unable to track the reference current at turn on and off due to the lack of dc link voltage (the voltage demand at turn on/off increases to $\pm 415\ X\ \frac{1500}{1065}$). The lack of dc link voltage, along with using a common-phase converter result in an extension in the conduction period. Fig. 8.23b shows the torque waveforms revealing 29% TR due to commutation. Based on Fig. 8.14, the proposed TCF reduces the commutation TR from 106% (when conventional control method is deployed) to 29%. But, the rms current increases from 11.6A to reach 11.91A using the proposed TCF.

### 8.7.4 Operation at low speeds with square wave current profiles

In this subsection a comparison is presented between Srm performance at low speed fed by conventional square wave current profiles and the proposed current profiles. The comparison highlights the effect on developed torque and torque ripple.

Fig. 8. 24a compares two current profiles, the first is the conventional square wave profile used at low speeds in the CCC mode while the second is the proposed current profile as per Fig. 8.12. Both current profiles have the same rms value of 11.36A and hence the same thermal operating conditions (the proposed profile has higher peak value). Fig. 8.24b shows that the proposed current profile generates 25N.m average torque with zero commutation TR. But the square wave current

170

profile produces 26N.m average torque (that is a 4% torque gain) however, with severe commutation TR reaching 48%.
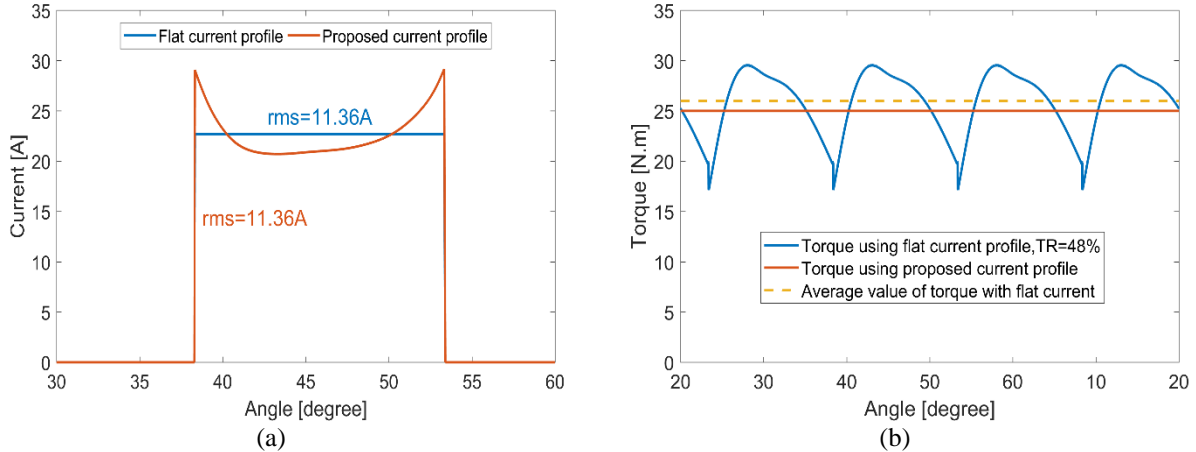


Fig. 8.24 Performance of SRM at low speed using square wave and proposed current profiles: (a) Current waveforms and (b) Torque waveforms

It must be noted that the proposed TCF generates current profiles based on magnetic data of SRM. The magnetic characteristics are obtained either experimentally or by FEA by exciting one stator phase. Hence, the effect of mutual coupling, different flux path lengths and any machine asymmetry are not accounted for. However, these initial current profiles, stored on controller memory, can be fine-tuned.

The SRM can be bench tested in a high performance test rig using a high accuracy converter (switching frequency well above 100kHz with SiC switches thus ensuring near zero switching ripple) along with precise torque and position measurement. This single high precision test bench will be expensive, but more precise profile will result that account modelling deficiencies.

Different torques and speeds can be tested and assessed. One of the main advantages of the proposed TCF is that at any instant only one phase (with high Nm/A) needs to be controlled. For each test point the angle dependant single controlling phase current is slightly adjusted to eliminate any detected TR. The stored current profiles data is updated. Long and short flux paths may mean that not each phase is fed with the identical current profile. Nevertheless, the method of storing data can account for this.

Finally, it is assumed that all SRM produced are identical. In EV production every 1000th SRM (for example) may be test to see if manufacturing changes have occurred.

## 8.8 Summary

A new TCF has been proposed and investigated, which exploits maximum utilization of dc link voltage at phase turn-on and turn-off. This extends the zero TR speed range significantly. The new TCF is suitable for any SRM with any number of phases and stator/rotor pole number. Only magnetic characteristics (either obtained using FEA or experimentally) are needed. The proposed TCF is characterized by low switching losses as no switching is required for up to half the conduction period. In addition, soft switching is used as opposed to conventional TSFs that require either hard or at least hybrid switching.

## References

[7-1]  V. Vujičić, ''Minimization of Torque Ripple and Copper Losses in Switched Reluctance Drive,'' *IEEE Transactions on Power Electronics*, vol. 27, no. 1, pp. 388-399, Jan. 2012.

[7-2]  X. Xue, K. Cheng, and S. Ho, ''Optimization and Evaluation of Torque-Sharing Functions for Torque Ripple Minimization in Switched Reluctance Motor Drives,'' *IEEE Transactions on Power Electronics*, vol. 24, no. 9, pp. 2076-2090, Sept. 2009.

[7-3]  D. Lee, J. Liang, Z. Lee, and J. Ahn, ''A Simple Nonlinear Logical Torque Sharing Function for Low-Torque Ripple SR Drive,'' *IEEE Transactions on Industrial Electronics*, vol. 56, no. 8, pp. 3021-3028, Aug. 2009.

[7-4]  J. Ye, B. Bilgin, and A. Emadi, ''An Extended-Speed Low-Ripple Torque Control of Switched Reluctance Motor Drives,'' *IEEE Transactions on Power Electronics*, vol. 30, no. 3, pp. 1457-1470, March 2015.

[7-5]  J. Ye, B. Bilgin, and A. Emadi, ''An Offline Torque Sharing Function for Torque Ripple Reduction in Switched Reluctance Motor Drives,'' *IEEE Transactions on Energy Conversion*, vol. 30, no. 2, pp. 726-735, June 2015.

[7-6]  Gan, J. Wu, Q. Sun, S. Yang, Y. Hu, and L. Jin, ''Low-cost direct instantaneous torque control for switched reluctance motors with bus current detection under soft-chopping mode,'' *IET Power Electronics*, vol. 9, no. 3, pp. 482-490, 9 3 2016.

[7-7]  Q. Sun, J. Wu, C. Gan, Y. Hu, and J. Si, ''OCTSF for torque ripple minimization in SRMs,'' *IET Power Electronics*, vol. 9, no. 14, pp. 2741-2750, 16 11 2016.

[7-8]  H. Li, B. Bilgin, and A. Emadi, ''An Improved Torque Sharing Function for Torque Ripple Reduction in Switched Reluctance Machines,'' *IEEE Transactions on Power Electronics*, vol. 34, no. 2, pp. 1635-1644, Feb. 2019.

# Chapter 9

## Conclusions and Future Research

This chapter summarizes the research, draws some conclusions about SRM drives for EV, and highlights the author's main contributions. Light is shed on aspects and topics for future research.

### 9.1 Summary and conclusions

In chapter 1 a brief overview on the thesis was presented highlighting the motivation for carrying out the research. Given the specification for EV, the SRM based drive was selected as a promising candidate, subject to specific limitations.

Chapter 2 presented the SRM structure highlighting the most common stator/rotor pole number configurations. The process of torque production, based on principles of electromechanical energy conversion, was discussed. SRM operation either in motoring or generating modes was demonstrated based on an approximate inductance profile. Although the SRM has a simple equivalent circuit, look-up tables for flux and torque (for different excitation levels and rotor positions) are needed to reflect the severe non-linearity of the machine. Controlling the SRM below and above base speed was illustrated, highlighting the difference between CCC and AAC. Finally, detailed design steps for initializing the SRM dimensions were presented.

Chapter 3 classified and reviewed the most common power converters used to feed the SRM. The difference between hard and soft switching converters was demonstrated. The main merits and drawbacks of each topology were highlighted. Finally, a comparison between power converters was presented which revealed that a double-arm converter with two phases sharing a common switch is the most suitable converter for EV applications.

A novel asymmetric NPC converter with inherent dc link voltage-boosting capacitors for a four-phase SRM drive was proposed in chapter 4. Analysis of the proposed converter during motoring and braking resulted in a design approach for sizing the dc link boost-capacitors. The proposed converter improves SRM drive performance at low and high speeds. The boost voltage increases the motor base speed, hence output power and efficiency. The SRM power to weight ratio with

173

voltage boosting capability is competitive with the PMSM and has the advantage of a higher torque to weight ratio. Regenerative braking can be deployed for efficient and fast braking action. The new converter allows series connection of fast, low-voltage, efficient switches. Topology penalties are increased number of gate drives and increased control complexity when introducing NPC intermediate dwell states.

Chapter 5 investigated the effect of utilizing rotor conducting screens to decrease SRM effective unaligned inductance. A detailed analytical approach, based on flux tube method, was proposed to calculate the effective unaligned inductance for a screened SRM. The proposed method was assessed on four different SRMs (two 3φ SRMS and two 4φ SRMs), where acceptable agreement between the proposed method and FEA was recorded.

Chapter 6 studied the effect of utilizing rotor conducting screens along with dc link voltage boosting-capacitors to enhance SRM performance. The effect of using conducting screens of different electrical conducting materials, thicknesses and shape on SRM performance was presented. Using a film screen with low electrical conductivity results in higher resistance to the induced voltage, hence the eddy current is smaller. Increased resistivity results in a reduced eddy current decay time constant.

A multi-objective optimization problem based on non-dominated sorting was formulated to elicit the optimal screen shape. Four designs are advised with respect to the developed torque, efficiency and weight of added material. A 3.5 cost ratio between copper and aluminium suggests that aluminium screens are lighter and cheaper than copper screens. However, torque improvement using aluminium screens is inferior to that of copper screens. Shifting the screen below the rotor pole tip (below the air gap) offers a trade-off between developed torque and efficiency.

DC link voltage boosting improves the power to weight performance but with increased semiconductor voltage stresses as a consequence of boost capacitor voltages in excess of the dc voltage source. An SRM with rotor conducting screens and dc link voltage-boosting improves SRM power to weight ratio to be competitive with an equivalent PMSM, but with the penalty of inevitable screen eddy current loss.

Because drive efficiency is of paramount importance in EV applications, chapter 6 clearly established that the use of rotor conducting screens, which although increases the base speed, is

untenable due to the inevitable associated Joules losses. But DC link voltage boost is a potential method for SRM performance enhancement in EV applications.

Chapter 7 classified, reviewed and assessed some of the most popular torque ripple, TR, minimization techniques. Most methods give low torque ripple (excluding switching ripple). Voltage-boosting significantly reduces the TR during commutation between two phases, for all torque methods by offering higher voltage during turn on/off. This highlights that optimal utilization of available dc link voltage extends the region over which the SRM can operate with zero TR (theoretically).

A new torque control function, TCF, was proposed in chapter 8. It offers maximum utilization of dc link voltage, hence, extending the zero TR speed range significantly. The new TCF is suitable for any SRM with any number of phases and stator/rotor pole number. Only magnetic characteristics (either obtained using FEA or experimentation) are needed. The proposed TCF is characterized by low switching losses as no switching is required for up to half the phase conduction period. In addition, a soft switching mode is used as opposed to conventional TSFs requiring either hard or at least hybrid switching modes.

## 9.2   Author's contribution

**The thesis contributions can be summarized into three drive components, as follows:**

*1) Converter contribution:*
- A new NPC converter was proposed for 4φ SRM drives. It uses semiconductor devices with lower voltage rating implying lower cost, smaller size, higher efficiency and faster response. The number of devices (but of lower voltage rating), along with the number of gate drives, are increased.
- The proposed converter improves SRM drive performance at low and high speeds. The boost voltage increases motor base speed, hence output power and efficiency. The SRM power to weight ratio with voltage boosting capability is competitive with the PMSM and has the advantage of a higher torque to weight ratio.
- Regenerative braking can be deployed for efficient and fast braking action.
- The proposed topology, which is based on the NPC, adds minimal cost to the converter when compared with the conventional common-phase topology.

175

- The PWM adopted in this control strategy uses only 0% and 100% duty cycles for the switches which enables the sampling (phase current) frequency to be twice the switching frequency for more accurate operation with lower switching losses and current ripple noise.

- Taking advantage of the multilevel feature allows reduced current ripple and hence noise, especially at low speeds.

- The adopted control strategy allows device losses to be symmetrical about the central leg which is a drawback in the prior state of the art converter topologies that cause asymmetry stress distribution.

2) *Machine contribution:*

- A detailed analytical method, based on flux tube method, was proposed to calculate the effective unaligned inductance for a screened SRM.

- The effect of using conducting screens of different materials, thicknesses and shape on SRM performance was presented. Using a film screen with low conductivity results in higher resistance to the induced voltage, hence the eddy current is smaller. Increased resistivity results in a reduced eddy current decay time constant.

- An SRM with rotor conducting screens and dc link voltage-boosting improves SRM power to weight ratio to be competitive with an equivalent PMSM, but with the penalty of inevitable screen eddy current loss.

- Because drive efficiency is of paramount importance in EV applications, the thesis clearly establishes that the use of rotor conducting screens, which although increases the base speed, is untenable due to the inevitable associated Joules losses. DC link voltage boost is a potential method for SRM performance enhancement in EV applications.

3) *TR contribution*

- A new TCF was proposed which offers maximum utilization of dc link voltage (either with or without boosting). Hence, extending the zero TR speed range significantly.

- The maximum SRM speed range with theoretically zero TR (that is, commutation ripple is eliminated and the ripple is only due to switching) is determined.

- The new TCF is suitable for any SRM with any number of phases and stator/rotor pole number. Only magnetic characteristics (either obtained using FEA or experimentation) is needed.

- The concept of TCF is generalized to include more than two phases conducting simultaneously (as opposed to traditional TSFs which are all based on a maximum of two phases conducting simultaneously).

- The proposed TCF is characterized by low switching losses as no switching is required for up to half the conduction period. In addition, a soft switching mode is used as opposed to conventional TSFs requiring either hard or at least hybrid switching modes.

- Commutation torque ripple and switching torque ripple can be assessed independently, by using current source phase current to assess commutation torque ripple and a voltage source model to assess switching ripple.

## 9.3  Future research

Some interesting topics could be further researched, such as:

*1  Converter:*

➢ Voltage boosting with 4 independent asymmetrical half bridges and with >30° conduction requires the complication and cost of 4 boost circuits, if maximum boost benefit is to be gained. Partial boosting can be achieved with 2 boost circuits with partially overlapping half bridges sharing a common boost circuit. The viability of such an arrangement can be assessed.

➢ The proposed converter could be deployed for 6φ SRM (less torque ripple) using three independent bridges. Namely, phases A and D forming bridge 1, B and E forming bridge 2 and finally, C and F forming bridge 3. Current sensors reduction from 6 (one for each phase) to 3 (one for each bridge) would be applicable as each two phases sharing a common switch are $90^0$ electrical displaced. Hence, there is no overlap between the two phases within each bridge. The viability of six phases against the need for 20,000rpm speeds can be assessed (more phases more core losses).

*2*  *Machine*

➢ Current SRMs are designed based on a fixed dc rail. Voltage boosting may afford opportunity to design the machine to take advantage of the boosting characteristics. For example, because of the extra voltage, the number of turns may be altered to improved specific characteristics.

➢ Odd phase number machines offer short flux path features (lower core losses) during commutation. This property can be partially achieved by using a 16/12 machine (90º rotor flux paths as opposed to 180º). Given an upper speed of 20,000rpm the trade-off between shorter flux paths and increased commutation losses can be investigated.

➢ Radial core distortion has not been investigated in this thesis. Given some of the current profiles involve conduction at alignment, the resultant radial forces need assessment, as does the extent of their mitigation given the re-enforcement offered by the water cooling jacket used in EV.

➢ Given the simple coil winding arrangement in the SRM, and water cooling, advanced manufacturing techniques may offer higher copper density (slot fill factor) improvement possibilities, for example with square section conductors.


3  *TR minimization:*

➢ For the TCF proposed in chapter 8, an ASHB based converter with voltage-boosting (4 boost-capacitors and 4 blocking diodes) could be deployed to further improve the zero TR speed range with the penalty of higher converter cost and size.

➢ Investigating the effect of varying the turn on angle on reducing peak/rms current without sacrificing the zero TR speed range at different torque levels, conduction periods and with/without voltage-boosting.

# Appendix A

## Main SRM Specifications

This appendix gives the specifications of the SRM used in simulations and for experimentation.

Table A.1 SRM SPECIFICATIONS

| Parameter | Value |
| --- | --- |
| No. of motor phases $m$ | 4 |
| Stator/rotor poles $N_s/N_r$ | 8/6 |
| Number of turns per pole $N$ | 90 |
| Rated voltage | 415V |
| Phase resistance $R$ | 0.8Ω |
| Stack length | 155mm |
| Shaft radius | 15mm |
| Rotor outer radius | 45mm |
| Thickness of rotor yoke | 15mm |
| Ratio of rotor pole arc to pole pitch | 0.35 |
| Length of air gap | 1mm |
| Stator inner radius | 46mm |
| Stator outer radius | 83mm |
| Thickness of stator yoke | 12mm |
| Ratio of stator pole arc to pole pitch | 0.42 |

# *Appendix B*

# *Test SRMs Specifications*

This appendix gives the specifications of three test SRMs used to validate the method proposed in chapter 5 for calculating the effective value of unaligned inductance for screened SRM.

Table B.1 TEST SRMs SPECIFICATIONS

| Parameter | Value | Value | Value |
|---|---|---|---|
| No. of motor phases $m$ | 3 | 4 | 3 |
| Stator/rotor poles $N_s/N_r$ | 6/4 | 8/6 | 6/4 |
| Number of turns per pole $N$ | 125 | 77 | 268 |
| Stack length | 100mm | 200mm | 60.37mm |
| Shaft radius | 15mm | 14mm | 14mm |
| Rotor outer radius | 50mm | 49.8mm | 51.03mm |
| Thickness of rotor yoke | 15mm | 16mm | 10.5mm |
| Ratio of rotor pole arc to pole pitch | 0.4 | 0.36 | 0.4 |
| Length of air gap | 0.5mm | 0.5mm | 0.25mm |
| Stator inner radius | 50.5mm | 50.3mm | 51.28mm |
| Stator outer radius | 90mm | 95mm | 95mm |
| Thickness of stator yoke | 14.5mm | 12mm | 10.5mm |
| Ratio of stator pole arc to pole pitch | 0.5 | 0.4 | 0.4 |

# Appendix C

## *SRM with Rotor Conducting Screens Results*

This appendix gives the results for different screen shapes assessed for creating the Pareto frontier as in chapter 6.

Table C.1 SRM SCREENS RESULTS

| Screen | Material | Weight of added material [kg/m] | Developed torque [N.m] | Efficiency [%] |
|--------|----------|----------------------------------|-------------------------|-----------------|
| 1 | CU | 1.618 | 24.81 | 68.24 |
| 2 | CU | 3.18 | 27.48 | 67.88 |
| 3 | CU | 4.686 | 29.26 | 69.52 |
| 4 | CU | 6.134 | 30.34 | 70.95 |
| 5 | CU | 7.526 | 30.88 | 71.87 |
| 6 | CU | 8.862 | 31.16 | 72.4 |
| 7 | CU | 10.14 | 31.16 | 72.4 |
| 8 | CU | 11.36 | 31.16 | 72.4 |
| 9 | CU | 12.53 | 31.16 | 72.4 |
| 10 | CU | 13.64 | 31.16 | 72.4 |
| 11 | CU | 14.69 | 31.16 | 72.4 |
| 12 | CU | 15.69 | 31.16 | 72.4 |
| 13 | CU | 16.62 | 31.16 | 72.4 |
| 14 | CU | 17.5 | 31.16 | 72.4 |
| 15 | CU | 18.33 | 31.16 | 72.4 |
| 16 | CU | 1.56 | 24.69 | 72.55 |
| 17 | CU | 3.07 | 26.85 | 72.13 |
| 18 | CU | 4.516 | 28.19 | 73.44 |
| 19 | CU | 5.908 | 29.05 | 74.64 |
| 20 | CU | 7.24 | 29.5 | 75.44 |
| 21 | CU | 8.523 | 29.5 | 75.44 |
| 22 | CU | 9.745 | 29.5 | 75.44 |
| 23 | CU | 10.91 | 29.5 | 75.44 |
| 24 | CU | 12 | 29.5 | 75.44 |

| | | | | |
|---|---|---|---|---|
| 25 | CU | 13.07 | 29.5 | 75.44 |
| 26 | CU | 14.07 | 29.5 | 75.44 |
| 27 | CU | 15 | 29.5 | 75.44 |
| 28 | CU | 15.89 | 29.5 | 75.44 |
| 29 | CU | 16.7 | 29.5 | 75.44 |
| | | | | |
| 30 | CU | 1.505 | 24.59 | 76.1 |
| 31 | CU | 2.954 | 26.2 | 75.49 |
| 32 | CU | 4.346 | 27.3 | 76.54 |
| 33 | CU | 5.682 | 27.93 | 77.52 |
| 34 | CU | 6.96 | 28.27 | 78.17 |
| 35 | CU | 8.183 | 28.27 | 78.17 |
| 36 | CU | 9.35 | 28.27 | 78.17 |
| 37 | CU | 10.46 | 28.27 | 78.17 |
| 38 | CU | 11.5 | 28.27 | 78.17 |
| 39 | CU | 12.5 | 28.27 | 78.17 |
| 40 | CU | 13.44 | 28.27 | 78.17 |
| 41 | CU | 14.33 | 28.27 | 78.17 |
| 42 | CU | 15.15 | 28.27 | 78.17 |
| | | | | |
| 43 | CU | 1.45 | 24.59 | 79 |
| 44 | CU | 2.84 | 25.83 | 78.35 |
| 45 | CU | 4.177 | 26.54 | 79.05 |
| 46 | CU | 5.456 | 27.15 | 79.9 |
| 47 | CU | 6.678 | 27.34 | 80.4 |
| 48 | CU | 7.843 | 27.34 | 80.4 |
| 49 | CU | 8.95 | 27.34 | 80.4 |
| 50 | CU | 10 | 27.34 | 80.4 |
| 51 | CU | 11 | 27.34 | 80.4 |
| 52 | CU | 11.94 | 27.34 | 80.4 |
| 53 | CU | 12.8 | 27.34 | 80.4 |
| 54 | CU | 13.64 | 27.34 | 80.4 |
| | | | | |
| 55 | Al | 0.47 | 23.97 | 71.4 |
| 56 | Al | 0.923 | 25.53 | 68.63 |
| 57 | Al | 1.36 | 26.92 | 69.07 |
| 58 | Al | 1.78 | 27.92 | 70.05 |

| | | | | |
|---|---|---|---|---|
| 59 | Al | 2.184 | 28.54 | 70.9 |
| 60 | Al | 2.57 | 28.9 | 71.5 |
| 61 | Al | 2.94 | 29.11 | 71.91 |
| 62 | Al | 3.297 | 29.11 | 71.91 |
| 63 | Al | 3.64 | 29.11 | 71.91 |
| 64 | Al | 3.957 | 29.11 | 71.91 |
| 65 | Al | 4.263 | 29.11 | 71.91 |
| 66 | Al | 4.55 | 29.11 | 71.91 |
| 67 | Al | 4.824 | 29.11 | 71.91 |
| 68 | Al | 5.08 | 29.11 | 71.91 |
| 69 | Al | 5.32 | 29.11 | 71.91 |
| | | | | |
| 70 | Al | 0.453 | 24 | 75.22 |
| 71 | Al | 0.89 | 25.27 | 72.8 |
| 72 | Al | 1.31 | 26.31 | 73.02 |
| 73 | Al | 1.714 | 27.13 | 73.81 |
| 74 | Al | 2.1 | 27.6 | 74.5 |
| 75 | Al | 2.473 | 27.84 | 75 |
| 76 | Al | 2.828 | 27.84 | 75 |
| 77 | Al | 3.166 | 27.84 | 75 |
| 78 | Al | 3.48 | 27.84 | 75 |
| 79 | Al | 3.8 | 27.84 | 75 |
| 80 | Al | 4.1 | 27.84 | 75 |
| 81 | Al | 4.36 | 27.84 | 75 |
| 82 | Al | 4.62 | 27.84 | 75 |
| 83 | Al | 4.85 | 27.84 | 75 |
| | | | | |
| 84 | Al | 0.437 | 24.05 | 78.35 |
| 85 | Al | 0.857 | 25 | 76.17 |
| 86 | Al | 1.26 | 25.82 | 76.25 |
| 87 | Al | 1.649 | 26.42 | 76.8 |
| 88 | Al | 2.02 | 26.81 | 77.4 |
| 89 | Al | 2.374 | 27 | 77.77 |
| 90 | Al | 2.713 | 27 | 77.77 |
| 91 | Al | 3.03 | 27 | 77.77 |
| 92 | Al | 3.33 | 27 | 77.77 |
| 93 | Al | 3.63 | 27 | 77.77 |

| 94 | Al | 3.9 | 27 | 77.77 |
|-----|-----|------|-------|-------|
| 95 | Al | 4.16 | 27 | 77.77 |
| 96 | Al | 4.4 | 27 | 77.77 |
| | | | | |
| 97 | Al | 0.42 | 24 | 79.1 |
| 98 | Al | 0.82 | 24.81 | 78.5 |
| 99 | Al | 1.21 | 25.4 | 78.8 |
| 100 | Al | 1.58 | 25.92 | 79 |
| 101 | Al | 1.94 | 26.1 | 79.2 |
| 102 | Al | 2.28 | 26.23 | 79.3 |
| 103 | Al | 2.6 | 26.23 | 79.3 |
| 104 | Al | 2.9 | 26.23 | 79.3 |
| 105 | Al | 3.19 | 26.23 | 79.3 |
| 106 | Al | 3.46 | 26.23 | 79.3 |
| 107 | Al | 3.7 | 26.23 | 79.3 |
| 108 | Al | 3.96 | 26.23 | 79.3 |

# Appendix D

## Experimental Test Rig

This appendix gives a description of the experimental test rig used to implement the power converter proposed in chapter 4.

A photograph of the test rig is shown in Fig D.1.
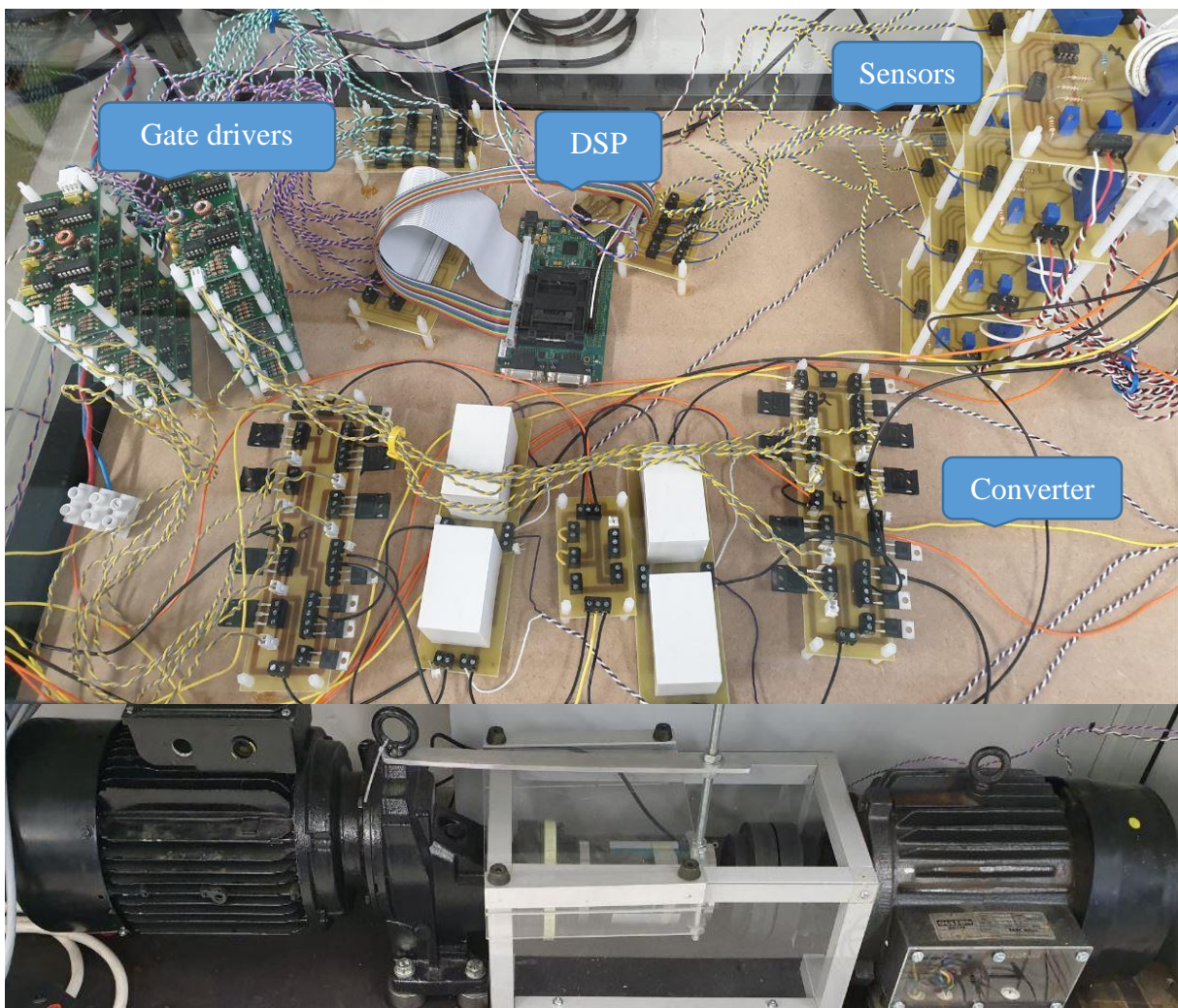


Fig. D.1 Experimental test rig

The experimental test rig is composed of:

- An SRM with specifications given in Appendix A loaded with induction machine.
- The proposed power converter.
- Digital signal processor (DSP).
- Gate driving circuits.
- Voltage and current sensors.

### I.   *DSP*

The main task of the DSP is to read the voltages of the four boost-capacitors along with the four currents of the SRM windings. Based on the proposed control law, the DSP generates the required gating signals to drive the power converter. The DSP used in the experimentation is TMS320F28335 shown in Fig. D.2.



Fig. D.2 TMS320F28335 DSP

The major features justifying this choice could be summarized as follows:

- ✓ Up to 88 digital input/output pins.
- ✓ 16 channels of 12-bit analogue to digital converter.
- ✓ Up to 18 enhanced PWM.
- ✓ Easily programmed using MATLAB/Simulink package.
- ✓ Fast processing speed (150MHZ).
- ✓ High performance 32-bit central processing unit.

## II.    *Gate driving circuits*

The gate drivers are used to isolate the DSP from the power converter. A photograph of the used gate driver is given in Fig. D.3.



Fig. D.3 Gate driving circuit

## III. *Voltage and current sensors*

A photograph showing the voltage and current measurement board is illustrated in Fig. D.4.



(a)                                          (b)
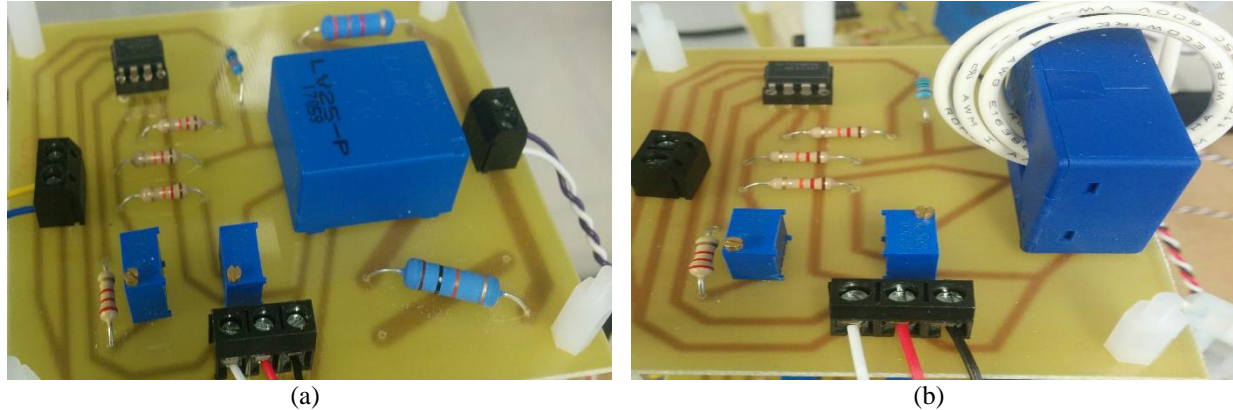
Fig. D.4 Measurement board: (a) Voltage, and (b) Current

Voltage sensors (LEM LV 25-P) with data sheet shown in Fig. D.5a, along with current sensors (LEM LA 55-P) with data sheet shown in Fig. D.5b are used to measure the voltage and current respectively.



# Voltage Transducer LV 25-P

For the electronic measurement of currents: DC, AC, pulsed..., with galvanic separation between the primary circuit and the secondary circuit.

$I_{PN}$ = 10 mA
$V_{PN}$ = 10 .. 500 V
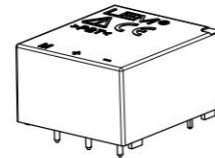
### Electrical data

| | | | | |
|---|---|---|---|---|
| $I_{PN}$ | Primary nominal rms current | 10 | | mA |
| $I_{PM}$ | Primary current, measuring range | 0 .. ± 14 | | mA |
| $R_M$ | Measuring resistance | $R_{M\ min}$ | $R_{M\ max}$ | |
| | with ± 12 V  @ ± 10 mA$_{max}$ | 30 | 190 | Ω |
| | @ ± 14 mA$_{max}$ | 30 | 100 | Ω |
| | with ± 15 V  @ ± 10 mA$_{max}$ | 100 | 350 | Ω |
| | @ ± 14 mA$_{max}$ | 100 | 190 | Ω |
| $I_{SN}$ | Secondary nominal rms current | 25 | | mA |
| $K_N$ | Conversion ratio | 2500 : 1000 | | |
| $U_C$ | Supply voltage (± 5 %) | ± 12 .. 15 | | V |
| $I_C$ | Current consumption | 10 (@ ± 15 V) + $I_S$ | | mA |

### Accuracy - Dynamic performance data

| | | | |
|---|---|---|---|
| $X_G$ | Overall accuracy @ $I_{PN}$, $T_A$ = 25 °C @ ± 12 .. 15 V | ± 0.9 | % |
| | @ ± 15 V (± 5 %) | ± 0.8 | % |

### Features

- Closed loop (compensated) current transducer using the Hall effect
- Insulating plastic case recognized according to UL 94-V0.

### Principle of use

- For voltage measurements, a current proportional to the measured voltage must be passed through an external resistor $R_1$ which is selected by the user and installed in series with the primary circuit of the transducer.

(a)

## Current Transducer LA 55-P

$I_{PN}$ = 50 A

For the electronic measurement of currents: DC, AC, pulsed..., with galvanic separation between the primary circuit and the secondary circuit.

### Electrical data

| | | | $T_A$ = 70 °C | | $T_A$ = 85 °C | | |
|---|---|---|---|---|---|---|---|
| | | | $R_{M\,min}$ | $R_{M\,max}$ | $R_{M\,min}$ | $R_{M\,max}$ | |
| $I_{PN}$ | Primary nominal RMS current | | 50 | | | | A |
| $I_{PM}$ | Primary current, measuring range | | 0 ... ±70 | | | | A |
| $R_M$ | Measuring resistance | | | | | | |
| | with ±12 V | @ ±50 A $_{max}$ | 10 | 100 | 60 | 95 | Ω |
| | | @ ±70 A $_{max}$ | 10 | 50 | 60 [1] | 60 [1] | Ω |
| | with ±15 V | @ ±50 A $_{max}$ | 50 | 160 | 135 | 155 | Ω |
| | | @ ±70 A $_{max}$ | 50 | 90 | 135 [2] | 135 [2] | Ω |
| $I_{SN}$ | Secondary nominal RMS current | | 50 | | | | mA |
| $N_P/N_S$ | Turns ratio | | 1 : 1000 | | | | |
| $U_C$ | Supply voltage (±5 %) | | ±12 ... 15 | | | | V |
| $I_C$ | Current consumption (±2) | | 10 (@ ±15 V) + $I_S$ | | | | mA |

**Features**

- Closed loop (compensated) current transducer using the Hall effect
- Insulating plastic case recognized according to UL 94-V0.

**Advantages**

- Excellent accuracy
- Very good linearity

(b)

Figure D.5 Sensors specification: (a) Voltage, and (b) Current

The sensors are implemented with a conditioning circuit as shown in Fig. D.6. for both voltage and current.
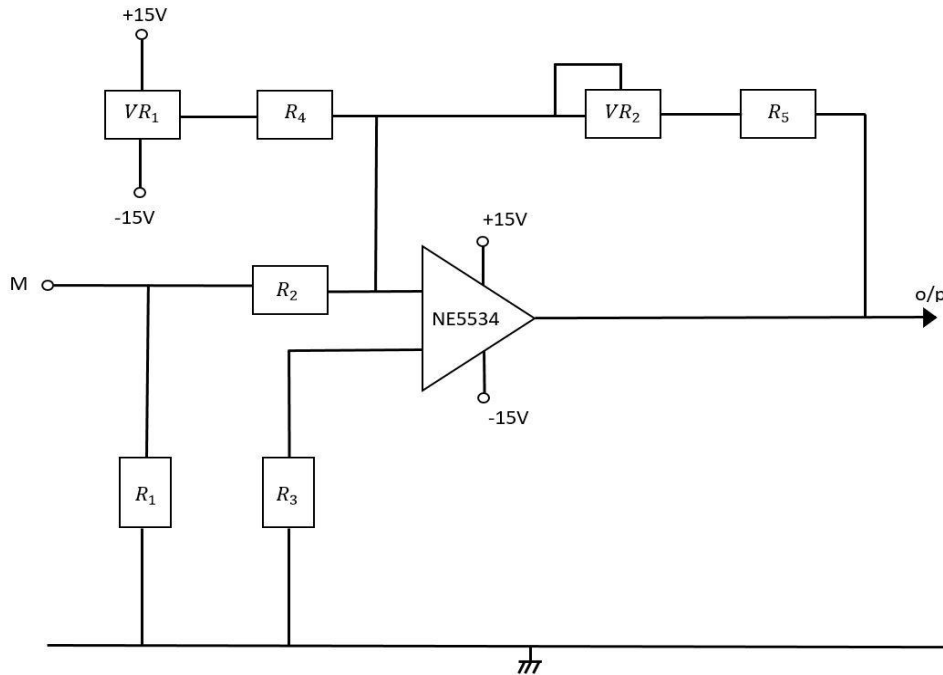


Fig. D.6 Conditioning circuit for voltage and current measurement

For both circuits:

$R_2 = R_3 = R_4 = 12k\Omega$ $(fixed\ value)$

$VR_1$(For offset adjustment) $= VR_2$ (For gain adjustment) $= 10k\Omega$ $(variable\ resistor)$

$gain = \frac{VR_2 + R_5}{R_2}$ (<1 to minimize the effect of noise, so $R_5$ is chosen to be 2.2k$\Omega$ and $VR_2$ is adjusted on 5k$\Omega$ for 0.6 gain value).

### Current board:



Fig. D.7 Current transducer terminals

$\frac{NI}{1000} * R_1 * gain = 3.3V$ (According to transducer specifications $R_1$ is in the range of 135$\Omega$-155$\Omega$, so a value of 150$\Omega$ is chosen).

### Voltage board:
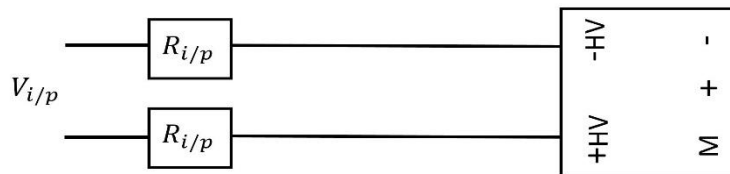


Fig. D.8 Voltage transducer terminals

$10mA * 2.5 * R_1 * gain = 3.3V$ (According to transducer specifications $R_1$ is the range of 100$\Omega$-350$\Omega$, so a value of 220$\Omega$ is chosen).

$2R_{i/p} = \frac{V_{i/p}\ (max)}{10mA}$ (For 165V max voltage, 16.6k$\Omega$ overall input resistors are chosen).

# *Appendix E*

# *List of Figures*

# *Appendix F*

# *List of Tables*

# *Appendix G*

# *Publications*

---

[1] A. A. Abdel-Aziz, K. H. Ahmed, S. Wang, A. M. Massoud and B. W. Williams, "A Neutral-Point Diode-Clamped Converter With Inherent Voltage-Boosting for a Four-Phase SRM Drive," in *IEEE Transactions on Industrial Electronics*, vol. 67, no. 7, pp. 5313-5324, July 2020.

**Abstract:**

This article proposes a new asymmetric neutral-point diode-clamped (NPC) multilevel converter for a four-phase switched reluctance motor drive. The inbuilt NPC clamping capacitors are used for both voltage level clamping and also as dc rail voltage-boosting capacitors to increase the output power of the motor, particularly for high-speed electric vehicle applications. The new converter allows regenerative energy to be recovered back to the dc supply for rapid machine braking, thus increasing overall drive efficiency. Analysis of the different modes of converter operation, along with design equations for sizing the voltage-boosting capacitors, is detailed. The effect of capacitance on boost voltage and increased motor base speed is presented. Simulation and experimental results confirm the effectiveness of the proposed converter.